Extension of Particle Image Velocimetry to Full-scale Turbofan Engine Bypass Duct Flows

William Mallory George

Thesis submitted to the faculty of the Virginia Polytechnic Institute and State University
in partial fulfillment of the requirements for the degree of

Master of Science
In
Aerospace Engineering

K. Todd Lowe
Joseph A. Schetz
Walter F. O'Brien

April 28, 2017
Blacksburg, Virginia

Keywords: Particle Image Velocimetry, Full-Scale Turbofan, Bypass Duct, Loss Mechanisms, Spatial Sampling Error

Extension of Particle Image Velocimetry to Full-scale Turbofan Engine Bypass Duct Flows

William Mallory George

ABSTRACT

Fan system efficiency for modern aircraft engine design is increasing to the point that bypass duct geometry is becoming a significant contributor and could ultimately become a limiting factor. To investigate this, a number of methods are available to provide qualitative and quantitative analysis of the flow around the loss mechanisms present in the duct. Particle image velocimetry (PIV) is a strong candidate among experimental techniques to address this challenge. Its use has been documented in many other locations within the engine and it can provide high spatial resolution data over large fields of view. In this work it is shown that these characteristics allow the PIV user to reduce the spatial sampling error associated with sparsely spaced point measurements in a large measurement region with high order gradients and small spatial scale flow phenomena. A synthetic flow featuring such attributes was generated by computational fluid dynamics (CFD) and was sampled by a virtual PIV system and a virtual generic point measurement system. The PIV sampling technique estimated the average integrated velocity field about five times more accurately than the point measurement sampling due to the large errors that existed between each point measurement location. Despite its advantages, implementation of PIV can be a significant challenge, especially for internal measurement where optical access is limited. To reduce the time and cost associated with iterating through experiment designs, a software package was developed which incorporates basic optics principles and fundamental PIV relationships, and calculates experimental output parameters of interest such as camera field of view and the amount of scattered light which reaches the camera sensor. The program can be used to judge the likelihood of success of a proposed PIV experiment design by comparing the output parameters with those calculated from benchmark experiments. The primary experiment in this work focused on the Pratt and Whitney Canada JT15D-1 aft support strut wake structure in the bypass duct and was comprised of three parts: a simulated engine environment was created to provide a proof

of concept of the PIV experiment design; the PIV experiment was repeated in the full scale engine at four fan speeds ranging from engine idle up to 80% of the maximum corrected fan speed; and, finally, a CFD simulation was performed with simplifying assumptions to provide insight and perspective into the formation of the wake structures observed in the PIV data. Both computational and experimental results illustrate a non-uniform wake structure downstream of the support strut and support the hypothesis that the junction of the strut and the engine core wall is creating a separate wake structure from that created by the strut main body. The PIV data also shows that the wake structure moves in the circumferential direction at higher fan speeds, possibly due to bulk swirl present in the engine or a pressure differential created by the support strut. The experiment highlights the advantages of using PIV, but also illustrates a number of the implementation challenges present, most notably, those associated with consistently providing a sufficient number of seeding particles in the measurement region. Also, the experiment is the first to the author's knowledge to document the use of PIV in a full scale turbofan engine bypass duct.

Extension of Particle Image Velocimetry to Full-scale Turbofan Engine Bypass Duct Flows

William Mallory George

GENERAL AUDIENCE ABSTRACT

Recent advances in aircraft engine design have reduced the effects of components with major reductions in engine efficiency. Because of this, lesser contributors such as bypass duct geometry could now become limiting factors. Particle image velocimetry (PIV) is a strong candidate among experimental techniques to investigate the flow around the loss mechanisms present in the bypass duct. It can provide high spatial resolution data over large fields of view and its use has been documented in many other locations within the engine. In this work it is shown that these characteristics allow the PIV user to reduce the error associated with sparsely spaced point measurements. A synthetic flow was generated by computational fluid dynamics (CFD) and was sampled by a virtual PIV system and a virtual generic point measurement system. Due to the large errors that existed between each point measurement location, the PIV sampling technique estimated the average flow about five times more accurately than the point measurement sampling. Despite its advantages, implementation of PIV can be a significant challenge. To reduce the time and cost associated with iterating through experiment designs, a software package was developed which incorporates basic optics principles and fundamental PIV relationships, and calculates experimental output parameters of interest such as the amount of light that reaches the camera sensor. The program can be used to judge the likelihood of success of a proposed PIV experiment design by comparing the output parameters with those calculated from benchmark experiments. The primary experiment in this work focused on the aft support strut wake structure in the Pratt and Whitney Canada JT15D-1 bypass duct. It was comprised of three parts: a PIV experiment design proof of concept using a simulated engine environment; a full scale engine PIV experiment was repeated at four fan speeds ranging from engine idle up to 80% of the maximum-fan speed; and, finally, a simplified CFD simulation was performed to provide insight and perspective into the PIV data. Both computational and experimental results illustrate a non-uniform wake structure

downstream of the support strut and support the hypothesis that the junction of the strut and the engine core wall is creating a separate wake structure from that created by the strut main body. The PIV data also shows that the wake structure moves in the circumferential direction at higher fan speeds, possibly due to bulk swirl present in the engine or a pressure differential created by the support strut. The experiment highlights the advantages of using PIV, but also illustrates a number of the implementation challenges present such as providing consistent seeding in the measurement region. Also, the experiment is the first to the author's knowledge to document the use of PIV in a full scale turbofan engine bypass duct.

Acknowledgements

First and foremost, I would like to thank the Lord, my Father, for His strength to pursue my dreams and for all the challenges, opportunities, and blessings He has bestowed upon me. Through Him, all is possible. Next I would like to thank my advisor and mentor, Dr. Todd Lowe, for his guidance and support throughout my time here in Blacksburg. For this opportunity, I am extremely grateful. Additionally, I would like to thank Dr. Schetz and Dr. O'Brien for serving on my committee and for providing helpful insight whenever I had a question. Thank you to my sponsors at Pratt & Whitney, specifically Justin Urban, Andy Consiglio, and Darren Wind and thank you to my colleagues that put a tremendous effort into this project alongside me, Hannah Kirk, Matthew Boyda, Tamy Guimarães, Hameed Talebian, and Dustin Frohnapfel. I want to thank all of my friends and family who have been so instrumental in my success. I want to thank my parents, Kirk and Kim George, and my brother, Brian George, for always pushing me to be better and fulfil my God given potential. I want to thank my grandparents, Don and Sharon Griffith, and Betty Runyan. I want to thank my extended family, Judi, Bobbi, Mike, Susan, Ed, Cindy, Mark, Kristi, Mike, Kippi, Kevin, Sarah, Michael, Kaitlyn, Eric, Kayla, Christopher, Katherine, and Thomas. I want to thank my friends, especially Devon, Brandon, Colin, Josh, Matt, Tyler, Eric, Dan, Marcie, Sean, Kara, Tamy, Nick, Kyle, Chi, and Matthew. To everyone I have not named, thank you for this has truly been a group effort. Lastly, I want to dedicate this work to my late grandfathers, Papa John "Bugs" Mallory, Grandpa Warren Runyan, and Papa Bob George. I hope I've made you proud.

Table of Contents

List of Figures

List of Tables

Nomenclature

Acronyms

CAD	Computer aided design
CCD	Charged coupled device
CFD	Computational fluid dynamics
CFS	Corrected fan speed
EDA	Experimental Design Aid
Nd:YAG	Neodymium-doped yttrium aluminium garnet
Nd:YLF	Neodymium-doped yttrium lithium fluoride
PIV	Particle image velocimetry
RANS	Reynolds averaged Navier-Stokes
SST	Shear stress transport

Letters and Symbols

$\boldsymbol{\alpha}$	Angle of camera relative to laser sheet
$\boldsymbol{D_a}$	Lens aperature diameter
$\boldsymbol{d_a}$	The diameter of aberrated image of a point source
$\boldsymbol{d_p}$	Particle mean diameter
$\boldsymbol{d_r}$	Pixel pitch (size of pixels on CCD)
$\boldsymbol{d_s}$	Particle diffraction-limited spot diameter
$\boldsymbol{d_\tau}$	Approximate particle image diameter
$\boldsymbol{\delta_Z}$	Depth of focus
$\boldsymbol{\delta_z}$	Depth of field
dt	Time between laser pulses
$\boldsymbol{E}$	Local normalized error
$\boldsymbol{f}$	Lens focal length
$\boldsymbol{f^\#}$	Lens aperture number

J_0	Laser output power
l_x	Field of view, x direction
l_y	Field of view, y direction
$\dot{m}$	Mass flow rate
M_0	Magnification
μ_f	Fluid dynamic viscosity
N	Fan rotational velocity [rad/s]
N_x	CCD size in x direction
N_y	CCD size in y direction
ρ	Density
ρ_0	Stagnation density
ρ_p	Particle density
RI_{medium}	Refractive index of the medium
RI_{real}	Real component of the refractive index of the particle
T_0	Stagnation temperature
$T_{0,st\ day}$	Standard day stagnation temperature
τ_p	Particle dynamic response time
u	Fluctuating velocity
V	Local velocity
$w_{sampled}$	Sampled stream-wise velocity
w_{true}	Synthetic flow stream-wise velocity
w_∞	Representative synthetic flow freestream stream-wise velocity
Ω	Solid angle subtended by the lens aperture at a particle at the center of the measurement plane
λ	Laser beam wavelength
Δy_0	Height of laser sheet
Z_0	Image distance
z_0	Object distance (distance between camera and measurement plane)
Δz_0	Thickness of laser sheet

1 Introduction

Particle image velocimetry (PIV) is an advanced laser diagnostics technique applicable to a wide range of flows, and is capable of producing a data plane of densely packed velocity vectors [1]. Although previously confined to laboratory bench-top settings, its maturation has expanded its reach into more complex environments. One such environment is a full-scale turbofan engine, which, depending on the area under study, may feature any combination of tight spaces, high temperatures, high vibrations, or highly turbulent flow. Any one of these has the potential to greatly increase the difficulty associated with the experiment. However, the benefits of a successful PIV experiment involving a full-scale turbofan engine are more than enough to warrant the trials and failures encountered along the way. Most notably, PIV provides quantified flow visualization. It allows for the observation of entire flow features or how these features may convect downstream in a flow. PIV can provide insight into a flow that may have previously only been quantified by a small set of temperatures or pressures. In addition to this insight, PIV can be used to calculate turbulence statistics [2], [3], or observe transient phenomena [4], but in general, it provides a means by which to efficiently acquire data at a large number of locations.

Despite the difficulties, several research groups have successfully applied PIV techniques to full-scale turbofans or turbofan components. The generation of distorted inlet flows has been characterized in part by Nelson [5] and Guimarães et al. [6]. Schröder et al. [7] investigated the engine inlet ground vortices and jet exhaust of an Airbus A320 in ground operations while illuminating many of the difficulties and solutions of such a large-scale experiment. Notable work implementing PIV in compressors has been accomplished by Wernet et al. [8], Liu et al. [9], Estevadeordal et al. [10], and Brandstetter et al. [11]. Similarly, Willert et al. [12] and Sadanandan et al. [13] have reported on model combustors and Gallier et al. [14] , Lang et al. [15], Porreca et al. [16], and Kegalj, Schiffer [17] have documented work in turbines. Lastly, full-scale exhaust flows measured with PIV have been examined by Skeen [18] and the previously mentioned Schröder et al. [7], [19].

However, to the author's knowledge, no work has documented the use of PIV in the bypass duct of a full-scale turbofan engine.

The lack of PIV experimentation in this area can likely be attributed to the larger potential gains featured in other regions, such as the compressor. That being said, turbomachine designers are constantly pursuing means of increasing overall efficiency, even if by only hundredths of a percent [20], [21], [22]. There are numerous loss mechanisms downstream of the fan in the bypass duct including struts, fuel pipes, bleed ports, and the duct walls themselves. Epstein [22] discusses the trend of turbofan manufacturers increasing the propulsive efficiency by increasing the bypass ratio and decreasing the fan pressure ratios of the engine. He continues stating that by doing so, the impact of the fan rotor on fan stream propulsive efficiency decreases and the effect of the duct geometry increases. It is imperative then that focus is placed on understanding the aerodynamics of the loss mechanisms in the bypass duct as well as how to mitigate them.

To address the first focus, PIV will be shown to preferable to other techniques such as five-hole-probes or hot wire anemometry. Although PIV is a more complex experimental technique and likely requires more time up front for planning and setup, once the experiment is running, PIV can produce a vast wealth of information in a fraction of the time of other methods. It serves primarily as a flow visualization method which can be particularly beneficial in determining the wake structure of a loss mechanism, or the interaction between rotors and stators, for example. It can shed light on how flow phenomena evolve with downstream distance or how flow features fluctuate at a given location over time. PIV is also advertised as a non-intrusive method; however, this is only partially true for turbofan experiments due to the close-quarter nature of many of the flows under study. For example, measuring inlet and exhaust flows can be perfectly non-intrusive; however, when studying a compressor for example, one generally needs to use endoscopes in order to illuminate the measurement plane with the laser sheet but also so that the cameras can have optical access inside the compressor to capture the image, e.g., as in Kegalj and Schiffer [17].

Typically, many modern aerodynamic experiments, such as the ones listed, are accompanied by a computational fluid dynamics (CFD) solution. In some of these cases, the CFD model may require verification and/or validation before it is accepted as true.

Stern et al. [23] defines verification as a process for assessing the simulation numerical uncertainty whereas validation is a process for assessing simulation modeling uncertainty by using benchmark experimental data. The methodology behind verification and validation is well described by Stern et al. [23] and Oberkampf and Trucano [24]. Grace and Taghipour [25] add that it can be argued that it is never possible to truly validate a model according to its legalistic definitions, but it can be validated in a practical sense if it matches within error bounds of multiple independent experiments.

There are obviously several ways by which to acquire data to achieve practical validation of a CFD model. A few examples are listed here. Coleman and Stern [26] and Jessup [27] utilized a three-component laser-Doppler velocimetry (LDV) system. Santiago et al. [28] and Brown et al. [29] used pulsed-wire anemometry to measure velocity time series. Dunham [30] outlined two experiments, one of an axial-flow compressor rotor and the other of an axial-flow turbine inlet stator blade row. The first measured total pressure, absolute flow angle, and total temperature by using a combination cobra head probe with a thermocouple, and then also measured static pressure with a wedge probe. The second experiment utilized a 5-hole probe. Lastly, Oberkampf and Smith [31], Sheng and Fox [32] and Ceccio [33] discussed how PIV can be used to validate CFD.

One problem with many of these techniques, however, arises when the flow under study is large and complex, potentially with high-order three dimensional gradients and/or with small spatial scale flow features. In such a scenario, point measurement techniques are likely to be less effective due to the interpolation that must occur between measurement locations. Even if the number of locations was increased and spacing between locations decreased, the total time required to acquire the data in such a test is likely prohibitively high. A method such as PIV is uniquely suited to this application with its ability to capture both large fields of view (greater than 0.3 m x 0.3 m) while maintaining small spatial scale resolution. The greatest downside to PIV is its complexity and the many sources of potential error that arise from it. While many point measurement techniques, such as commercial pressure transducers, can achieve accuracies greater than $\pm$0.1% of the full-scale and some as high as $\pm$0.03% [34], the often referenced uncertainty for the estimation of the displacement in an ideal PIV experiment is 1-2% of the full-scale velocity [3]. In many non-ideal cases, this value can be even higher [35], [36]. That said, PIV should still

be the method used to validate CFD models of large regions that contain high order gradients and small spatial scale flow phenomena because of PIV's capability to reduce the spatial sampling error associated with point measurements in a time efficient manner.

As researchers continue to mature PIV, enabling application to new experimental environments, the implementation of PIV should be made simpler so that experimentalists of broad experience can effectively use the technique. This is not a trivial task, and it will require many incremental steps along the way. One area where PIV can be improved is in the process of designing the experiment. Generally speaking, the likelihood of success of a modern PIV experiment, as well as its capability of producing the desired field of view, scattered light intensity, seed dispersal density, among other considerations, is heavily dependent on the experience of the experimenter, and trial and error. However, the information to quickly determine if a proposed PIV setup would be successful is available in the literature. It is best summarized by Adrian and Westerweel [3]. That said, it can be a daunting or, in the least, a time consuming task to attempt to use known optical laws and relationships to figure out if camera and laser positions, lens magnifications, laser power, and a number of other experimental parameters will produce the desired results. By considering basic optics physics, Mie scattering theory, and an equation for mean exposure [3], a proposed PIV experiment can be quantitatively compared to previously successful PIV experiments. These comparisons can serve as a basis to judge the likelihood of success of the proposed design. This can be done quickly and efficiently, reducing the number of design iterations of novice PIV experimentalists, and perhaps serving as a risk reduction tool for more experienced users.

In this thesis, contributions to the application of PIV are discussed. For large and complex flows with high order gradients, PIV has been shown to be several times more accurate than a generic point measurement technique due to PIV's superior spatial resolution. A software package named Experimental Design Aid (EDA) has been developed to quantitatively compare PIV experiments in order to judge the likelihood of a proposed design being successful. Lastly, PIV data acquisition was performed successfully in the bypass duct of a full-scale operating turbofan engine and used in conjunction with a coarse CFD model to gain a better understanding of a loss mechanism in the bypass duct

and the wake structures it generates. To the author's knowledge, this is the first instance of PIV data acquisition in the bypass duct of a full-scale engine documented in the literature.

The chapters of this work are outlined as follows. Chapter 2 provides a brief overview of particle image velocimetry. Chapter 3 discusses spatial sampling error for PIV and a generic point measurement technique and compares the differences. Chapter 4 describes the development and application of the Experimental Design Aid (EDA) software package, as well as desirable features that should be implemented in the future. Chapter 5 describes the methodology of the JT15D-1 experiment, the accompanying CFD analysis, the development of an interim risk reduction experiment in a simulated engine environment, and the specifics of the final experiment that utilized the Virginia Tech JT15D-1 research engine. Chapter 6 compares the experimental and computational results. Lastly, Chapter 7 presents the conclusions of this thesis and the recommended future work.

2 Particle Image Velocimetry

Particle image velocimetry is a well-established, quantitative flow visualization technique and generally does not require any form of intrusion into the flow, with the exception of the particles inserted into the flow. PIV has been evolving over the last 20 plus years [1] and is utilized over a wide range of flow scales from tens of micrometers [37] to tens of meters [38]. Additionally, PIV can produce a variety of results including the traditional 2D-2-component (planar PIV), 2D-3-component (stereo PIV) [39], 3D-3-component tomographic PIV [40], and 2D-3-component plus acceleration (multi-pulse PIV) [41]. Adrian and Westerweel [3] provide extensive information on a large number of applications and theory relating to PIV.

The concept of PIV is fairly simple even if its implementation is less so. Traditional planar 2-component PIV will be described here. Microscopic particles are inserted into the flow, upstream of the desired measurement plane. The particles travel downstream, ideally following the exact motion of the flow. The measurement plane is then illuminated with a light sheet created by a double pulsed laser. Precise timing, high resolution cameras photograph the particles that are illuminated in the measurement plane during the two laser pulses. The two pulses are separated by some amount of time, typically on the order of microseconds, so that the particles are in different locations in the two frames that make up the image pair. Next, images are broken up into smaller interrogation regions. The first and second frames from each interrogation region are analyzed using an image cross-correlation algorithm in order to determine the most probable displacement of the particles within that particular interrogation region. This process is repeated for every interrogation region in the image so that a pixel displacement vector field is generated. A pixel space-real world space calibration converts the pixel displacements into meter displacements and the time between pulses is then used to calculate the velocity vectors. This process is illustrated by Figure 1.

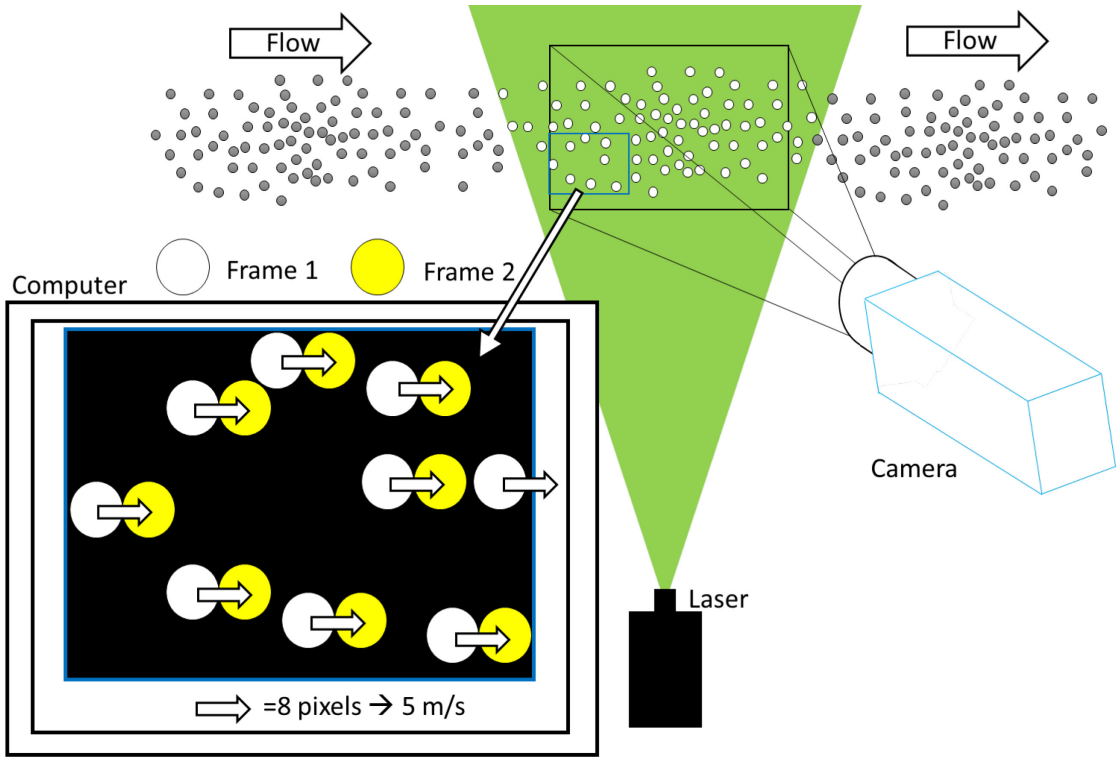

Figure 1 – PIV data acquisition process

One of the drawbacks to PIV is the complexity and number of systems and processes that make up a PIV experiment. This makes implementation more difficult, and also introduces a variety of potential sources of error. Many times the error is estimated as the velocity that corresponds with a 0.1 pixel displacement. However, Charonko and Vlachos [35] point out that this is true only in ideal scenarios and this value is often referenced erroneously. For a detailed discussion on PIV uncertainty and the uncertainty in the measurements for the work detailed in this thesis, the reader is referred to Appendix A.1.

3 Assessment of Spatial Sampling Error

3.1 Methodology

When acquiring data for the practical validation of CFD, the most desired experimental data set would be the one that most accurately represents the flow being modeled. One of the problems associated with acquiring this dataset with point measurement techniques arises when the flow measurement region is large and includes small spatial scale features and/or high order gradients. In such a situation, the experimentalist is faced with the task of deciding whether to acquire a strenuous amount of data over a long period of time, a large amount of data but over a short period of time at the risk of more blockage and a higher influence on the flow, or a reasonable number of data points but at the risk of not capturing some of the flow features. PIV on the other hand, while not capable of the same measurement accuracy as many point measurement techniques, is able to capture both a large plane of data and small spatial scale features in a timely and efficient manner. The ability of PIV to capture such a higher spatial resolution compared to a typical point measurement experiment is what ultimately makes it a more accurate choice in the example that will be shown.

For this example, a synthetic flow field was generated using CFD. It is the same geometry and measurement plane as the experiment that will be discussed later in Section 5.5.2.1. However, it is not the final solution. Rather it was an interim solution that simply serves as the synthetic flow needed for this example. For now, the geometry will remain ambiguous as it is irrelevant to this analysis. The synthetic flow is depicted in Figure 2 and Figure 3. The unstructured grid of CFD data was interpolated into a rectangular mesh grid of data points with a spacing of 0.18 mm in the horizontal direction and 0.34 mm in the horizontal direction.

The next step involved the technique appropriate sampling of the synthetic flow data. For the probe sampled case, data acquisition locations were centered on 4° circumferential intervals and approximately 7.4 mm radial intervals as shown by the black dot markers in Figure 2. A 1 mm diameter region was created around each of these locations and all the

synthetic flow data within this region was averaged into a single "sampled" value. The initially sampled value was then multiplied by an uncertainty factor of $\pm 0.01\%$ of the max sampled stream-wise velocity to calculate the final sampled value. Although achieving a measurement accuracy of 0.01% is extremely difficult in practice, this value was chosen to make a simple two order of magnitude difference with the PIV uncertainty value and also to demonstrate it is the spatial resolution that matters rather than the measurement accuracy. The final sampled value was then applied as the sampled value to all the "nearest neighbor" locations in the original synthetic flow mesh grid, shown in Figure 4. The numbered markers are at the same locations for Figure 2 through Figure 7 and will be referenced during the analysis portion of this example.

The PIV sampled case was treated very similarly. First, interrogation regions were set up to mimic the resolution achieved in the experiment detailed in Section 5.5.2.1. This resulted in interrogation regions about 2.2 mm x 2.2 mm in size with 0% overlap. The corners of the interrogation regions are displayed as the black dot markers in Figure 3. Again, the synthetic flow data within this region were averaged into a single value and multiplied by an uncertainty factor of $\pm 1\%$ of the max sampled stream-wise velocity. This value served as the representative value for all of the original synthetic flow mesh grid locations within the interrogation region borders as depicted in Figure 5.

In both cases, the local normalized error was calculated as one hundred times the absolute difference between the sampled value and the true value, normalized by a representative stream-wise velocity ($w_\infty = 150$ m/s) taken from an undisturbed region of the synthetic flow, given in Equation (3.1).

$$E_i = 100 * \frac{\left| w_{sample,i} - w_{true,i} \right|}{w_\infty} \tag{3.1}$$

This set of data provided an opportunity for qualitative analysis of the error, but was also used quantitatively to produce a mean error and a mass averaged mean error where the latter is described by Equation (3.2),

$$\bar{E} = \frac{\sum \dot{m} E_i}{\sum \dot{m}} = \frac{\sum |V_i| E_i}{\sum |V_i|} \tag{3.2}$$

which is simplified assuming constant density and area, and where $|V_i|$ is the magnitude of the local three-component velocity. Furthermore, the distributions of local normalized error were visualized using histograms with bin widths of 0.5% of the normalizing velocity.

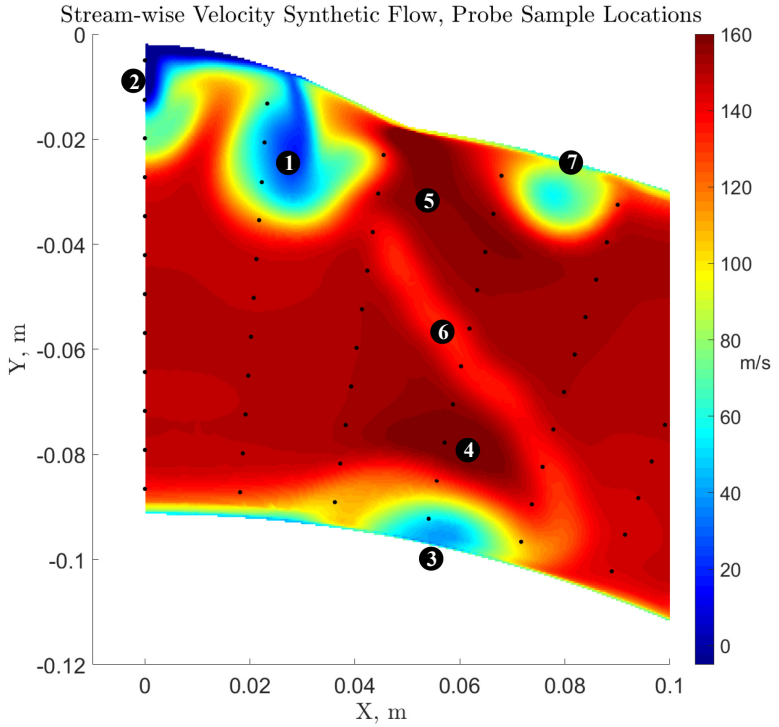

Figure 2 – Synthetic stream-wise velocity with probe sampling locations

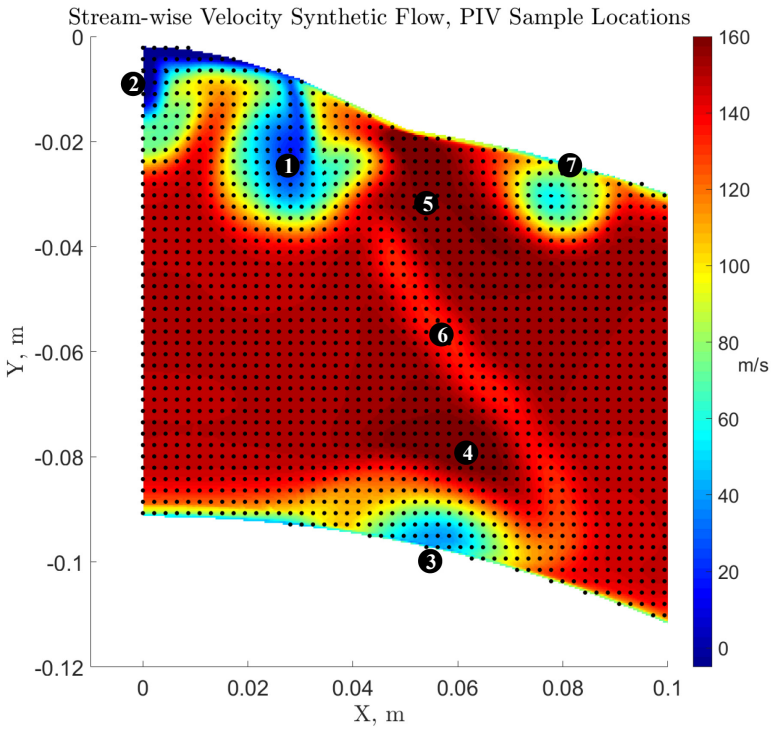

Figure 3 – Synthetic stream-wise velocity with PIV sampling interrogation regions (dots mark corners of the interrogation regions)

3.2 Results and Discussion

Beginning with qualitative observations, it is clear that the PIV sampled data, even with its two-magnitude higher uncertainty, gives more insight than the probe sampled data in terms of identifying the size and location of the various flow features. That said, knowing what the true solution is, one can definitely see the corresponding elements in the probe sampled data. For example, one can make out the existence of the three largest wake structures in the flow (locations 1-3), as well as the accelerated regions in the top and bottom interior corners of the strut wake (locations 4-5). One might be able to convince themselves that the less pronounced strut wake (location 6) is present in the probe sampled data, and if all three components of velocity are available, it will begin to become apparent that these are also vortical structures (refer to Appendix A.3). There is no debating, however, that the wake structure in the top right (location 7) is completely absent in the probe sampled data.

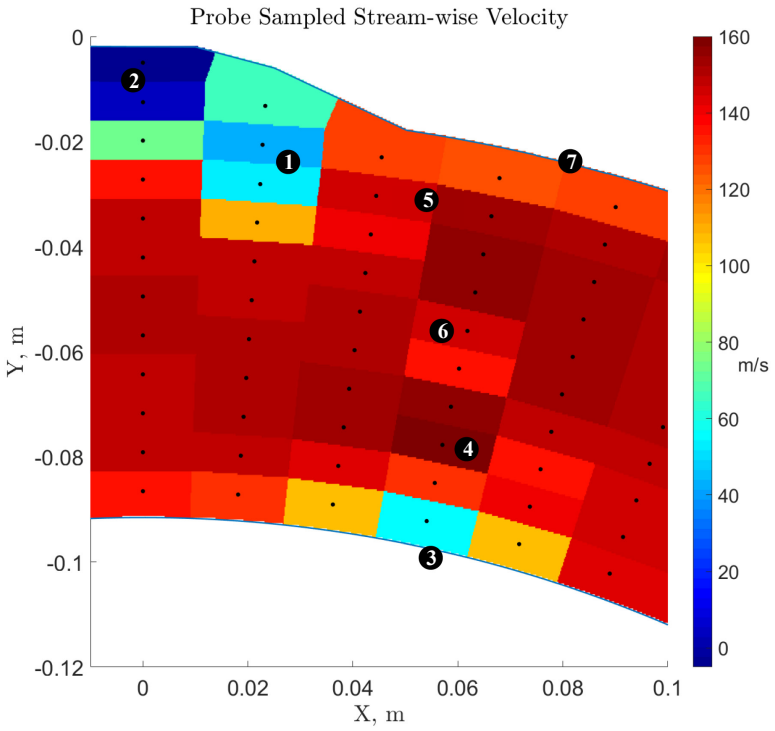

Figure 4 – Probe sampled stream-wise velocity

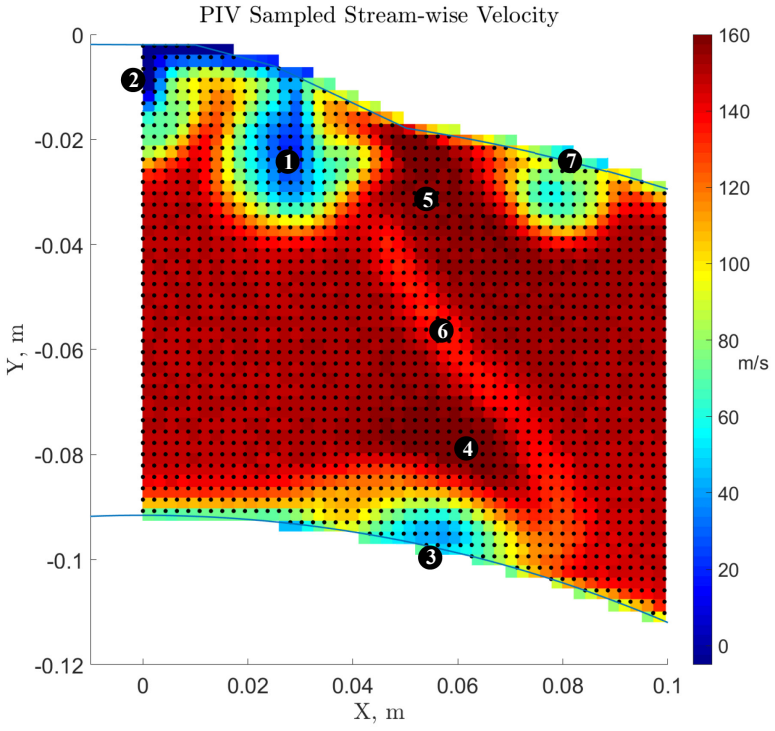

Figure 5 – PIV sampled stream-wise velocity

This obviously occurred because the location 7 feature happened to fall in between two of the probe locations. One may argue that in a real world scenario, this would not happen. If the point is to validate the CFD, then it would be ensured that there would be measurements inside any CFD predicted flow features as prominent as the one at location 7. The counter argument to that statement is, if a flow feature exists that is not captured by the CFD, one would not know to acquire probe measurements at that location. Furthermore, if the CFD incorrectly predicts the existence of a flow feature, it is entirely possible a scientist or engineer observes the pattern expected to be in the experimental data when there may not be a pattern at all. This returns to the point made by Grace and Taghipour [25] that it is never possible to validate a CFD model. The model may be consistent with all of the data with which the model has been compared, but other tests or data may invalidate specific regions of or the entire model. The core issue is not when a perfect CFD simulation is validated with perfect experimental data, but when imperfect CFD is attempted to be compared with imperfect experimental data and limited knowledge is actually available on the 'true' solution.

To analyze this in a more quantitative manner, a point by point error was calculated that normalized the absolute difference between the synthetic flow and the sampled result by a representative freestream stream-wise velocity from a region of the flow unaffected by the support strut. This error is shown qualitatively in Figure 6 and Figure 7, as a probability density function in Figure 8 and Figure 9, and lastly as mean values in Table 1.

The discontinuities in the local normalized error shown in Figure 6 and Figure 7 are due to the difference between the sampled data and the synthetic data on a point by point basis. The synthetic flow is made up of effectively continuous data with smooth gradients. Conversely, the sampled data features drastic changes in velocity from one region to the next. This results in a sharp discontinuity along a given region edge. Also, the normalized error values are clipped at a value of 10% because the areas of lower error (0-3%) were of more interest.

For convenience, each region that has a constant sampled value will be referred to as a cell. For the probe sampled case, a cell is the region of points that are closest to a given sampled location. For the PIV sampled case, a cell is simply the interrogation region. As a

result, the PIV sampled case is made up of a much larger number of cells than the probe sampled case.

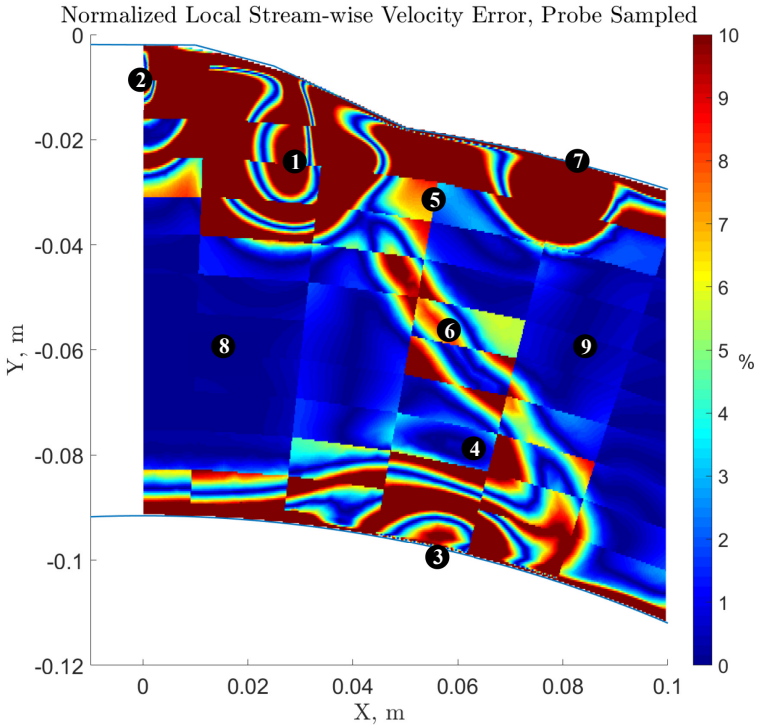

Figure 6 – Normalized local stream-wise velocity error distribution, probe sampled

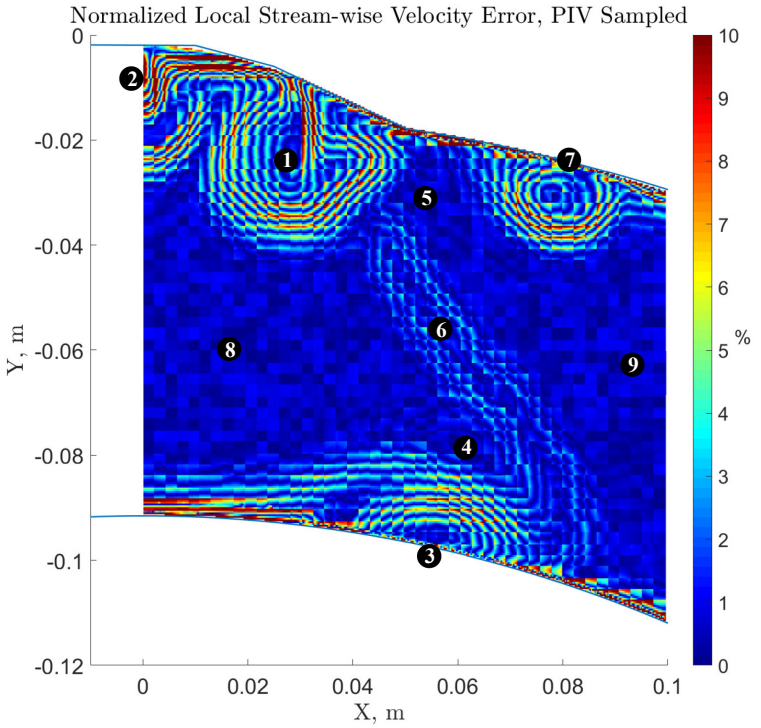

Figure 7 – Normalized local stream-wise velocity error distribution, PIV sampled

For both cases, a general trend can be seen in each cell. There is a region of the cell that is very near to zero percent normalized error, while other regions within the cell (typically the corners) will feature relatively higher normalized error. The extent of this difference is linked to the gradient of the underlying synthetic flow which the cell is trying to represent. It is clearly most severe in areas such as locations 1, 2, and 7. Two major observations can be made from this. One, in areas containing low gradients (locations 8 and 9), the probe sampled data performs the best where its accuracy is unmatched by the PIV sampled data. The uncertainty in the PIV measurement ultimately prevents it from precisely measuring these areas, giving it a tiled floor appearance. However, its error is not excessive. In the previously mentioned high gradient regions though, both methods feature errors larger than 10%. The difference, and the main reason why PIV is more suitable to this application, is that the PIV sampled data also features the aforementioned regions of error that are very near to zero in each cell. The probe sampled data is nearly all above 10% in locations 1, 2 and 7 but the PIV sampled data is a much closer estimator in these locations.

To further this point, Figure 8 and Figure 9 display the normalized error as a probability density function with 0.5% bins. For this measurement region and the given spacing, both the probe and PIV sampling achieve an equal likelihood of estimating the stream-wise velocity with less than a 0.5% error. However, the PIV sampling is much more likely than the probe sampling to estimate the error within the interval of 0.5% - 1.5%. Closer observation (Figure 9) reveals that the probe sampled data is spread over a much larger interval than the PIV sampled data. In fact, errors in the probe sampled data are as high as 45% in some regions whereas the PIV sampled data is largely less than 5% error with only some regions falling in the greater than 10% range.

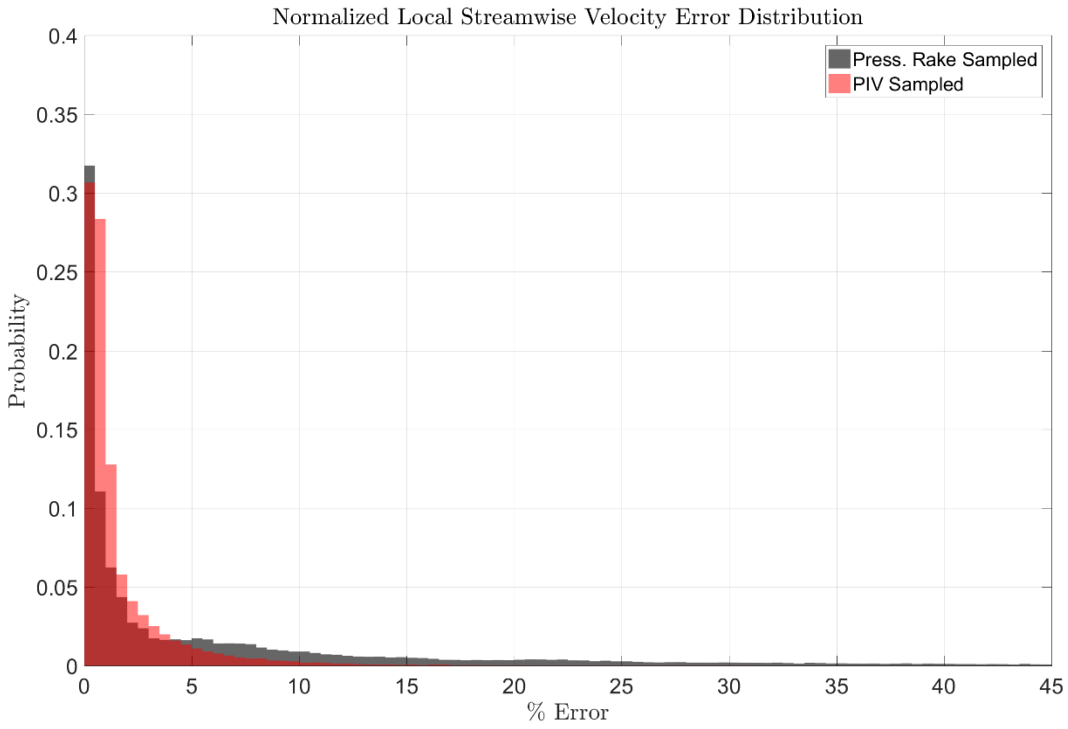

Figure 8 – Normalized local stream-wise velocity error distribution

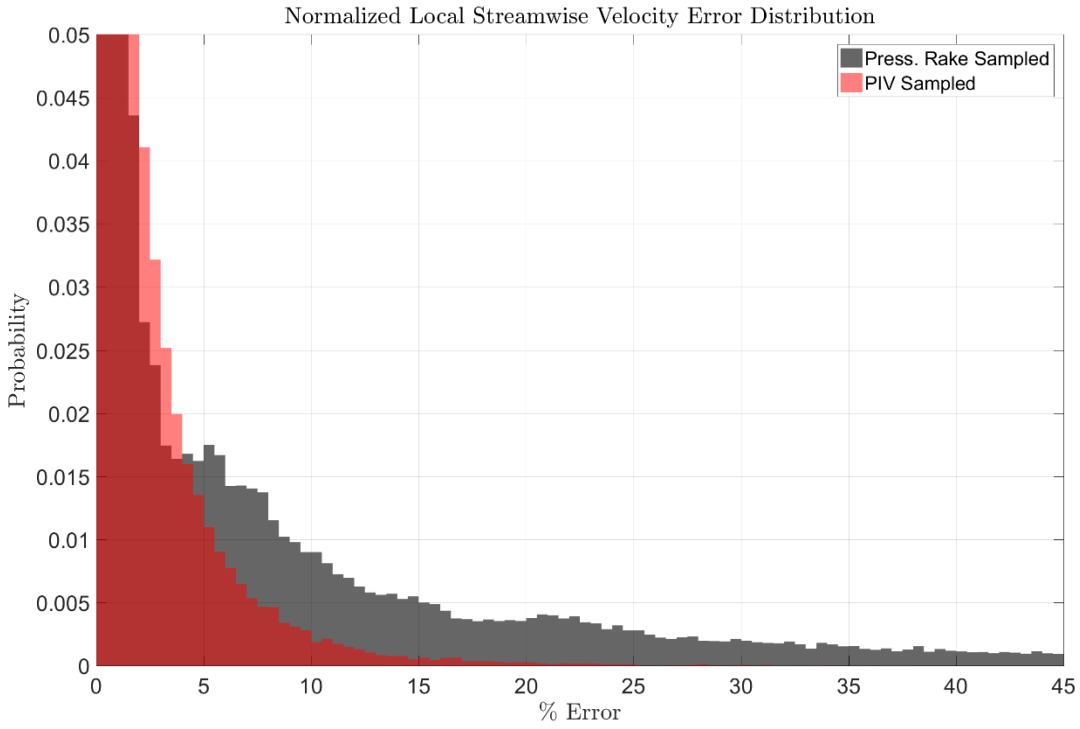

Figure 9 – Normalized local stream-wise velocity error distribution, smaller interval

Lastly, after obtaining both the mean and the mass averaged mean of the local normalized errors, given in Table 1, it remains clear that over this sizable measurement plane, the PIV sampled data is about five times more accurate than the probe measurement. This is because of the inherent spatial sampling error associated with interpolating between point probe measurements. The difference between the mean values and the mass average values is due to the majority of the error occurring in regions of lower velocity. The mass average calculation places lesser emphasis on those regions and thus produces a smaller error. Still, the PIV sampling was about five times more accurate over the measurement plane than the probe sampling, regardless of the averaging method. Although the figures above only show the stream-wise velocity error, similar trends were found for the in-plane velocities. The mean errors for the in-plane velocities can also be found in Table 1 and the associated figures illustrating are given in Appendix A.3.

Table 1 – Mean normalized local velocity error

Velocity Component	**W (stream-wise)**	**U (horizontal)**	**V (vertical)**
Mean PIV Sample Error	1.67%	1.25%	1.11%
Mean Probe Sampled Error	7.28%	5.07%	5.42%
Mass Average PIV Sample Error	0.15%	0.12%	0.11%
Mass Average Probe Sampled Error	0.64%	0.49%	0.50%

The final practical element which needs to be considered is the implementation of each of the two techniques. There is no reason why the probe sampling method could not obtain the same spatial resolution as PIV. However, doing so would result in either (a) a completely blocked flow because of the number of probes or rakes being placed in it, or (b) a much more time consuming if a single probe is traversed along two axes. For the sake of comparison, consider a traversing probe method is designed such as the one described in Frohnapfel [42], where data acquisition takes about 5 seconds per measurement plus 3 seconds for settling plus 2 seconds for traverse movement to the next location. In the example described in this section there are 58 probe measurement locations so the test would only take about 10 minutes in an ideal scenario. However, to acquire the same resolution as the PIV in this example, 1819 individual measurements need to be taken, resulting in a test time slightly over 5 hours. Furthermore, any transient effects, notably the

ambient pressure and temperature, would be present throughout the data and would need to be accounted for. PIV on the other hand could acquire this entire set of measurements 2000 times over in the 10 minutes that the probe measurement requires for its low spatial resolution measurement.

In summary, PIV was shown to have a significant qualitative and quantitative advantage over a generic point measurement system when attempting to accurately estimate large flow fields that exhibit small spatial scale flow features and high order gradients. Although point measurement techniques can achieve higher spatial resolutions to negate the spatial sampling error illustrated, doing so will likely necessitate a more time consuming experiment.

4 Experimental Design Aid (EDA) Software Package

This chapter details the motivation for and the development of a tool to quickly judge the likelihood of a PIV experiment setup being successful. Additionally, the optics theory and PIV relationships that make up the program, the program capabilities, and future desired features are discussed.

4.1 Motivation and Overview

Designing and constructing a PIV experiment is usually an iterative and time consuming process. Intuition and experience can shorten the process, but it generally remains a daunting task for newcomers. Furthermore, pushing PIV to larger fields of view, where scattered light intensity is severely diminished, limits the number of people available with the experience and intuition to determine the impact of various experiment design choices on the quality of the results. However, by incorporating several basic optics principles and a few derived relationships, the EDA software package quickly provides any engineer or scientist with the information to make a judgement on the likelihood of success of a proposed PIV experiment setup.

PIV should be an easy to access tool that anyone can use to investigate a flow of interest. EDA takes one step towards that end by allowing researchers to compare output metrics such as mean exposure with that of previously successful experiments. Several design iterations can then be tested in a short amount of time until the desired field of view, pixels per particle image, mean exposure, and others experimental parameters are achieved.

4.2 Input Variables

The following input variables are currently incorporated into the software calculations through the import of an excel file. Sample values are provided in Table 2.

Table 2 – EDA Input Variables

Input	Value	Unit	Description
d_p	0.3	micrometer	Particle mean diameter
J_0	320	mJ/pulse	Laser output power
λ	532	nm	Laser beam wavelength
N_x	2048	pixels	CCD size in x direction
N_y	2048	pixels	CCD size in y direction
d_r	7.4	micrometer	Pixel pitch (size of pixels on CCD)
f	75	mm	Lens focal length
z_0	2	m	Object distance (distance between camera and measurement plane)
$f^\#$	5.6	[]	Lens aperture number
Δz_0	2	mm	Thickness of laser sheet
Δy_0	0.4	m	Height of laser sheet
α	42	degrees	Angle of camera relative to laser sheet (0=forward scatter, 90=side scatter, 180=backscatter)
Q_e	0.55	[]	Camera Quantum Efficiency (# of photons sensed)/(# of photons hit detector)
d_a	0	m	The diameter of aberrated image of a point source
RI_{real}	1.454	[]	Real component of the refractive index of the particle
RI_{medium}	1.000273	[]	Refractive index of the medium

4.3 Optics Equations

Equations and symbols will follow forms shown in Adrian and Westerweel 2011 [3]. The magnification of the camera lens will be calculated first. Equations for the paraxial lateral magnification and the Gauss lens law can be used to solve for the magnification in terms of the focal length of the lens and the object distance.

$$M_0 = \frac{Z_0}{z_0} \qquad \frac{1}{Z_0} + \frac{1}{z_0} = \frac{1}{f} \quad \rightarrow \quad M_0 = \frac{f}{z_0 - f} \tag{4.1}$$

Next the field of view in the x and y direction is given as

$$l_x = \frac{N_x d_r}{M_0} \qquad l_y = \frac{N_y d_r}{M_0} \tag{4.2}$$

The diameter of the lens aperture can be calculated from

$$D_a = \frac{f}{f^\#} \tag{4.3}$$

The depth of field of the image is the distance in z over which the diameter of a particle image is nearly independent of z because it is dominated by diffraction.

$$\delta z \cong 4\left(1+\frac{1}{M_0}\right)^2 f^{\#^2}\lambda \tag{4.4}$$

The depth of focus, the distance over which the camera can be translated while keeping the image in focus, is given as

$$\delta Z \cong \delta z M_0^2 \tag{4.5}$$

The solid angle subtended by the lens aperture at a particle at the center of the measurement plane is given by Pol and Balakumar [43] as

$$\Omega = \frac{D_a^2 M_0^2}{f^2(1+M_0^2)} \tag{4.6}$$

The image distance is then

$$Z_0 = f(1+M_0) \tag{4.7}$$

The particle diffraction-limited spot diameter will be

$$d_s = 2.44(1+M_0)f^{\#}\lambda \tag{4.8}$$

The approximate particle image diameter will then be

$$d_\tau \cong \left(M_0^2 d_p^2 + d_s^2 + d_a^2\right) \tag{4.9}$$

This can be used to calculate the number of pixels that make up a particle image with the ideal range being two to four pixels.

$$\frac{pixels}{particle\ image} \approx \frac{d_\tau}{d_r} \tag{4.10}$$

A third-party software called MiePlot (v4.5) [44] is used next to incorporate the Mie scattering principles [45] and calculate the intensity of the light that is scattered from the particles based on the laser wavelength, camera angle relative to the measurement plane, particle size and refraction properties, and refractive properties of the medium (generally air or water). Figure 10 shows the scattered light intensity as a function of scattering angle for the sample values given. Figure 11 illustrates how changing the particle radius can radically alter the intensity of the scattered light, ultimately influencing the ideal design location to place the camera in order to optimize for the greatest possible light intensity.

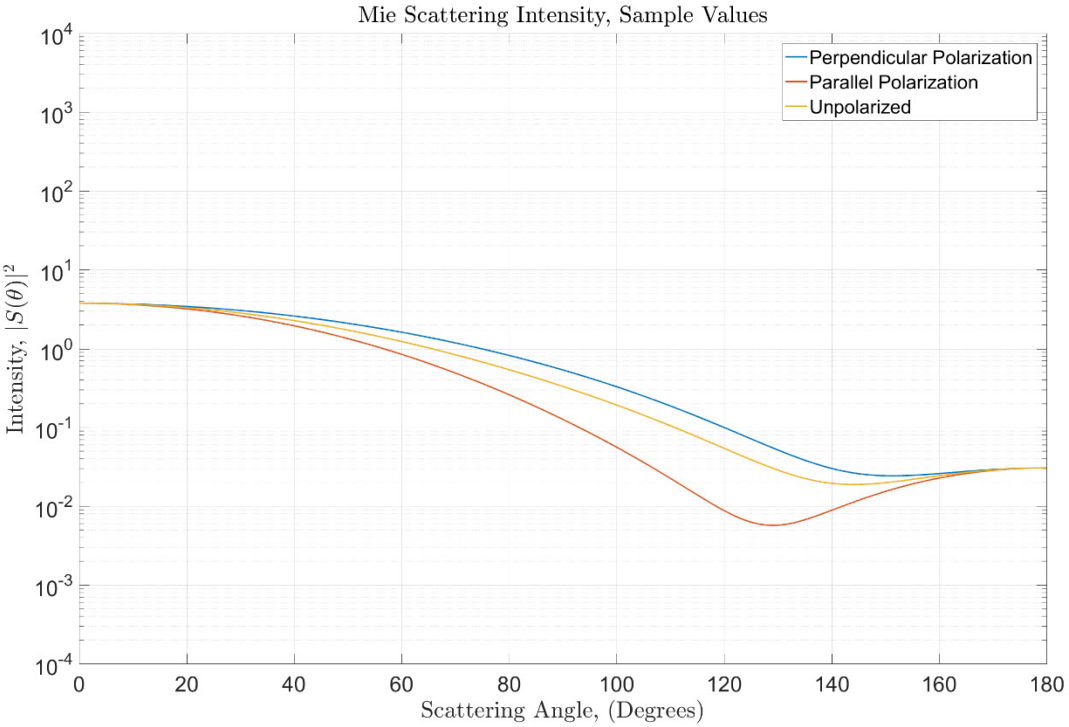

Figure 10 – Intensity vs scattering angle for given sample values

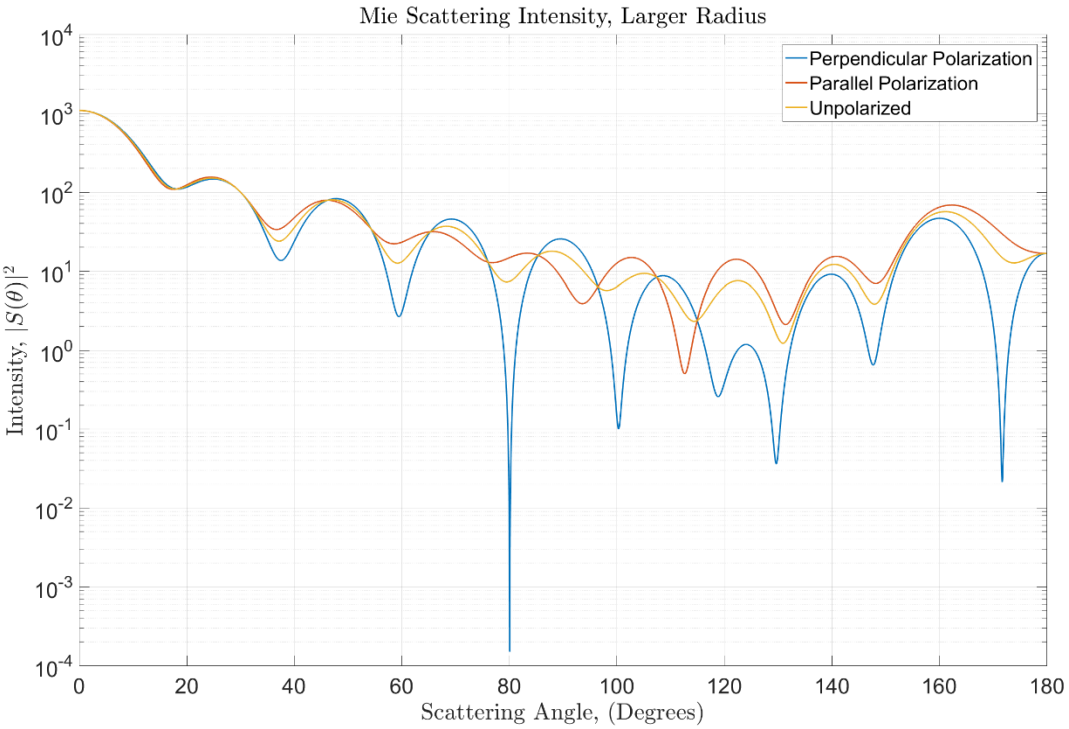

Figure 11 – Intensity vs scattering angle for a particle with larger radius

Additionally, MiePlot has the ability to calculate the scattered light intensity as a function of particle radius rather than as a function of the scattering angle. This could prove potentially beneficial if it can be shown that a larger particle does not produce sufficiently more intense scattered light to justify (in the general case) its increased time lag due to its increased size. This feature is shown in Figure 12 below where increasing a particle radius from 0.8μm to 0.9μm actually decreases the scattered light intensity. Although this aspect of MiePlot is not currently implemented into EDA, it is under consideration for future versions.

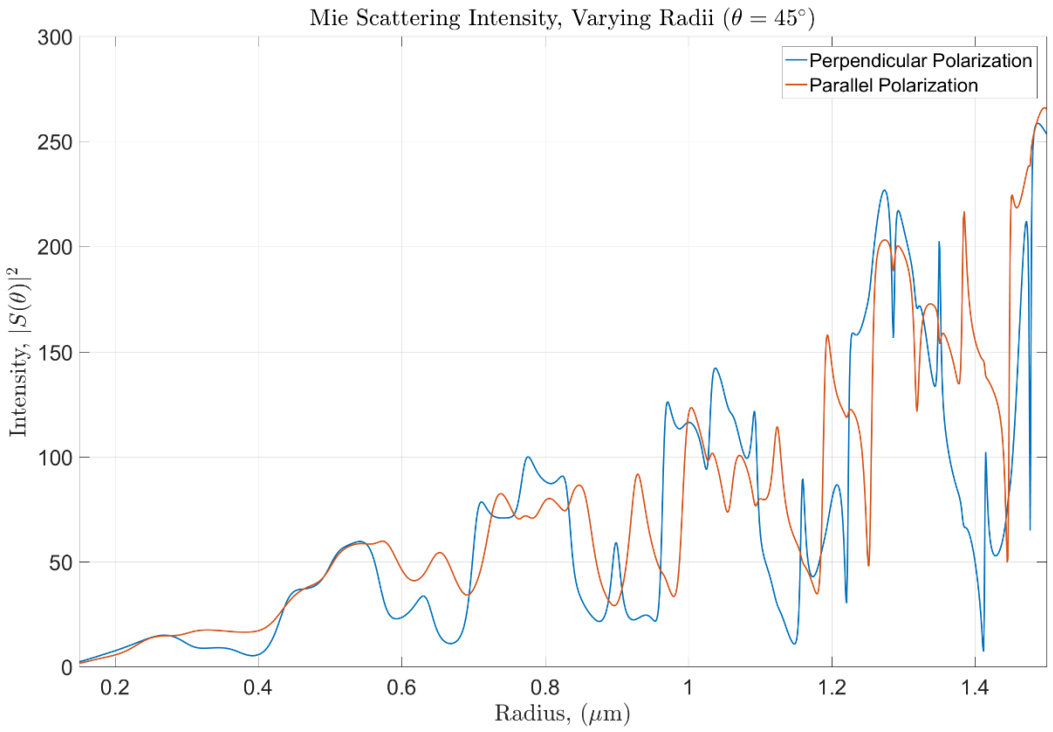

Figure 12 – Intensity vs particle radius, scattering angle = 45°

The scattered light intensity from MiePlot is exported as a text file and subsequently imported into MATLAB. The data is then used to calculate the mean exposure (Equation (4.11), [3]) where the integral component is calculated using the central difference method on the scattered light intensity data output from MiePlot over the range of the solid angle subtended by the lens aperture.

$$\bar{\varepsilon}_p = \frac{\lambda^2 J_0 \int_\Omega |\sigma|^2 d\Omega}{\pi^3 \left[M_0^2 d_p^2 + 2.44^2 (1+M_0)^2 f^{\#^2} \lambda^2 + d_a^2\right] \Delta y_0 \Delta z_0} \tag{4.11}$$

Adrian and Westerweel [3] describe mean exposure as the integral of the light intensity over the time that the light-sensitive surface at the image plane is exposed to the scattered light, averaged over the area of the particle image. A greater value of mean exposure, assuming a constant background intensity, lends itself to achieving a greater signal to noise ratio and therefore stronger correlations during the image cross-correlation process of the PIV calculation. As such, the value of mean exposure is best suited to serve as the main output metric for determining the likelihood of success of an experimental setup.

One can then compare the mean exposure of the particle images in the proposed design with the mean exposure of the particle images in previously successful experiments, as shown in Figure 16. To increase the likelihood of the proposed design being successful, it is advised that it has a greater value of mean exposure than the benchmark experiments.

To summarize, the output variables of most interest at the present time are the field of view dimensions, l_x and l_y, the depth of field δ_z, the number of pixels per particle image, and the mean exposure. With these four metrics, any proposed design can be rapidly compared to a growing database of successful experiments, examples of which are shown below.

4.4 Use as a Comparative Tool

In this example, two parameters were varied; the distance between the camera and the laser plane (shown as the x-axis), and the camera lens aperture (shown as the different colored lines in the legend). If there is a desired minimum field of view, one can clearly see in Figure 13 how far away the camera will need to be for a given lens focal length, regardless of the aperature setting ($f^{\#}$).

Figure 14 illustrates how one can achieve a desired depth of field by altering the aperture setting, where having a wider aperture (smaller $f^{\#}$) leads to a smaller depth of field. These decisions must be balanced, however with the capability of obtaining other desirable experiment characteristics such as the number of pixels that make up a particle image, Figure 15, or a sufficiently high mean exposure, Figure 16. In these cases, a wider aperture

results in fewer pixels per particle image but also in an increase in the amount of light that reaches the camera sensor.

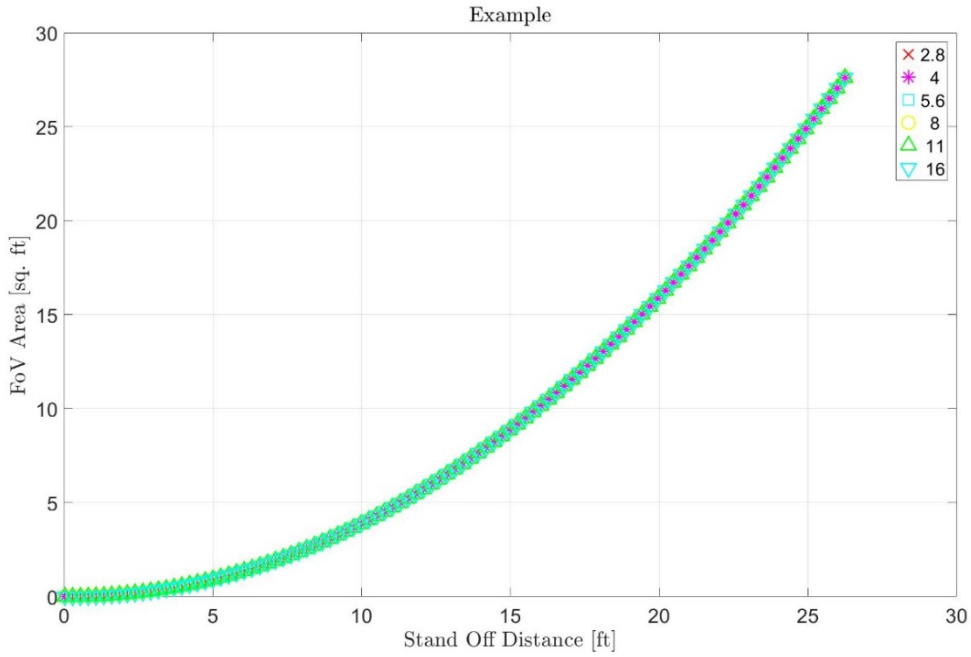

Figure 13 – Field of view area

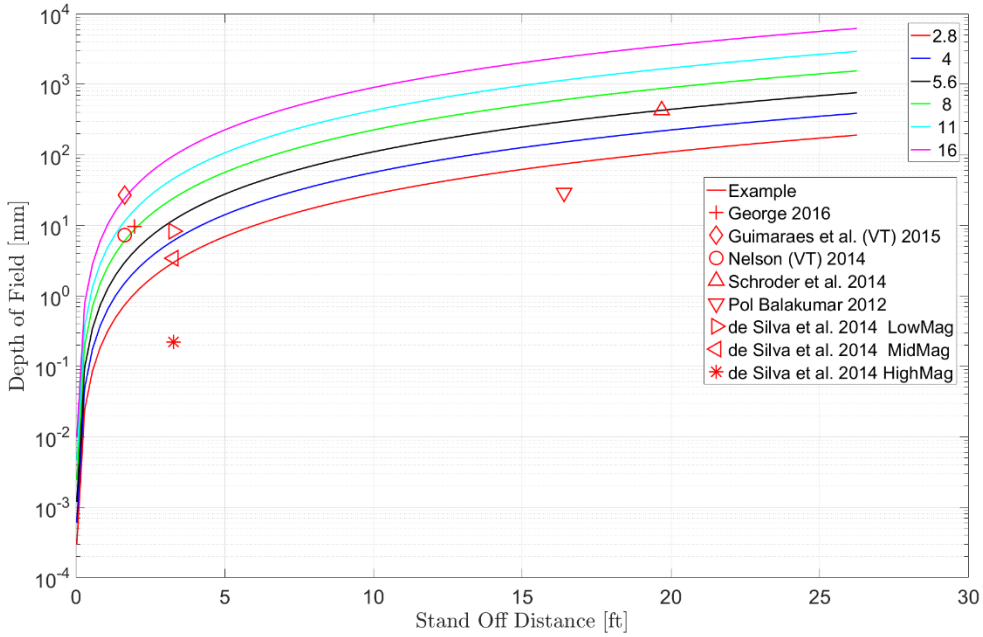

Figure 14 – Depth of field

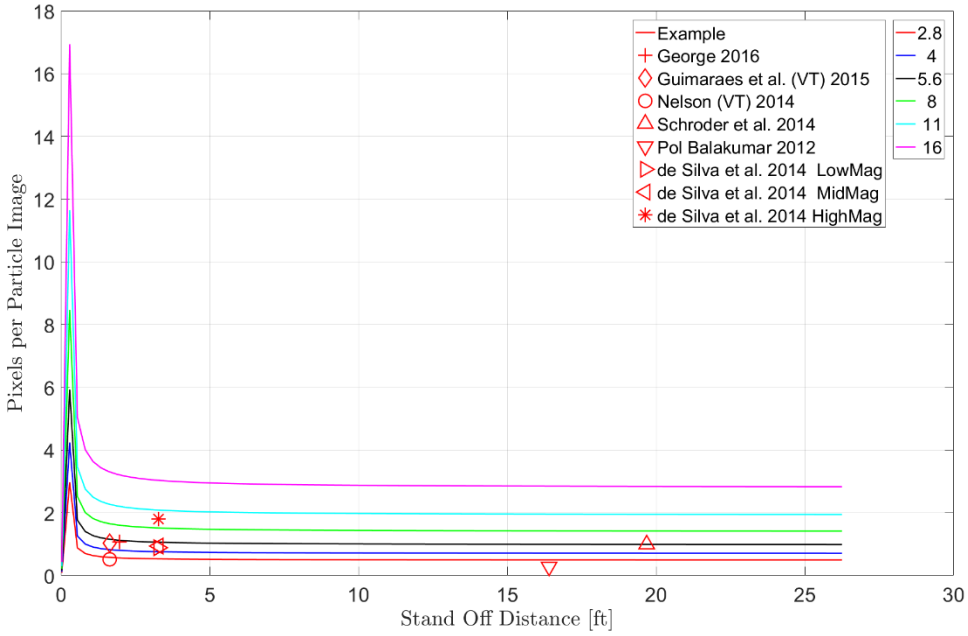

Figure 15 – Pixels per particle image

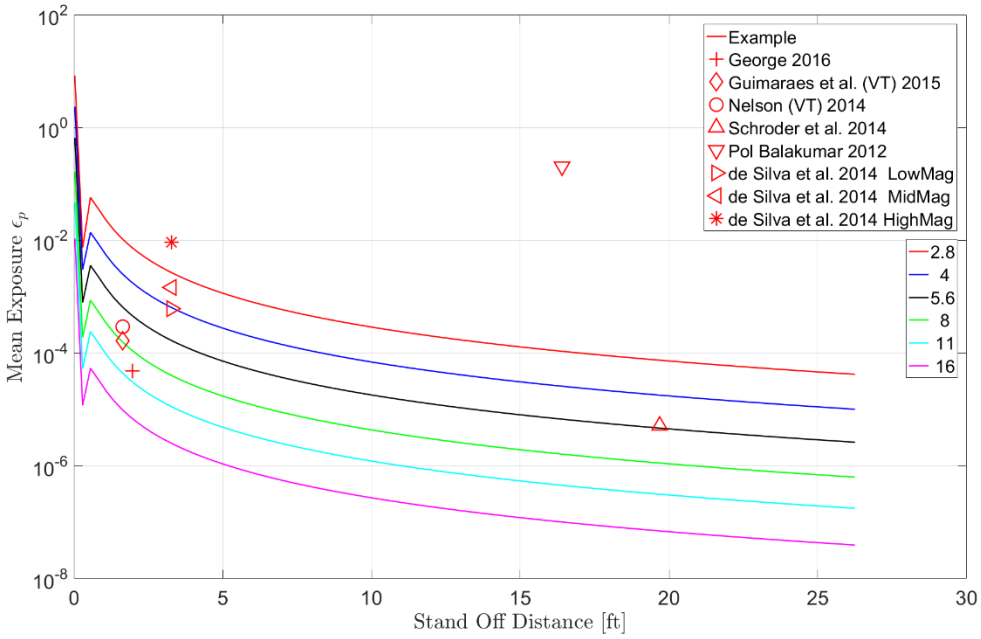

Figure 16 – Mean exposure

Additionally, results can be compared with a set of other experiments relavent to the study which are shown as various shape markers. For this example, George 2016 (square marker) represents the design used in this study and is described in detail in Section 5.5.2.1.

Guimarães et al. [6] (diamond marker) and Nelson [5] (circle marker) represent studies of distorted inflow that also utilized the Virginia Tech JT15D-1 research engine. Schröder et al. [7] (triangle marker) represents an experiment performed by the German Aerospace Center (DLR) of the engine intake of an Airbus A320 in ground operation with a very large field of view (approximately 43 x 16 in^2). Pol Balakumar [43] (upside down triangle marker) represents another large scale PIV experiment that measured about 30 x 39 in^2. Lastly, the three de Silva et al. markers [46] (triangle pointing right, triangle pointing left, and asterisk) represent a single experiment that used multiple camera systems at an experiment relative low, medium, and high magnifications to capture a large total field of view (approximately 31 x 17 in^2) in addition to a very large dynamic spatial range. The last three of the aforementioned experiments pushed PIV toward the highest fields of view and therefore lesser amounts of scattered light. For this reason, they were selected as appropriate benchmarks for this study. It is strongly recommended that a future experiment be conducted that seeks out the lower limit for mean exposure, the point at which experiments are not likley to be successfully. In this way, proposed experiments need not be compared with other experiments but rather a known boundary. Knowing the location of this boundary would also provide the experimenter with more flexibility in the setup design, allowing for a larger field of view or longer stand-off distance.

4.5 Summary and Future Additions

EDA is a comparative tool to help minimize the time and cost associated with iterating through PIV experimental designs. Because it is strictly a comparative tool at the present time, it is ultimately limited by the amount of information available from the other experiments serving as benchmarks. If for instance, a relavent experiment does not include what particles were used, or what power setting the laser was operating at, then assumptions must be made regarding those parameters and that inherently affects where the benchmark falls on the mean exposure figure. It is the authors intent that this program continues to be developed and evolves from a comparative tool into a predictive one. It is feasible that there is a lower threshold of mean exposure at which point obtaining sufficient signal to noise ratio is too difficult. EDA could be used in an attempt to map out exactly where that threshold is.

Additionally, as further optical relationships or even PIV specific relationships are added to the software package, its design power and potential will continue to grow. The following features are recommended additions. Incorporating the particle dynamic response into the program would be a great benefit, providing the designer with insight of the flow tracking abilities of the proposed particle. Integrating the Mie scattering analysis within the program, rather than using a third party software (MiePlot) would help clean up the user interface and make for a more efficient program. On that same front, compiling the entire analysis into a single graphical user interface would greatly enhance the user experience as well as the ease of use. Final enhancements include displaying of error bars to represent a range of refractive indices if they are unknown (this is generally the case), and providing an analysis of the effect of the background or image contrast on the signal to noise ratio (or peak ratio in the image cross correlation analysis).

5 Experimental Setup

5.1 Experiment Overview and Objectives

In order to better understand the flow through the bypass duct, as well as to work towards quantifying the impact of various loss mechanisms in the duct on the fan system's total pressure and efficiency, this work sought to acquire PIV measurements within proximity to one or multiple loss mechanisms in the bypass duct, downstream of the fan. To this end, the experiment was broken down into the following components: identification of the loss mechanism under study, CFD analysis of the flow surrounding the loss mechanism, a risk reduction experiment using a simulated engine environment, the full-scale experiment using the test stand JT15D-1, and a thorough and detailed analysis of the results. The following sections are dedicated to each of these components, with the results discussed in the next chapter.

5.2 JT15D at the Virginia Tech TurboLab

The Turbomachinery and Propulsion Research Laboratory (TurboLab) at Virginia Tech has hosted many engines over the years since its inception in 1970. Each engine has served a valuable purpose towards advancing the research efforts of the group. In the late 1980's, NASA donated two modified Pratt and Whitney JT15D-1 turbofan engines to the TurboLab. Throughout the 1980's, these two engines were used for engine noise research at NASA Langley Research Center. The JT15D-1, shown in Figure 17, is a 21-inch diameter engine with a bypass ratio of 3.3 and capable of 2,200 lbf. Additional design parameters are shown in Table 3 [47].

Figure 17 – JT15D-1 in the Virginia Tech TurboLab

Table 3 – JT15D-1 Design Parameters

Fan Speed	16,000 RPM
Core Speed	32,000 RPM
Mass Flow Rate	73.1lbm/s
Fan Pressure Ratio	1.5
Bypass Ratio	3.3
Thrust	2,200 lbf
Fan Diameter	21 in
Number of Blades	28
Span Averaged Chord Length	2.74 in
Blade Tip Mach Number	1.3

The two JT15D-1's Virginia Tech now operate additionally have fan blades that have been modified to include mid-span shrouds and part-span stiffeners to make them more robust and tolerant of inflow distortions. With several hundred hours of operation time between the two engines, they have been put to good use. Recently, most of that time has been spent studying inlet distortions and their effects on the fan blade [5], [6], [42], [47] as part of an effort towards integrating the engines with the aircraft fuselage.

5.3 Identification of the loss mechanism

The first step in the experiment was to identify which loss mechanism(s) to study and there were a variety of options. Whichever option was chosen not only needed to be capable of providing intriguing aerodynamic characteristics, but it also had to be accessible in terms of the PIV cameras and laser. Some of the proposed loss mechanisms near the bypass duct exhaust are shown in Figure 18, where the bypass nozzle has been removed. In Figure 18b, a support strut can be see that is bolted to the engine's core, then passes through a shroud, the bypass duct, and the engine's outer wall before connecting to the engine's mounting structure. In Figure 18c, a number of struts, pipes, and other various loss creating geometries are present. The support strut is shown external to the engine in Figure 19. The bottom of the strut bolts to the core wall and the top bolts to the engine mount structure.

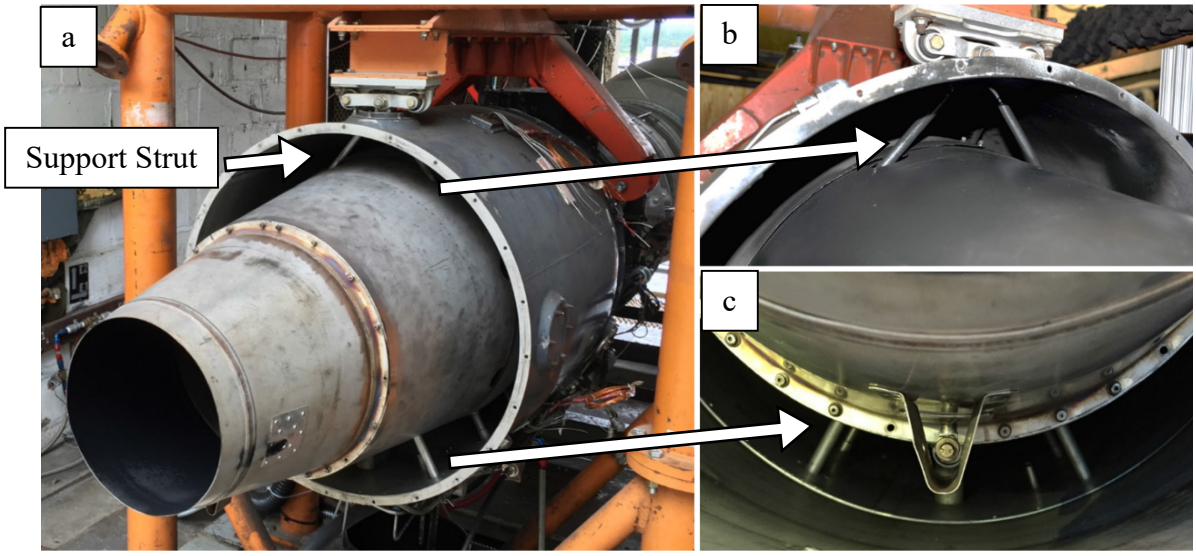

Figure 18 – Loss mechanisms in the JT15D-1 bypass duct (a). Aft support strut (b). Various struts, pipes, and loss generating geometries (c).

Figure 19 – Aft support strut removed from the JT15D-1 engine

Of the proposed loss mechanisms, the support strut in the top half of the duct was chosen as the most interesting and practical to study. Located in relative isolation, the strut could be easily photographed by the PIV cameras from a number of locations. Similarly, the PIV laser would easily reach most regions within close proximity to the strut. The struts, pipes, and ports in the lower half of the engine presented a more troublesome situation. Depending on which loss mechanism could have been chosen, any number of the other loss mechanisms would have made optical access much more difficult, if not impossible. Additionally, the isolation of the support strut would allow for a more definitive analysis of the flow around it, whether it be upstream or downstream. One can imagine a scenario where one of the lower half loss mechanisms was chosen revealing an interesting wake captured by the PIV. However, the cause or causes of this feature may not be determined due to the coupled interaction of all the struts, pipes, and ports present. In this sense, the support strut would provide a much more "controlled" experiment where one could say with more certainty that any effect observed up or downstream was caused by the support strut.

Another added benefit of choosing this particular strut emanated from its shape. The strut is effectively a 0.5-inch diameter circular cylinder, which has been the subject of countless studies. Having this large pool of resources to compare to would prove beneficial during the analysis portion of the experiment.

5.4 CFD Simulation

As previously mentioned, a CFD analysis was one component of the larger experiment under study. The primary purpose of this analysis was not to serve as a representation of the 'true' flow under study or calculate performance characteristics, but rather provide an estimation of the large scale flow physics in the bypass duct. This would provide a simplified flow visualization which could be used to support observations from the PIV experimental data. In light of this intent, various simplifying assumptions were made to balance solution accuracy with computational time.

5.4.1 JT15D-1 Model

The three-dimensional model of the Virginia Tech research engine was generated using SolidWorks 2014. Engine parts were measured independently. Irregularities in the parts as well as bends, imperfections, or damage due to age made this a difficult process. However, the cross section of the final model was compared with that provided by Cook [48] and the discrepancies in the regions of focus were minimal.

The main intention of this model was to capture the largest geometric features in the top quarter of the bypass duct. All of the pipes and struts in the lower three quarters of the bypass duct were ignored for simplicity. Additionally, smaller features and irregularities including bolts, dents, and bleed ports, among others were ignored, again for simplicity. The bypass duct model is shown in Figure 20, while Figure 20b highlights the support strut of the model and Figure 20c shows the cross section of the model.

A model of the "fluid" geometry that was to be used in the CFD solver was then created by filling the cavity of the bypass duct model. Only one half (circumferentially) of the bypass duct fluid was modeled with the intention of imposing a symmetry boundary condition on the center plane during the CFD simulations. The fluid model measured approximately 32 inches axially and about 27 inches radially at its maximum, Figure 21.

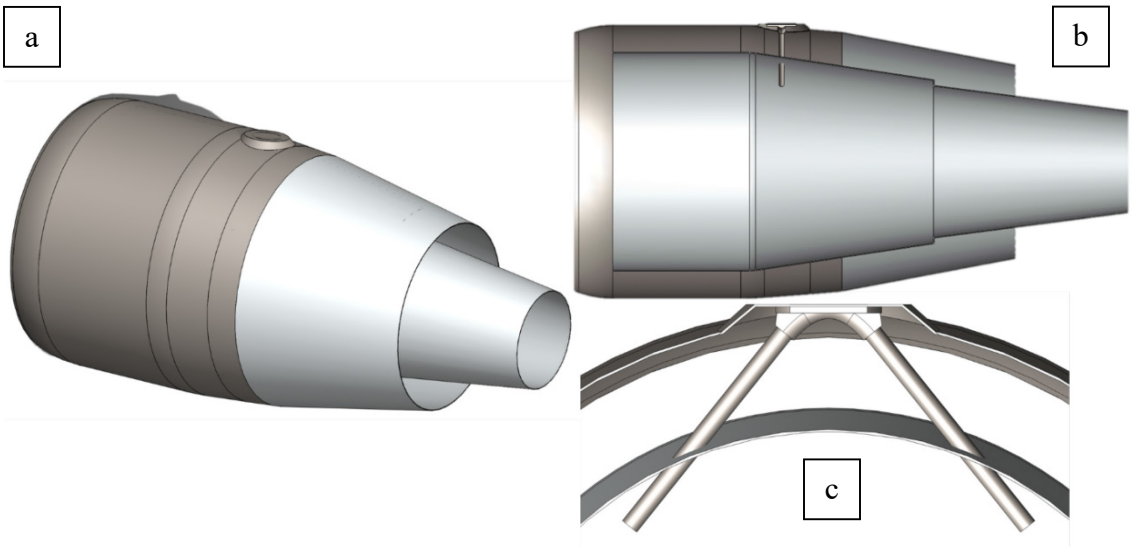

Figure 20 – CAD model of relevant components of the JT15D-1 (a). Centerline cross-section of CAD JT15D-1 (b). Span-wise cross-section of CAD JT15D-1 (c).

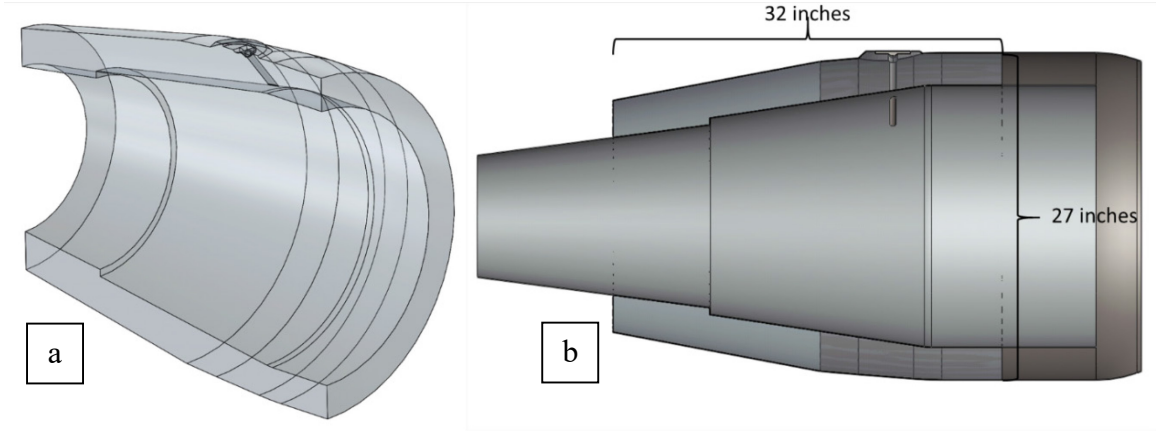

Figure 21 – Fluid 'geometry' (a). Fluid geometry location within the bypass duct (b).

5.4.2 Meshing and Grid Convergence

Next, the fluid model was discretized using an unstructured mesh in ANSYS Meshing, a component of the ANSYS Workbench software suite. In general, the following guidelines were followed in the creation of the mesh. When compared to the global average element size, smaller elements were used on the top symmetry surface to generate a more refined solution within close proximity of that area. Since the focus of the study was on the wake region of the strut, the smallest elements and smallest growth rates were located there, again to create a more refined solution in that area. Inflation layers were located on all the walls to calculate and better represent the boundary layer flow. In these regions it is desirable that the element height corresponds to a non-dimensional wall height

$\left(y^+ = \frac{yu_*}{\nu},\ u_* = \text{friction velocity}\right)$ value less than 5 so that a wall model is applied only to the laminar sublayer, while the inner layer, outer layer, and beyond are solved directly [49], [50]. However, due to the relatively large size of the model being simulated, this refinement would have required a prohibitively large number of elements, at least when considering the original intent to serve as a first approximation. It is advisable for the next round of simulations however, that this refinement is pursued and more powerful computing resources are utilized.

In order to ensure to a reasonable degree that the solution is independent of the mesh and element size, a rough grid convergence study was performed. A coarse mesh was used initially. Then, the number of elements was increased with each iteration until there was a minimal difference between the current and previous solution. For this experiment, the focus was on the largest of flow structures. As such, the criterion for grid convergence was based on qualitative observations of the major flow features' shape and magnitude when compared to the previous iteration.

The final mesh consisted of 9.8 million elements and 2.8 million nodes. Element faces were as large as 5 mm in the free stream and 1mm on the strut surface. Inflation layers were 2 mm thick on all of the wall surfaces and consisted of 15 layers with a growth rate of 1.1. Figure 22 shows the final mesh in its entirety. Figure 23 shows a cutout of the final mesh that passes through the support strut under study.

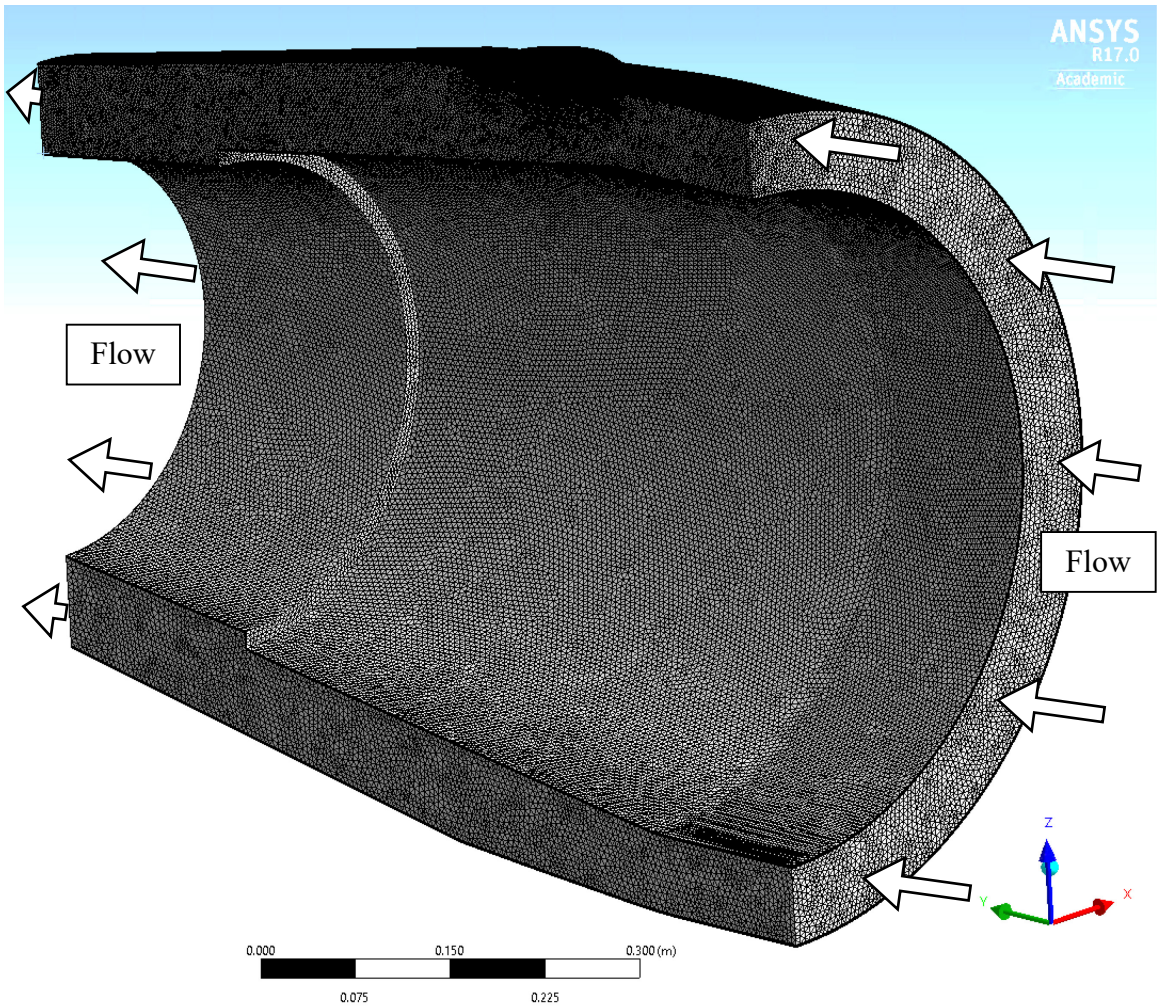

Figure 22 – Final mesh discretization

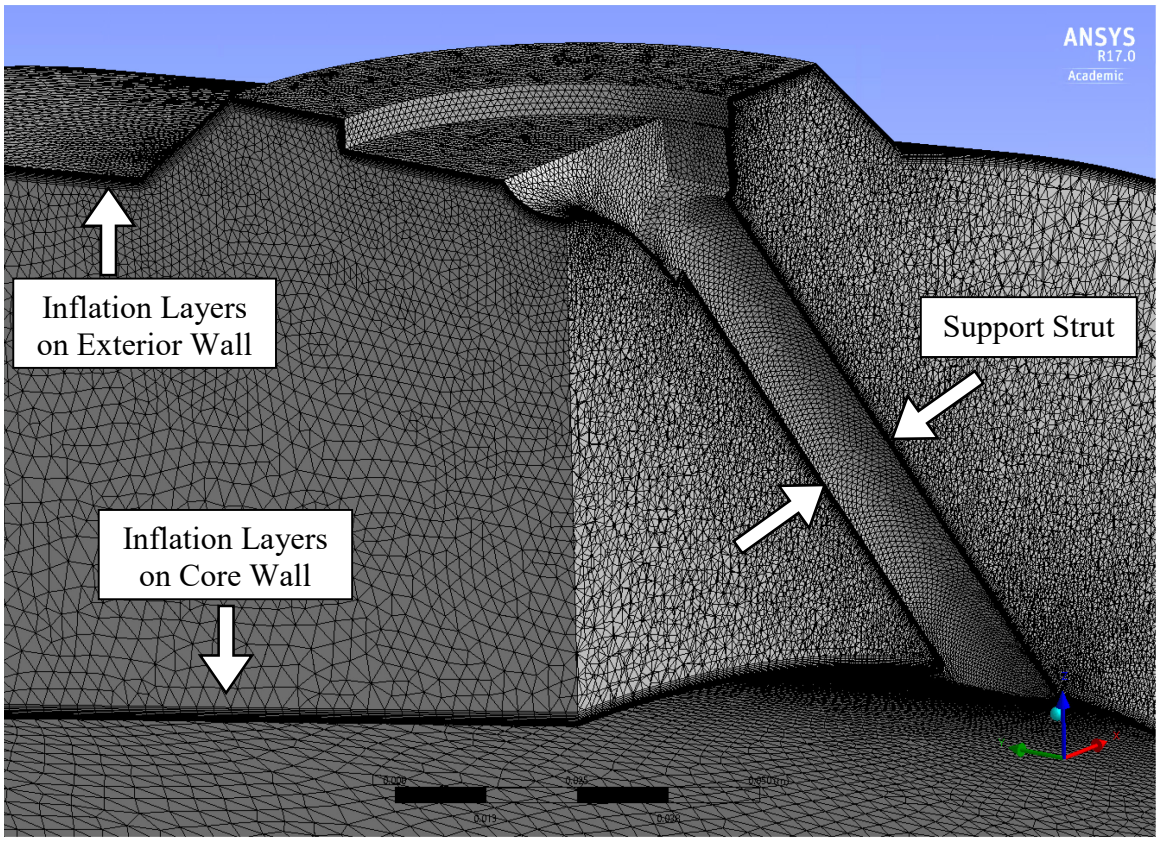

Figure 23 – Final mesh discretization slice plane illustrating finer mesh in vicinity of support strut

5.4.3 Selection of Boundary Conditions

During the experimental portion, total temperatures and pressures were collected 9 inches upstream of the strut for all fan speed cases. This allowed a much more representative boundary condition to be applied at the inlet. For more details on the collection of data, refer to Section 5.6.2.1. The average measured total pressure and total temperature for a given fan speed was enforced as uniform inlet conditions for the simulation. Similarly, the ambient pressure was measured during the experiment and an average value (measured during the same time as the upstream measurements) was enforced at the nozzle exit plane as the outlet condition. As previously mentioned, the fluid geometry represented only half (circumferentially) of the bypass duct, and symmetry boundary conditions were enforced on the top and bottom centerline faces. All of the surfaces such as the bypass duct case, nozzle, and strut were enforced as adiabatic, smooth, no slip walls. The enforced boundary condition locations are shown in Figure 24.

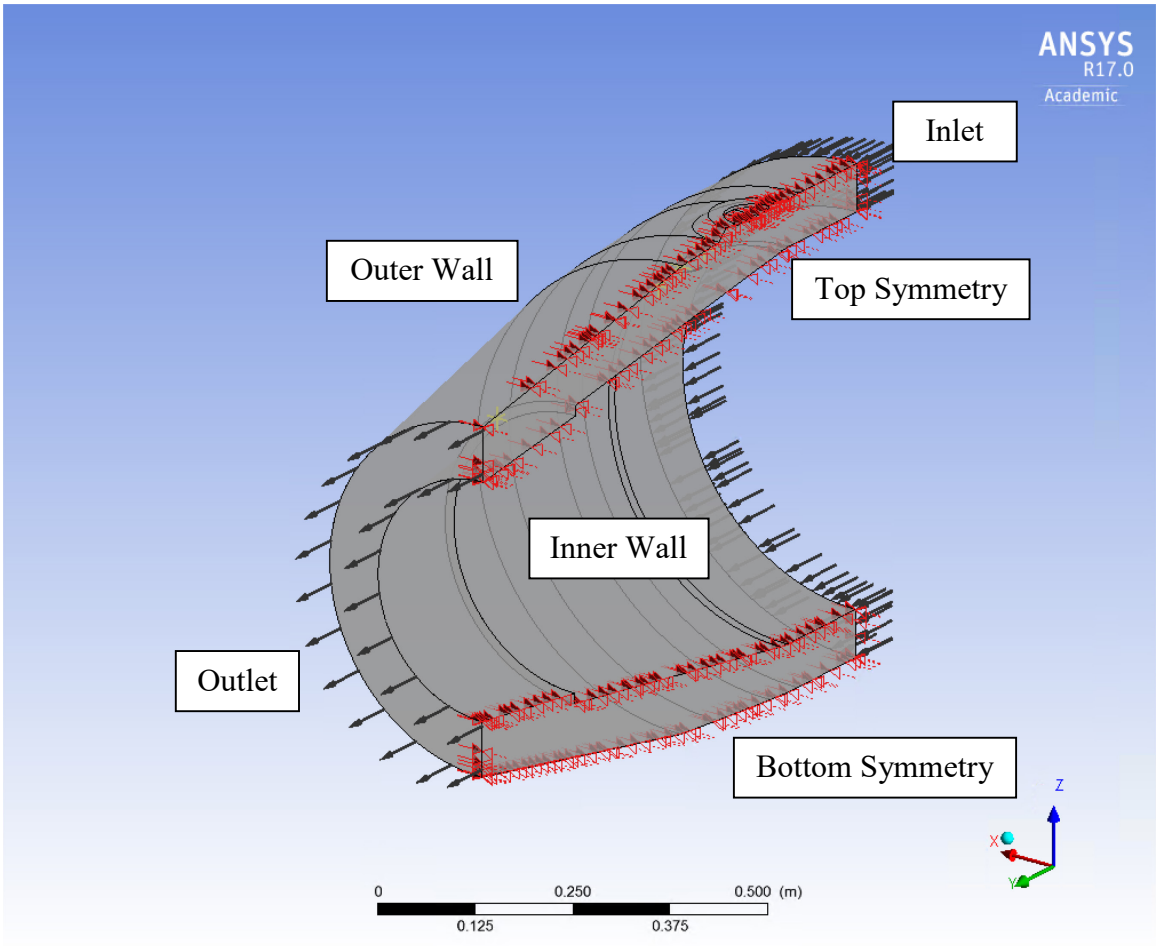

Figure 24 – Boundary condition locations

The CFD simulation was performed for two test cases representing two fan speeds, idle (35% max corrected fan speed, CFS) and 80% CFS. The 80% case was chosen as it was the highest fan speed in which experimental data was collected, and was the closest to expected engine cruise conditions. The idle case was also chosen since the experimental data collected at this speed contained much less noise, and would therefore serve as a better comparison between experimental and computational results. Table 4 shows the values for the enforced boundary conditions for both test cases.

Table 4 – Enforced Boundary Condition Values

Fan Speed	Idle (35%CFS)	80% CFS
Inlet Total Pressure [MPa]	0.105721	0.12406
Inlet Total Temperature [K]	298.2409	309.8565
Inlet Turbulence Intensity [%]	5	5
Outlet Pressure	0.094538	0.09529

5.4.4 Solution specifications

In both test cases, the decision was made to initially set the fluid material properties to that of air at 25° C which fixed the fluid density as a constant. The error associated with treating this problem as an incompressible one in the value of ρ_0/ρ is approximately 2.7% at the Idle case and 11% at the 80% CFS case due to the Mach numbers for these cases being about 0.18 and 0.36 respectively. This error analysis was performed using isentropic relations presented in Hill, Peterson [51]. The coarse grid convergence study was performed with these settings. One more solution was generated following this process with the fluid material properties set to that of air as an ideal gas, thus allowing for compressibility. The largest effect of this change was a substantial decrease in velocity at many locations. In the 80% CFS case for example, velocities were about 20 m/s lower in the compressible case than in the incompressible case. This provided results much closer to the experimental data. As such, the compressible solution will be shown and discussed for the remainder of this work.

The k-ω SST turbulence model was used for this solution. Reardon [50] gives a brief overview of some of the most well-known zero-equation, one-equation, and two-equation turbulence models. He further describes the benefit of the k-ω SST model, with its ability to use the k-ε model in the free stream away from the walls and then use a blending function that transitions to a k-ω formulation at the wall.

5.4.5 Convergence Criterion

The solver was allowed to run for several thousand iterations until a convergence criterion was met. For this experiment, that convergence was represented partially by obtaining residuals less than 10E-04. Additionally, several monitors were placed inside the fluid geometry to allow for observation of various metrics at a given location. Pressure and

velocity were monitored at a number of axial locations and were considered converged when the pressure was fluctuating less than 1 Pa and the velocity less than 0.01 m/s over hundreds of iterations.

5.4.6 Limitations of CFD simulation

A number of simplifying assumptions were made to reduce the size and complexity of this simulations. Some have already been mentioned in the previous subsections, however all the assumptions and their implications will be listed here for clarity.

Beginning with the modeling of the geometry, at the location where the strut passed through the core shroud, there was a hole that was considerably larger than the strut that was not modeled in the CFD. The hole can be seen in Figure 25. The region where the strut passes into (which cannot be seen in Figure 25) is a cavity space between the core flow and the bypass flow and could be producing very complicated flow interactions at the strut-core junction. Because the CFD models this junction as a simple wall, the complicated interactions will most likely not be accurately represented.

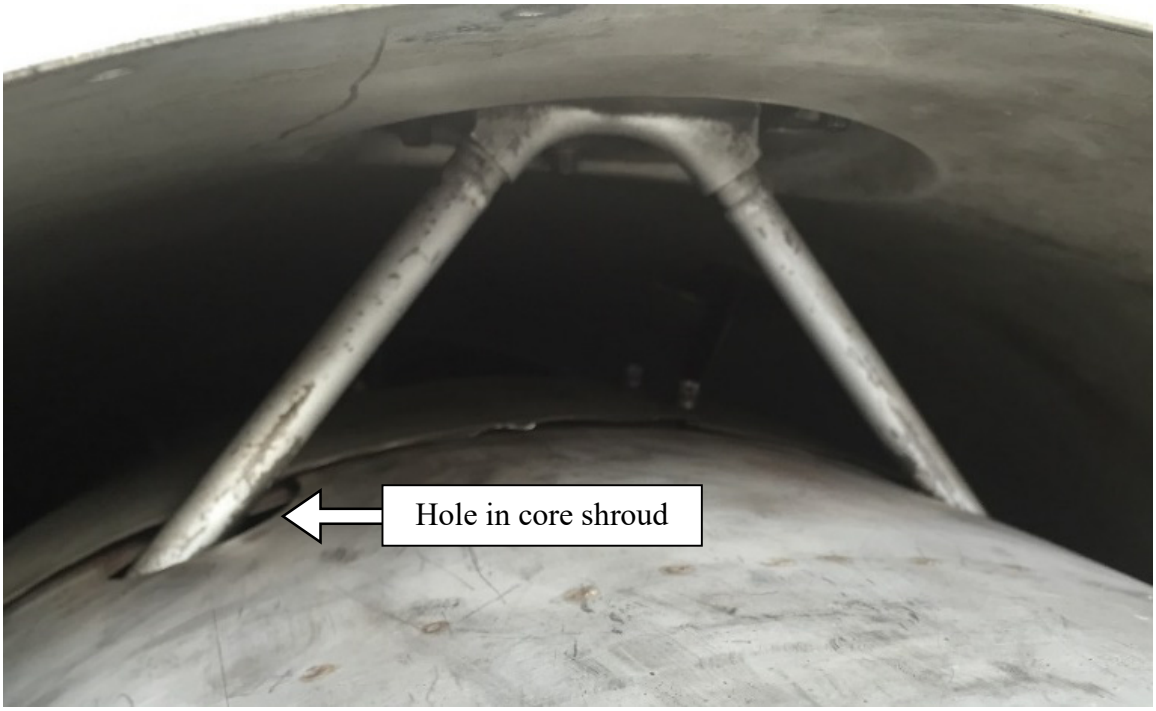

Figure 25 – Aft support strut in the bypass duct and depiction of hole in the core shroud

Next, the inlet boundary conditions for the simulations were simplified to a state of uniform total pressure and total temperature by taking an average of the experimental radial measurements of the same variables. Realistically, all the variables at this stage will vary

with radius, including the bulk swirl of the flow. However, this radial variation was not modeled. Also, the turbulence intensity was set at 5% but experimental results will show this value should likely have been set higher. Neglecting the radial distribution of pressure and therefore velocity along with a low value of turbulence could have a significant impact downstream as any non-uniformities at the inlet could produce complex flow evolutions and unique interactions when the flow encounters the strut.

With regards to the mesh, although it was refined over the course of several iterations, it is not resolved to the extent of a high fidelity simulation, nor was it intended to. The area requiring the most refinement is in the near wall regions where the first element y+ value was greater than 30 at some locations. This assumption could result in an inaccurate modeling of the boundary layer which would impact the development and characteristics of the wake structure.

The last major assumption that will be discussed here is the use of a steady Reynolds averaged Navier-Stokes (RANS) simulation to model a circular cylinder in a subcritical Reynolds flow. This is the single largest limiting assumption of the simulation described within this work. The flow around a circular cylinder in a subcritical Reynolds number flow (about $\mathrm{Re} < 2 \times 10^5$ [52]) is inherently an unsteady one. Numerous examples exist of the poor performance exhibited of steady RANS CFD to model the separated wakes created by bluff bodies including Rodi [53], Lakehal and Rodi [54], and Iaccarino et al. [55]. The issue is that when the flow is not statistically stationary, Reynolds averaging is not the same as time averaging in part because of the omission of periodic vortex shedding [55]. To correct for this, an unsteady RANS model can be applied but at greater computational cost. Despite low accuracy in regions of separation, steady RANS is still capable of producing fairly accurate results elsewhere in the flow [55]. Because of the intent of this CFD simulation as well as the computational cost of pursuing more accurate methods and the complexity of the flow under study, a steady RANS model was selected for this work.

5.5 Simulated Engine Environment

This section describes the components of the simulated engine experiment, most of which are also implemented in the full-scale JT15D-1 experiment. For most of the

components, the specifications of the equipment used are given, and the design process and methodology behind the experiment design are discussed.

5.5.1 Objectives

The intent of simulating the engine before testing at the test stand was multi-faceted. Mainly, the focus was to replicate the optical setup as closely as possible to that used in the full-scale experiment in order to reduce test stand time, reduce the overall cost of the experiment (fuel, operators, modifications, etc.), and identify any design flaws. Of the potential design defects that needed to be ruled out, some were common to all PIV experiments, such as inadvertent laser glare and insufficient light reaching the cameras. Others were more specific to this experiment. This included internal engine hardware potentially blocking/limiting the camera's fields of view, less than ideal laser expansion through the outer engine wall window, incorrect implementation/performance of the external calibration plus self-calibration (the calibration process will be discussed further in the design section), trouble utilizing the camera remote focusers, and lastly, excessive window distortions degrading the image quality.

Secondary objectives of the experiment included performing two tests, one with the support strut in its usual position within the bypass duct as well as a test where the support strut was removed. This would help isolate any effects the strut was causing from effects due to other geometric features of the bypass duct. Additionally, Pitot-static pressure probe measurements would take place after the strut and no strut cases in order to provide rough validation of the PIV measurements.

5.5.2 Experiment Design

5.5.2.1 Wind Tunnel

The Virginia Tech Lab 33 Wind Tunnel, also known as the Boundary Layer Tunnel, as its alternative name suggests was originally used for boundary layer experiments. It is capable of providing flows around 1.3 kg/s which translates to a velocity of roughly 44 m/s for its given exhaust area (0.1016m x 0.2413m) and ambient air conditions (Bennington [56]). From the intake, the air travels to a large chamber (approximately 1.5 m^2) where PIV seed can be added through a port on the top of the chamber. The air then passes through a honeycomb and three screens to serve as flow straighteners while the duct decreases in area, accelerating the flow to its exhaust velocity [56]. In the time since the tunnel's service

for boundary layer experiments, it has been repurposed to provide the flow for the simulated engine test. This involved removing the boundary layer test section, air conditioner, and recirculation duct that originally comprised it, so that it appears as shown in Figure 26.

Figure 26 – Virginia Tech Lab 33/Boundary Layer Wind Tunnel

5.5.2.1 Simulated Engine

The simulated JT15D would largely be composed of spare parts from one of the Virginia Tech TurboLab JT15D's, which had recently been decommissioned. Only the necessary parts were used which effectively included everything downstream of the turbine: the core exhaust nozzle, core shroud, bypass duct casing, bypass nozzle, and the support strut. These components were recreated into 3D computer models using hand measurements, as was illustrated in Section 5.4.1.

Supporting the engine proved a troublesome task. Typically, the engine is mounted from above using two support struts, one located aft (the one under study) as well as another located forward on the engine and subsequently on a component that was not part of the

simulated engine that had been built. Even if it was, mounting from above would not be a viable option since one of the desired tests involved removing the aft support strut.

It was decided to support the engine from the bottom making use of two holes that existed in the bottom of the core nozzle. Threaded adjustable steel rods were designed such that they would pass through existing ports in the bypass duct and rest underneath the two aforementioned holes in the core nozzle. This method provided the most stability, while also allowing for implementation ease and flexibility. Additional support of the core was provided for the aft end by resting it on an H-beam while additional support of the bypass duct was provided for the forward end by placing a hydraulic jack underneath it. The support legs, hydraulic jack and simulated engine are shown in Figure 27.

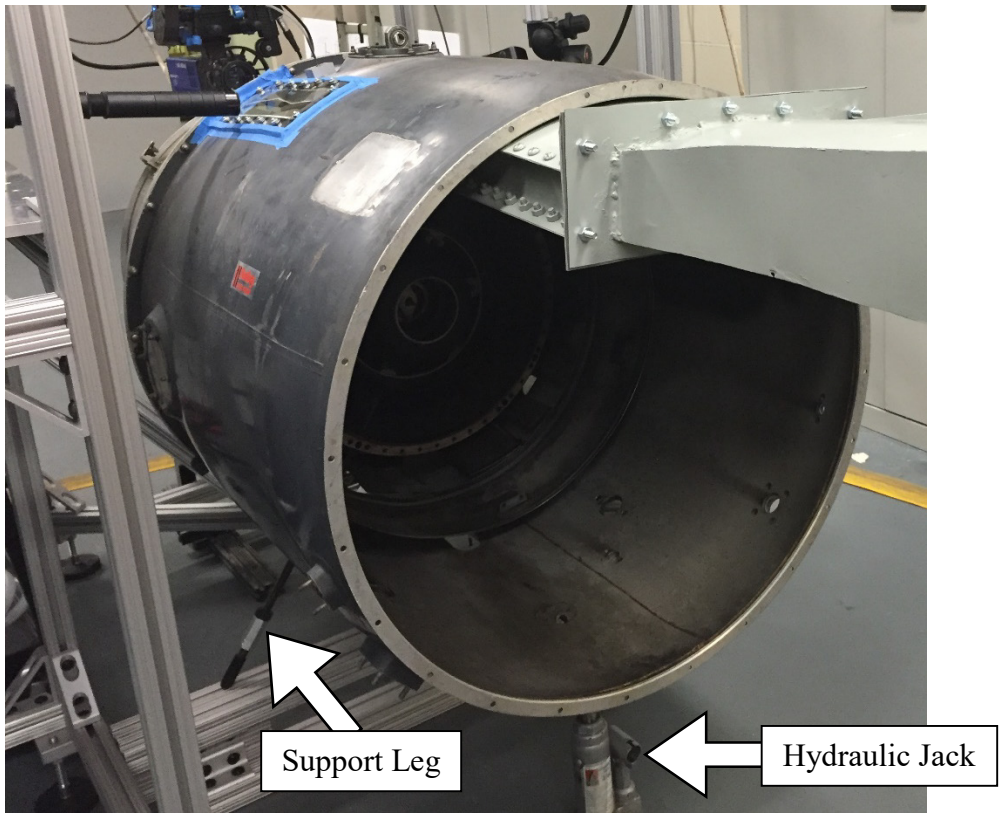

Figure 27 – Simulated engine support structure

The final modifications to the simulated JT15D involved spray painting the interior of the bypass duct flat black to reduce any laser glare where the laser sheet would impinge on the bypass duct walls, as well as cutting holes out of the core nozzle and bypass duct casing to serve as the windows for the PIV cameras and laser respectively. The design methodology regarding the size and location of the windows will be detailed in a later

section. Once the simulated engine had been built, it was moved into position such that the wind tunnel duct extended in between the bypass duct casing and core shroud as shown in Figure 28

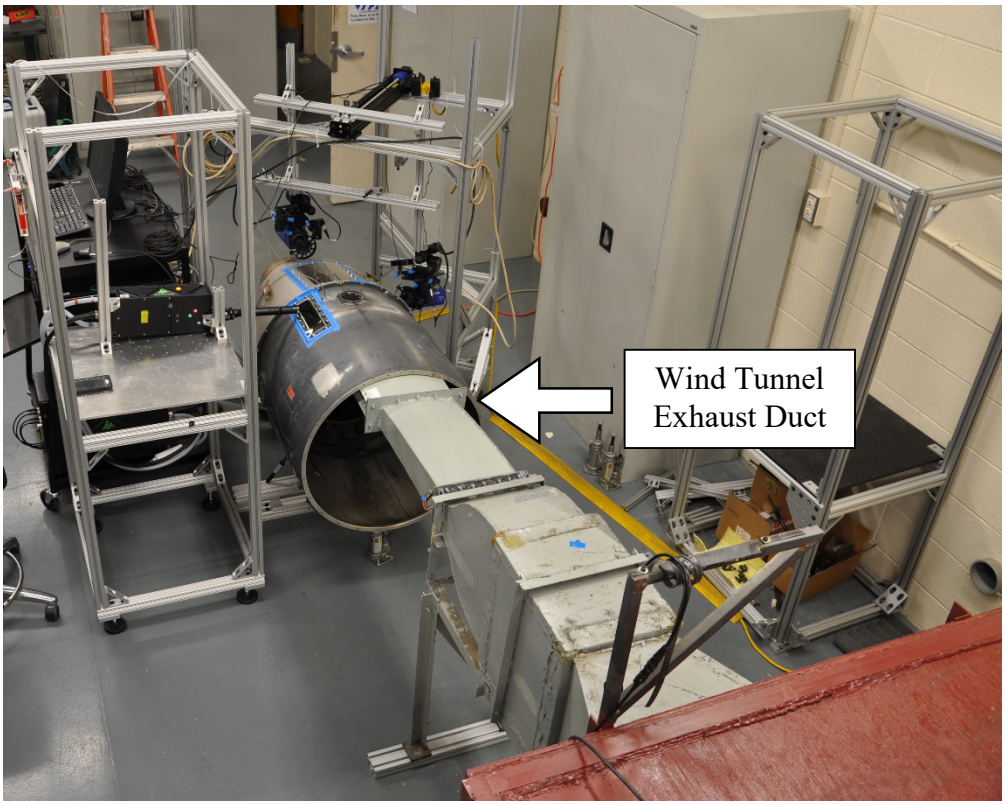

Figure 28 – Simulated engine and wind tunnel exhaust duct

5.5.2.1 Seed Insertion

This experiment utilized Concept Smoke Systems's Colt 4 Smoke machine, shown in Figure 29. Similar to what is used in theatrical productions, the Colt 4 produces microscopic particles of a glycerine-water mixture that make up the company's Smoke Fluid A. Concept states the particles range in size between 0.2-0.3 micron and have a relative density of 1262 kg/m^3 at 20 °C. These properties were used to calculate a particle time lag of 0.3 μs using Stokes' drag solution, Equation (5.1), from Crowe et al [57],

$$\tau_p = \frac{\rho_p d_p^2}{18\mu_f} \tag{5.1}$$

The Colt 4 does not come standard with any time of connect fitting for its output, rather it simply projects the smoke out of its front. With this in mind, the Colt 4 was aligned

within close proximity to the wind tunnel's intake duct instead of attempting to construct a connection between the Colt 4 and the tunnel.

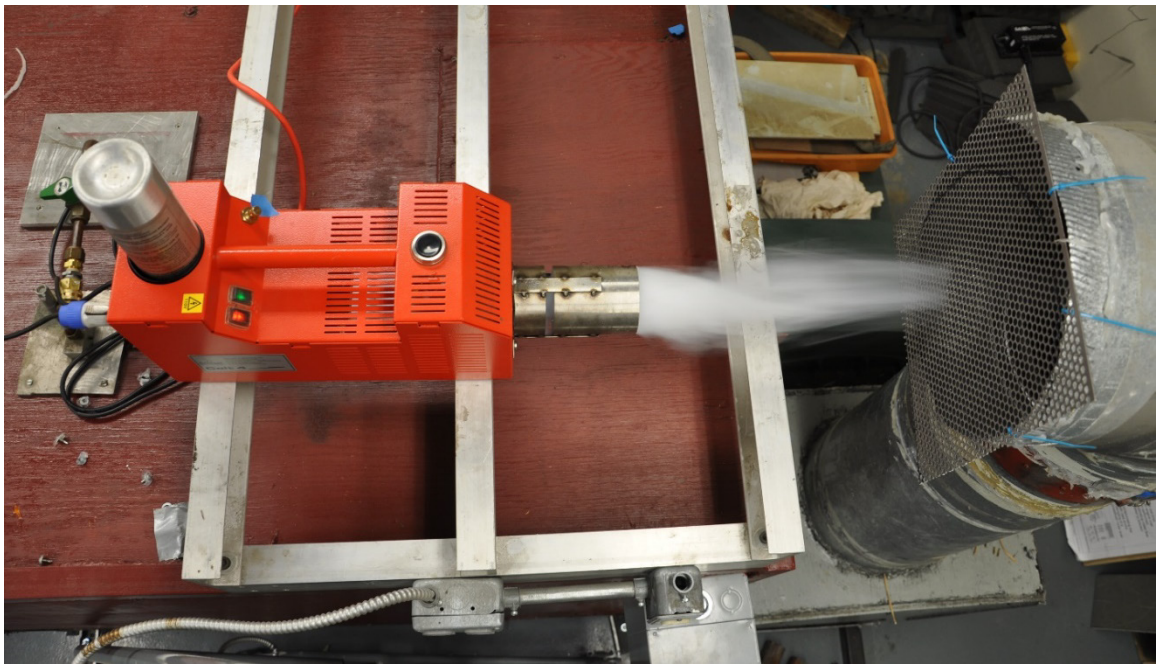

Figure 29 – Colt 4 smoke machine

5.5.2.1 PIV System Specifications and Design Process

The laser used was a Quantel EverGreen 200 dual-pulse Nd:YAG laser, capable of 200 mJ/pulse at a wavelength of 532 nm. The EverGreen also bolstered a maximum pulse repetition rate of 15 Hz and a pulse width $\leq$ 10 ns. As the design for the simulated engine experiment came together, a number of possible measurement planes (and therefore laser sheet locations) were discussed. To provide the most flexibility, a 9.5-inch by 2-inch window was constructed in the bypass duct casing. The possibility of both an upstream and downstream measurement (relative to the support strut) was particularly enticing. Such a measurement could lend itself to more easily calculating the momentum deficit caused by the strut, especially if both measurements occurred simultaneously. However, it was determined that an upstream measurement would prove much more difficult, potentially requiring multiple camera positions and increased engine modifications.

As such, the final design located the laser sheet 4.5 strut diameters, or 2.25 inches, downstream of the support strut, Figure 30. This would allow for clear observation of the support strut wake as it developed downstream. Additionally, moving the laser sheet to that

location downstream would reduce the amount of laser glare on the strut seen by the cameras while also observing the strut wake move back in forth (instead of observing a steadier stagnation bubble immediately downstream of the support strut). In order for the laser sheet to reach the measurement plane in such a fashion, the laser was position outside the engine as shown in Figure 31. An extension tube was connected to the collimator which was attached to the laser housing so that the laser would pass through a -20 mm and then a -10 mm focal length cylindrical lens that would begin expanding the laser into a laser sheet immediately before it passed through the window and entered the engine.

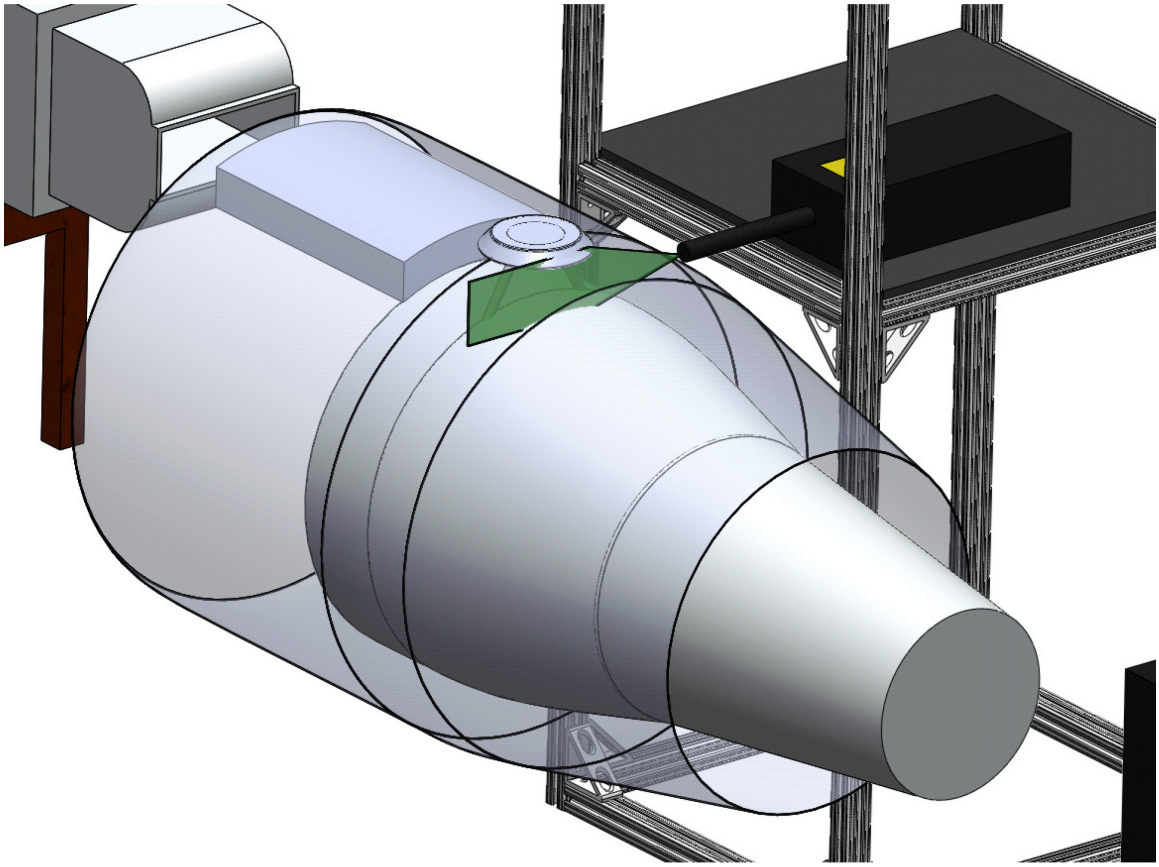

Figure 30 – CAD model JT15D-1 and design laser sheet/measurement plane

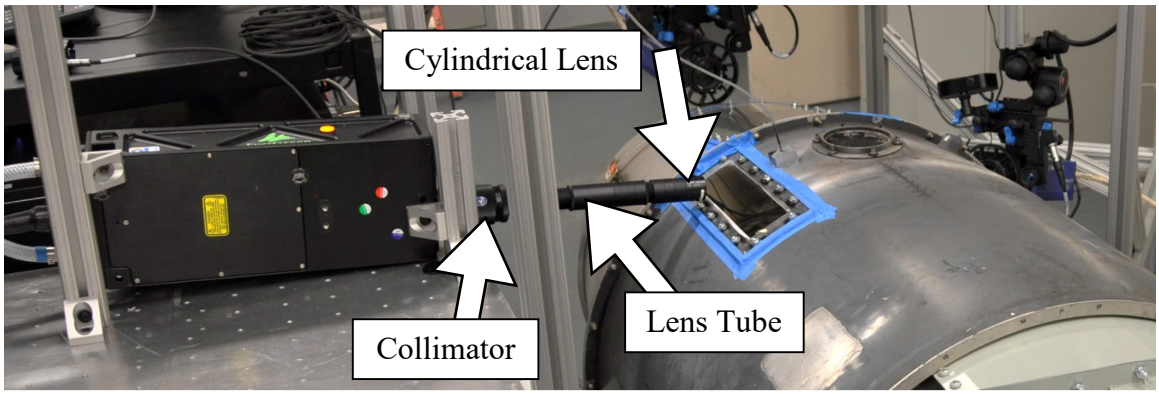

Figure 31 – Laser head and extending optical tube setup

Two LaVsion Imager Pro 4 X 4M high sensitivity, high resolution cameras were used during this experiment, Figure 32. These cameras feature 4-megapixel resolution at 2048 by 2048 at 14 frames per second. The pixels are 7.4x7.4 μm in size and the camera sensor can image wavelengths between 290 and 1100 nm while having a max quantum efficiency of 55% at 500 nm.

Figure 32 – LaVision Imager Pro 4 X 4M camera

Positioning the cameras was an iterative process that utilized computer models to ensure minimal or no geometric obstructions, EDA to maximize particle image intensity and field of view while minimizing hardware setup and modification time, and intuition from constructing the simulated engine to minimize engine modifications. To briefly summarize the EDA software package described in Chapter 4, it combines optical relationships and a

derivation for mean exposure [3] into a simple to use package so that a novice PIV experimentalist can iterate through several experimental designs until the desired field of view, depth of field, scattered light intensity, etc. are achieved.

Figure 33 illustrates the design process followed for this study. First a database of relevant experiments was compiled. It was composed of the following experiments: Guimarães et al. [6] (diamond marker) and Nelson [5] (circle marker) represent studies of distorted inflow that also utilized the Virginia Tech JT15D-1 research engine, Schröder et al. [7] (triangle marker) represents an experiment performed by the German Aerospace Center (DLR) of the engine intake of an Airbus A320 in ground operation with a very large field of view (approximately 43 x 16 in^2), Pol Balakumar [43] (upside down triangle marker) represents another large scale PIV experiment that measured about 30 x 39 in^2, and lastly, the three de Silva et al. [46] markers (triangle pointing right, triangle pointing left, and asterisk) represent a single experiment that used multiple camera systems at an experiment relative low, medium, and high magnifications to capture a large total field of view (approximately 31 x 17 in^2) in addition to a very large dynamic spatial range. Schröder et al., Pol and Balakumar, and de Silva et al. pushed PIV toward the highest fields of view and therefore lesser amounts of scattered light.

Next, several design iterations were tested. From Figure 33, it was possible to compare the expected mean exposure of the design with the various benchmarks listed. If the proposed design was very near or below the lowest benchmark, then it was deemed to have too low a likelihood of success. The next design would then be developed to try to acquire more scattered light. This must of course also be balanced with the other desired output metrics like field of view. The final design is represented by the various colored lines in Figure 33. Each color represents a different camera lens aperture setting over a range of stand off distances (distances between the laser sheet and the cameras). Finally, the George 2016 marker (plus) represents the final design parameters of the tested experiment in this study. It can be seen that it was designed to achieve a mean exposure value about a magnitude higher than the lowest benchmark.

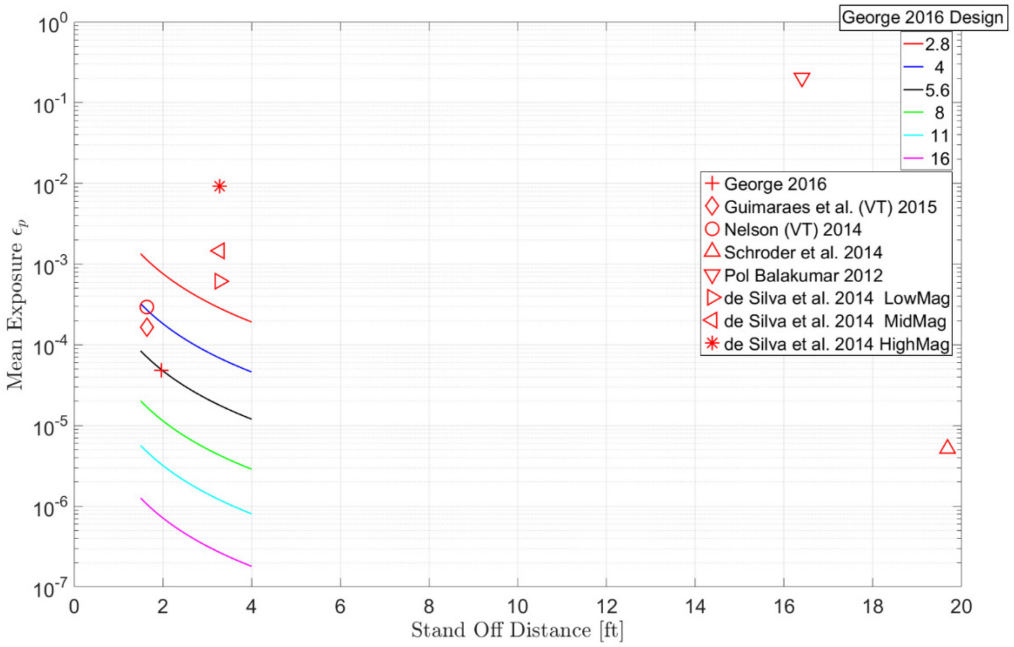

Figure 33 – Mean exposure values for benchmark experiments, proposed experiment designs, and final design

The developed solution, Figure 34, located camera 1 in the paraxial location relative to the laser sheet, rotated only slightly so as to focus on the location in the measurement region where the wake of the port side support strut would appear. Camera 2 was located on the port side, approximate 50 degrees from the engine center line (40 degrees from forward scatter), and again rotated such that it was focused on the measurement region location of the port side support strut wake. They were about positioned about 21.6 inches and 14.6 inches, respectively, away from the measurement plane. Due to the extreme angle of Camera 2, a Scheimpflug adapter [58] was used to alter the focal plane of the camera so that it more closely aligned with the measurement plane.

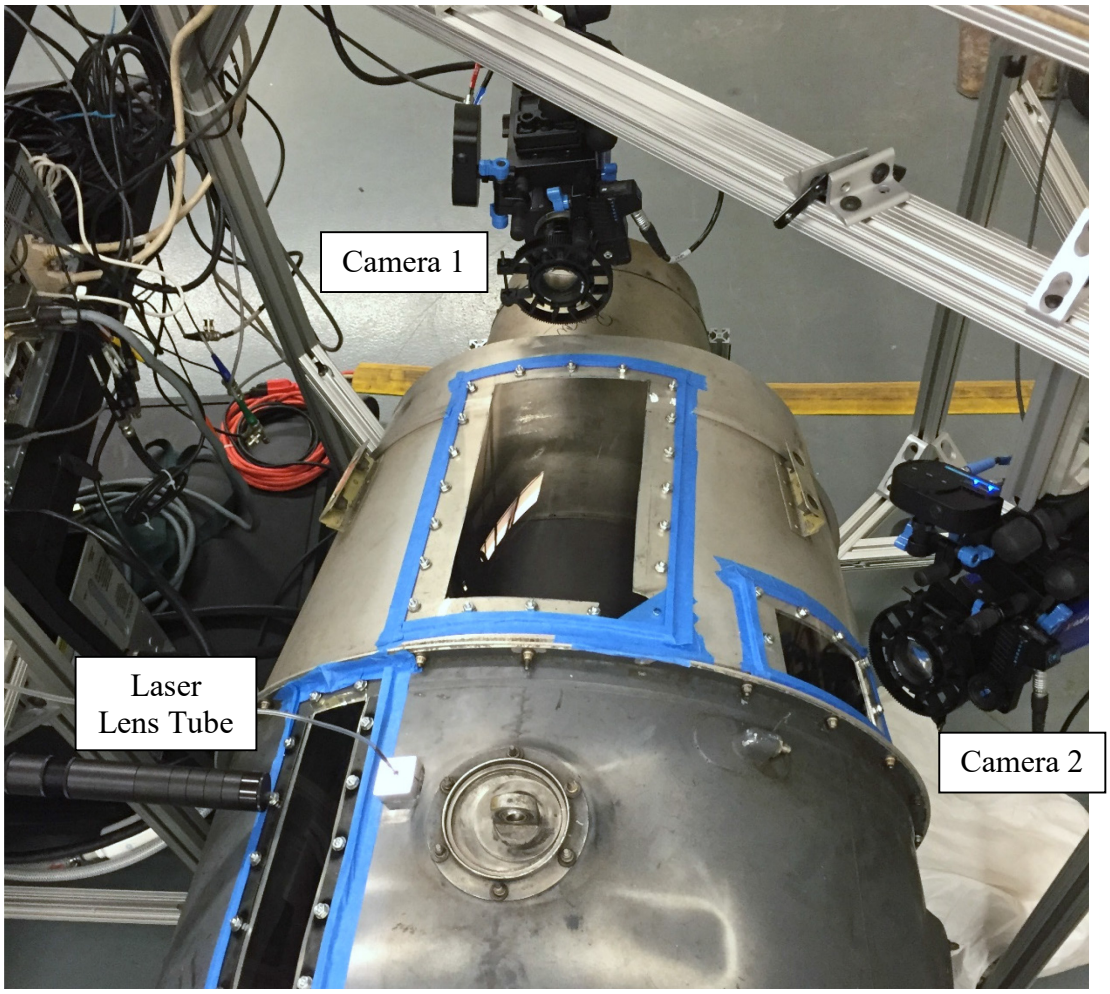

Figure 34 – Final simulated engine experimental setup

This arrangement offered several benefits. The most important is it takes advantage of forward scatter and therefore is capable of brighter particle images and higher signal to noise ratios. The brightness of the particles as they appear in the images, also known as scattered light intensity, is a function of the angle between the camera and laser sheet. As Figure 35 shows, the brightest intensity appears when the camera is nearly looking back at the laser, a scattering angle approximately zero, also known as forward scatter. It then decreases as the angle is increased, through the region of side scatter, before the intensity begins to increase again (although at a much lower level compared to the forward scatter regime) as the camera approaches the point where it is nearly looking in the same direction as the laser, a scattering angle approximately 180 degrees, also known as back scatter. These camera locations could have very easily been flipped symmetrically about the engine centerline, however such a design would have placed one of the cameras in back scatter,

resulting in lower particle image brightness, lower signal to noise ratio, and less flexibility to make fine adjustments to the laser power and camera aperture settings as desired. This arrangement also allowed for the widest field of view of the port side support strut wake in the measurement plane as could be designed while avoiding any geometric obstructions.

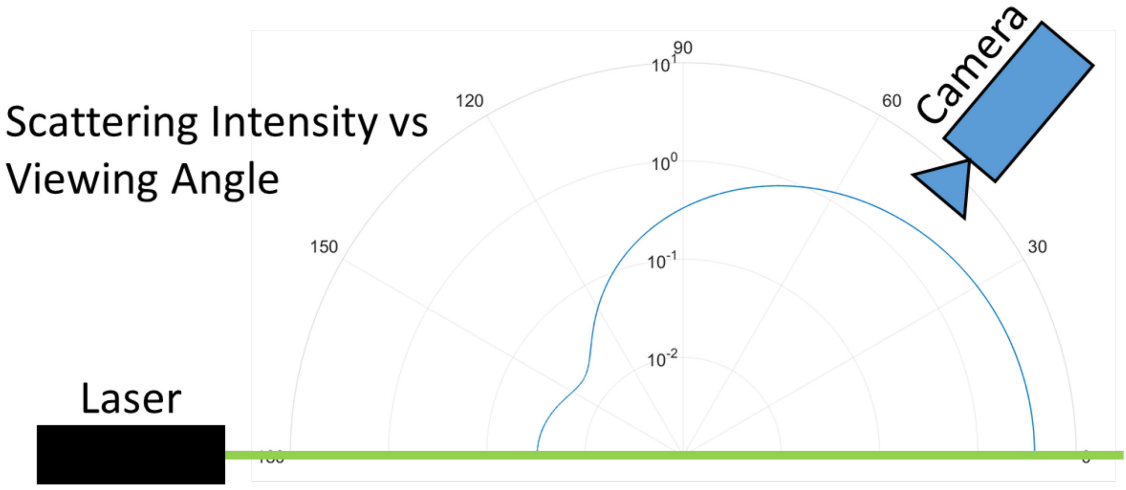

Figure 35 – Mie scattering: light intensity vs scattering angle

Final notes on the testing hardware related to the cameras are as follows. The windows to accommodate this design measured 12 x 6 square inches for camera 1 and 4.5 x 3 square inches for camera 2 and were made of flexible 3 mm cast acrylic with an anti-glare coating on both sides and an anti-smudge coating on the interior side. Pertaining to the cameras themselves, 532 nm lens filters were used to block out any other sources of light in addition to minimizing the risk of laser damage to the camera sensors. Remote focusers were also employed, shown in Figure 36. They would be extremely useful during the full-scale engine test when the engine was running but the cameras' focus needed slight adjustment. These focusers work by placing a gear around the camera focus ring and adjusting it via an electric motor attached to another gear. The system works very well and is capable of very fine adjustments, however, the focus lens ring is rather large, and limits how close the cameras are able to be positioned next to the windows. This topic will be discussed further in future sections.

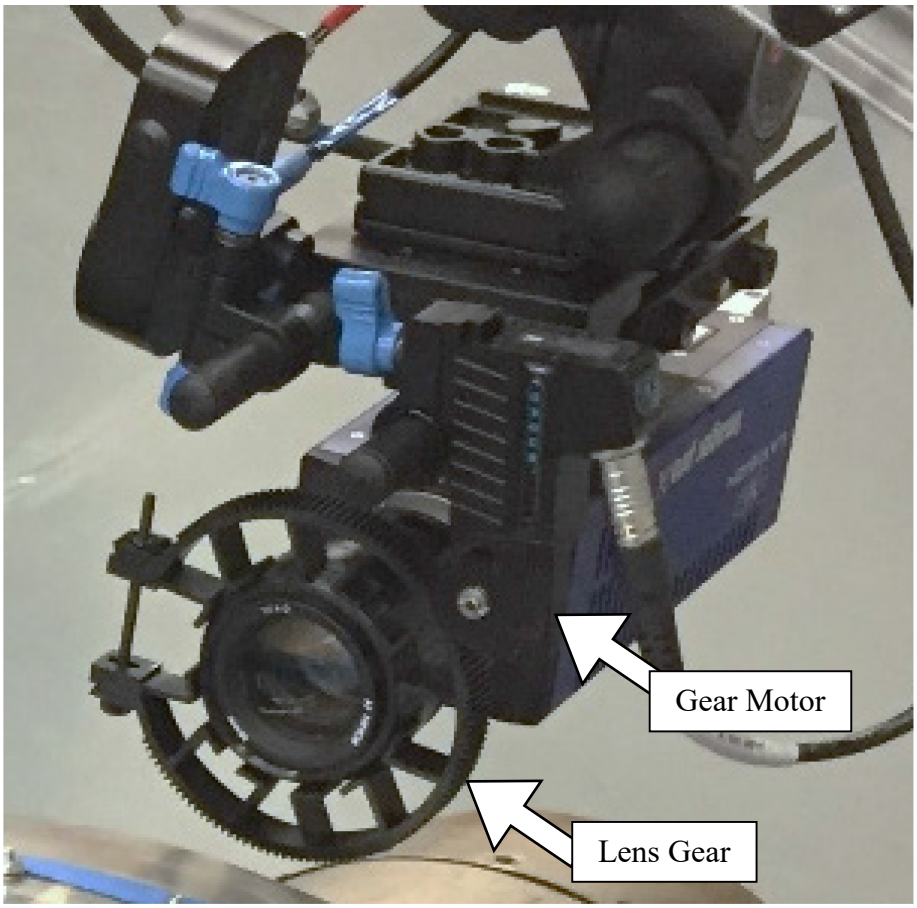

Figure 36 – PIV camera remote focus system

5.5.2.2 Data Recording Specifications

As mentioned previously, this experiment was performed at two test conditions: support strut in place and no support strut in place. For both cases however, all components of the optics system remained in their respective positions, and in the same configuration. Nikon 50 mm lenses were used at aperture settings of 5.6 and 16 for camera 1 and camera 2 respectively. At that magnification and distance to the measurement plane, the result was a spatial resolution of 22.35 pixels per mm.

The laser, although capable of producing 200 mJ/pulse, was used at a lower, yet sufficient, power setting. The collimator and cylindrical lens combined to form a laser sheet approximately 3 mm in thickness and 101.6 mm in height. Sampling occurred at 4 Hz with a time between laser pulses (dt) of 8 μs. In total, 10,000 images were acquired for both the strut and no strut test cases.

5.5.2.3 Calibration

This experiment incorporated an external calibration plus self-calibration, Wieneke [59]. Self-calibration is a method by which to compensate for misalignment between the calibration plate and the light sheet. It can be used in conjunction with an external calibration but it is important that the optical path, the distances between the cameras and the calibration target, as well as the distances related to the locations of mediums of varying indices of refraction remain unchanged with respect to the optical path between the cameras and the light sheet during the actual experiment. This concept is illustrated in Figure 37.

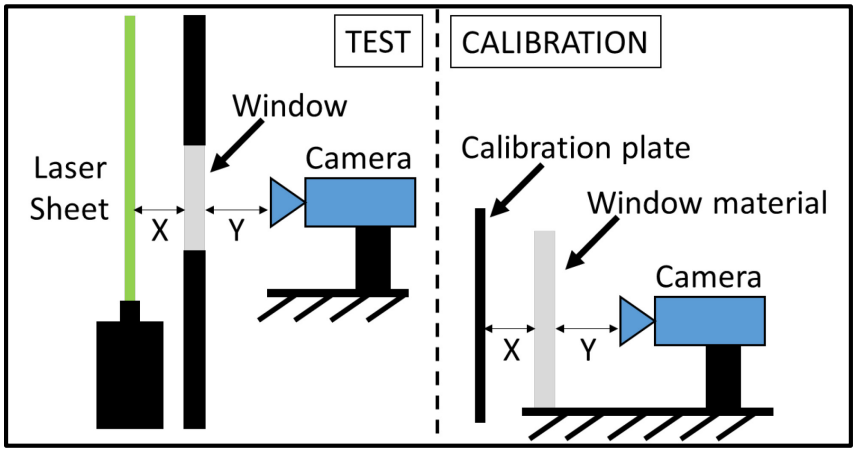

Figure 37 – External calibration process

Other methods were discussed, but the external was determined to be the most practical at the present time. Some of the other techniques involved cutting an additional slit in the engine to slide the calibration down through, others involved manufacturing a custom calibration plate. The external technique however, provided a method that initially required no modifications to the engine, and did so with a minimal cost in time and resources.

An external calibration would be implemented as follows. The cameras would be mounted to a coupled traverse system that would allow the cameras to retract away from the engine at an approximate angle of 45 degrees. Once retracted, a rig would be attached to the camera support system that would hold replica windows (of the same curvature as those mounted to the simulated engine) the exact distance away from the two cameras as the other windows would be during the test. Finally, the calibration plate would also be mounted to the camera support structure so that it was located the same distance away from the cameras and windows as the laser sheet will be during the test. Once the calibration images were taken, the replica windows and calibration sheets would be removed, and the

cameras would be traversed back to their original positions near the simulated engine. Following the acquisition of images with the seeded flow on, the self-calibration technique in LaVision DaVis would be used to correct for minor discrepancies between the position and angle of the calibration plate with respect to the cameras, and the position and angle of the laser sheet.

During the construction phase of the experiment, a method was not able to be developed that would sufficiently hold the replica windows to the same curvature as those on the simulated engine. In lieu of this, it was decided that it would be better to simply perform the calibration the same way as was just described but without the curved replica windows rather than mount a non-curved replica window in its place.

5.5.2.4 Pitot-Static Measurements

Following the PIV measurements, "steady-state" total pressure measurements were desired to calculate velocity to validate the PIV results. A standard Pitot-static pressure probe was used in junction with an inclined differential manometer that had a capable range of 0-6 inches of water. Probe access to the measurement plane 4.5 diameters downstream of the support strut was limited. The most practical option involved removing the window used by camera 1 and patching the hole except for a small slit near the forward edge of the hole as shown in Figure 38. This resulted in dynamic pressure measurements 10.5 diameters downstream of the support strut location. The test was repeated for the no support strut case as well.

The probe was traversed from the core nozzle to the bypass duct casing as well as the full width of the window hole which it was submersed in. The resulting grid was approximately 18 x 10 with a few extra points beyond that due to the curvature of the engine. Grid points were spaced by approximately 0.669 inches in the horizontal direction and 0.143 inches in the vertical direction. Measurements were made roughly every 30 seconds to allow the probe to "settle," but also in order to allow time to observe and record the measurement of the manometer.

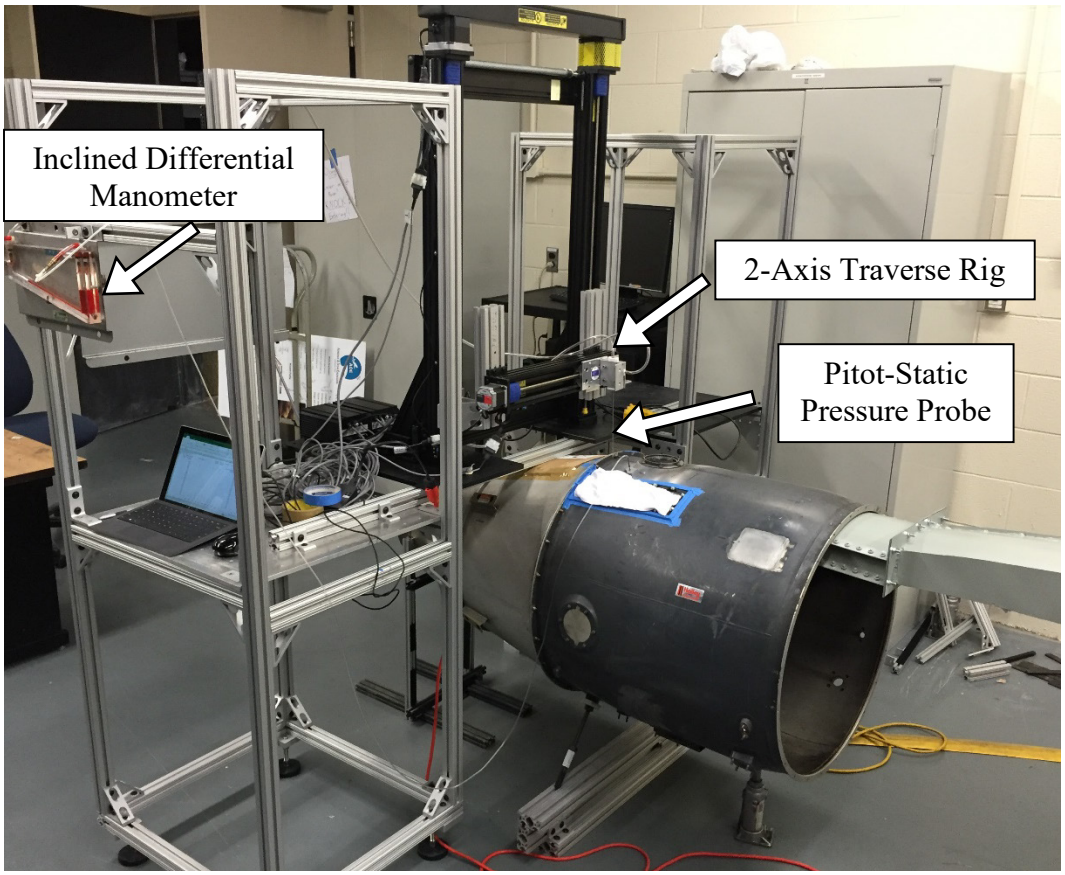

Figure 38 – Pitot-static pressure probe measurement setup

5.5.3 Experiment Results

Although the results from this experiment were not intended for analysis other than verifying the functionality of the optical setup, they are included here for completeness. First, Figure 39 and Figure 40 depict the test case with the support strut in place and is most similar to what will be replicated in the full-scale test. Specifically, Figure 39 illustrates the stream-wise velocity from the PIV data and Figure 40 shows the corresponding velocity calculated from the Pitot-static pressure data. Please recall the pressure data was acquired further downstream and a direct and exact comparison between the two methods is not warranted. Also note the coordinate system origin for the Pitot-static probe data does not correspond with the same location as the origin for the PIV data. Similarly for the no strut test case, Figure 41 shows the stream-wise velocity from the PIV data and Figure 42 illustrates the stream-wise velocity calculated from the Pitot-static pressure data. The in-plane velocity PIV data is included in Appendix A.3.

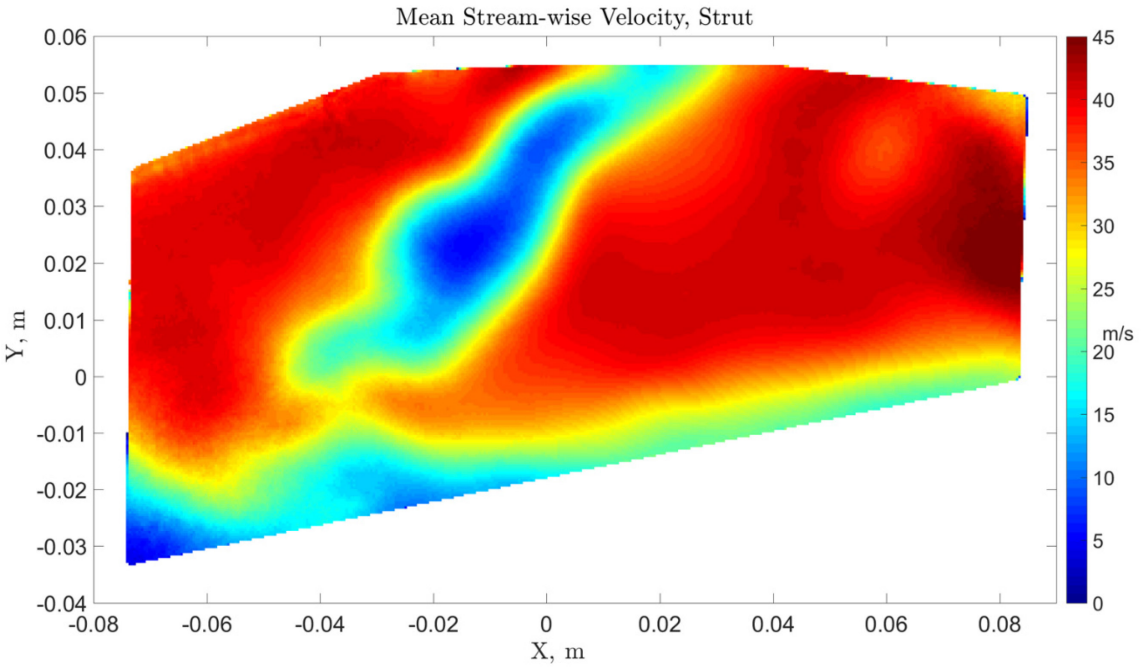

Figure 39 – Simulated engine with strut stream-wise velocity, PIV

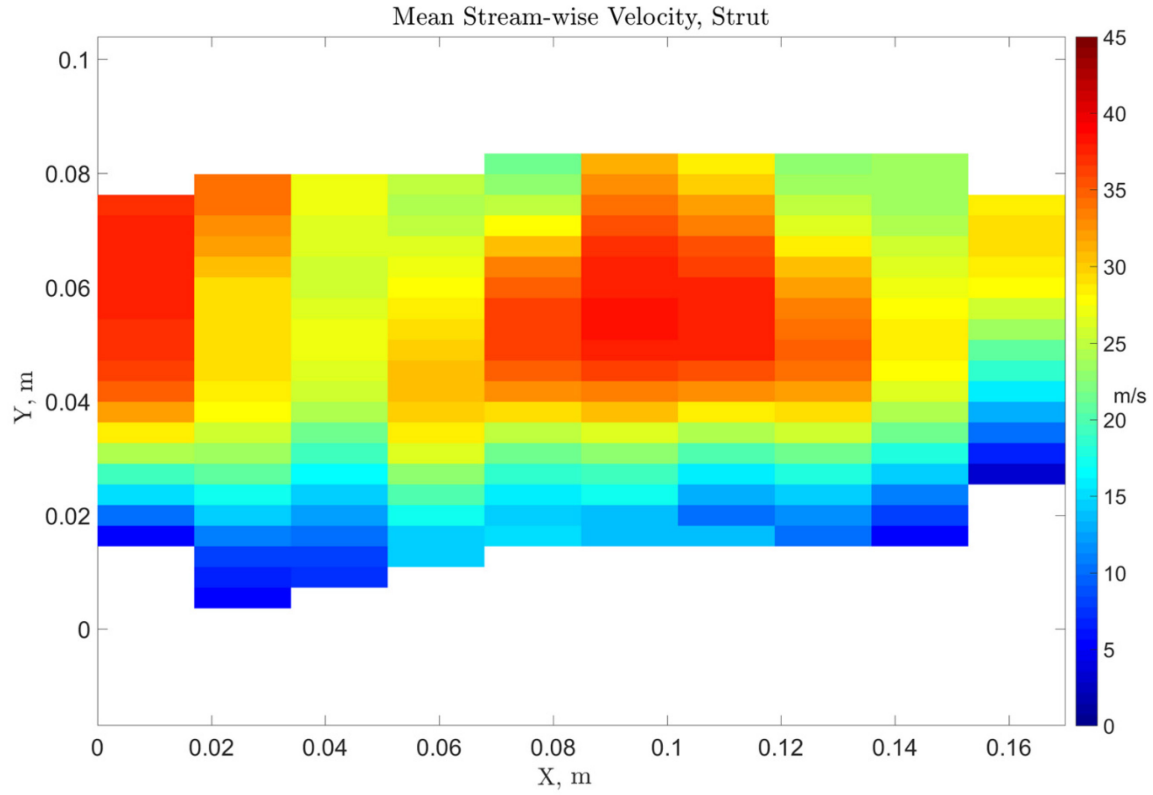

Figure 40 – Simulated engine with strut stream-wise velocity, calculated from Pitot-static dynamic pressure

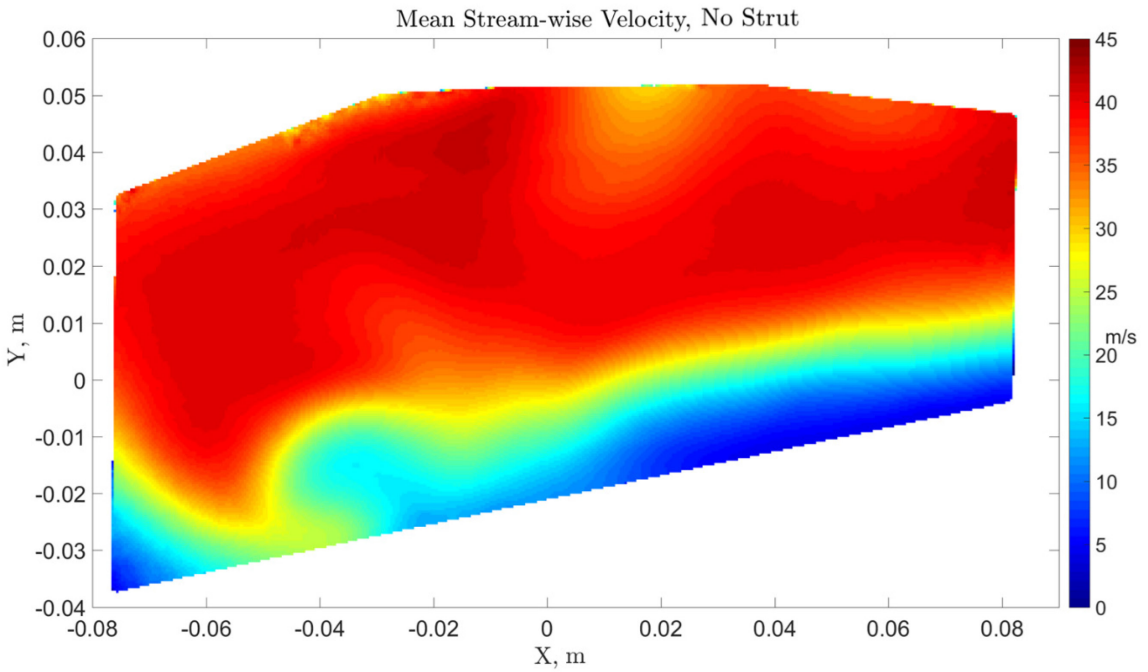

Figure 41 – Simulated engine without strut stream-wise velocity, PIV

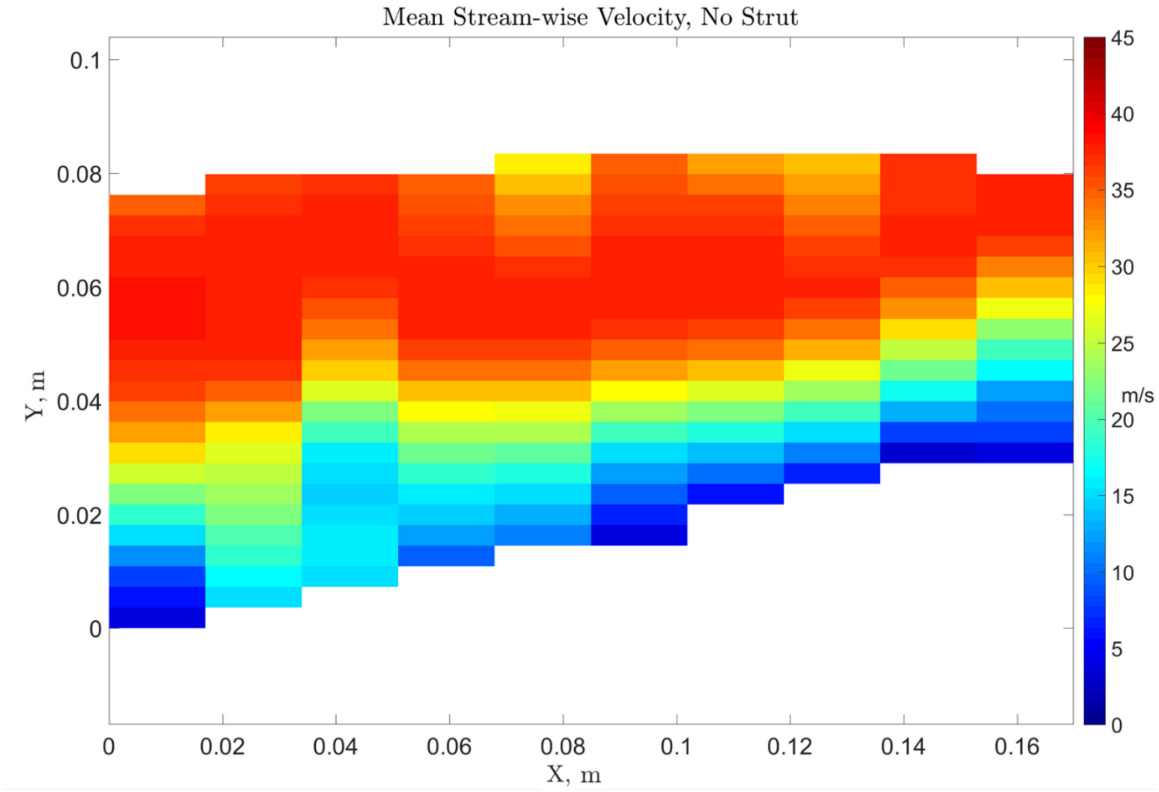

Figure 42 – Simulated engine without strut stream-wise velocity, calculated from Pitot-static dynamic pressure

5.5.4 Simulated Engine Experiment Summary

In summary, a risk reduction experiment was performed in a simulated engine environment. The intent was to replicate the optical setup as closely as possible to what would be used for the test stand engine experiment. This would allow for a number of concerns and potential problems to be mitigated before the full-scale experiment, reducing the time and cost necessary of the full-scale experiment, while minimizing if not eliminating the number of unnecessary modifications made to the research engine. Pitot-static probe measurements were used to validate the simulated engine environment PIV measurements.

The risk reduction experiment proceeded very well and accomplished exactly what was intended. Camera and laser locations were confirmed to produce the desired field of view, depth of focus, and scattered light intensity. The quality of the seed insertion and the images was very high, resulting in strong correlations during the vector calculation. A number of large scale flow features were identified and traced back to upstream causes. Examples include the wake from the strut, a shear layer from a small gap between the wind tunnel exhaust and the core wall, and a vortex from within the wind tunnel exhaust. It is worth mentioning again that a full analysis was not completed on the velocity vector fields because the focus was on ensuring the setup could produce the desired results rather than the results themselves. As such, some design changes were deemed necessary but they will be detailed further in the following section.

5.6 Test Stand JT15D-1

5.6.1 Modifications to Experiment Design

Following the completion of the simulated engine experiment, many necessary modifications were apparent before proceeding with the test stand experiment. Some of them will be described here. First, the laser needed to be redirected around one of the posts that made up the engine support structure, depicted in Figure 43.

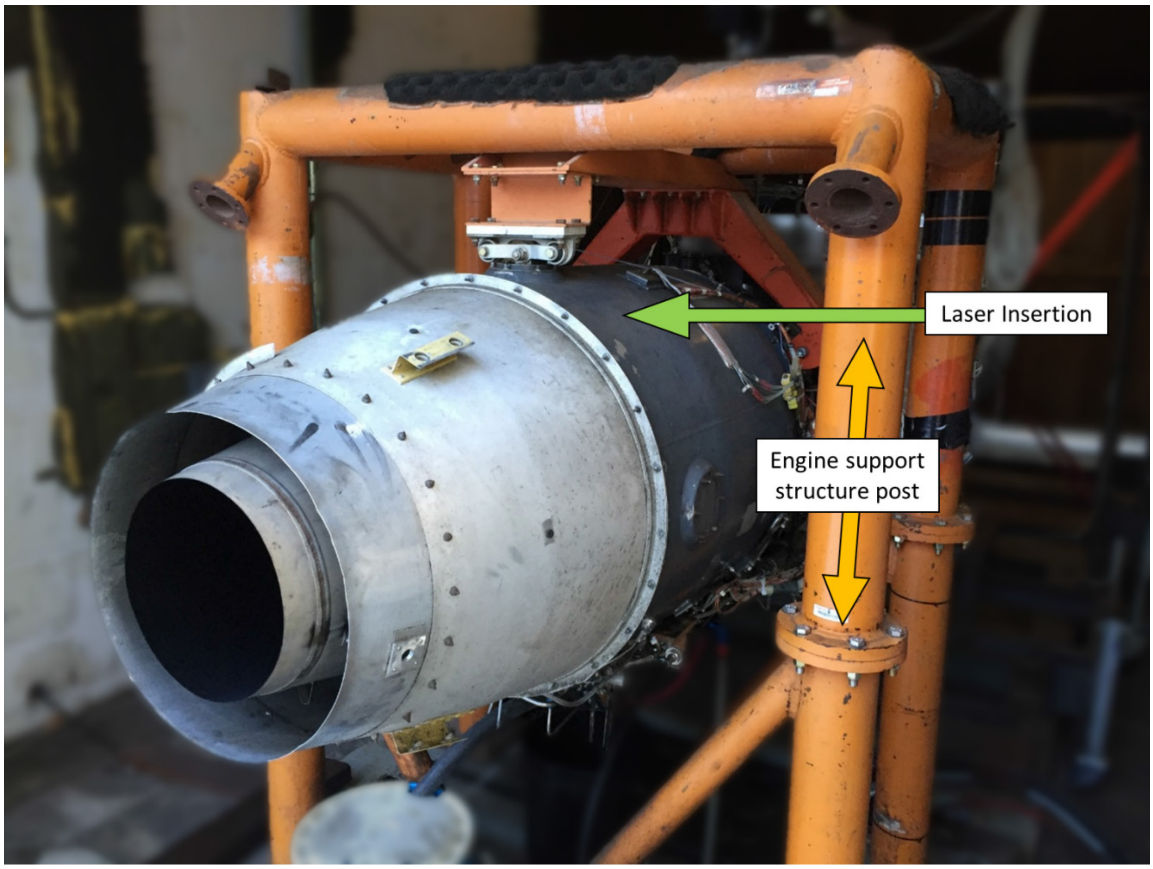

Figure 43 – Unmodified JT15D-1

This post was located directly in the desired pathway of the laser. Two high power mirrors were used to maneuver the laser beam around the post before passing through the cylindrical lenses and expanding into the engine, illustrated in Figure 44. Furthermore, since measurements were only going to be made at one plane (2.25 inches downstream of the support strut), the laser window no longer needed to be 9.5 inches long. Instead the laser window was redesigned to be 1.25 inches tall by 0.25 inches wide to minimize permanent modifications to the research engine, shown in Figure 45.

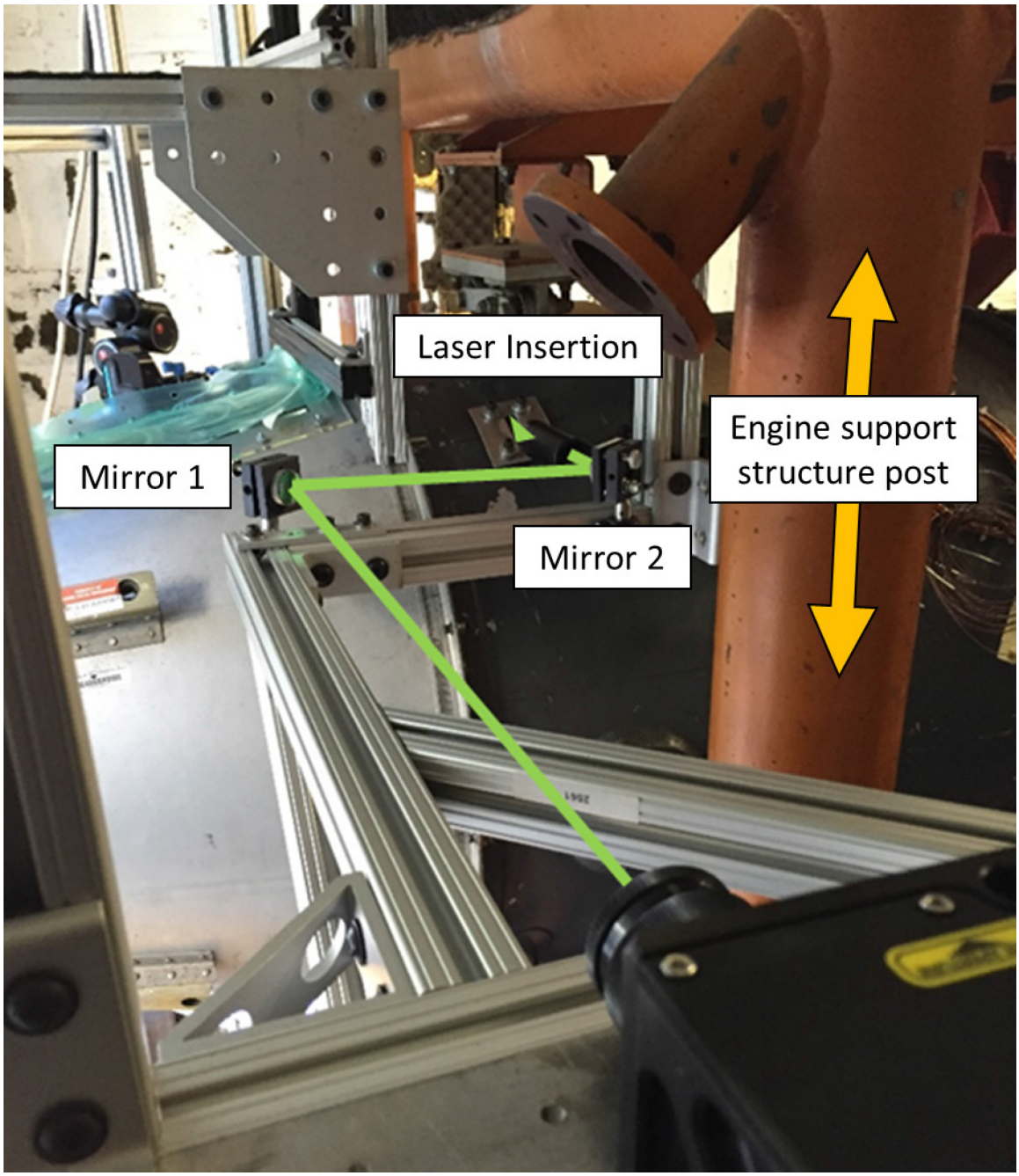

Figure 44 – Laser insertion path

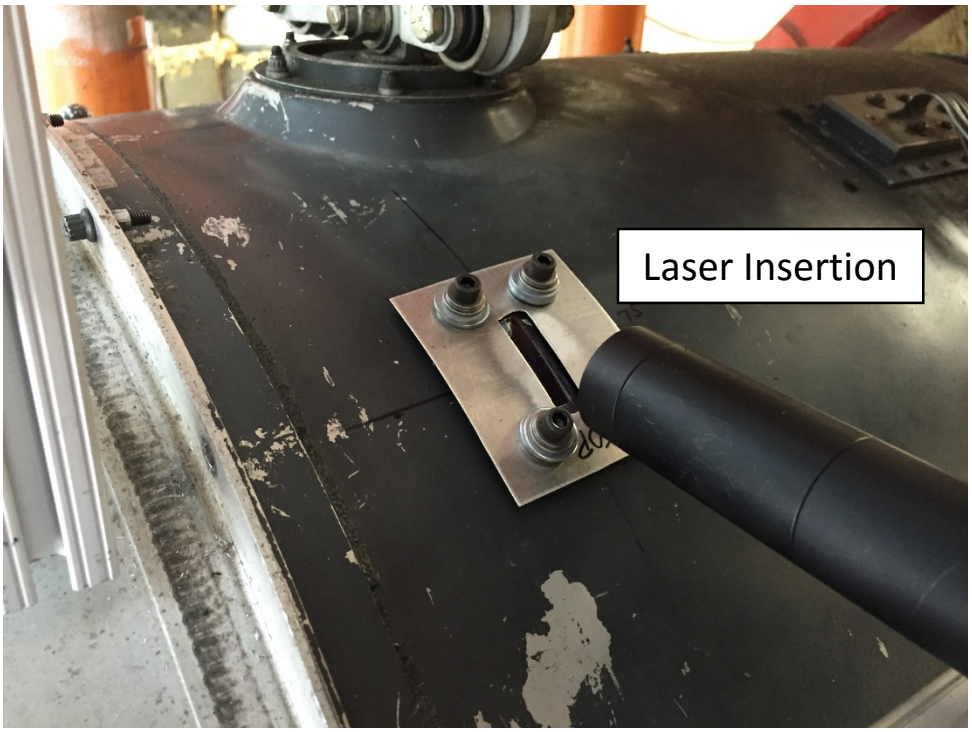

Figure 45 – JT15D-1 laser window

With regards to the cameras, camera 1 was determined to be too close to the engine exhaust so a 3 inch 90-degree mirror was used to redirect the cameras field of view back into the engine while the camera was held vertical and safely away from the engine exhaust, Figure 46. Also, the remote focusers were removed from the experiment. The decision was made because the focus rings limited how close the cameras could be positioned to the windows, and thus restricted the cameras from maximizing their field of view. The original focus rings used in the simulated engine experiment were 4 inches in diameter. New, smaller rings were designed and constructed using additive manufacturing that were only 2.75 inches in diameter. However, once the experiment was built around the test stand, it became apparent that the field of view still needed to be larger, so the focusers were removed.

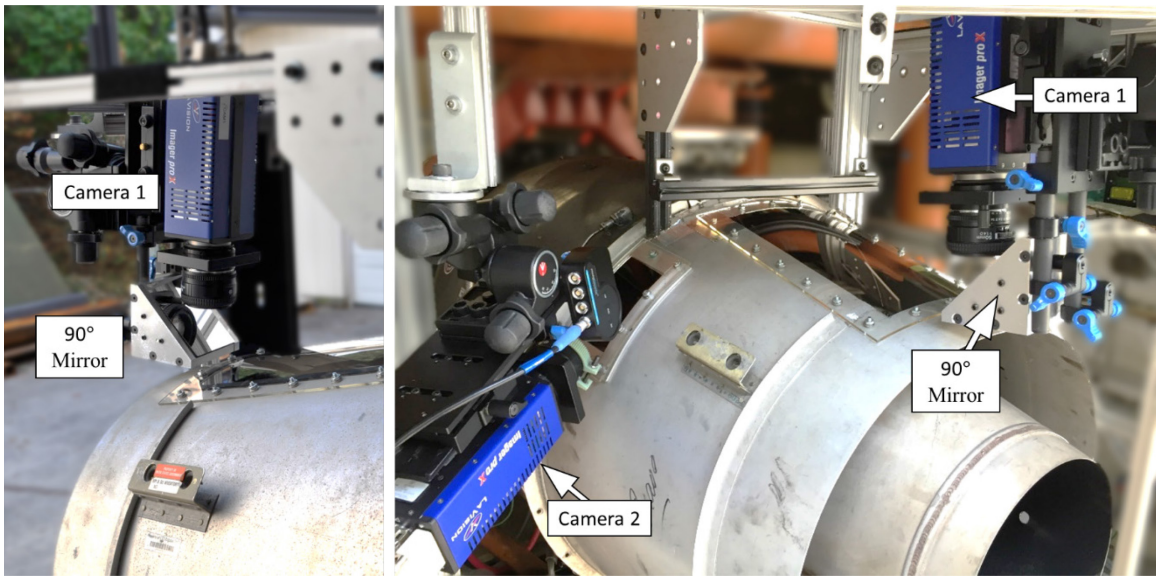

Figure 46 – Camera 1 redirect

The calibration procedure was heavily modified. The original intention had been to traverse the cameras back, place replica windows (with same curvature as the test windows) in the same relative position relative to the cameras, and then position a calibration plate in the same relative position of the laser sheet during the test. Once the calibration images had been acquired, the plate and replica windows would be removed and the cameras would be traversed back to their original positions. However, adequate replica windows could not be constructed so it was decided to remove the entire nozzle that the windows were mounted on. The cameras would be retracted, no longer with a traverse but rather the whole structure would be moved back to provide the necessary clearance between the nozzle and the engine, the nozzle would be placed in the same relative position relative to the cameras, and again the calibration plate would be placed in the same relative position as the laser sheet during the test, Figure 47.

To minimize errors, the camera support rig and nozzle mount rig were aligned using three points before their retracting, during the calibration, and prior to test. Two of the points were bolt holes in the nozzle that connected the nozzle to the bypass duct case and were aligned with a component of the camera support structure. The third point was a mark on the nozzle exhaust that was aligned with another component of the camera support structure. Additionally, the laser sheet during test was a known distance forward of the

location where the nozzle and bypass duct case are bolted together. This distance was replicated on the nozzle mount rig to position the calibration plate during the calibration procedure.

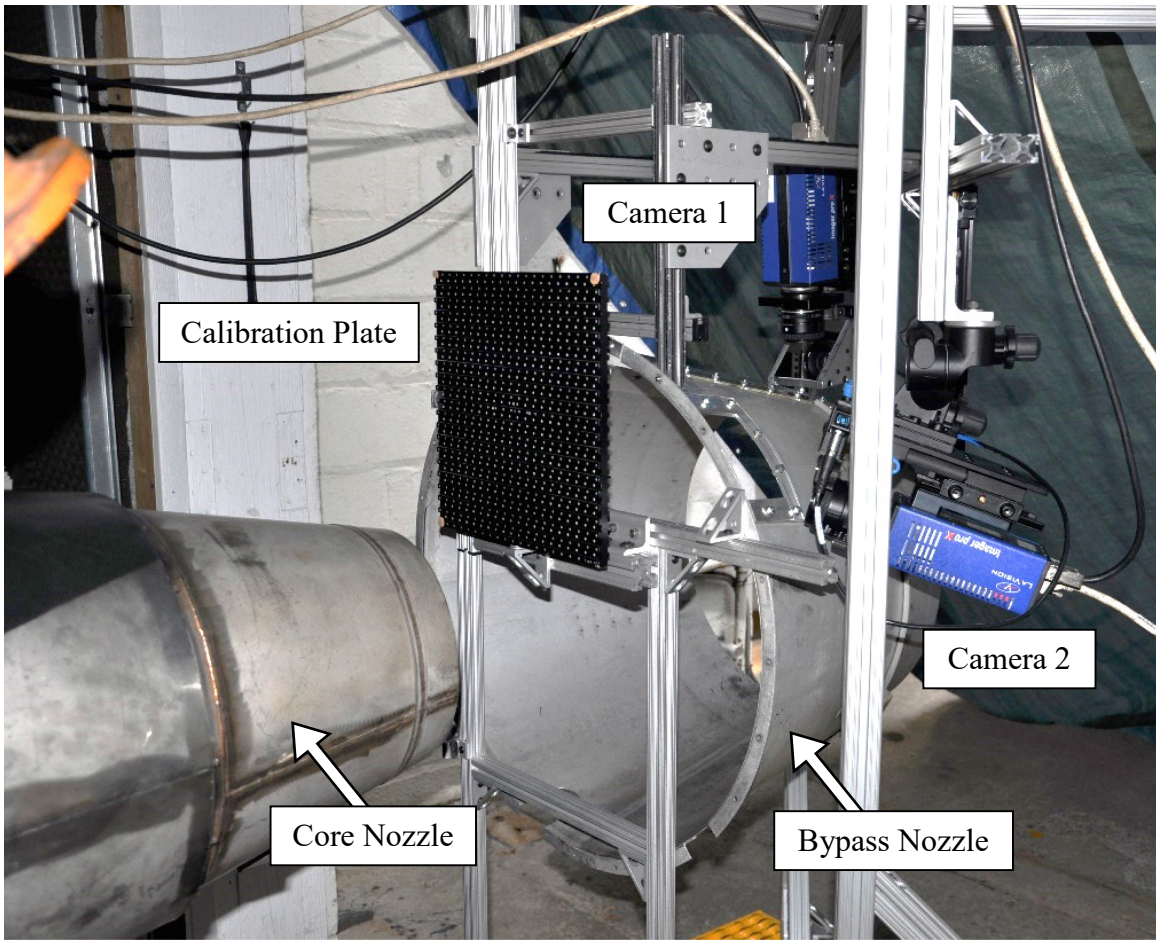

Figure 47 – Retracted nozzle during external calibration process

Another modification made to the camera support structure revolved around the concern of engine vibration. In previous experiments with the JT15D, a mechanical link existed between the engine and the cameras [5]. The resulting images were not usable due to the vibrations the cameras experienced. Although this experiment did not link the cameras to the engine, vibrations could travel through the concrete foundation on which the engine and camera support structure both rested. To minimize vibrations, both the camera support structure and the laser support structure were tightened down using galvanized steel cables. Once testing began, camera vibrations were observed using the accelerometer in an iPhone which measured negligible accelerations less than 0.4 m/s^2 at the highest fan speed, the test case of most concern.

Seed insertion needed to be done differently than it was for the simulated engine for obvious reasons. Nelson [5] tested several methods of seed insertion for an engine inlet PIV experiment that included both methods internal and external to the engine inlet bell mouth. It was determined that the methods tested internal to the bell mouth caused a noticeable flow disruption and were therefore not appropriate for the inlet experiment. Rather seed was introduced to the intake by two external seeders, one above and projecting seed in the opposite direction of the intake, and one on the ground angled from the side projecting the seed towards the intake.

It was determined for this experiment that other design aspects were higher priority and so the previously successful method of Nelson was adopted with the exception that only one seeder was going to be used. Initially, the seeder was located on the ground off to the side. However, the final design introduced the seed from above. In this design, the smoke machine was located on the ground projecting the seed into a PVC pipe which carried it to a leaf blower above the engine. The leaf blower propelled the particles forward where the air intake of the inlet bell mouth captured the particles and transported them into the engine. This process is shown in Figure 48 below.

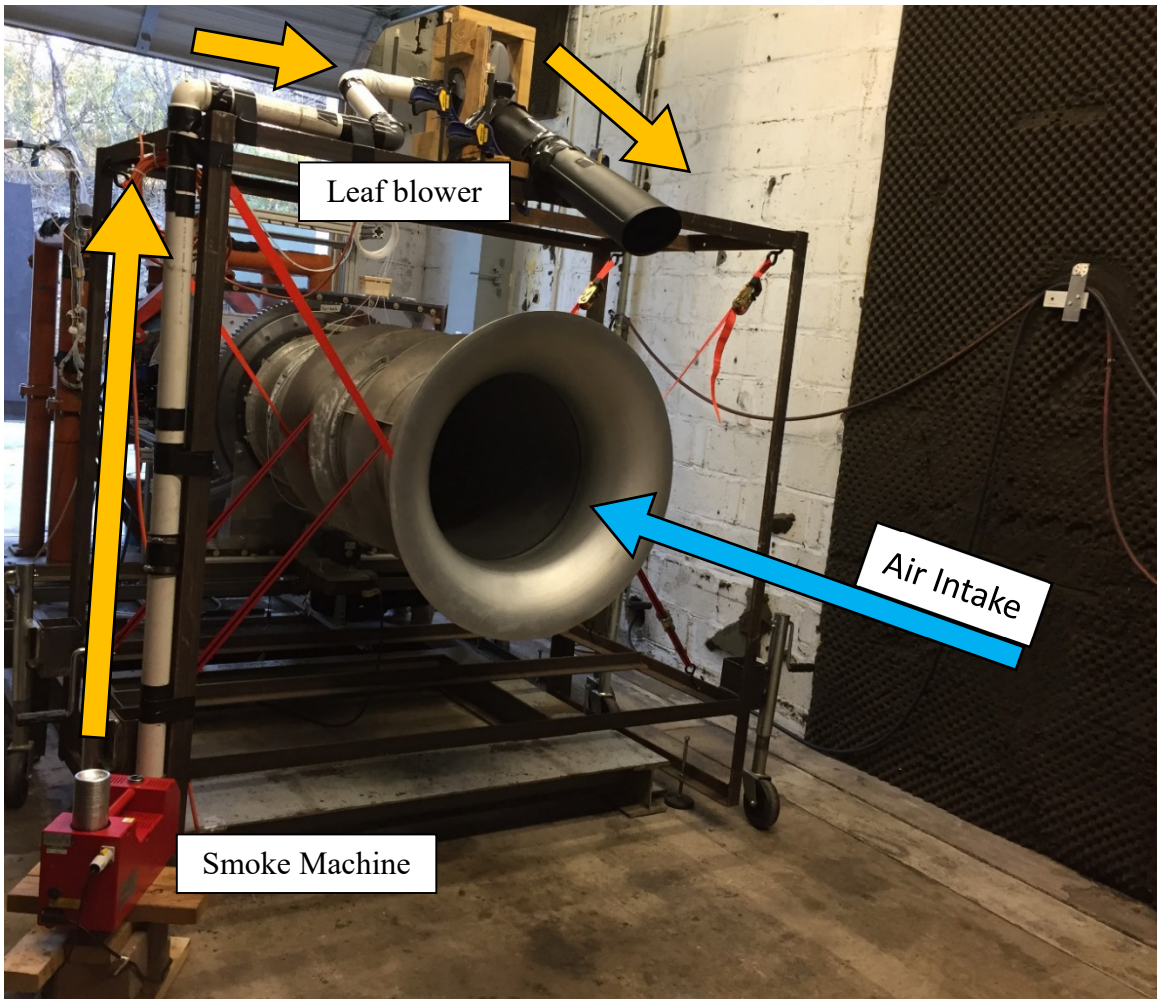

Figure 48 – JT15D-1 seed insertion

The last major modification occurred after testing had begun and the engine was observed to move more than originally thought. At the most, then engine moved forward about 3/16 of an inch. Since the laser window was only ¼ inch wide and the laser passed through the center of the window when the engine was at rest, the laser did not pass through the window but rather illuminated the bypass duct case at the higher fan speeds. To correct for this, the second laser mirror was rotated so that it would pass through the window at a particular fan speed/test case and a new self-calibration would be performed. Every time the laser sheet was moved from its "calibrated" position, a new-self calibration was performed to correct for the small discrepancy.

The final design setup appeared during the test as it does in Figure 49 below.

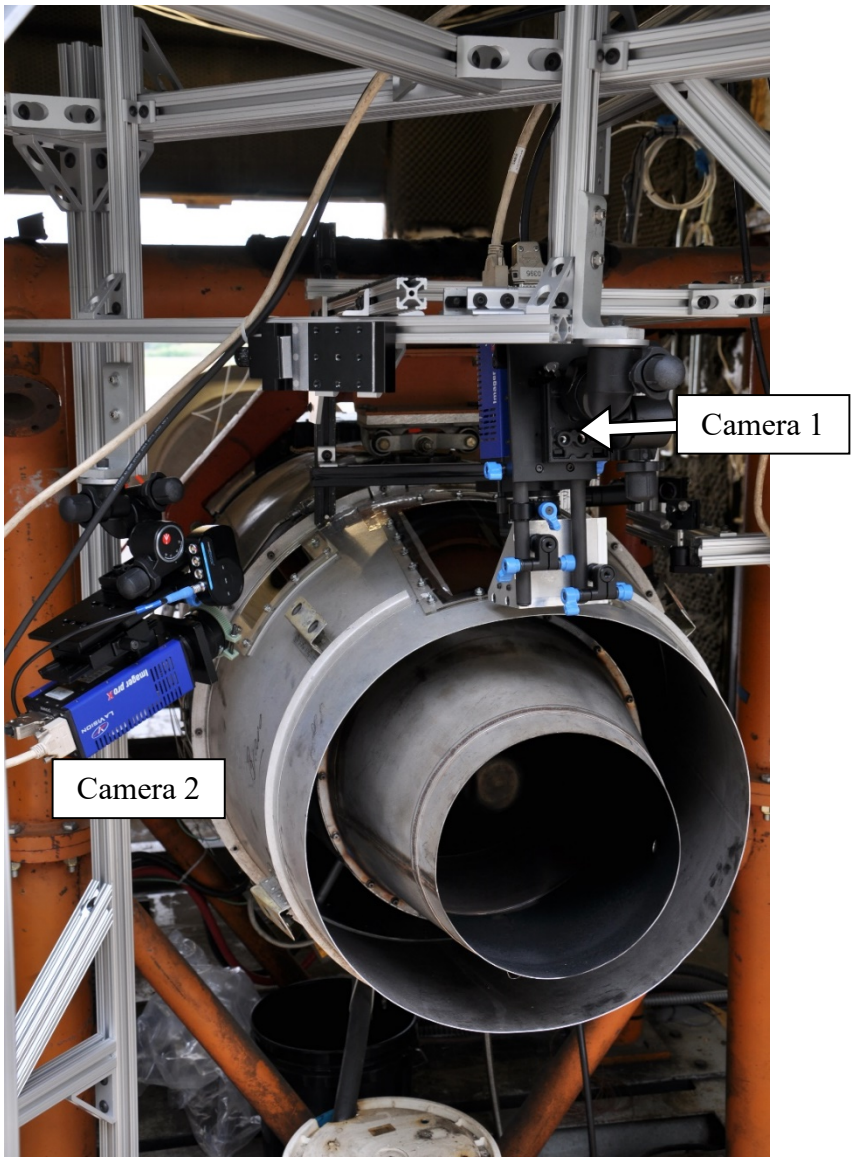

Figure 49 – Final experimental design setup

5.6.2 Data Recording

PIV measurements would be acquired at multiple fan speeds in order to observe any changes, if any, in the wake of the support strut due to the difference in mass flow. Additionally, any PIV specific measurement difficulties related to the internal flow measurements at higher velocities were to be investigated. This mainly includes the capability to consistently provide sufficient particles to the measurement region as well as achieving correct timing between the laser and cameras using dt values less than 6μs. The fan speeds to be used were idle (35%), 60%, 70%, and 80% of the maximum corrected fan speed. Corrected fan speed is given by Hill, Peterson [51] as $CFS = N/\sqrt{T_0/T_{0,st\ day}}$,

where N is the fan rotational velocity in radians per second. For simplicity, percent of maximum corrected fan speed will be simply referred to as CFS from this point forward, i.e. 80 percent maximum fan speed is 80% CFS.

At each of the four test conditions, a minimum of 5000 image pairs were to be acquired. This was done largely as an uncertainty reduction technique. Generally, PIV experiments in the laboratory will consider 1000 image pairs to be sufficient to accurately calculate the mean velocity flow field. However, due to the increased difficulty of achieving consistent particle density in the measurement plane, more images were desired. All else held constant, increasing the image count from 1000 to 5000 has the benefit of decreasing the standard error of the mean up to 55%. Shown in Table 5 through Table 9 are all of the relevant specifications for the test stand JT15D experiment. For more detailed descriptions of the hardware and decisions regarding experiment design, please refer to Section 5.5.2. Table 9, specifically, gives the mean value for the measured stagnation properties from the probe rake 9 inches upstream of the support strut. Flow characteristics are also provided in the form of Reynolds and Mach numbers. There was a malfunction in the data acquisition system during the 70% CFS test so the corresponding values for that case are not available.

Table 5 – Colt 4 Smoke Machine Specifications

Seed Insertion: Concept Colt 4 Smoke Machine	
Insertion Position	2 feet above, 3 feet upstream of top of bell mouth
Composition	>50% Glycerine, <50% Deionised Water
Diameter	≈0.2-0.3μm
Density	1262 kg/m^3
Time Lag	≈0.3μs (assuming 0.3μm diameter)

Table 6 – Quantel EverGreen 200 Specifications

Laser: Quantel EverGreen 200 Double-Pulse Nd:YAG	
Wavelength	532
Energy per pulse	200 mJ/pulse
Position	57.15mm downstream of support strut
Sheet Thickness	3 mm
Sheet Height	101.6 mm
Sheet Forming Optics	-20 mm followed by -10 mm cylindrical lens

Table 7 – LaVision Imager Pro X 4M Specifications

Cameras: LaVision Imager Pro 4 X 4M	**CAM1**	**CAM2**
Acquisition Rate Used	4 Hz	
Resolution	2048x2048 pixels	
Pixel Pitch	7.4 μm	
Quantum Efficiency	55% @ 500 nm	
Stand Off Distance	0.55 m	0.37 m
Scattering Angle	91°	40°
Scheimpflug configuration	N	Y
Lens Aperture	5.6	16
Lens Filter	532 nm	
Lens Focal Length	50 mm	
Resulting Spatial Resolution	22.35 pix/mm	
Resulting Field of View	150 mm x 125 mm	

Table 8 – PIV system timing specifications

Timing (dt)	**[μs]**
Idle (35%)	9
60%	7
70%	4
80%	3, 4

Table 9 – Mean measured stagnation properties and calculated flow properties

Fan Speed	Idle (35%CFS)	60% CFS	80% CFS
Inlet Total Pressure [kPa]	106	113	124
Inlet Total Temperature [K]	298	304	310
Strut Reynolds Number ≈	50,000	80,000	101,000
Mach Number ≈	0.18	0.28	0.36

5.6.2.1 Temperature and Pressure Rake

During the experiment, a pre-existing temperature and pressure rake was utilized to acquire total temperatures and total pressures. The rake was located 9 inches upstream of the support strut and the PIV measurement plane. Also, it was located slightly on the starboard side. As shown in the background of Figure 50, the rake consisted of six pressure probes and five temperature probes. The support strut is the object in the foreground of Figure 50. The intent was to use the information from these probes in junction with the velocimetry data and the quasi-one dimensional model derived in Appendix A.2 in order to describe the total pressure loss created by the support strut. Additionally, the pressures and temperatures measured by the rake were used to produce boundary conditions in the CFD calculations. Of the six pressure probes, only five were functional with the faulty probe being the most in-board probe. Similarly, only four of the five temperature probes were functional, with the faulty probe being the most out-board probe.

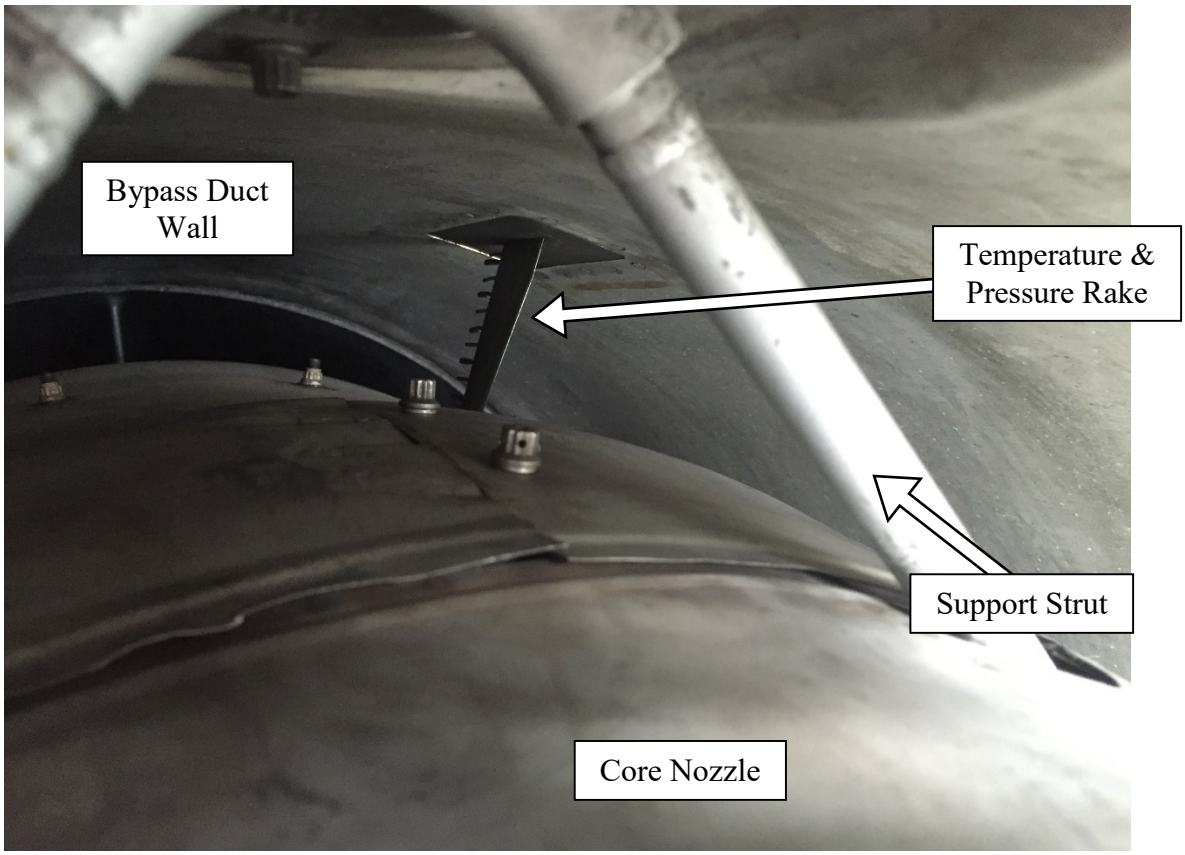

Figure 50 – JT15D-1 bypass duct pressure and temperature rake

The pressure probes were connected to a Scannivalve ZOC17 ±15 psig pressure scanner using 4.7625 mm internal diameter Tygon PVC clear tubing that was about 20 feet long. Data was collected at 128 Hz over a 5 second interval during the simultaneous acquisition of the PIV data, but at a rate of about once every 200 images. The data over this 5 second span were than averaged into one measurement. The ZOC17 is capable of 0.08% full-scale accuracy.

Type K thermocouples were utilized in the temperature probes and were connected to a data acquisition system that utilized a custom National Instruments LabView software package. Temperatures were recorded similarly to the pressures, about once every 200 images during the PIV measurements for a 5 second span but at an acquisition rate of 4 Hz. Again, the measurements over this 5 second span were averaged into one data point.

5.6.2.2 Testing Overview and Procedure

The experiment was completed over the course of nine testing nights. It added ten hours to Virginia Tech's JT15D engine and consumed about 700 gallons of fuel. Additionally,

over 35,000 image pairs were captured at four engine speeds, and about 20 canisters of smoke fluid A were dispersed. Due to PIV's current necessity for darkness as well as the fact that the test cell doors need to be open to the outside, test prep would begin around dusk, and testing would commence once it was sufficiently dark

The testing procedure (following successful calibration) was as follows. First, the smoke machine would be turned to standby and warming. Second, all the optical windows were thoroughly cleaned and proper alignment was ensured between the camera support structure, the laser sheet, and the engine. After a final walkthrough of the test cell to remove potential foreign object debris, the engine would be started and brought up to idle. Once stable at idle, the seed blower would be turned on, followed by the seeder itself. A brief data capture would ensue, ensuring proper functioning of the laser, cameras, seeder, blower, temperature probes, and pressure probes. Once complete, the seeder would be turned to standby and the engine would be throttled up to test speed. Once running stable at the test speed, the seeder would be turned back on and another brief data capture would take place as a final check. Then, data acquisition would occur in 1000 image sequences (about 5 minutes). After each recording, the images would be quickly assessed for focus quality, seeding density, and sufficient light intensity, before proceeding to the next 1000 image acquisition.

A maximum of 5000 images (about 25-35 minutes) would be acquired before proceeding to switch the seeder to standby and shut down the engine. This was done because generally after this amount of time, the accumulation of seed on the camera and laser windows began to become noticeable in the images, making them appear foggy, Figure 51. On occasion, the tests would need to be stopped short of the 5000 image maximum. The most common cause of this stoppage was when a particularly large droplet of seed would accumulate in the engine and hit the laser window. Due to the window's small size, there was no room to maneuver the laser sheet around the droplet, necessitating an engine shutdown to clean the windows. Once the windows were cleaned, the process would resume. Testing usually spanned about three to four hours per night.

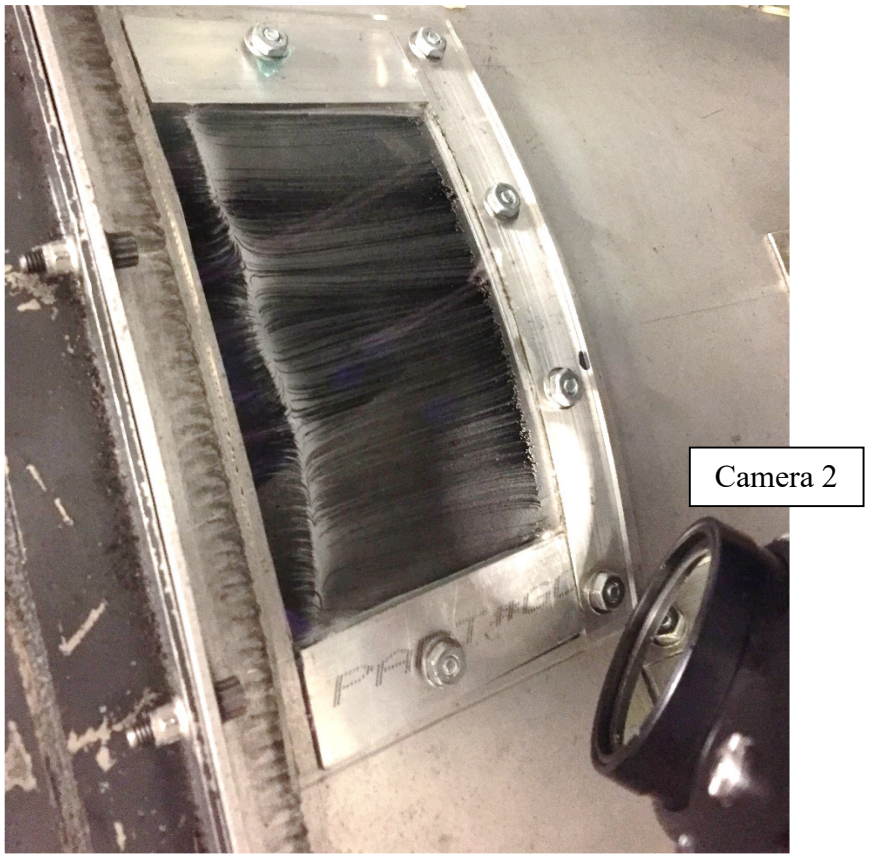

Figure 51 – JT15D-1 windows with accumulated particles

5.6.2.3 Post-Processing and Analysis

The image sets were processed in LaVision DaVis similar to the simulated engine experiment. First, a background image (that is an average of 10 images taken with the laser on but without particles in the flow) is subtracted from the image set to remove various glares or bright spots in the image. For this test, a glare was observed on the support strut that was caused by the laser light scattering off the particles and then reflecting off the support strut back at the camera. The method found to be most effective at reducing this particular glare on the support strut used a manually applied cropping window to effectively tell the processing algorithm to ignore the region of glare not corrected by the background subtraction. This prevented the calculation of vectors within this region but reduced the effect the glare would have on the calculation of the surrounding vectors. The resulting images were then processed with a multi-pass algorithm that incorporated two passes with adaptive shape interrogation windows of size 48x48 square pixels. Using

interrogation windows of an adaptive shape allows for locally optimized shapes that take advantage of local seeding density and flow gradients [60].

Further post-processing and analysis was completed in MATLAB. The turbulent nature of the flow resulted in inconsistent seeding, and therefore velocity vector data with higher levels of noise. In order to filter out spurious vectors, vectors with a peak ratio less than 1.1 or greater than 25 were deleted. This process and the reasoning behind it is detailed in Appendix A.1.

They Reynolds stress tensor was calculated only for the idle fan speed case. The nosier data at the higher fan speeds was accentuated in the fluctuation calculations. The stress tensor is calculated as Equation (5.2) below,

$$u_{ij} = u_i u_j \tag{5.2}$$

where u is the fluctuating velocity, or the difference between the mean value and the instantaneous value [2]. The diagonal components of the tensor make up the normal stresses while the off-diagonal terms are the shear stresses. Furthermore, the turbulent kinetic energy is defined to be half the trace of the Reynolds stress tensor [2].

6 Experimental and Computational Results and Discussion

6.1 Discussion Overview

This chapter will focus primarily on discussing what the PIV experiment was and was not able to accomplish in the full-scale JT15D-1 bypass duct. Mean stream-wise velocimetry data from each of the four fan speed test cases will be used to show the wake structure size and shape had little variation with respect to fan speed. One exception however was that an increase in the fan speed corresponded with an increase in horizontal displacement of the wake structure. The largest observation made from the PIV data was that the wake structure was not uniform along the length of the strut. Rather, it separates into at least two smaller structures that are potentially independent of one another. It will also be shown that while the current PIV experiment was able to acquire sufficient data to calculate the mean flow, it was unable to consistently capture instantaneous velocity data over the full field of view at fan speeds above idle. As such, turbulence data is also unavailable at these fan speeds.

In addition to discussing the implications of the PIV data, the CFD simulation results will be used where appropriate to help visualize the global flow features. As mentioned in Section 5.4.6, the simulation was limited by a number of simplifying assumptions. It was not intended to be representative of a high fidelity simulation, nor was it intended to be used for any type of performance analysis. Its purpose is to help orient the reader when analyzing the PIV data within the bypass duct, and to provide insight that could be used with intuition in order to better understand the wake structure downstream of the support strut.

As such, the CFD calculated stream-wise velocity taken from a strut mid-span location for the 80% CFS test case is shown in Figure 52 to give the reader a broad understanding of the large scale flow interactions. This data plane illustrates the flow slowing as it encounters the leading edge of the strut and then accelerating over and below the strut with

a wake forming directly behind it. Additionally, the recessed region at the top of the duct generates a shear layer as the faster moving flow passes below it. The wake structure seen just below the strut wake is caused by the interaction between the strut and the core wall at a different span-wise location. Eventually the wake structures become indistinguishable from the rest of the flow as it accelerates out of the nozzle exhaust.

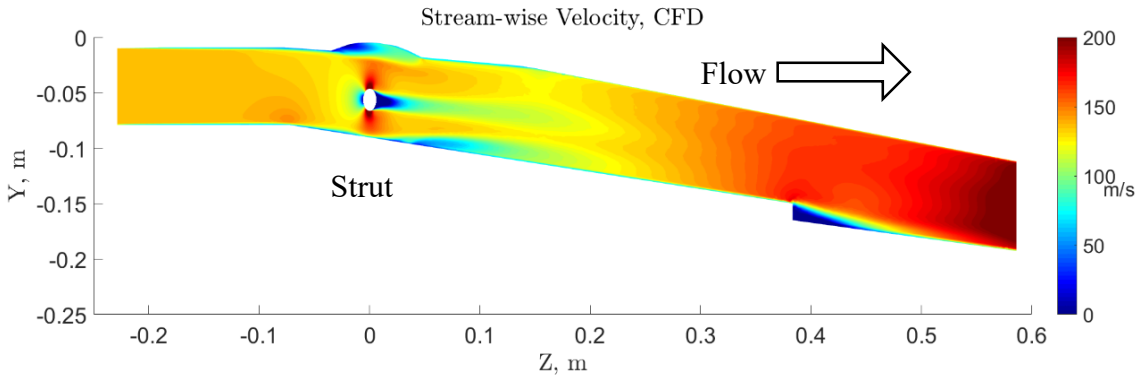

Figure 52 – CFD Stream-wise velocity, 80% CFS, mid-span location

6.2 Experimental Results and Computational Insight

Moving on to the experimental PIV data, the first observation made was that the wake structures downstream of the support strut were displaying little variation in size and shape regardless of the incoming flow velocity. Figure 53 through Figure 56 shows the stream-wise velocity for each of the four fan speed test cases as well as the minimal variation described. All experimental data are shown as approximately overlays over the computer model of the bypass duct. For the fan speed test cases above idle, laser glare on the strut prevented the acquisition of quality data along a line to the left of the strut wake as shown in Figure 53 through Figure 55. It was minimized as much as possible by the preventative measures listed in Appendix A.1, as well as in post-processing, but it could not be removed completely. With regards to qualitative observation, all cases display a clearly defined wake structure (1) with concentrated regions of slower flow (2) in addition to accelerated regions (3) on both sides of the strut wake, and a pinched wake region (4) in the middle.

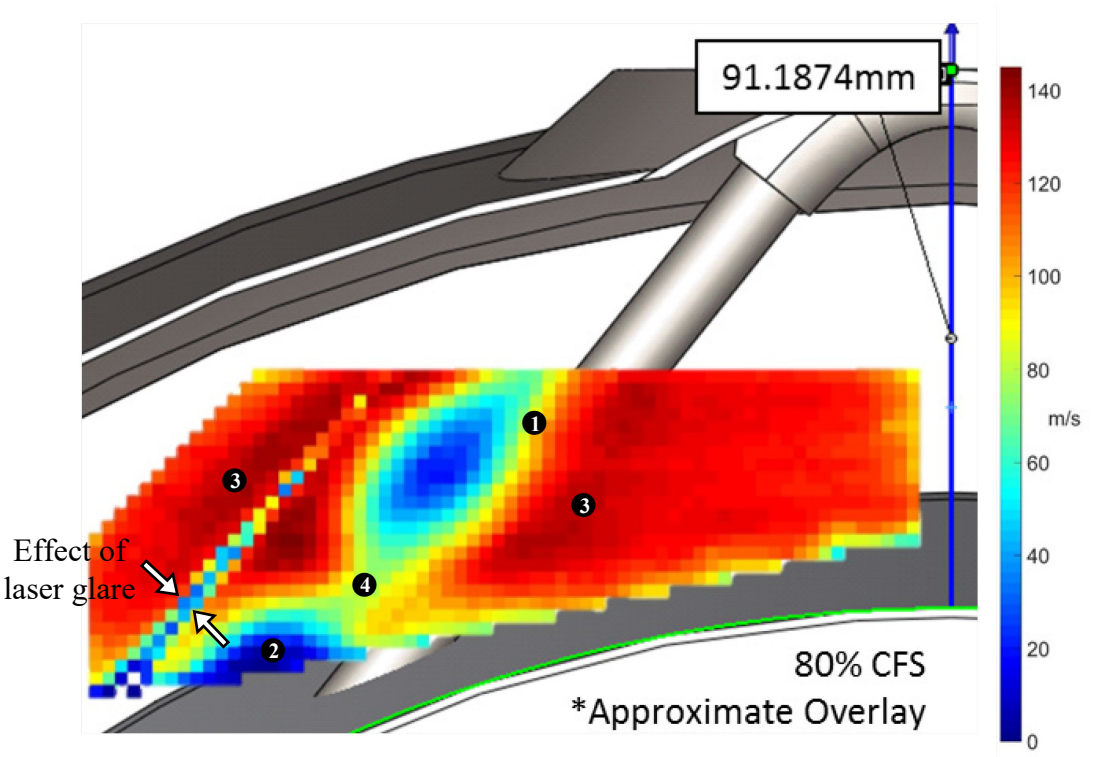

Figure 53 – PIV mean stream-wise velocity, 80% CFS

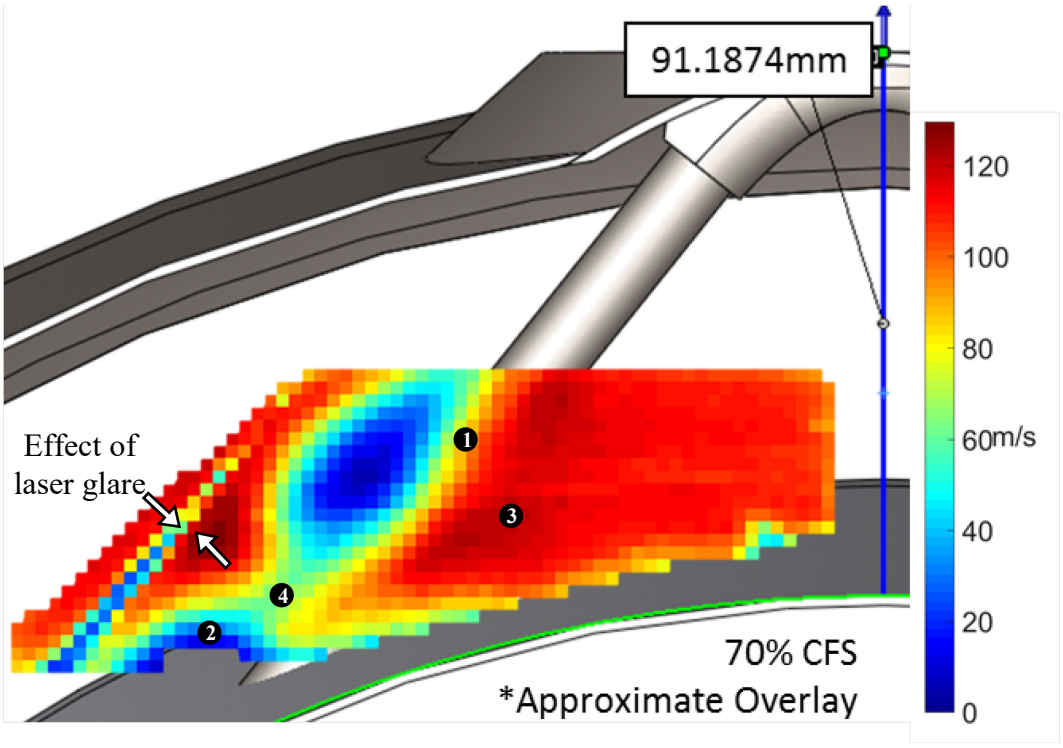

Figure 54 – PIV mean stream-wise velocity, 70% CFS

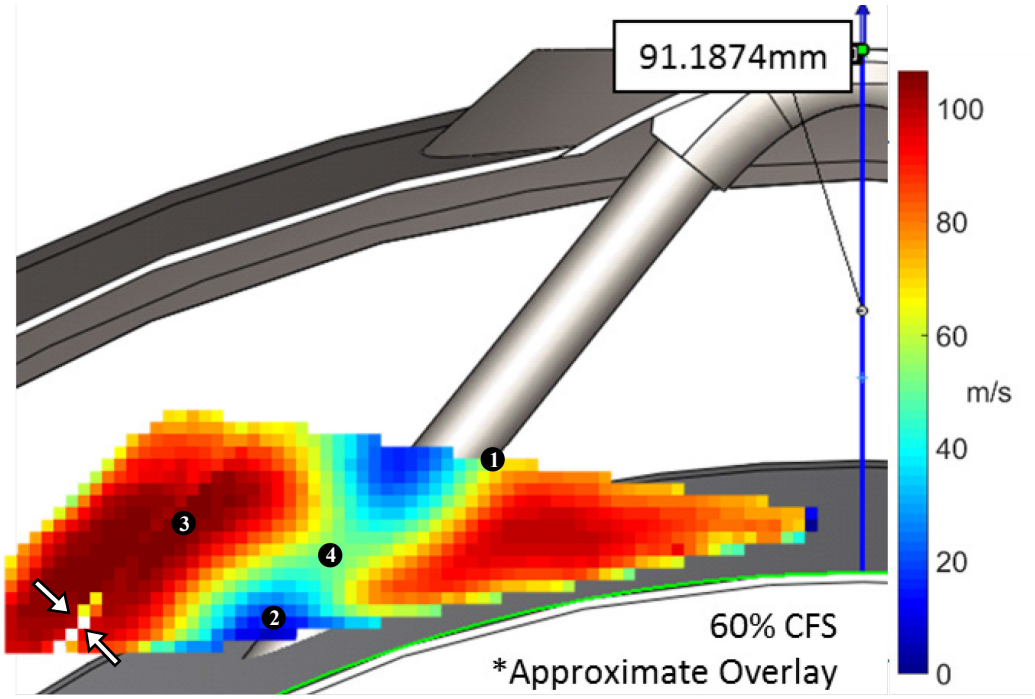

Effect of laser glare

Figure 55 – PIV mean stream-wise velocity, 60% CFS

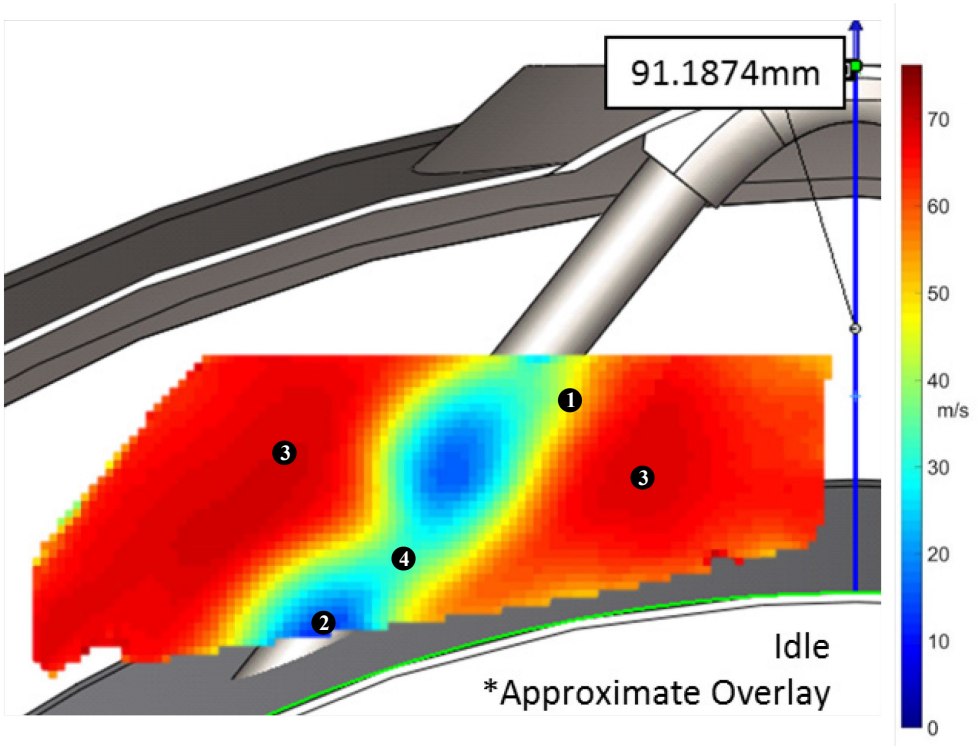

Figure 56 – PIV mean stream-wise velocity, Idle

This fact that the wake along the support strut is not uniform is the second major qualitative observation. The cause of this specific non-uniformity is not immediately clear. However, it is an issue that the CFD simulation, limited as it is, may be able to partially address.

For the 80% CFS case, an isosurface of vorticity as well as a number of axial planes were utilized to display a rough visualization of the flow evolution as it passes by the strut. The vorticity isosurface is shown in Figure 57 and Figure 58 and represents a vorticity magnitude of 9850 s^{-1} while the color depicts the stream-wise component of the vorticity. The planes' locations are shown in Figure 59, ranging from 4 diameters upstream to 4.5 diameters downstream (the PIV measurement plane). Furthermore, Figure 60 through Figure 64 illustrate the evolution of the wake structure for the 80% CFS case at the listed locations. Figure 60 shows the stream-wise velocity, Figure 61 and Figure 62 depict the stream-wise velocity at one diameter and two diameters downstream respectively, and Figure 63 and Figure 64 show the stream-wise vorticity at these same two planes. With the given coordinate system (shown in the bottom right hand side of the sub figures), the positive or red values of vorticity correspond with a counter clock-wise rotation in accordance with the right hand rule. All qualitative analysis will be performed from the perspective of the viewer for simplicity. Please note the color scaling for Figure 57 through Figure 64 (excluding Figure 59) is slightly different than that shown in previous figures because the figures were taken directly from within the ANSYS post-processing software. For the interested reader, the vertical and horizontal components of vorticity as well as larger versions of all the axial locations in Figure 60 are included in Appendix A.3.

Beginning with the strut-core interface, the CFD is predicting the formation of a horseshoe vortex ([61], [62]) with the vortical structure forming on the interior angle of the strut being the stronger of the two and persisting further downstream. Both structures then begin to move along the wall in accordance with inviscid flow theory and the image vortex on the other side of the wall ([63], [64]). Furthermore, Figure 61 and Figure 62 clearly illustrate a wake pinching effect near the wall at one diameter and two diameters downstream of the strut similar to what was observed in the PIV results at 4.5 diameters downstream. A different axial plane was used for the CFD data because at 4.5 diameters downstream, a large portion of the wake structures had already dissipated. Regardless, this

would seem to indicate that this junction of the strut and the wall is creating a wake structure at least partially separate from the wake created by the strut main body.

The wake non-uniformity can also be seen in the stream-wise vorticity. Figure 65 and Figure 67 show the stream-wise vorticity calculated from the PIV data at 4.5 diameters downstream and Figure 66 and Figure 68 show the stream-wise vorticity calculated from the CFD data at one diameter downstream. In both method sets, the horizontal and vertical components of velocity are drawn as quiver arrows over the vorticity data, and the axes have been scaled by the local duct height at the centerline. Both methods exhibit similar patterns of alternating rotating vortical structures along the strut, which have been numbered to illustrate this pattern.

Two of the major differences between the CFD prediction and the PIV measurement is the exact vertical location of each of the vertical structures and the absence of the horseshoe vortex in the PIV data. These discrepancies are likely due to the hole in the core wall and the cavity on the other side which was mentioned in Section 5.4.6 and shown in Figure 25. Because the CFD simulation modeled this as a strut-wall junction it predicted a horseshoe vortex. In reality, because the strut is never really in contact with a wall, the horseshoe vortex can never form. Instead, something potentially more complicated is generated at the same location as air is possibly flowing into and out of the cavity, in addition to passing around the strut. This could also allow the alternating vortical structure to continue further down the strut due to the absence of the wall.

From the CFD perspective, this is a very difficult problem to model. Any slight error in the application of boundary conditions could dramatically alter how the flow interacts with this geometry. As such, if future work were to experiment this specific interaction further, it is recommended that the problem be scaled down to simplify the problem as much as possible. All of the other engine duct geometry should be removed and simply investigate the interaction between an inclined circular cylinder that passes through a hole in a wall and into a cavity region. By removing all the other features of the duct, the simulation can focus all of the resources on this particular interaction. Additionally, it would make a transient high-fidelity simulation much more feasible.

Returning to the present work and to reiterate the important insight that the CFD provides. the strut is likely generating two separate wake structures. One is created by the

junction of the strut and the core. The other is created by the middle section of the strut. To this point, the stream-wise velocity data in Figure 60 at the one diameter and two diameter downstream locations illustrate the strut-core structure separating from the main strut structure and creating a pinched region similar to what is observed in the PIV experimental data.

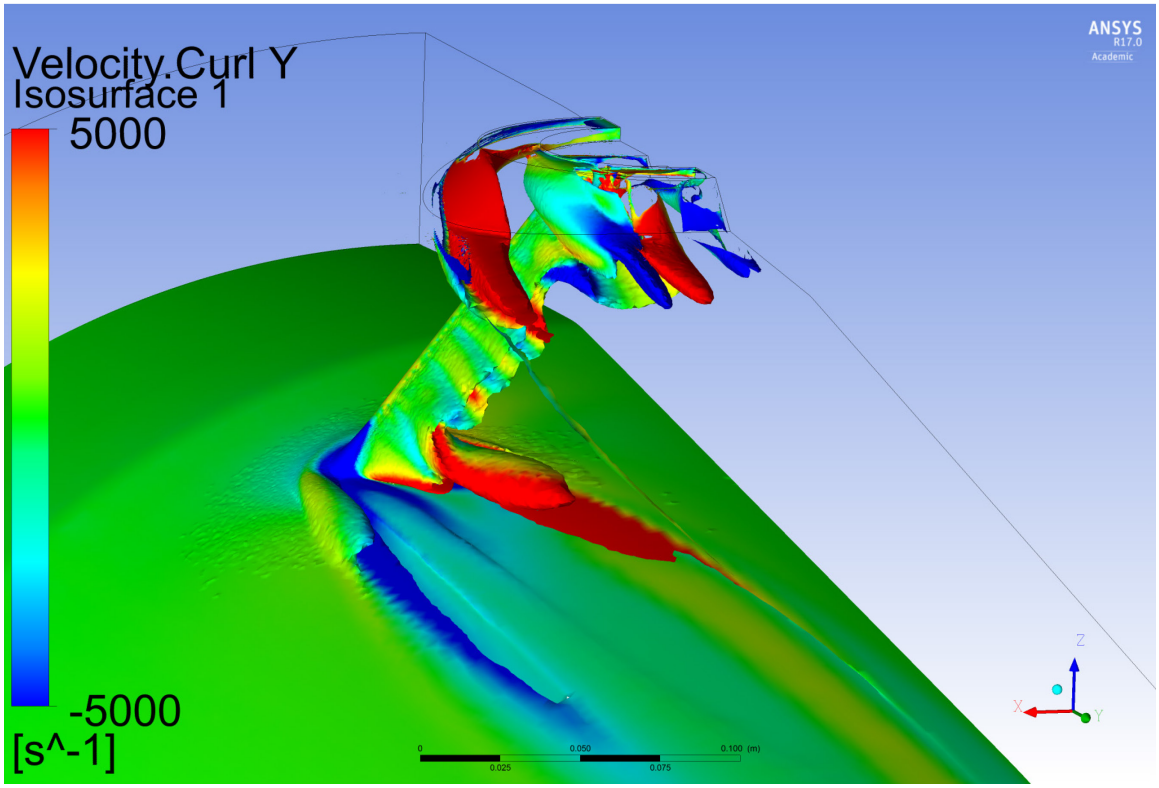

Figure 57 – Isosurface of vorticity, color corresponds to stream-wise vorticity specifically

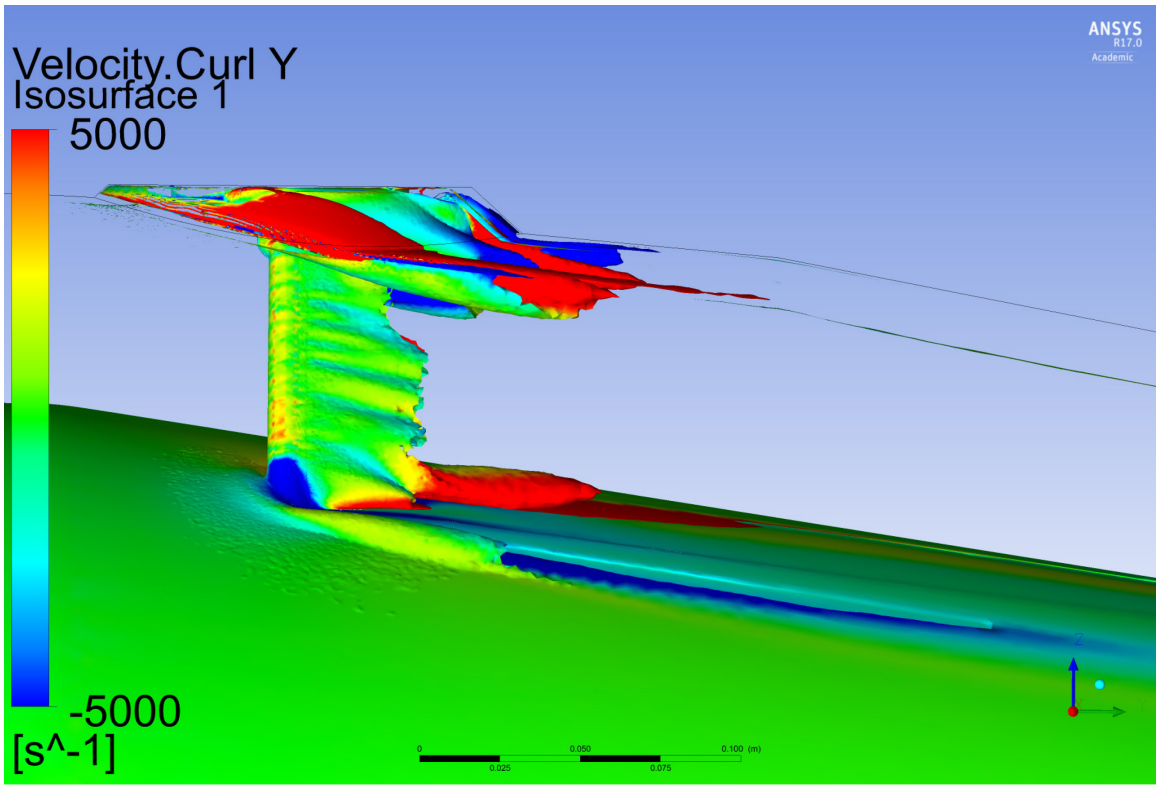

Figure 58 – Isosurface of vorticity, color corresponds to stream-wise vorticity specifically, side-view

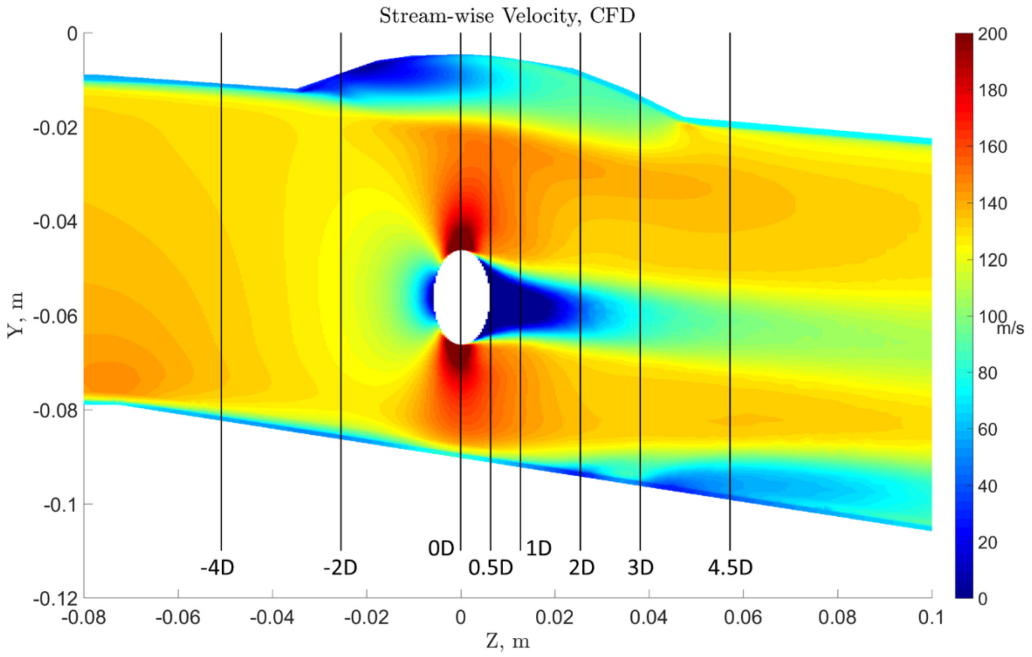

Figure 59 – Span-wise plane of stream-wise velocity with observation locations, 80% CFS

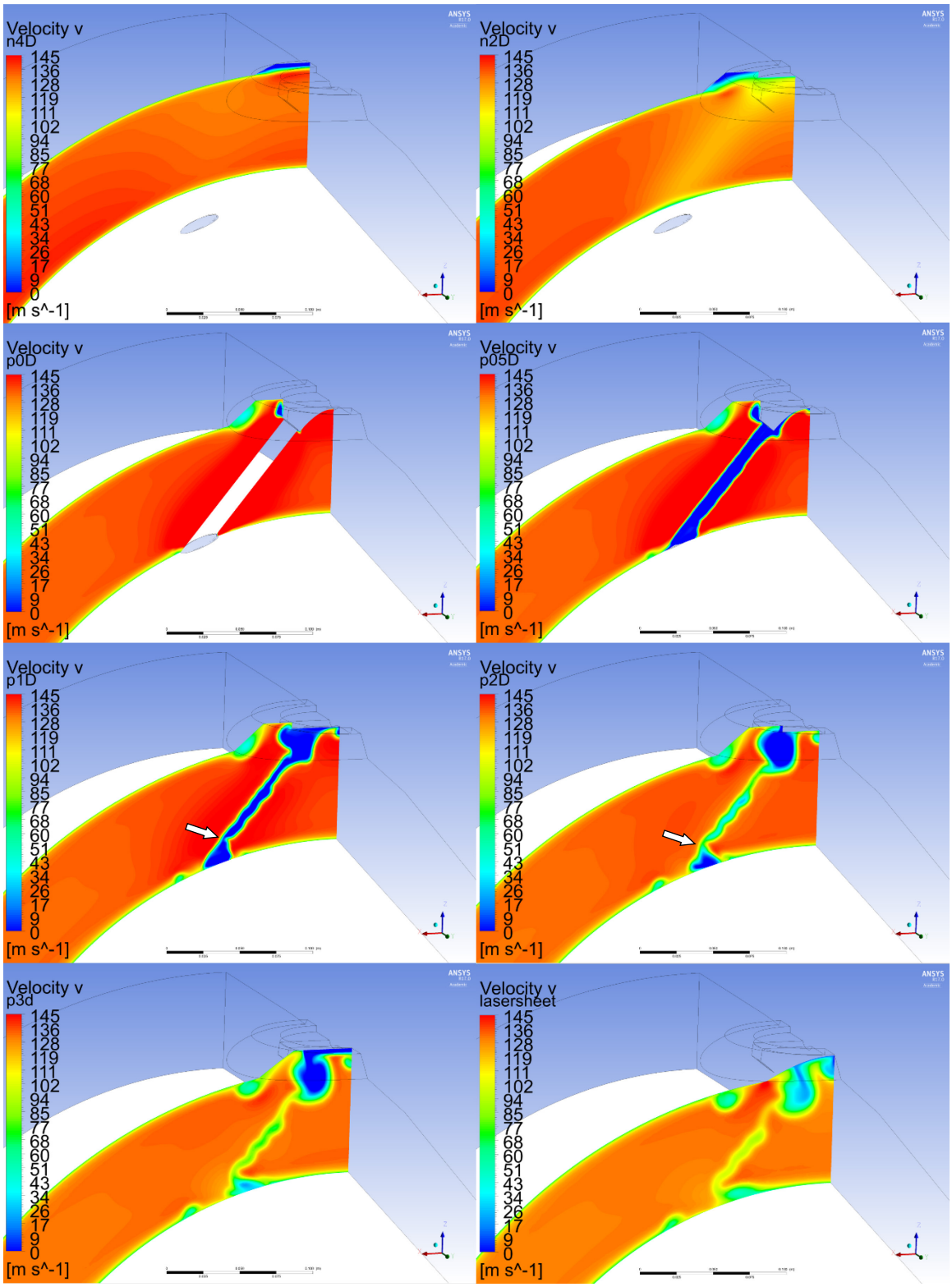

Figure 60 – Computational stream-wise velocity at eight axial locations, 80% CFS, arrows indicating pinched region at 1D and 2D downstream locations

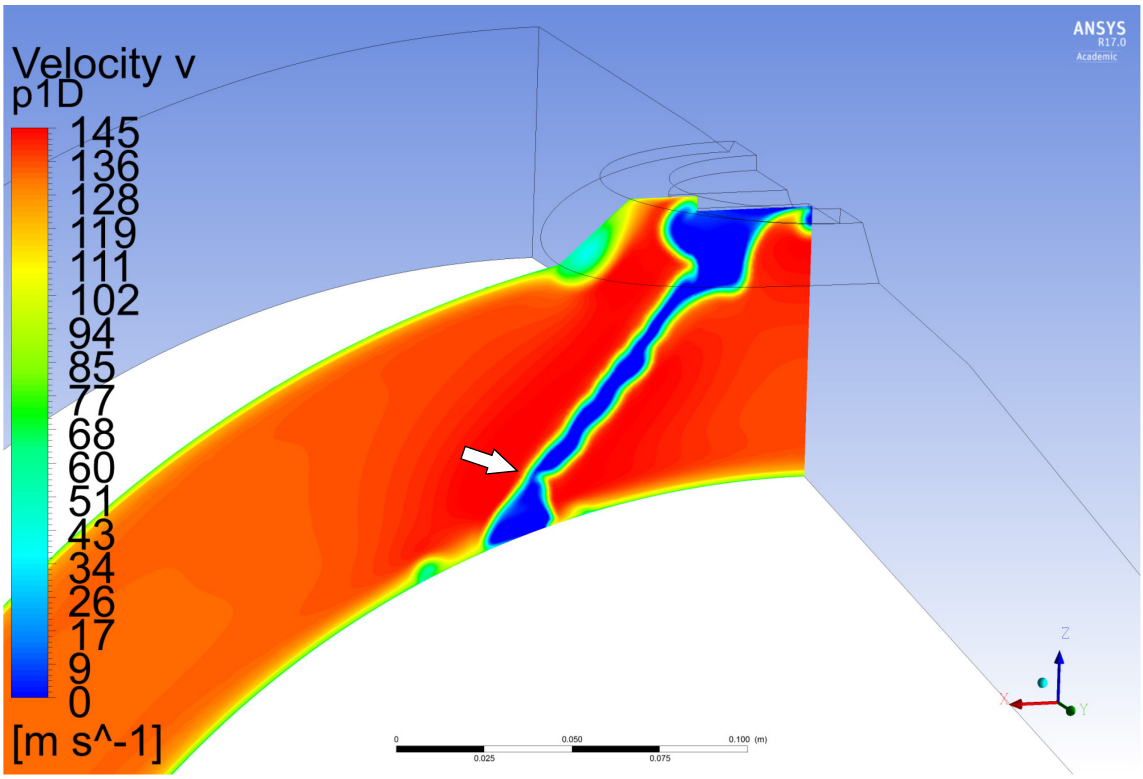

Figure 61 – Computational stream-wise velocity, one diameter downstream, 80% CFS, arrows indicating pinched region

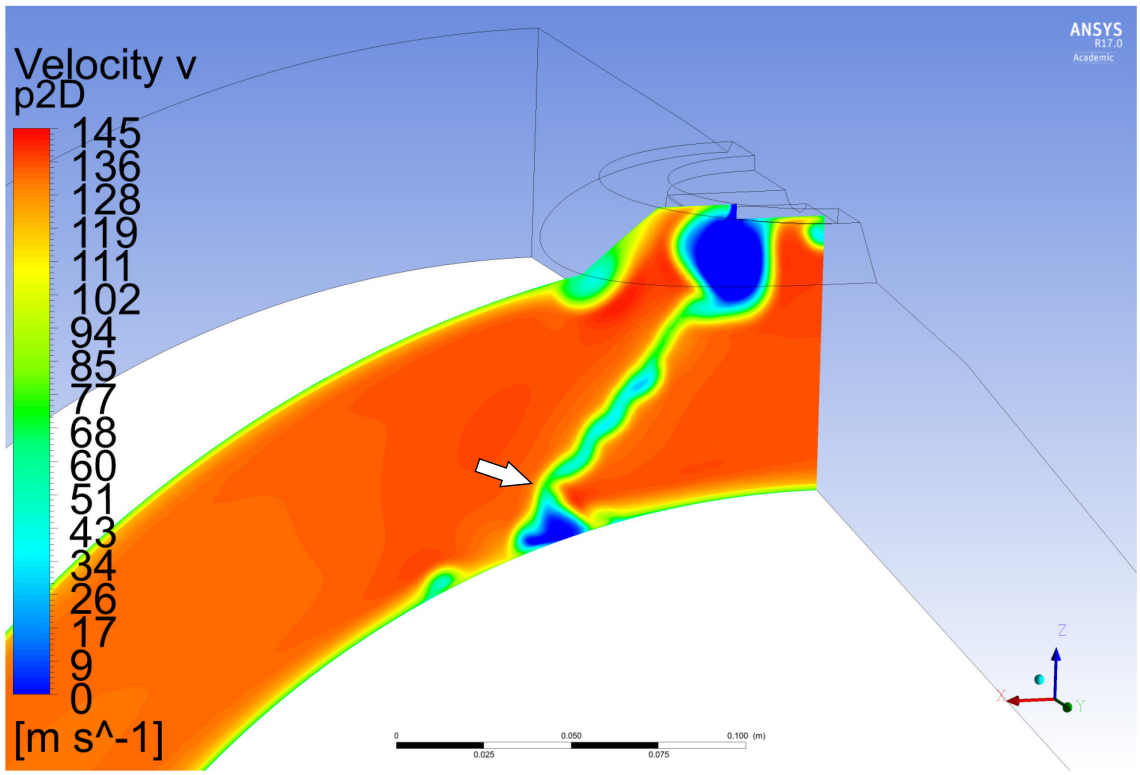

Figure 62 – Computational stream-wise velocity, two diameters downstream, 80% CFS, arrows indicating pinched region

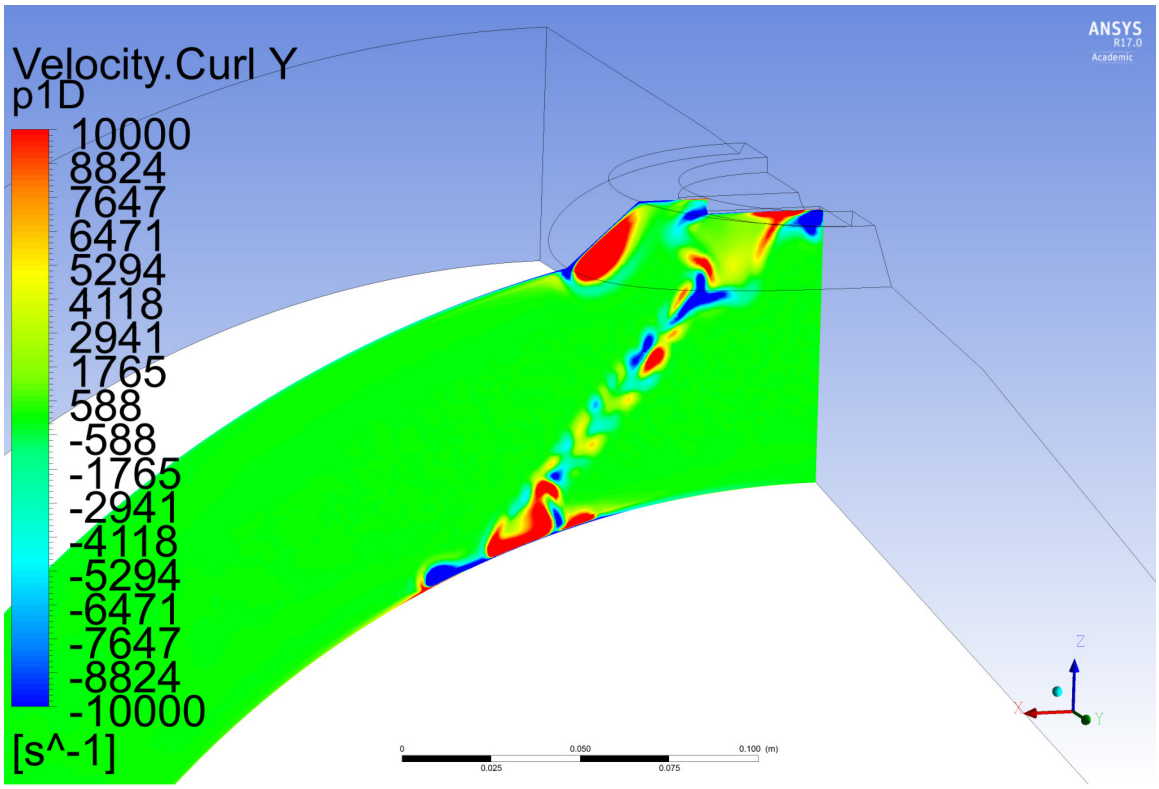

Figure 63 – Computational stream-wise vorticity, one diameter downstream, 80% CFS

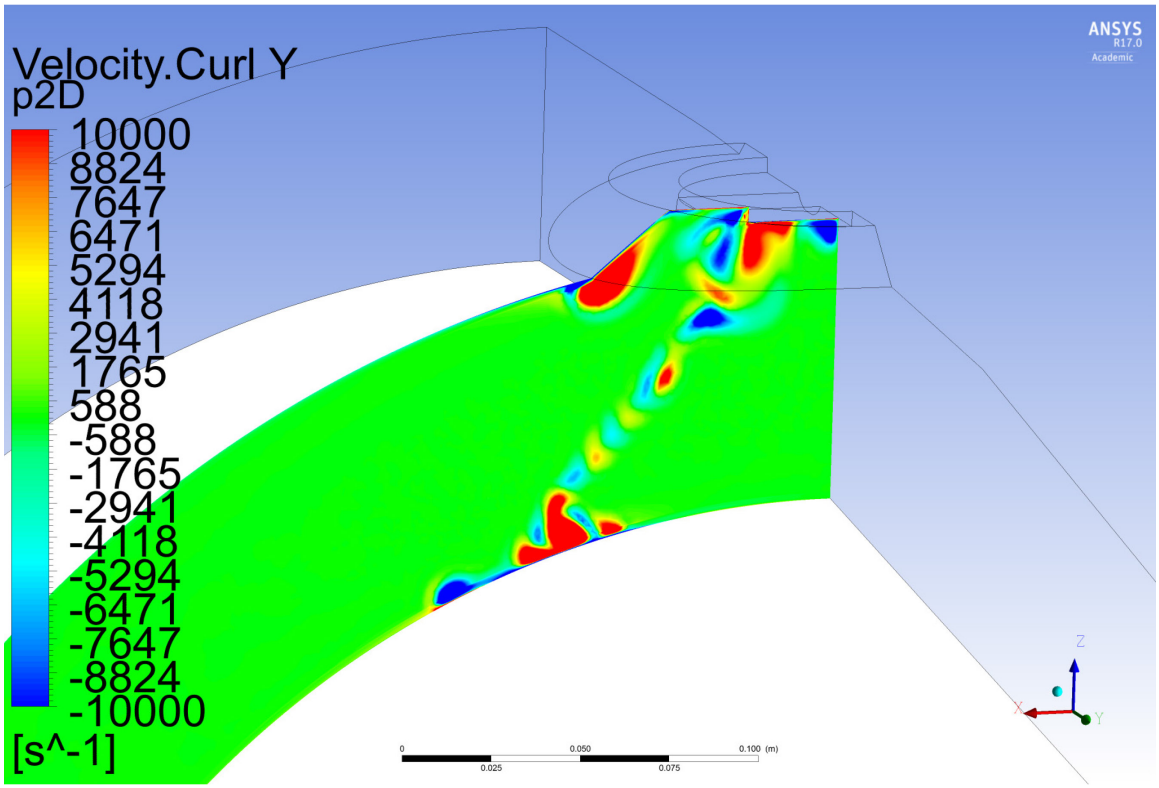

Figure 64 – Computational stream-wise vorticity, two diameters downstream, 80% CFS

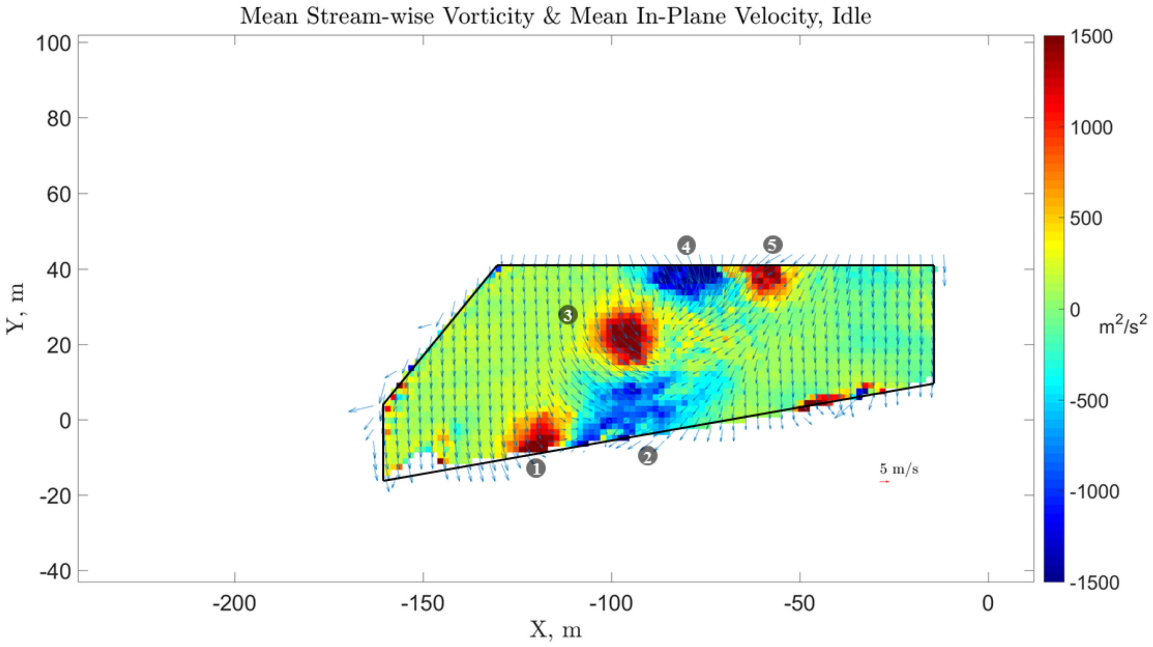

Figure 65 – Stream-wise vorticity contour and secondary flow velocity quiver, 4.5 diameters downstream, PIV, idle

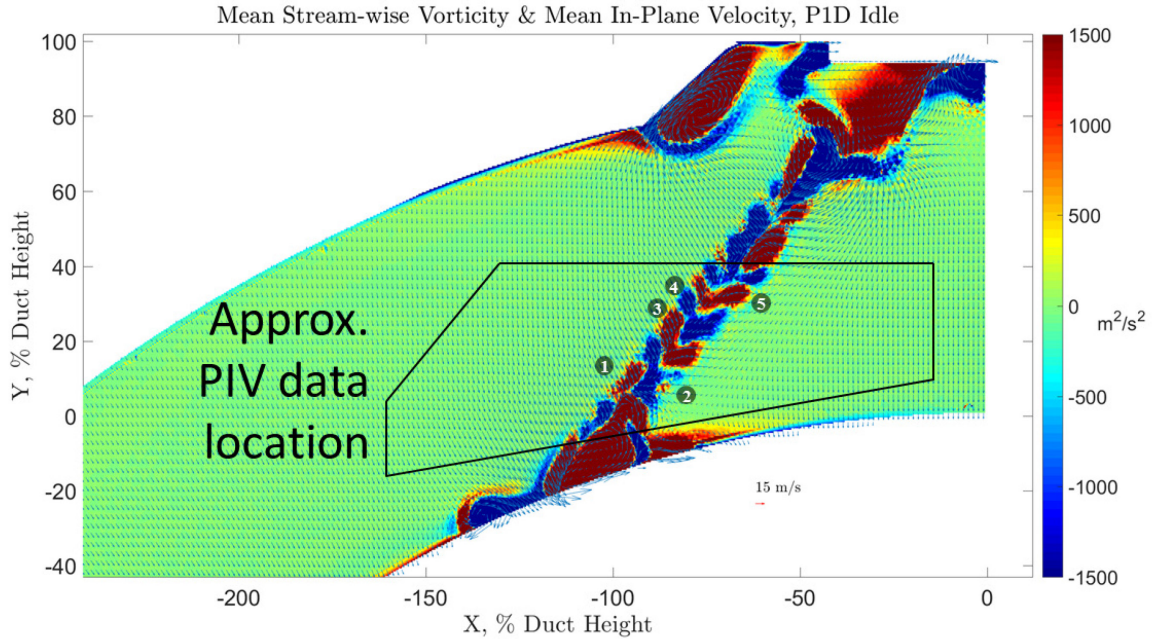

Figure 66 – Stream-wise vorticity contour and secondary flow velocity quiver, one diameters downstream, CFD, idle

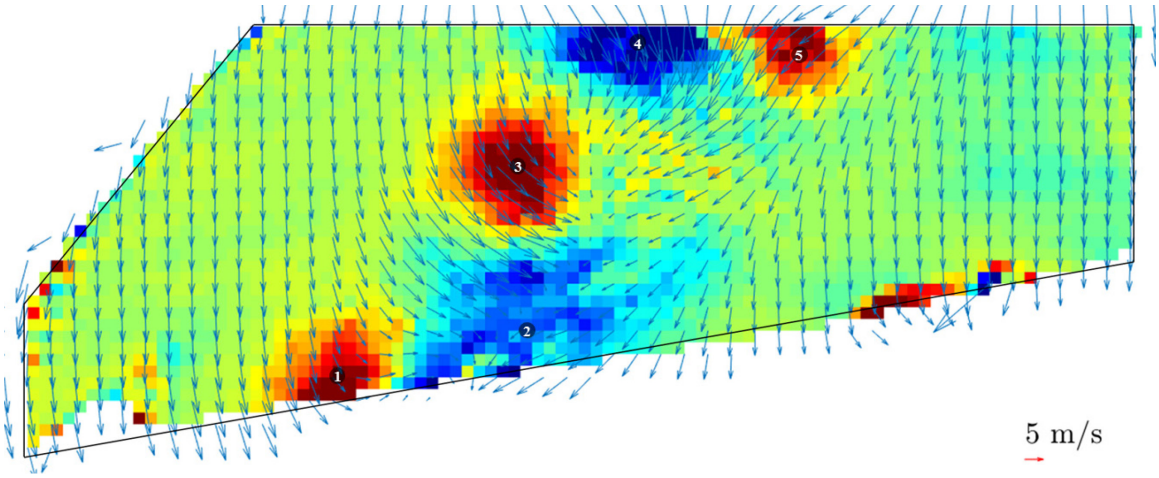

Figure 67 – Stream-wise vorticity contour and secondary flow velocity quiver, 4.5 diameters downstream, PIV, idle, magnified

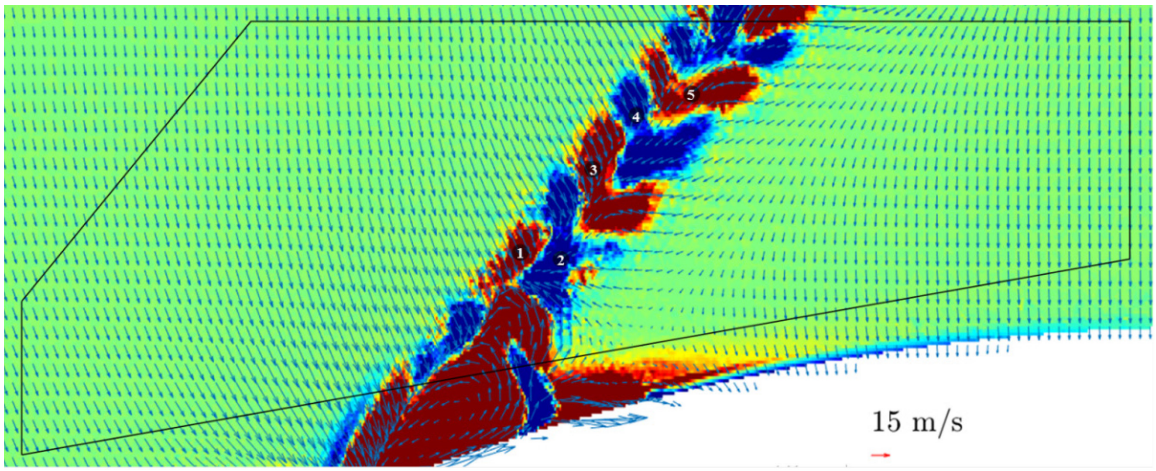

Figure 68 – Stream-wise vorticity contour and secondary flow velocity quiver, one diameters downstream, CFD, idle, magnified

The next point of discussion is the horizontal location of the wake structure with respect to the support strut location. Referring back to Figure 53 through Figure 56, it can be observed that as the fan speed is increased, the location of the wake structure is displaced further and further towards the outboard side of the strut. A number of possible explanations have been explored, but each has at least one fallacy that prevents it from being a conclusive argument. Two of the more plausible explanations will be discussed here.

The first hypothesis is that there is a bulk swirl present in the counter clockwise direction (aft looking forward) that increases as the fan speed increases. This would explain why the wake structure shifts to the left in the PIV data. It would also predict that the wake structure

from the right support strut (which was not in the PIV measurement field of view) would also move to the left. Furthermore, it could explain why neither of the CFD test cases predicted a movement of the wake structure since the simulation produced a uniform axial velocity at the inlet and not one with a bulk swirl. However, just downstream of the fan blades in the bypass duct is a set of exit guide vanes. At design conditions, the majority of the bulk swirl produced by the fan should be removed by the guide vanes which should redirect the flow in the axial direction. This is done because any velocity not in the axial direction does not contribute to thrust and is therefore lost energy. Regardless, the reason this presents an issue for the hypothesis is because it would suggest that if any case was going to produce a deviation from axial flow, it would be the fan speed that was furthest from design (cruise) conditions, which for this experiment would be the idle test case. However, as was shown in the PIV data, the exact opposite was observed. The wake at idle was directly behind the strut, suggesting axial flow, and the wake at 80% CFS was displaced furthest to the left, suggesting some component of tangential flow.

The second hypothesis revolves around a pressure differential forcing the wake structures from both struts to be forced away from each other. If the two support struts acted together to slow the flow between them and accelerate the flow on the outboard side, it could create a low pressure region on the outboard side of either strut. This could cause the wake structures downstream of the strut to move away from the locally higher pressure near the centerline and into the low pressure regions. Contrary to the first hypothesis discussed, the second hypothesis would predict that the structure from the right support strut (which was not in the PIV measurement field of view) would be moving to the right. This hypothesis should be supported by the horizontal component of the PIV data at the higher fan speeds by depicting in general the flow moving to the left (outboard side). However, Figure 69 for the 80% CFS case clearly shows the mean velocity in the wake structure is to the right (inboard side).

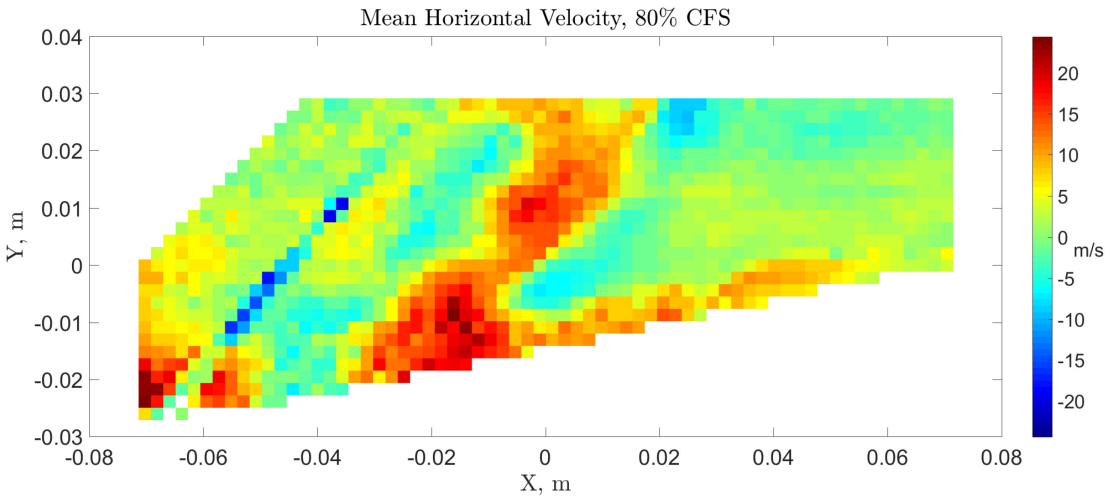

Figure 69 – PIV mean horizontal velocity, 80% CFS

Although both arguments present plausible causations of the horizontal displacement of the wake structures at higher fan speeds, both also have evidence that strongly counters its validity. If future experiments could acquire a field of view that captured the wake structure produced by both struts, it could provide further evidence with which to support or contradict these arguments. As was mentioned, the bulk swirl hypothesis predicted both wake structures moving towards the left or in the counter clockwise direction (aft looking forward), whereas the pressure differential hypothesis predicts both wake structures would move away from the centerline. Being able to capture both wakes in the experimental data would aid in further supporting one of these two arguments while further countering the other.

The final point of discussion is an area in which the PIV experiment performed weaker than desired. Acquiring consistent, instantaneous velocimetry data proved especially difficult at the higher fan speed test cases. This is almost entirely because of the inability of the seed insertion system to provide ample and adequately spaced particles over the majority of the measurement field of view in the majority of the images. For comparison, one of the better raw images acquired for the 80% CFS test case is shown in Figure 70 and a typical raw image from the simulate engine experiment is shown in Figure 71. For the higher fan speeds, many of the images had little to no particles in them. When the particles were present, they were often located relatively closely together which ultimately reduces the contrast and signal to noise ratio of each individual particle, making valid vector

calculation more difficult. To reiterate what has already been said, this is why so many images were taken so that over the whole ensemble, there would be a sufficient number of valid points to produce a valid representation of the mean flow.

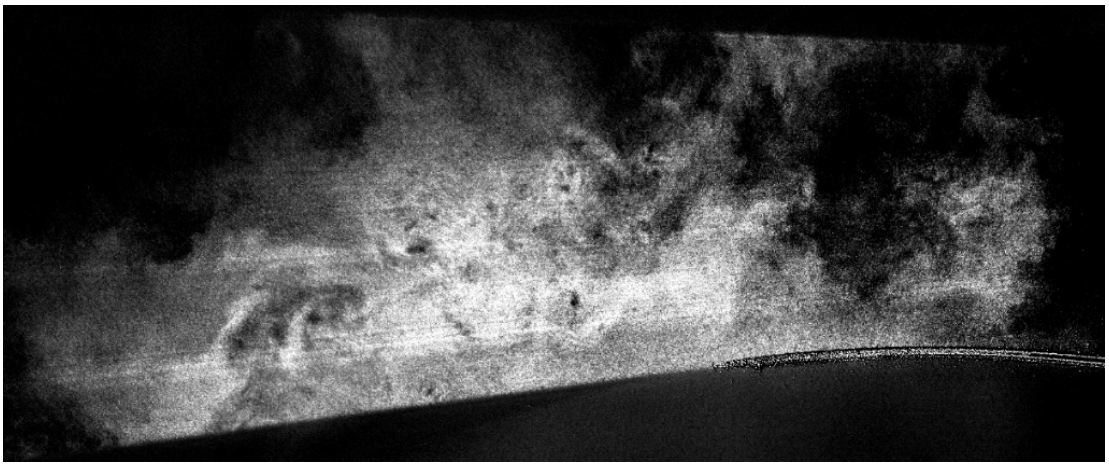

Figure 70 – Raw image of particles in full-scale duct flow, 80% CFS

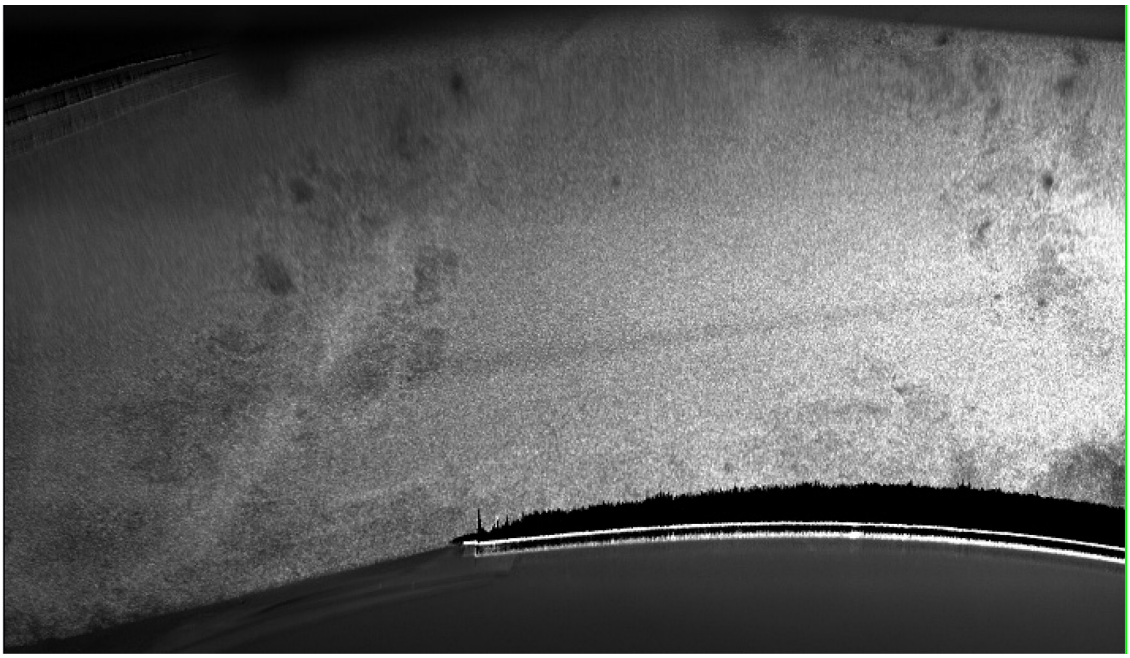

Figure 71 – Raw images of particles in simulated engine duct flow

The fact that instantaneous data was so sparse at the higher fan speeds meant in general that the data was noisier and that the turbulence statistics, which are based off of the instantaneous data, was incomprehensible. However, there were a few instances in which the particle density throughout the image was sufficient to illustrate an instantaneous velocity vector field. One example of the 80% CFS case is shown in Figure 72 and

magnified in Figure 73. Figure 72 displays some of the same characteristics observed in the mean flow, such as the accelerated regions around the strut (1) and the concentrated wake regions (2). The magnified data in Figure 73 also illustrates multiple examples of the three-dimensional turbulence present in the flow. In addition to all the uncorrelated structures, there are a number of coherent vortical structures present. An out-of-plane vortex is observed at location 1. This is likely a vortex shed from the top side of the cylinder that is rotating about an axis with a direction roughly equal to the axis of the strut. Locations 2 – 4 feature smaller vortices that appear to be rotating at least partially about the stream-wise direction. The location 2 vortex is rotating counter-clockwise, the two vortices at location 3 form a counter-rotating vortex pair, and the vortex at location 4 is rotating clockwise. All of these observations are simply to point out that although the majority of the data here has been presented as mean flows, this flow should not be misinterpreted as steady or free of three-dimensional turbulence.

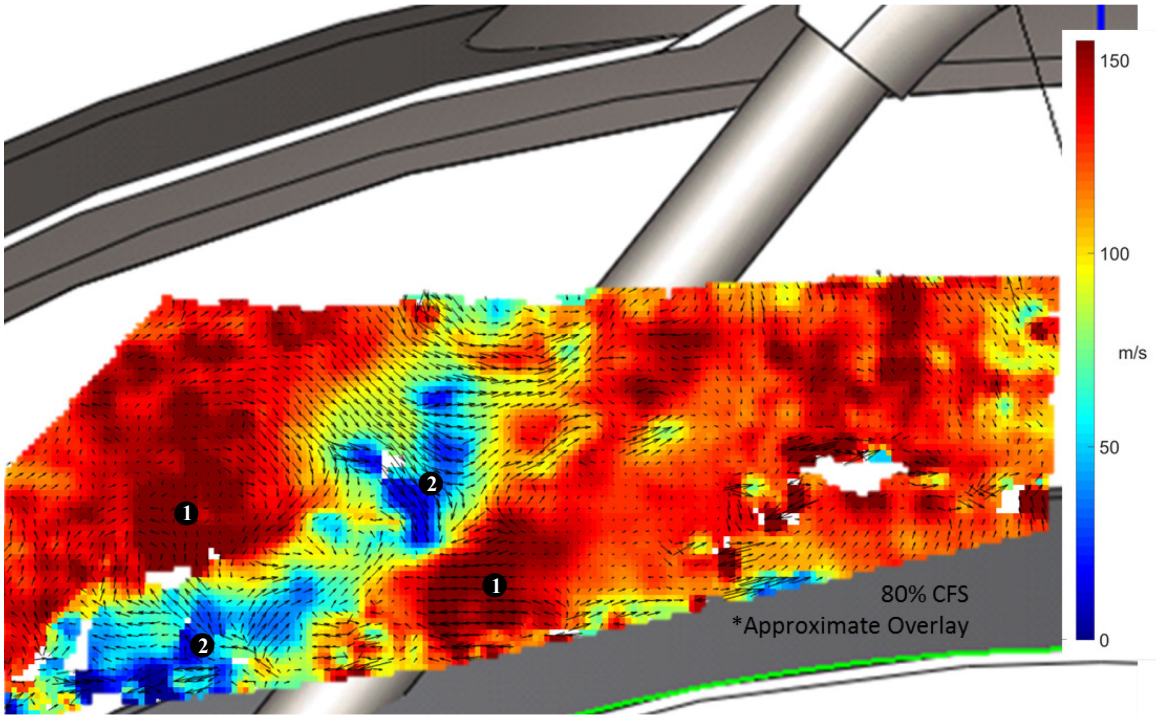

Figure 72 – Instantaneous PIV stream-wise velocity contour, in-plane velocity vector arrows

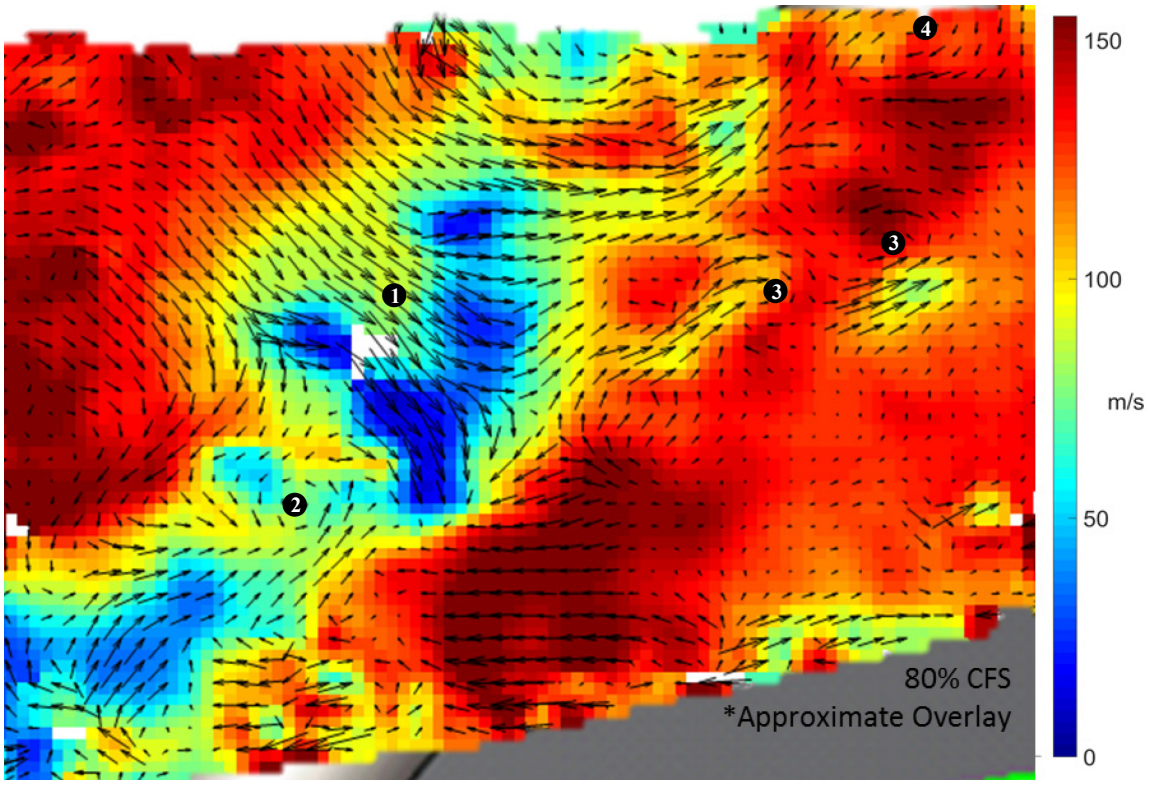

Figure 73 – Instantaneous PIV stream-wise velocity contour, in-plane velocity vector arrows, magnified

Although consistent instantaneous data could not be acquired at the higher fan speed test cases, it was acquired for the idle test case. From this data the normal components of the Reynolds stress tensor for the flow could be calculated. Additionally, The horizontal stress, vertical stress, and stream-wise stress components for the idle fan speed case are shown in Figure 74, Figure 75, and Figure 76 respectively. Visualizing the Reynolds stress components is a good means of visualizing the turbulence since half of the sum of the normal components is equal to the turbulent kinetic energy [2].

From the Reynolds stresses, it can be observed that the turbulence is strongest in the stream-wise and horizontal directions, which was expected. Consider a 2-dimensional circular cylinder flow. The vortices that are shed reside in the plane normal to the cylinder axis. For this experiment, since the strut is most closely aligned in the vertical direction, it was expected that the largest vortices shed off it would reside in a plane most closely aligned with the stream-wise-horizontal plane.

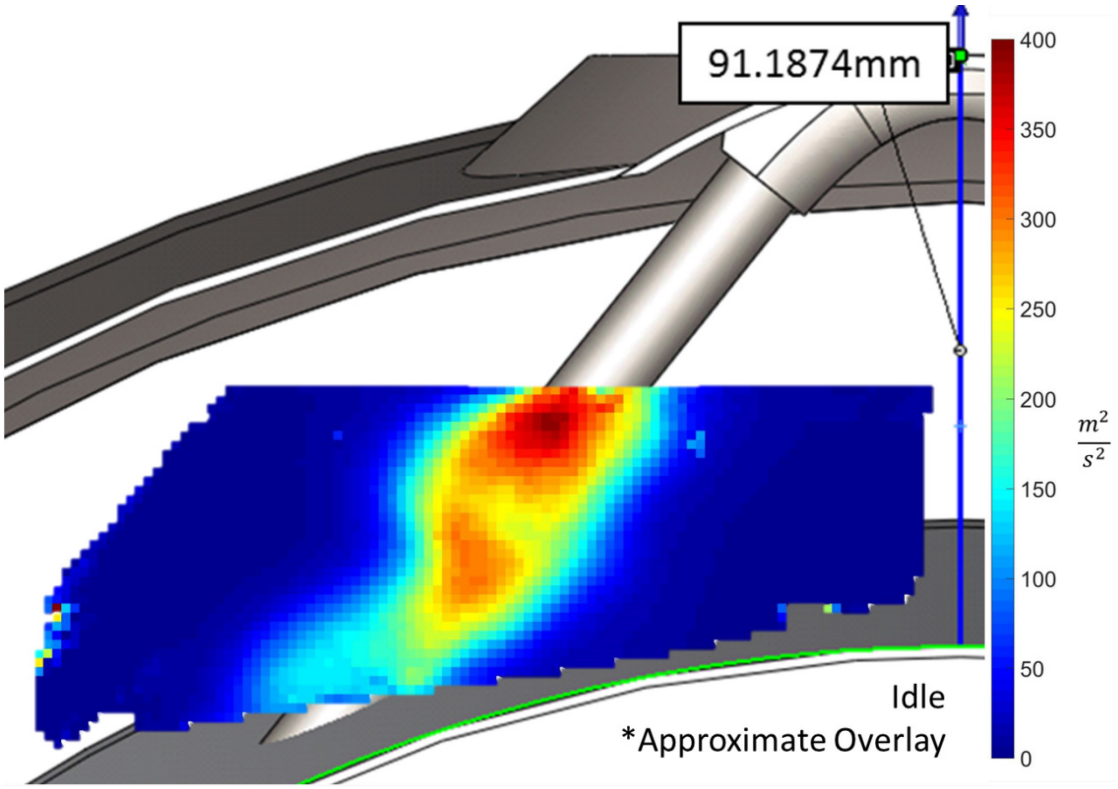

Figure 74 – Horizontal Reynolds stress component, idle fan speed case

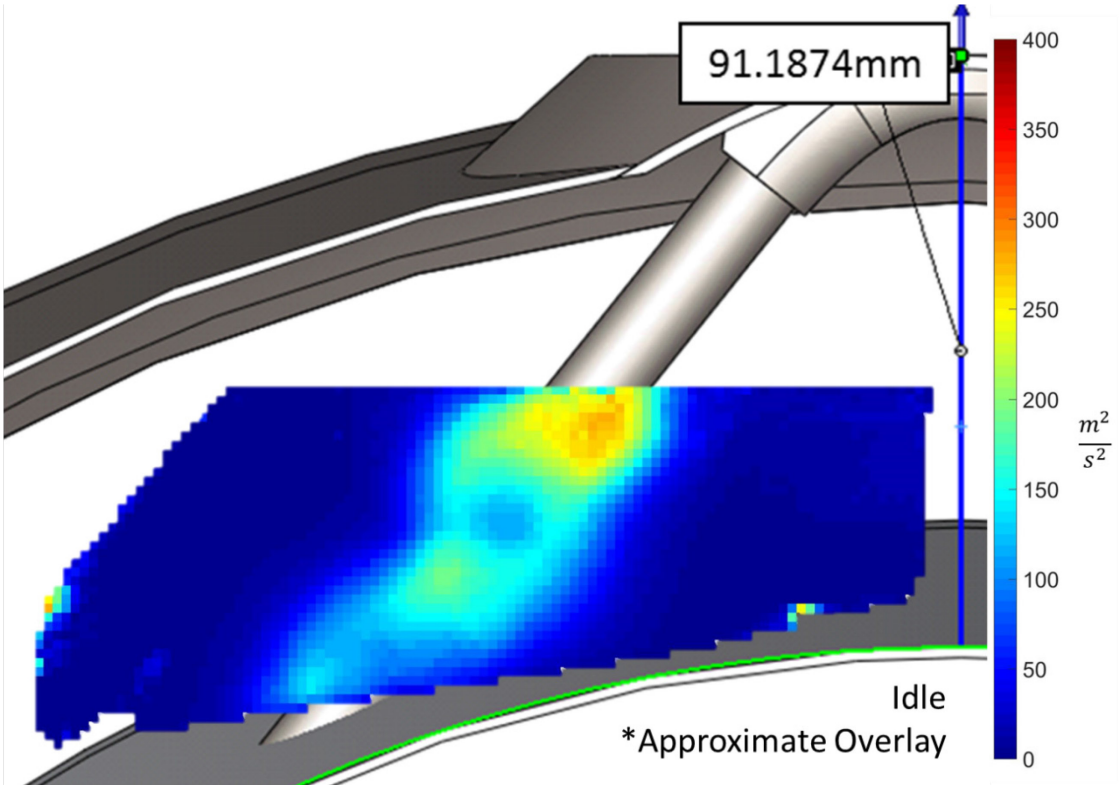

Figure 75 – Vertical Reynolds stress component, idle fan speed case

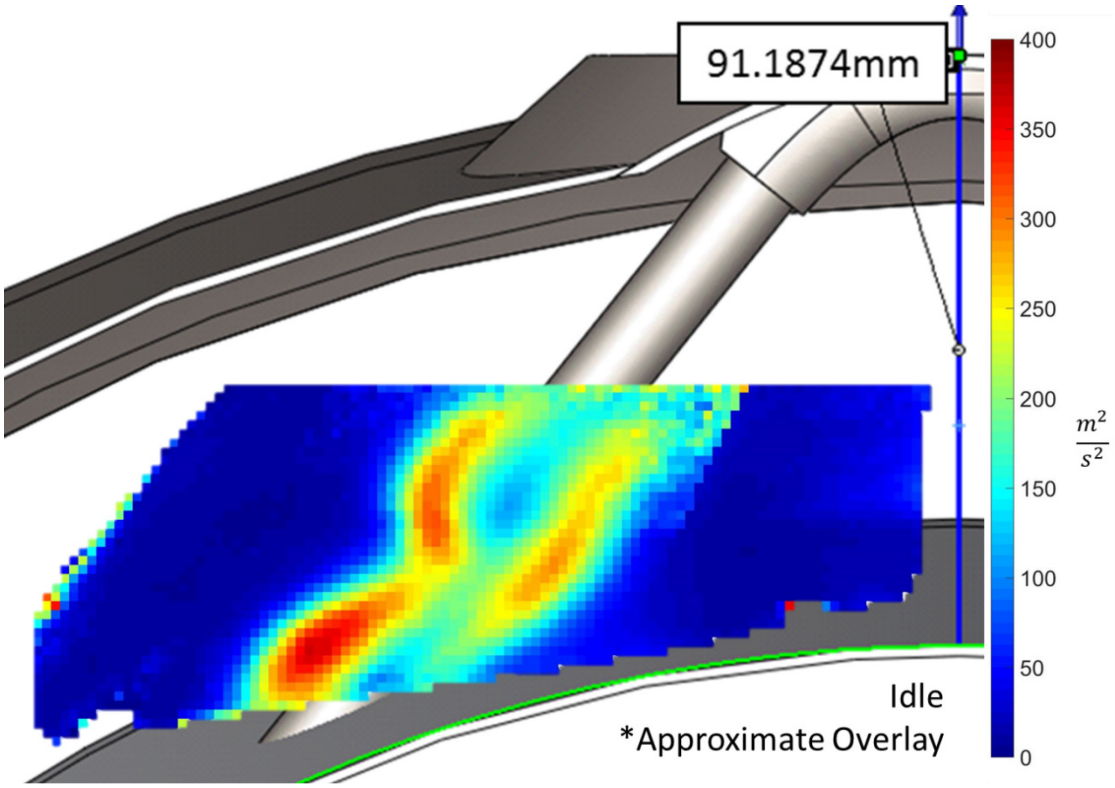

Figure 76 – Stream-wise Reynolds stress component, idle fan speed case

6.3 Experiment Summary

Overall, initial efforts to acquire PIV data inside the bypass duct of a full-scale JT15D-1 were successful. All three components of velocity were obtained at four different fan speed test cases and used to calculate the mean velocity flow field downstream of the aft support strut in the bypass duct. In addition to the PIV experimental work, a complementary CFD simulation was performed to provide a rough visualization of the global flow characteristics and provide insight and perspective where applicable. Both sets of data were used to show that this particular loss mechanism in the bypass duct was producing a wake structure that was not uniform along the direction of the strut. Furthermore, the interaction between the strut, the core shroud wall, and the cavity space on the other side of the wall is producing a complex wake structure that is likely independent from the wake structure formed from the strut main body. For all fan speed test cases, the size and shape of the wake structure was observed to have little variation. However, it was shown to move laterally toward the outboard direction with increased displacement at the higher fan speed test cases. Two hypotheses were presented, but neither

are completely supported by the experimental data. Although the PIV was successful for the most part, the current design had difficulty acquiring quality instantaneous velocimetry data at fan speeds above idle. This was due to the seed insertion system which produced inconsistent performance.

7 Conclusions

A stereo particle image velocimetry (PIV) experiment was conducted successfully in the bypass duct of an operating full-scale turbofan engine. This is the first time to the author's knowledge that this has been achieved and documented in the literature. The experiment utilized external calibration plus self-calibration to attempt to minimize modifications to the engine and reduce the time required at the test stand. The design of the experiment was aided by the development of a software package known as Experimental Design Aid (EDA). EDA is a tool to efficiently iterate through PIV experiment designs in order to achieve a desired output such as field of view or light intensity. A simulated engine environment risk reduction experiment was executed in advance of the full-scale test in order to assess the optical design of the PIV experiment, reduce time at the test stand, and reduce the number of modifications made to the research engine. Complementary computational fluid dynamics (CFD) solutions were generated for two of the experimental fan speed test cases and were used to provide a rough visualization of the large scale flow interactions within the bypass duct and insight where appropriate. A spatial sampling error analysis was performed for point measurement techniques and compared with the capability of PIV measurements by using a synthetic CFD flow field.

The following observations and conclusions were made. EDA was effective in its ability to quickly calculate field of view, depth of field, and mean exposure, among other variables, and allowed for rapid design evolution. The external calibration plus self-calibration method worked but the implementation was not without its flaws. Execution of the proposed calibration method was cumbersome and less practical than intended. Future efforts to acquire data in the same measurement plane as described herein should focus on the design and placement of a custom fit calibration plate. However, the best method of practice for data acquisition at other locations will need to be determined on a case by case basis.

Overall, the experiment was successful and acquired data at four fan speeds form idle (35% max corrected fan speed (CFS)) up to near cruise at 80% CFS. Similar wake

structures were observed at all fan speeds, with large circular deficits connected by pinched wake regions. The notable exception was that the wake structures appeared to displace laterally by an increasing amount as the fan speed was increased. Two current hypotheses were provided, but neither were completely supported by experimental results. The largest area of improvement for future internal engine experiments needs to be seed insertion. At the measurement plane, seeding density was irregular in both the temporal and spatial sense leading to many images with little to no particles. This affected the ability of the PIV system to consistently capture full instantaneous velocity vector fields and therefore turbulence statistics at fan speeds above idle.

An analysis of the spatial sampling error associated with PIV and point measurement techniques showed PIV can be several times more accurate than a sparsely sampled grid of point measurements in a large region of high order gradients and small spatial scale flow phenomena. Even though the point measurement was specified to be two orders of magnitude more accurate at the actual measurement location, the error that existed in between the measured locations was much greater for the point measurement technique. This of course was due to the much greater space between measured locations as compared with PIV.

Additional future work for the experiment should include an improved seed insertion method as mentioned previously. The current best proposed idea involves utilizing a collection volume to mitigate the effects of the smoke machine's irregular smoke output, and a gridded pipe structure (similar to Nelson [5]) to insert particles uniformly into the flow. The wakes generated by this structures should not be of concern due to the large distance and rotating fan blades that exist between the seed insertion structure and the measurement plane. The use of a custom calibration plate should be compared with the implementation practicality of external calibration plus self-calibration, and the endoscopic PIV should be explored as an alternative to the large windows used in this experiment.

For the CFD component of the work, a number of simplifying assumptions were made that severely limited the use of the results for detailed analysis. The complexity of the flow problem is such that it is likely that anything less than an extremely thorough and high-fidelity simulation will struggle to produce results comparable to the experimental results.

Lastly, EDA can be greatly improved by the addition of a graphical user interface (GUI), additional PIV relationships such as particle dynamic response and the impact of background light intensity on signal to noise ratio, and potentially most importantly, use it as a means to determine if a common lower threshold of mean exposure exists for successful PIV experiments.

References

[1] R. J. Adrian, "Scattering particle characteristics and their effect on pulsed laser measurements of fluid flow: speckle velocimetry vs particle image velocimetry," *Appl. Opt.*, vol. 23, no. 11, pp. 1690–1691, Jun. 1984.

[2] S. B. Pope, *Turbulent Flows*. Cambridge, UK: Cambridge University Press, 2000.

[3] R. J. Adrian and J. Westerweel, *Particle Image Velocimetry*. Cambridge: Cambridge University Press, 2011.

[4] A. Vogel and W. Lauterborn, "Time-resolved particle image velocimetry used in the investigation of cavitation bubble dynamics.," *Appl. Opt.*, vol. 27, no. 9, pp. 1869–1876, May 1988.

[5] M. A. Nelson, "Stereoscopic PIV Measurements of Swirl Distortion on a Full-Scale Turbofan Engine Inlet," M.S. thesis, Aerospace and Ocean Eng. Dept., Virginia Tech, Blacksburg, Virginia, 2014.

[6] T. Guimarães, K. T. Lowe, M. Nelson, W. F. O'Brien, and C. Kirk, "Stereoscopic PIV measurements in a turbofan engine inlet with tailored swirl distortion," in *31st AIAA Aerodyn. Meas. Technol. Gr. Test. Conf.*, June 22-26, 2015, Dallas, TX, AIAA 2015-2866.

[7] A. Schröder *et al.*, "Application of image based measurement techniques for the investigation of aeroengine performance on a commercial aircraft in ground operation," in *17th Int. Symp. Appl. Laser Tech. to Fluid Mech.*, July 7-10, 2014, Lisbon, Portugal.

[8] M. P. Wernet, "Development of digital particle imaging velocimetry for use in turbomachinery," *Exp. Fluids*, vol. 28, no. 2, pp. 97–115, Sep. 2000.

[9] B. Liu, X. Yu, H. Liu, H. Jiang, H. Yuan, and Y. Xu, "Application of SPIV in turbomachinery," *Exp. Fluids*, vol. 40, pp. 621–642, Jan. 2006.

[10] J. Estevadeordal, S. E. Gorrell, and W. W. Copenhaver, "PIV Study of Wake-Rotor Interactions in a Transonic Compressor at Various Operating Conditions," *J. Propuls. Power*, vol. 23, no. 1, pp. 235–242, 2007.

[11] C. Brandstetter, F. Wartzek, J. Werner, H.-P. Schiffer, and F. Heinichen, "Unsteady Measurements of Periodic Effects in a Transonic Compressor With Casing Treatments," *J. Turbomach.*, vol. 138, p. 051007, May 2016.

[12] C. E. Willert, C. Hassa, G. Stockhausen, M. Jarius, M. Voges, and J. Klinner, "Combined PIV and DGV applied to a pressurized gas turbine combustion facility," *Meas. Sci. Technol.*, vol. 17, pp. 1670–1679, Jun. 2006.

[13] R. Sadanandan, M. Stöhr, and W. Meier, "Simultaneous OH-PLIF and PIV measurements in a gas turbine model combustor," *Appl. Phys. B*, vol. 90, pp. 609–618, 2008.

[14] K. Gallier, P. Lawless, and S. Fleeter, "Investigation of seal purge flow effects on the hub flow field in a turbine stage using particle image velocimetry," in *36th AIAA/ASME/SAE/ASEE Jt. Propuls. Conf. Exhib.*, July 16-19, 2000. Huntsville, AL, AIAA-2000-3370.

[15] H. Lang, T. Mørck, and J. Woisetschläger, "Stereoscopic particle image velocimetry in a transonic turbine stage," *Exp. Fluids*, vol. 32, pp. 700–709, Apr. 2002.
[16] L. Porreca, M. Hollenstein, A. I. Kalfas, and R. S. Abhari, "Turbulence Measurements and Analysis in a Multistage Axial Turbine," *J. Propuls. Power*, vol. 23, no. 1, pp. 227–234, 2007.
[17] M. Kegalj and H.-P. Schiffer, "Endoscopic PIV measurements in a low pressure turbine rig," *Experiments in Fluids*, vol. 47, pp. 689–705, Jul. 2009.
[18] A. Skeen, "The Development of High-Speed PIV Techniques and Their Application to Jet Noise Measurement," Ph.D. dissertation, School of Engineering, University of Warwick, Coventry, United Kingdom, 2006.
[19] A. Schröder, R. Geisler, D. Schanz, B. Wrede, and J. Agocs, "Flow field investigations in the free bypass jet flow of a V2527 engine at Ground Operation using SPIV," in *54th AIAA Aerosp. Sci. Meet.*, January 4-8, 2016, San Diego, CA, AIAA 2016-0108.
[20] J. Heidmann, "Improving Engine Efficiency Through Core Developments," in *49th AIAA Aero Sci. Meeting,* January 4-7, 2011, Orlando, FL.
[21] C. E. Hughes, "Aircraft Engine Technology for Green Aviation to Reduce Fuel Burn," in *3rd AIAA Atmos. Sp. Environ. Conf.*, June 27-30, 2011, Honolulu, HI.
[22] A. H. Epstein, "Aeropropulsion for Commercial Aviation in the 21st Century and Research Directions Needed," in *51st AIAA Aerosp. Sci. Meet. Incl. New Horizons Forum Aerosp. Expo.*, January 7-10, 2013, Grapevine, TX, AIAA 2013-0001.
[23] F. Stern, R. V. Wilson, H. W. Coleman, and E. G. Paterson, "Comprehensive Approach to Verification and Validation of CFD Simulations—Part 1: Methodology and Procedures," *J. Fluids Eng.*, vol. 123, pp. 793–802, Dec. 2001.
[24] W. L. Oberkampf and T. G. Trucano, "Verification and Validation in Computational Fluid Dynamics," *Progress in Aerospace Sciences*, vol. 38, pp. 209–272, 2002.
[25] J. R. Grace and F. Taghipour, "Verification and validation of CFD models and dynamic similarity for fluidized beds," *Powder Technol.*, vol. 139, pp. 99–110, 2004.
[26] H. W. Coleman and F. Stern, "Uncertainties and CFD code validation," *J. Fluids Eng. Asme*, vol. 119, pp. 795–803, Dec. 1997.
[27] S. D. Jessup, "An experimental investigation of viscous aspects of propeller blade flow," Ph.D. dissertation, School of Eng. and Architecture, The Catholic University of America, Washington, D.C., 1989.
[28] J. L. Santiago, A. Martilli, and F. Martin, "CFD simulation of airflow over a regular array of cubes. Part I: Three-dimensional simulation of the flow and validation with wind-tunnel measurements," *Boundary-Layer Meteorol.*, vol. 122, pp. 609–634, 2007.
[29] M. J. Brown, G. D-, R. E. Lawson, D. S. Decroix, and R. L. Lee, "Comparison of Centerline Velocity Measurements Obtained Around 2D and 3D Building Arrays in a Wind Tunnel," in *Int.Symp. on Environmental Hydraulics*, December, 2001, Tempe, AZ.
[30] J. Dunham, "CFD Validation for Propulsion System Components," AGARD Advisory Report 355, AGARD, Nellie-Sur-Seine, France, May, 1998.

[31] W. L. Oberkampf and B. Smith, "Assessment criteria for computational fluid dynamics validation benchmark experiments," in *52nd Aerosp. Sci. Meet.*, January 13-17, 2014, National Harbor, MD, AIAA 2014-0205.
[32] J. Sheng, H. Meng, and R. O. Fox, "Validation of CFD Simulations of a Stirred Tank using Particle Image Velocimetry Data," *Can. J. Chem. Eng.*, vol. 76, pp. 611–625, Jun. 1998.
[33] S. L. Ceccio, "When Computations and Experiments Collide - Some Case Studies in CFD Validation." in *PIV Uncertainty Workshop,* May 11-13, 2011, 2011, Las Vegas, NV.
[34] "High Accuracy Pressure Transducers," *Omega Engineering*. [Online]. Available: http://www.omega.com/pptst/PX409_SERIES.html. [Accessed: 14-Apr-2017].
[35] J. J. Charonko and P. P. Vlachos, "Estimation of uncertainty bounds for individual particle image velocimetry measurements from cross-correlation peak ratio," *Meas. Sci. Technol.*, vol. 24, p. 065301, Mar. 2013.
[36] J. Westerweel, "On velocity gradients in PIV interrogation," *Exp. Fluids*, vol. 44, pp. 831–842, 2008.
[37] C. D. Meinhart, S. T. Wereley, and J. G. Santiago, "PIV Measurement of a Microchannel Flow," *Exp. Fluids*, vol. 27, pp. 414–419, 1999.
[38] M. Toloui, S. Riley, J. Hong, K. Howard, L. P. Chamorro, M. Guala, and J. Tucker, "Measurement of atmospheric boundary layer based on super-large-scale particle image velocimetry using natural snowfall," *Exp. Fluids*, vol. 55, 2014.
[39] A. K. Prasad, "Stereoscopic particle image velocimetry," *Exp. Fluids*, vol. 29, pp. 103–116, 2000.
[40] F. Scarano, "Tomographic PIV: principles and practice," *Meas. Sci. Technol.*, vol. 24, p. 012001, 2013.
[41] J. Westerweel, G. E. Elsinga, and R. J. Adrian, "Particle Image Velocimetry for Complex and Turbulent Flows," *Annu. Rev. Fluid Mech.*, vol. 45, pp. 409–436, 2013.
[42] D. J. Frohnapfel, "Experimental Investigation of Fan Rotor Response to Inlet Swirl Distortion," M.S. thesis, Mechanical Eng. Dept., Virginia Tech, Blacksburg, Virginia, 2016.
[43] S. Pol and B. J. Balakumar, "Large Field of View Particle-Image Velocimetry (LF-PIV): Design and Performance," in *50th AIAA Aerospace Sciences Meeting including the New Horizons Forum and Aerospace Expositions*, January 9-12, 2012, Nashville, TN.
[44] P. Laven, "MiePlot." *MiePlot.* [Online]. Available: http://www.philiplaven.com/mieplot.htm. [Accessed: 14-Apr-2017].
[45] H. C. Van De Hulst, *Light Scattering by Small Particles*, vol. 1. New York: John Wiley & Sons, 1957.
[46] C. M. de Silva *et al.*, "High spatial range velocity measurements in a high Reynolds number turbulent boundary layer," *Phys. Fluids*, vol. 26, no. 2, Feb. 2014.
[47] J. M. Bailey, "Full Scale Experimental Transonic Fan Interaction with a Boundary Layer Ingesting Total Pressure Distortion," Ph.D. dissertation, Mechanical Eng. Dept., Virginia Tech, Blacksburg, Virginia, 2016.
[48] Cook, D.L., "Development of the JT15D-1 Turbofan Engine," SAE Paper No. 720352, National Business Aircraft Meeting, Wichita, KS, March 15-17, 1972.

[49] J. A. Schetz and R. D. W. Bowersox, *Boundary Layer Analysis*, 2nd ed. Reston, Virginia: American Institute of Aeronautics and Astronautics, 2011.
[50] J. P. Reardon, "Computational Modeling of Radiation Effects on Total Temperature Probes," M.S. thesis, Aerospace and Ocean Eng. Dept., Virginia Tech, Blacksburg, Virginia, 2015.
[51] P. G. Hill and C. R. Peterson, *Mechanics and thermodynamics of propulsion*. Reading, MA: Addison-Wesley, 1992.
[52] P. W. Bearman, "On vortex shedding from a circular cylinder in the critical Reynolds number regime," *J . Fluid Mech*, vol. 37, no. 3, pp. 577–585, 1969.
[53] W. Rodi, "Comparison of LES and RANS calculations of the flow around bluff bodies," *J. Wind Eng. Ind. Aerodyn.*, vol. 69–71, pp. 55–75, 1997.
[54] D. Lakehal and W. Rodi, "Calculation of the flow past a surface-mounted cube with two-layer turbulence models," *J. Wind Eng. Ind. Aerodyn.*, vol. 67–68, pp. 65–78, 1997.
[55] G. Iaccarino, A. Ooi, P. A. Durbin, and M. Behnia, "Reynolds averaged simulation of unsteady separated flow," *Int. J. Heat Fluid Flow*, vol. 24, pp. 147–156, 2003.
[56] J. L. Bennington, "Effects of Various Shaped Roughness Elements in Two-Dimensional High Reynolds Number Turbulent Boundary Layers," M.S. thesis, Aerospace and Ocean Eng. Dept., Virginia Tech, Blacksburg, Virginia, 2004.
[57] C. T. Crowe, R. A. Gore, and T. R. Troutt, "Particle Dispersion By Coherent Structures in Free Shear Flows," *Part. Sci. Technol.*, vol. 3, no. 3–4, pp. 149–158, 1985.
[58] T. Scheimpflug, "Method of distorting plane images by means of lenses or mirrors," U.S. Patent 751,347, February 2, 1904.
[59] B. Wieneke, "Stereo-PIV using self-calibration on particle images," *Exp. Fluids*, vol. 39, pp. 267–280, May 2005.
[60] B. Wieneke and K. Pfeiffer, "Adaptive PIV fwith variable interrogation window size and shape," in *15th Int Symp Appl. Laser Tech. to Fluid Mech.*, July 5-8, 2010, Lisbon, Portugal.
[61] C. J. Baker, "The Turbulent Horshoe Vortex," *J. Wind Eng. Ind. Aerodyn.*, vol. 6, pp. 9–23, 1980.
[62] W. A. Eckerle and L. S. Langston, "Horseshoe Vortex Formation Around a Cylinder," in *Int. Gas Turbine Conference and Exhibit*, June 8-12, 1987, Dusseldorf, West Germany.
[63] T. L. Doligalski, C. R. Smith, and J. D. A. Walker, "Vortex Interactions With Walls," *Annu. Rev. Fluid Mech.*, vol. 26, pp. 573–616, 1994.
[64] L. M. Milne-Thompson, *Theoretical Hydrodynamics*. London: MacMillan, 1962.
[65] H. W. Coleman and W. G. Steele, "Experimental Uncertainty Analysis: A Basic Overview," in *PIV Uncertainty Workshop,* May 11-13, 2011, 2011, Las Vegas, NV.
[66] H. W. Coleman and W. G. Steele, *Experimentation, validation, and uncertainty analysis for engineers*, 3rd ed. Hoboken, NJ: John Wiley & Sons, 2009.
[67] S. J. Beresh and B. L. Smith, "Effects of Spatial Realignment in Stereo PIV Calibration," in *52nd AIAA Aerosp. Sci. Meet.*, January 13-17, 2014, National Harbor, MD, AIAA 2014-1101.
[68] S. Bhattacharya, J. J. Charonko, and P. P. Vlachos, "Stereo-particle image velocimetry uncertainty quantification," *Meas. Sci. Technol.*, vol. 28, p. 015301,

2017.
[69] J. Westerweel, “Efficient detection of spurious vectors in particle image velocimetry data,” *Exp. Fluids*, vol. 16, pp. 263–247, 1994.
[70] J. Westerweel and F. Scarano, “Universal outlier detection for PIV data,” *Exp. Fluids*, vol. 39, pp. 1096–1100, 2005.
[71] A. Sciacchitano, F. Scarano, and B. Wieneke, “PIV uncertainty quantification by image matching,” *Meas. Sci. Technol.*, vol. 24, p. 045302, Mar. 2013.
[72] B. Wieneke, “PIV uncertainty quantification from correlation statistics,” *Meas. Sci. Technol.*, vol. 26, p. 074002, Jun. 2015.
[73] A. Sciacchitano *et al.*, “Collaborative framework for PIV uncertainty quantification: comparative assessment of methods,” in *17th Int. Symp. Appl. Laser Tech. to Fluid Mech.*, July 7-10, 2014, Lisbon, Portugal.
[74] C. J. Käehler, “Single Pixel PIV, Single Particle PTV or Optical Flow Analysis? Resolution and Uncertainty Aspects,” in *PIV Uncertainty Workshop,* May 11-13, 2011, 2011, Las Vegas, NV.
[75] A. Spencer and D. Hollis, “Correcting for sub-grid filtering effects in particle image velocimetry data,” *Meas. Sci. Technol.*, vol. 16, pp. 2323-2335, Aug. 2005.
[76] D. Ragni, F. Schrijer, B. W. Van Oudheusden, and F. Scarano, “Particle tracer response across shocks measured by PIV,” *Exp. Fluids*, vol. 50, pp. 53–64, 2011.
[77] T. Persoons and T. S. O’Donovan, “High dynamic velocity range particle image velocimetry using multiple pulse separation imaging,” *Sensors*, vol. 11, pp. 1–18, 2011.
[78] B. H. Timmins, B. W. Wilson, B. L. Smith, and P. P. Vlachos, “A method for automatic estimation of instantaneous local uncertainty in particle image velocimetry measurements,” *Exp. Fluids*, vol. 53, pp. 1133–1147, 2012.
[79] B. J. Petrosky, K. T. Lowe, P. M. Danehy, C. J. Wohl, and P. I. Tiemsin, “Improvements in laser flare removal for particle image velocimetry using fluorescent dye-doped particles,” *Meas. Sci. Technol.*, vol. 26, p. 115303, 2015.
[80] A. Boomsma, S. Bhattacharya, D. Troolin, S. Pothos, and P. Vlachos, “A comparative experimental evaluation of uncertainty estimation methods for two-component PIV,” *Meas. Sci. Technol.*, vol. 27, p. 094006, Aug. 2016.
[81] S. J. Beresh, “Estimating Bias Uncertainties in PIV Data Using Complementary Measurements,” in *PIV Uncertainty Workshop,* May 11-13, 2011, 2011, Las Vegas, NV.
[82] B. Wieneke, “Generic a-posteriori uncertainty quantification for PIV vector fields by correlation statistics,” in *17th Int. Symp. Appl. Laser Tech. to Fluid Mech.*, July 7-10, 2014, Lisbon, Portugal.
[83] B. W. van Oudheusden, “PIV-based pressure measurement,” *Meas. Sci. Technol.*, vol. 24, p. 032001, Jan. 2013.
[84] X. Liu and J. Katz, “Instantaneous pressure and material acceleration measurements using a four-exposure PIV system,” *Exp. Fluids*, vol. 41, pp. 227–240, May 2006.
[85] R. Gurka, A. Liberzon, D. Hefetz, D. Rubinstein, and U. Shavit, “Computation of Pressure Distribution Using PIV Velocity Data,” in *Int. Work. on Particle Image Velocimetry*, September 16-18, 1999, Santa Barbara, CA.
[86] N. Fujisawa, S. Tanahashi, and K. Srinivas, “Evaluation of pressure field and fluid forces on a circular cylinder with and without rotational oscillation using velocity

data from PIV measurement," *Meas. Sci. Technol.*, vol. 16, pp. 989–996, Mar. 2005.
[87] R. de Kat, B. W. van Oudheusden, and F. Scarano, "Instantaneous planar pressure field determination around a square-section cylinder based on time-resolved stereo-PIV," in *17th Int. Symp. Appl. Laser Tech. to Fluid Mech.*, July 7-10, 2014, Lisbon, Portugal.
[88] R. de Kat and B. W. Van Oudheusden, "Instantaneous planar pressure determination from PIV in turbulent flow," *Exp. Fluids*, vol. 52, pp. 1089–1106, 2012.

A. Appendix

A.1. Uncertainty Analysis

The topic of uncertainty analysis for PIV experiments is one of great importance, however it is something that has proven extremely difficult to quantify due to the complexity of PIV experiments and the large number of potential error sources they are comprised of. Adding to the difficulty is the fact that most every PIV experiment is unique in the way that cameras are located relative to the laser sheet, the size and type of particles, the processing algorithm used, and the list goes on. This variety causes the error sources to have varying degrees of impact on the final result and makes the creation of a universal method by which to quantify the total measurement uncertainty elusive to say the least. That said, understanding the various sources of error and how these component uncertainties propagate through the measurement chain has been a focus point for researchers over the last ten years or so.

The errors discussed here fall into two types of categories: random error and systematic error. A good overview of this is presented by Coleman, Steele [65], Coleman, Steele [66]. Systematic errors are the fixed errors or biases that a device may have on the output. Random errors on the other hand are repeatability errors. So although the random error on a mean value for example can usually be mitigated by acquiring a sufficient number of data points, systematic error correction requires a fundamental understanding of the phenomenon creating the error.

Many sources of error that plague PIV experiments have been identified. Some have been studied extensively but fewer have been truly quantified. An incomplete list is presented below of the various errors and work done either to understand or to account for/mitigate the error. Calibration errors Wieneke [59], Beresh, Smith [67], calibration variation/camera and/or laser vibration Nelson [5], stereoscopic errors Wieneke [59], Bhattacharya et al. [68], variable magnification in an image, image aberration, vector validation Westerweel [69], Westerweel, Scarano [70], correlation error Sciacchitano et al [71], Wieneke [72], Charonko, Vlachos [35], Sciacchitano et al [73], pixel locking, spatial

resolution Käehler [74], Spencer, Hollis [75], particle dynamic response Ragni et al. [76], velocity dynamic range Persoons, O'Donovan [77], velocity gradients Timmins et al. [78], light refraction, laser flare Petrosky et al. [79], sampling error, particle concentration Käehler [74], processing algorithm Boomsa et al. [80].

Even after all this work however, the trouble remains as Beresh [81] states, with the "unknown unknowns." He continues, "there can be many unknown unknowns in any given PIV experiment that can be difficult to quantify and to even know of their existence may require repeated experiments of varying configurations" (2 component, stereo, multiple positions, etc.). With this understanding, it appears the best path forward at the present time is to have a firm understanding of the components of the PIV experiment and the general impact they have on the system uncertainty. Only then can the experimentalist attempt to mitigate the known potential errors as much as possible. If feasible for the given experiment, one can then follow the suggestion of Beresh [81] and acquire data at multiple locations from multiple configurations and compare how much the data varies. The novice PIV experimentalist is forewarned however from assuming the 'rule of thumb' that measurements are within 0.1 pixels as Charonko, Vlachos [35] points out that many inappropriately do even though this is only true under certain conditions, and in reality, the error can be less, or more often, it can be more Westerweel [36].

For this work, several of the methods discussed by the references above were employed. Notably during testing, self-calibration [59] was used to correct for discrepancies between the calibration plate and the light sheet, steel cables and isolated camera structures were utilized to avoid the camera vibrations seen in [Nelson 2014], and measurements were repeated at least five times more than the 'standard PIV experiment 1000 images.' This included acquiring images at the same fan speed after an engine restart or at a different time altogether. In the post-processing stage, the main form of combating error came in the form of using the peak ratio as a filter. The peak ratio, typically given the notation Q, is the ratio of the highest to the second highest correlation peak during the vector calculation process. If the image within a given interrogation region has a high signal to noise ratio with clear particle images, then the peak ratio will have a higher value. If the same image has poor signal to noise ratio or fuzzy particles that blur into the background, then the peak ratio will be much closer to one. Additionally, an image can have a very large peak ratio if

for example the interrogation region contains only background objects that aren't moving or if the scattered light off the particles is so intense that it saturates the camera sensor. For this work, a vector was considered invalid if it had a peak ratio value of less than 1.1 or greater than 25. These values were determined based on observations made from 3d histogram plots where the y and x axis were any of the three components of velocity and the peak ratio value respectively. Examples are shown in Figure 77 and Figure 78 for the 80% max corrected fan speed case. The region of high counts to the far right represents all the data points past that location in the x axis. One can see it appears nearly the same in both figures even though Figure 78 is over a much smaller peak ratio interval, meaning that nearly all the values in that region have a peak ratio greater than 25. This is used with the knowledge that peak ratios should not be this large and those values can therefore be safely eliminated. The lower bound for eliminating values was a iterative tradeoff between increasing confidence in the calculated vector displacements and leaving enough values from which to calculate an ensemble mean.

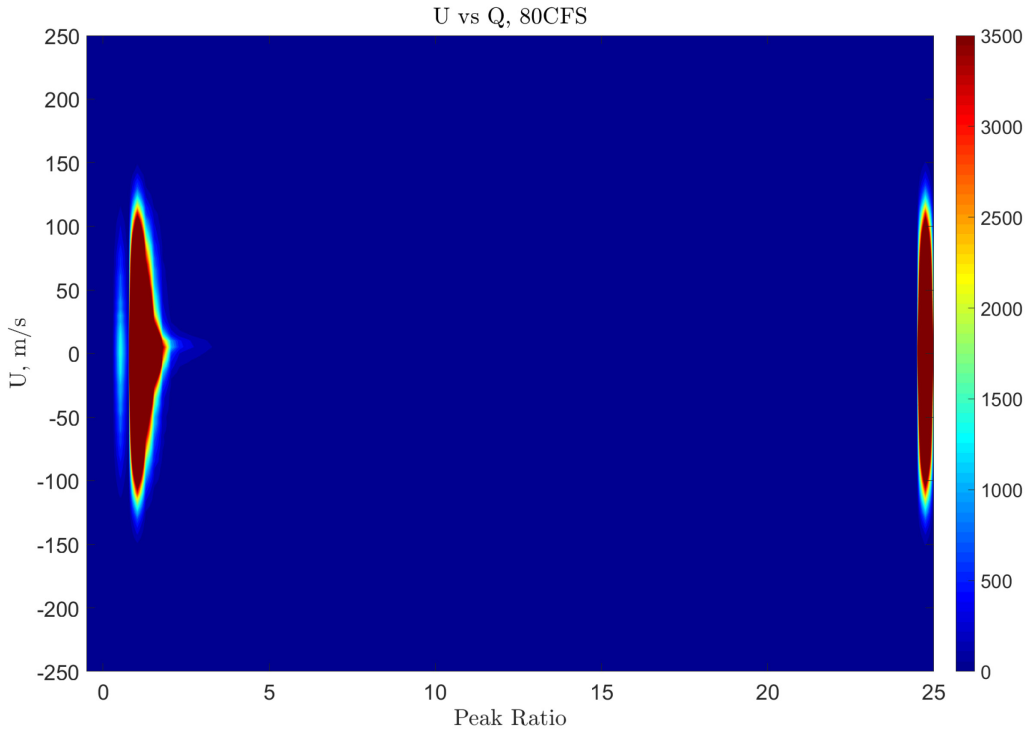

Figure 77 – Horizontal velocity vs peak ratio, 80% Max CFS

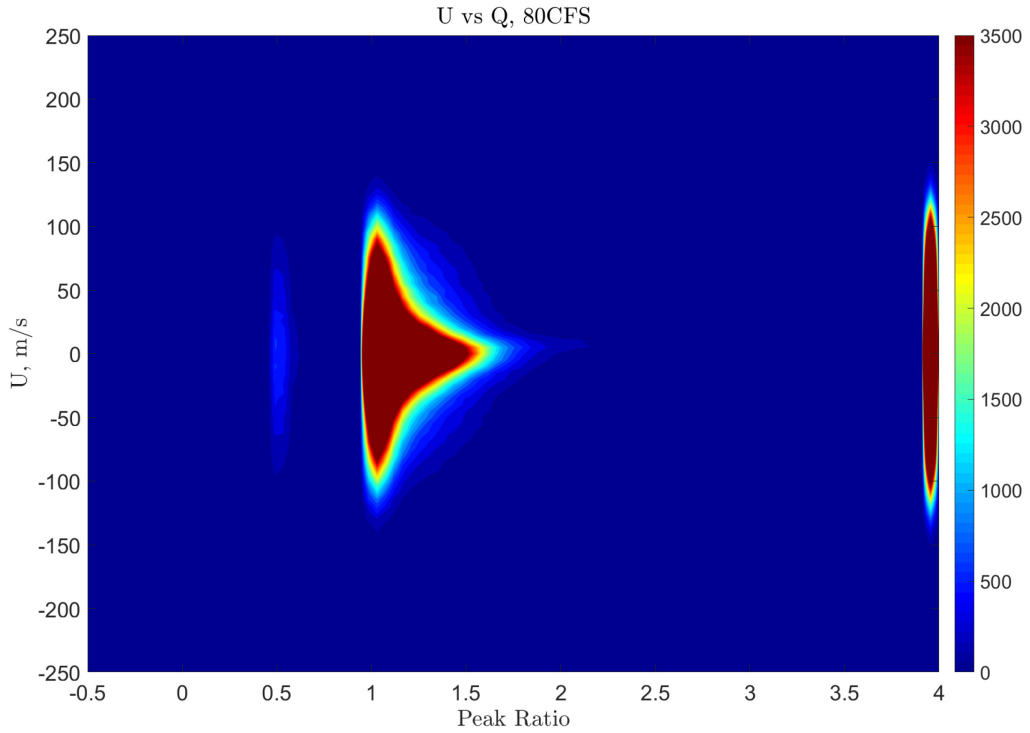

Figure 78 – Horizontal velocity vs peak ratio, 80% Max CFS, smaller interval

In addition to an analysis of the peak ratio, analyses were also performed of the velocity distributions at various locations, the displacement vector uncertainty, and the particle response time compared to the flow time scales. The velocity distributions not only provided valuable insight into how the flow was behaving differently from the mean flow, but it also allows for investigations into specific regions where the data is suspected to be incorrect. An example is shown in Figure 79 below where the data close to the boundary of the laser sheet in a region where the flow is much lower than the surroundings is generating questionable results. It can be seen that the mean value is based off of relatively few data points and the non-Gaussian distribution (especially the U component of velocity) is an indication that the data in the immediate vicinity of this location should probably not be trusted.

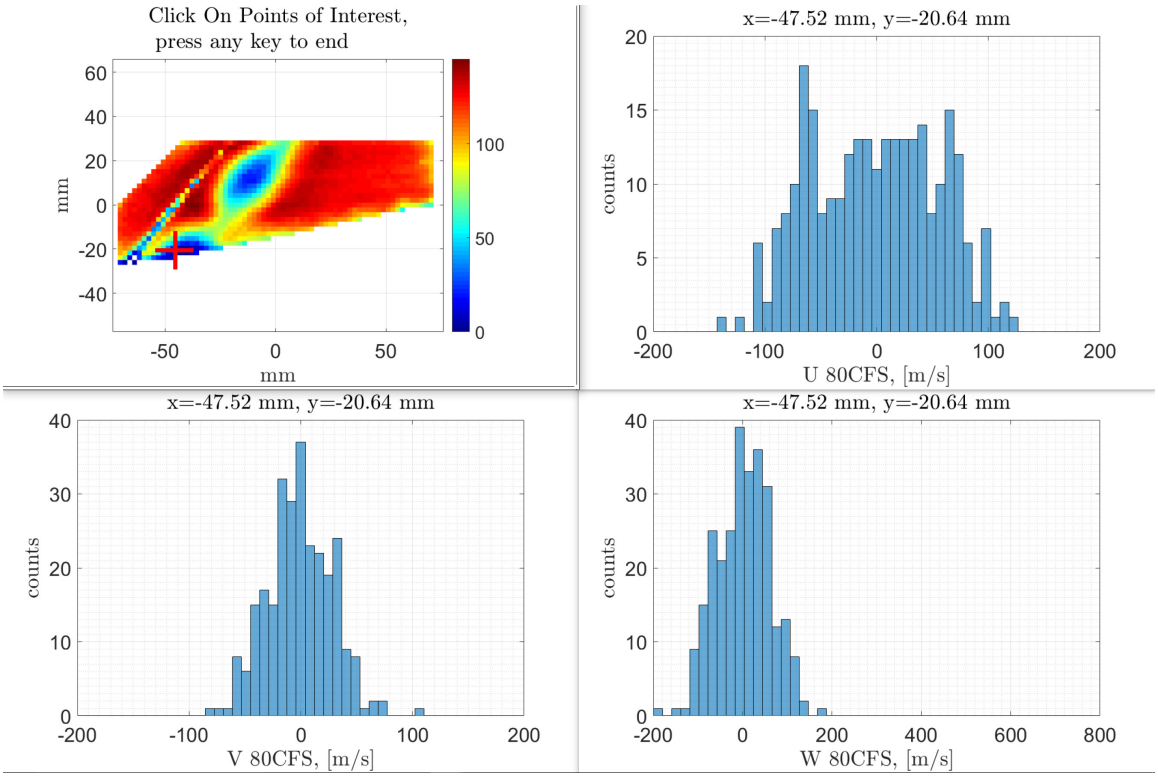

Figure 79 – Distribution of the 3 components of velocity at a location of questionable accuracy (marked by red plus)

For the particle response time, the process of Beresh [81] will be followed. The top left plot in Figure 79 shows the mean stream-wise velocity at the highest fan speed tested. The strongest gradients are taken to be in the x direction as about 100m/s gradient over 24 mm. This results in a fluid time scale $\tau_f \approx 240\mu s$. The fluid time scale was shown previously to be $\tau_p \approx 0.3\,\mu s$. This results in a $\tau_p/\tau_f \approx 0.002$. Beresh gives τ_p/τ_f ratios <1 are acceptable and values <0.1 are very good so by these measures the seed selection was an appropriate one.

Finally, during the vector calculation processing, the LaVision DaVis software is able to calculate the standard deviation and bias for vector components and vector length of the vectors in a single vector field, utilizing the work of Wieneke [82]. In the product manual's words this method quantifies the differences between two interrogation windows mapped onto each other by the computed displacement vector. Ideally they would match up perfectly, but in reality they seldom do. The resulting cross-correlation peak is therefore not symmetric, reflecting on the impact of each pixel on the cross-correlation peak shape. A statistical analysis of the peak shape is what is used to then derive the uncertainty of the

displacement vector. Figure 80 through Figure 82 show the resulting mean uncertainties for the three components of velocity at the highest fan speed tested. They are normalized by the maximum mean stream-wise velocity.

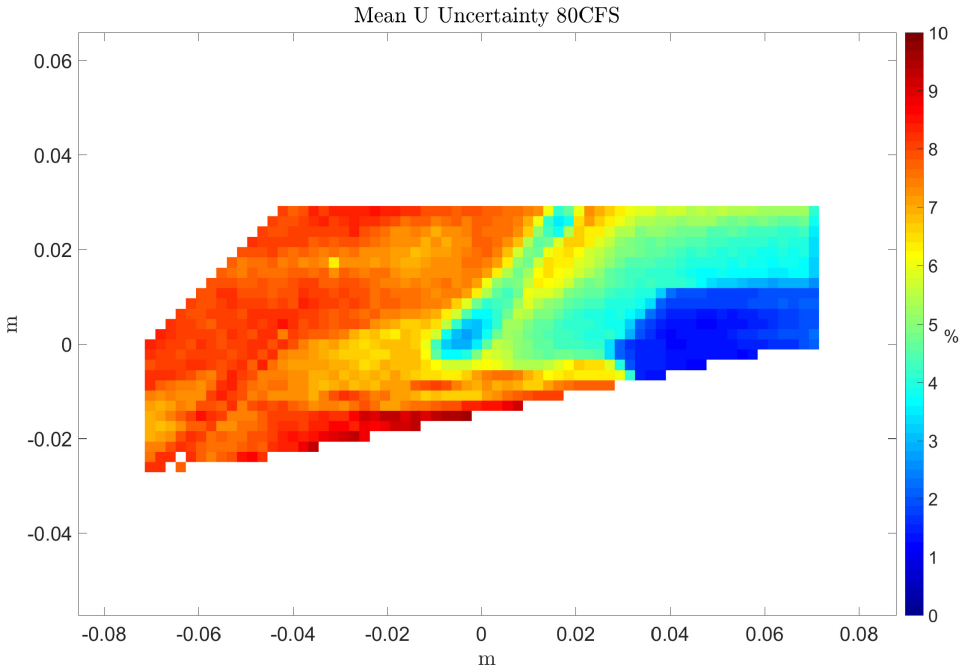

Figure 80 – Uncertainty in horizontal velocity component

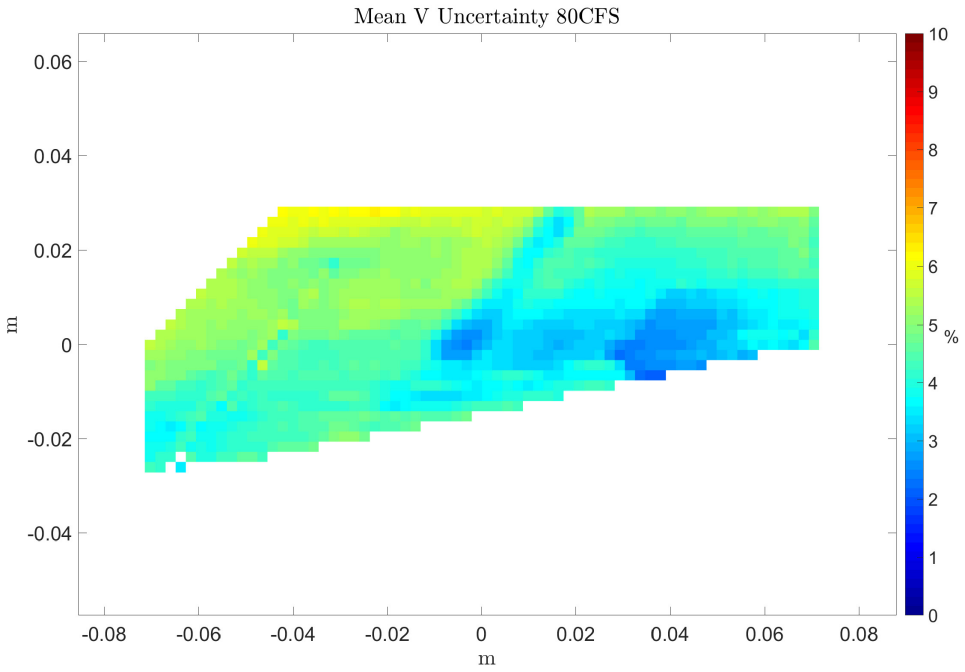

Figure 81 – Uncertainty in vertical velocity component

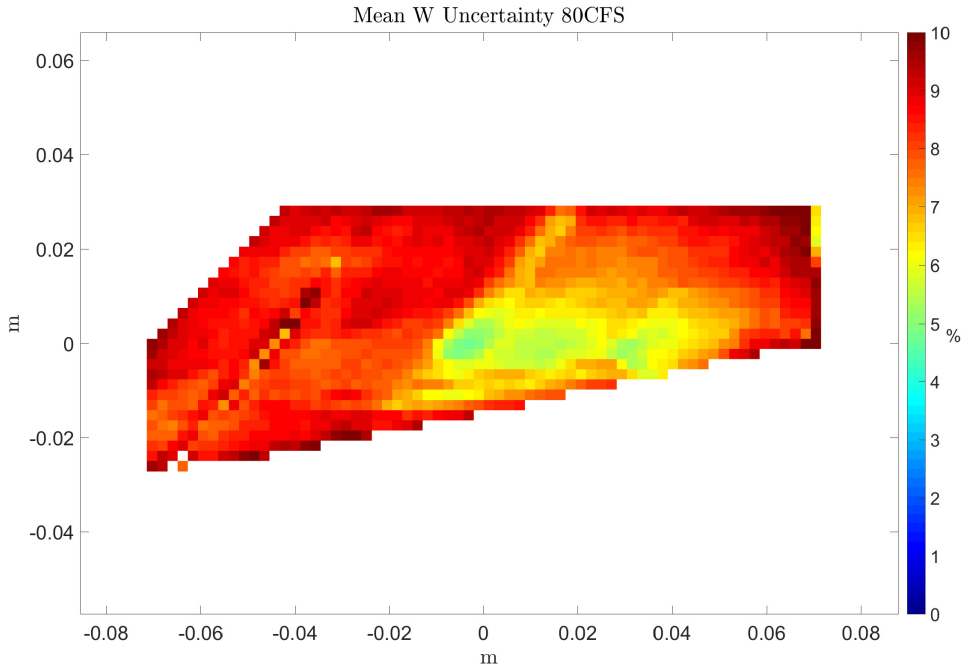

Figure 82 – Uncertainty in stream-wise velocity component

It is clear that the largest errors exist in the stream-wise component of velocity, followed by the horizontal component of velocity, followed lastly by the vertical component of velocity. This is expected. Due to the nature of the wake generating a highly turbulent flow, the largest fluctuations will be in the stream-wise direction. Because the strut is inclined at an angle closer to vertical rather than horizontal, any vortices shed from the cylinder are likely to be rotating closer to the x-z plane rather than the y-z plane, thus the second largest fluctuations will be in the horizontal direction. The fluctuations of course cause a number of things to happen over the course of the experiment. Most notably, it can cause a portion of the particles in a given interrogation region to be traveling in one direction while another portion are traveling in a different direction. These strong gradients ultimately impact the cross-correlation algorithm's ability to correctly calculate the displacement, mainly because there is not a correct displacement for that entire group of particles.

A possible explanation for the higher uncertainties on the left side of the measurement plane is as follows. The laser sheet entered the measurement plane from the right and expands as it moves toward the left. As it expands, the energy is dispersed over a greater area causing the particles to scatter less light. This in turn could impact the algorithm's ability to correctly calculate the cross-correlation by decreasing the signal to noise ratio.

Additionally, any movements of the laser sheet relative to the calibrated position by a pivot of the final mirror, shown in Figure 44 in Section 5.6.1, would be exacerbated the further away from the pivot position the laser sheet traveled. This discrepancy should have been corrected by the self-calibration process, but it is possible that it was not.

It is the author's judgement that the uncertainty of this experiment can best be reduced in the future by increasing the quality of the seed dispersion. The method used in this work generated large clusters of seed in some areas with minimal seed in others. The resulted in intermittent seeding downstream in the measurement plane, and when the seed was present, it was usually grouped fairly close together. This is not ideal. Ideally, the seed is spaced uniformly throughout the measurement plane and with a minimum spacing of several pixels. However, a method by which to guarantee this for this specific experiment has not yet been developed. It remains a task for future work.

A.2. Quasi-one dimensional total pressure model

It would be particularly beneficial if pressure could be directly calculated from PIV measurements. Although it has been done, it adds additional complexity to an already difficult experiment. To date, there are two main methods, one involves the momentum equation while the other involves the Poisson equation. Both methods are summarized in Oudheusden [83].

Assuming constant density, the pressure gradient can be computed from the momentum equation using the Navier-stokes equations as Equation (A.1) [83]:

$$\nabla p = -\rho\left(\frac{D\boldsymbol{u}}{Dt} - \nu\nabla^2\boldsymbol{u}\right) \tag{A.1}$$

where $D\boldsymbol{u}/Dt$ is the acceleration of a fluid particle from a Lagrangian perspective, better known as the material acceleration. Liu, Katz [84] showed that in a high Reynolds number flow field located away from boundaries, the material acceleration is dominant and the viscous term, $\mu\nabla^2\boldsymbol{u}$, is negligible. Even considering this somewhat constrictive simplification, acquiring the particle accelerations typically require a multi-pulse (three or four) PIV system as Liu, Katz [84]. Following the acquisition of the velocity data, the pressure field can be calculated by spatial integration of the pressure gradient assuming an applicable pressure boundary condition value is known.

Gurka et al. [85] provided the initial framework for the Poisson method by illustrating how to use the velocity vector information to solve inversely the Navier-Stokes equation to provide the pressure gradient needed for the Neumann boundary condition. The velocity data could then be used again to solve the pressure Poisson equation, Equation (A.2), [83].

$$\nabla^2 p = -\rho\nabla\cdot(\boldsymbol{u}\cdot\nabla)\boldsymbol{u} \tag{A.2}$$

While some authors have directly solved the Poisson equation Fujisawa et al. [86], others have attempted to simplify it by reducing it to a two-dimensional problem while still trying to include three-dimensional effects de Kat et al. [87], de Kat, Oudheusden [88]. Although free of the time derivatives that complicate the momentum equation approach, the Poisson approach still requires either some leaping assumptions or volumetric PIV before pressure can be calculated. Additionally, appropriate boundary conditions are needed for the pressure calculation as they were for the momentum equation approach.

Regardless of the method chosen, both methods employ somewhat restrictive assumptions while requiring additional knowledge of boundary conditions, which may or may not be available for a given experiment. Add in the complexity of a multi-pulse or time resolved PIV system, coupled with recommended requirements on spatial and temporal resolution in general [88] and the result is an experimental method that may be possible, but not seemingly practical in many applications. Take into further consideration that PIV experiments in or around full-scale turbofan engines are already less than ideal and it is clear that there is a need for a simple method by which pressure can be approximated from PIV data.

Towards that end, an estimate for the total pressure ratio across the loss mechanism in the fan duct has been developed as a function of upstream total temperature, downstream velocity, and the specific heat ratio of the fluid. Future experiments may incorporate more variables into the calculation, should they be available. The assumptions made herein were made such that the estimation would be as robust as possible given the information available from the experiment.

From isentropic relations, one can relate total pressure, static pressure, total temperature, static temperature, and the specific heat ratio at a given location by

$$\frac{p_0}{p} = \left(\frac{T_0}{T}\right)^{\frac{\gamma}{\gamma-1}} \tag{A.3}$$

where γ is the specific heat ratio. If it is assumed that the medium is an ideal gas, and the total temperature, density, and specific heat are constant, then the previous form can be manipulated to relate two locations (upstream and downstream of the loss mechanism) as

$$\frac{p_{02}}{p_{01}} = \frac{T_2}{T_1}\left(\frac{T_1}{T_2}\right)^{\frac{\gamma}{\gamma-1}} = \left(\frac{T_1}{T_2}\right)^{\frac{1}{\gamma-1}} \tag{A.4}$$

T_1 and T_2 can be found using $T_0/T = 1 + u^2/2C_pT$ which can be rearranged (again assuming constant total temperature) to the forms

$$T_2 = T_{01} - u_2^2\left(\frac{\gamma-1}{2\gamma R}\right) \qquad T_1 = T_{01} - u_1^2\left(\frac{\gamma-1}{2\gamma R}\right) \tag{A.5}$$

where R is the gas constant of the medium. The final pair of assumptions involve treating the upstream fluid as one of uniform total temperature and velocity. Furthermore, at some location in the measurement (downstream) plane, there are fluid particles largely

unaffected by the loss mechanism and wall boundaries and are traveling at the same velocity in the measurement plane as they were in the upstream plane ($u_2 = u_1$). By doing so, it is possible to calculate the total pressure ratio of the PIV measurement region to the assumed uniform inflow region as a function of the measured velocities (u_2), a measured total temperature (either in the upstream or measurement region, T_{01} or T_{02}), and the specific heat and gas constant of the fluid. The final relation is given in Equation (A.6):

$$\frac{p_{02}}{p_{01}} = \left(\frac{T_{01} - \frac{\gamma - 1}{2\gamma R} u_1^2}{T_{01} - \frac{\gamma - 1}{2\gamma R} u_2^2} \right)^{\frac{1}{\gamma - 1}} \tag{A.6}$$

This simple approach allows for qualitative and quantitative insight into the effect of the loss mechanism on the total pressure in the measurement region. However, it does not account for the mass flow through the region and is therefore limited to providing total pressure information solely on a point by point basis. In order to calculate a representative total pressure loss for the entire measurement region, a mass average can be calculated as

$$p_{0\,Avg} = \frac{\sum p_{0i} \dot{m}_i}{\sum \dot{m}_i} = \frac{\sum p_{0i} (\rho u A)_i}{\sum (\rho u A)_i} = \frac{\sum p_{0i} u_i}{\sum u_i} \tag{A.7}$$

where ρ and A are assumed constant. The total pressure loss in the measurement region caused by the loss mechanism can then be characterized by a single value.

The quasi-one dimensional total pressure model was applied to both the experimental and computational results, at the idle and 80% CFS test cases. Additionally, the computational results will allow for a rough assessment of the assumptions made while also providing a downstream pressure field to compare the model to.

First the assumption regarding constant total temperature was analyzed and the ratio of the downstream total temperature to the upstream total temperature is shown in Figure 83 and Figure 84. Less than a 1% error can be observed. Second, Figure 85 and Figure 86 portray the ratio of the downstream velocity to the upstream velocity. Clearly here there are regions in which errors exist that are greater than 10%. However, the method selects a 'freestream value' to use as its representative upstream velocity. So if a region such as location 1 and location 2 illustrated in Figure 85 and Figure 86, then the error is only about 4% - 5%.

It is important to note that the CFD is not without its own assumptions. These were described in Section 5.4, but the most impactful is likely the assumption of uniform inflow. The validity of such an assumption could obviously have a sizable impact on how the flow interacts with downstream geometric features. For now, however, the assumption was a necessary boundary condition to simplify the model. Overall, the assumption of constant temperature and constant velocity in the freestream are fair assumptions based on the results of CFD simulations. Additionally, unlike the sampling error analysis (Chapter 3) where the CFD solution was a synthetic flow and was therefore held as the true solution, in this case the CFD is a prediction just as the quasi-one dimensional model is. Therefore, the proceeding analysis will treat the CFD solution as a second measurement rather than as the known solution.

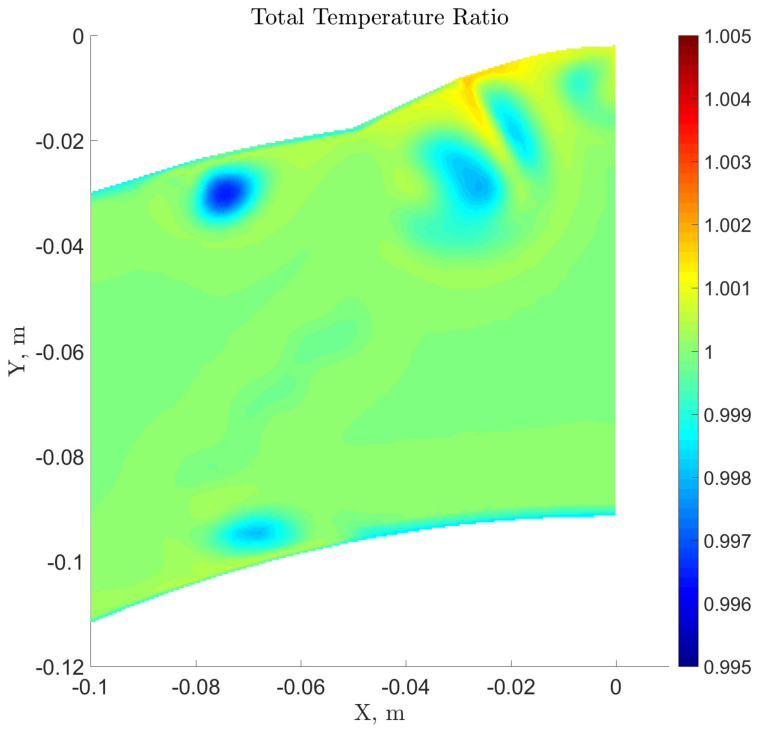

Figure 83 – Total temperature ratio, CFD 80% CFS

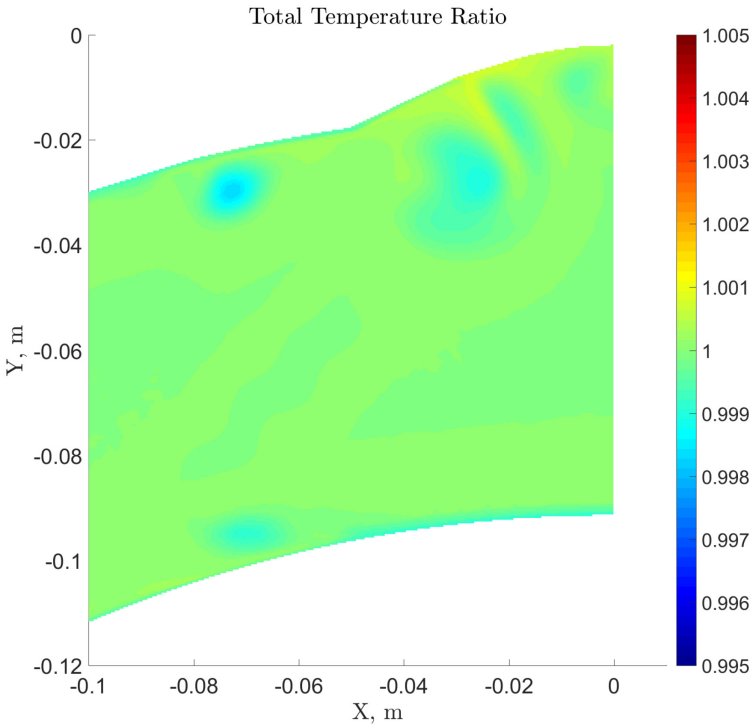

Figure 84 – Total temperature ratio, CFD Idle

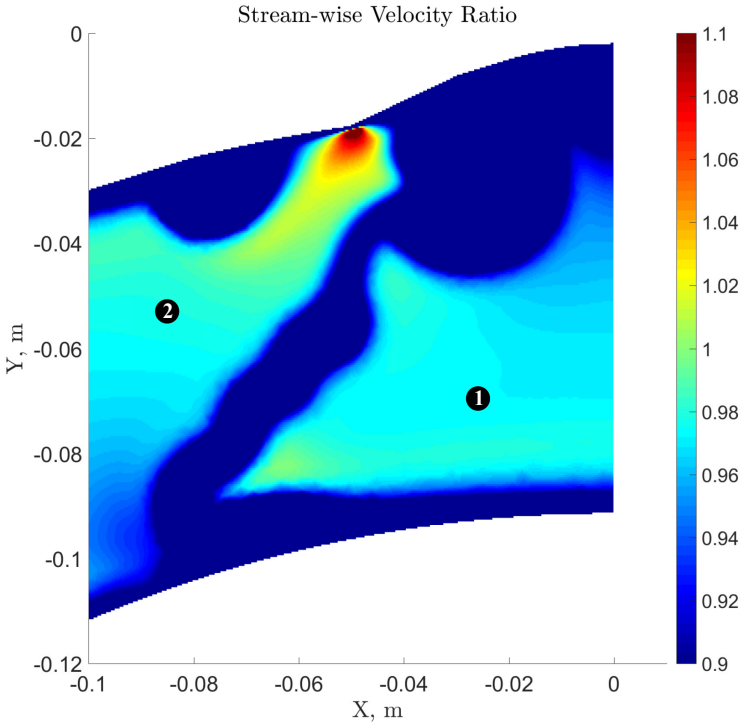

Figure 85 – Stream-wise velocity ratio, CFD 80% CFS

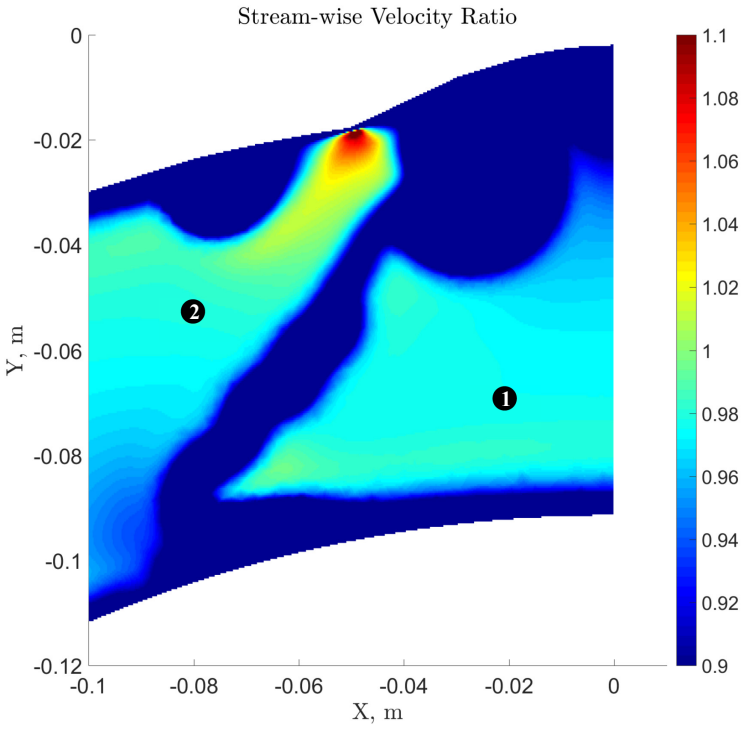

Figure 86 – Stream-wise velocity ratio, CFD Idle

Figure 87 shows the total pressure at the measurement plane as calculated by the CFD model. Similarly, Figure 88 shows the total pressure at the measurement plane as calculated by the quasi-one dimensional model when applied to the CFD measurement plane velocities and upstream boundary conditions. The estimates appear to be fairly close, but the quasi-one dimensional model seems to under predict the maximum deficit in each of the wake structures when compared with the CFD calculation. Figure 89 shows the absolute error of the quasi-one dimensional model's calculation compared to the CFD's calculation. It is clear the error is highest in the regions with the largest deficits. However, the error is never larger than about 5%.

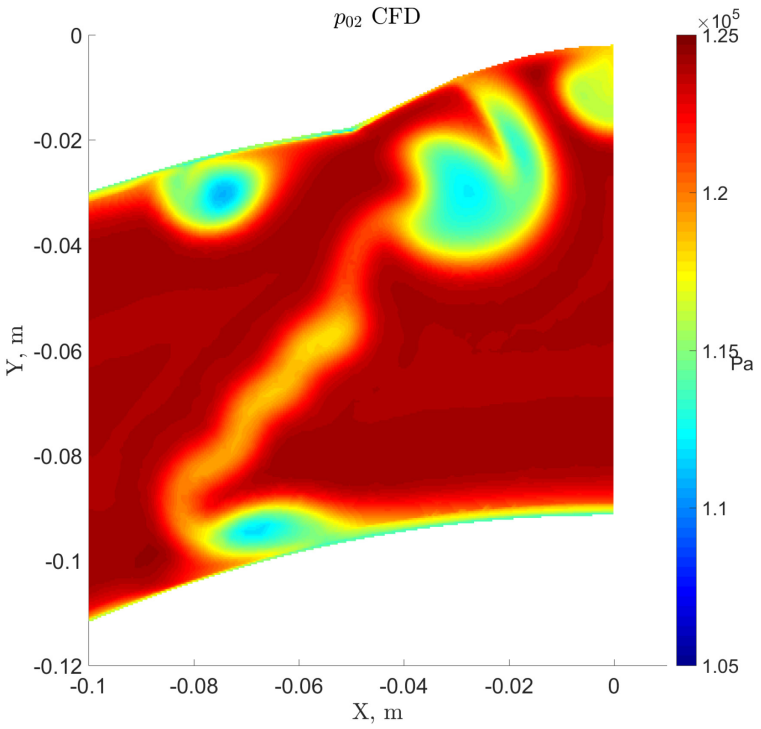

Figure 87 – Downstream total pressure, CFD 80% CFS

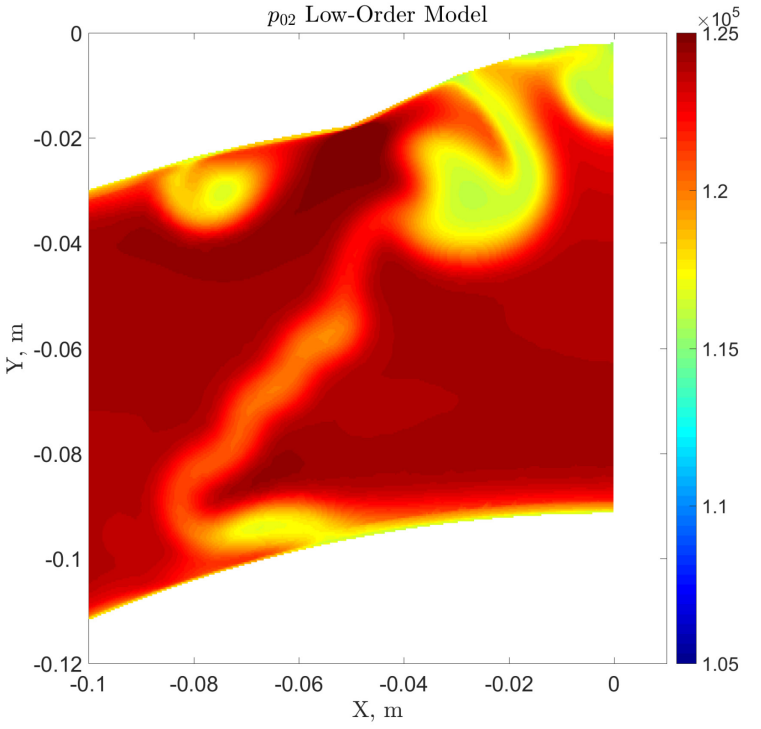

Figure 88 – Downstream total pressure, quasi-one dimensional model applied to CFD 80% CFS

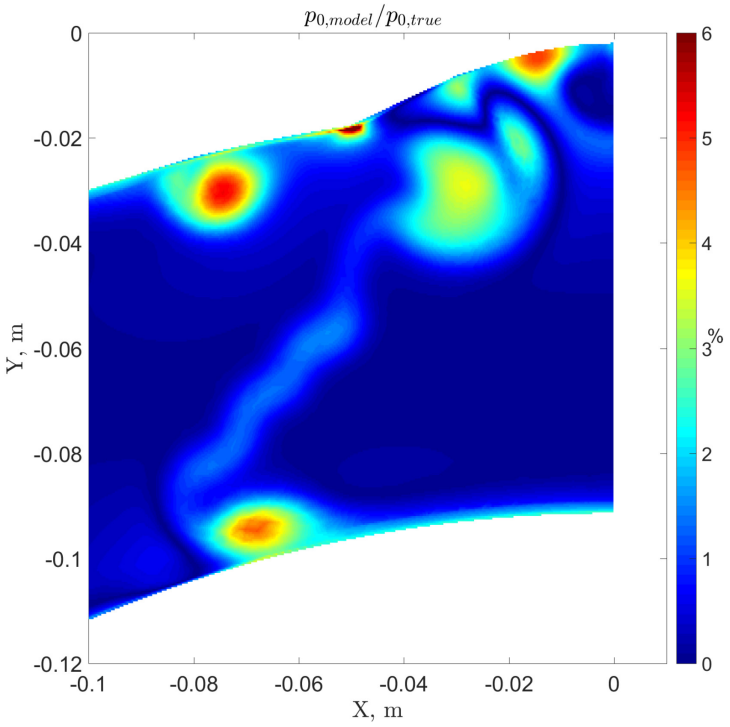

Figure 89 – Downstream total pressure error, quasi-one dimensional model and CFD 80% CFS

Figure 90 and Figure 91 portray the estimated total pressure ratio from the upstream location to the measurement plane based on the CFD data and the PIV data respectively. Although the magnitudes of the deficits appear to be fairly close, the largest differences stem back to the prediction and measurement of the size and locations of the various wake structures. Similar trends were observed for the idle fan speed case.

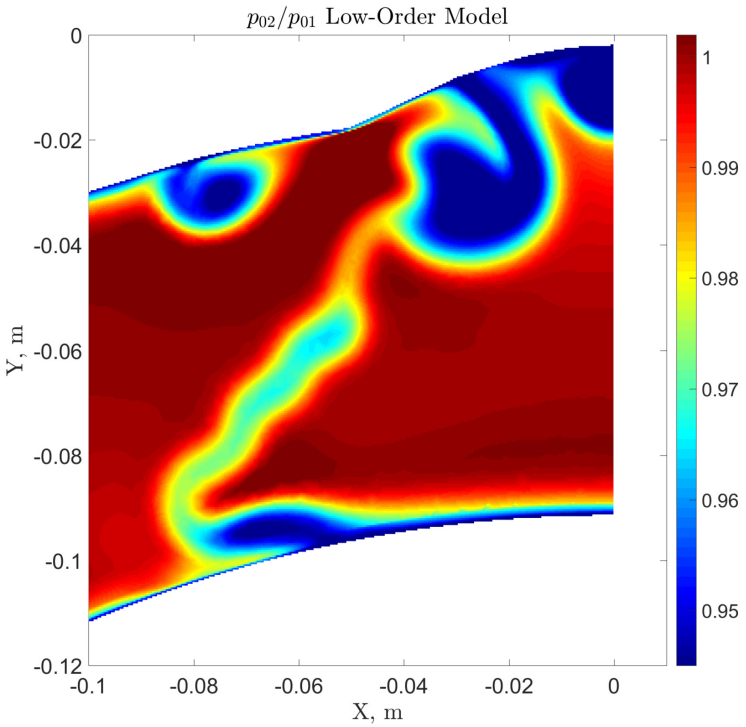

Figure 90 – Total pressure ratio, quasi-one dimensional model applied to CFD 80% CFS

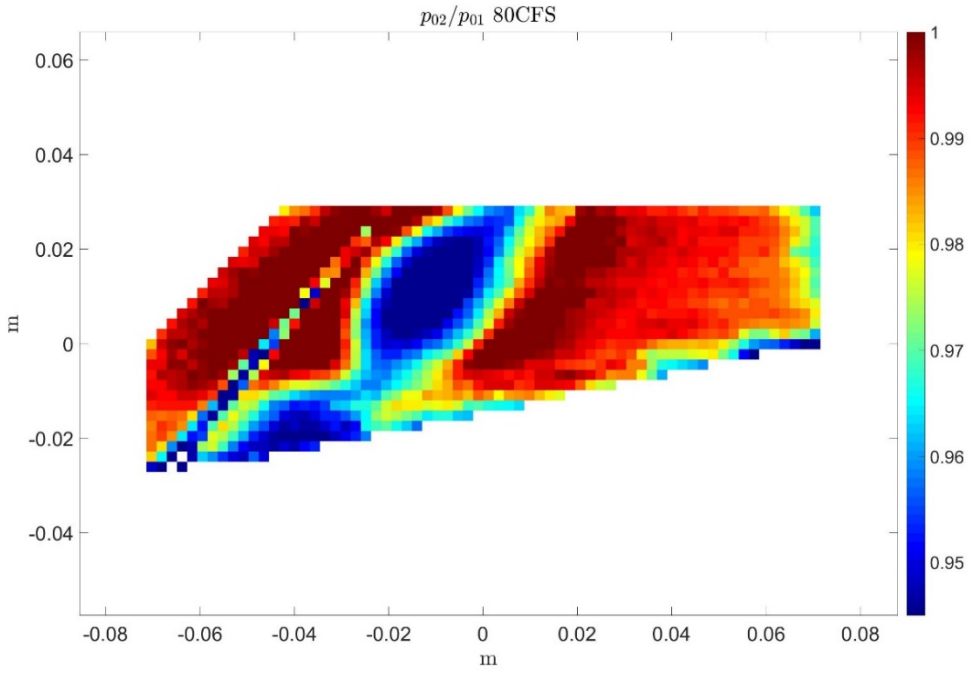

Figure 91 – Total pressure ratio, low order model applied to PIV data 80% CFS

For a more quantitative analysis, the mass average of the total pressure was calculated. The percent total pressure loss was then calculated by taking the ratio of the downstream to the upstream mass averaged total pressure value. The loss estimate % error was then calculated as the absolute difference between the CFD and quasi-one dimensional model total pressure loss estimation normalized by the CFD total pressure loss estimation. This conveys the same idea illustrated by Figure 87 and Figure 88, that the quasi-one dimensional model was under predicting the total pressure deficit when compared with the CFD estimation. Because the mass average value represents the value over the entire measurement region, and because of the poor overlap in data between the CFD and the PIV experimental results, a comparison in mass averaged total pressure loss would not be justified. However, Table 11 provides the mass averaged total pressure loss for the PIV data for potential future reference.

Table 10 – Measurement region mass averaged percent total pressure loss

Fan Speed	CFD	Quasi-1D Model	Loss estimate % error
Idle (35%CFS)	0.61%	0.50 %	18.3 %
80% CFS	1.26 %	0.90 %	29.0 %

Table 11 – Experimental measurement region mass averaged total pressure loss

Fan Speed	PIV Experiment
Idle (35% CFS)	0.2 %
60% CFS	0.6 %
70% CFS	1.1 %
80% CFS	1.2 %

Overall, the quasi-one dimensional total pressure model estimated values within reasonable proximity to those estimated by the CFD. The assumptions made are undoubtedly limiting though, and it is recommended that this model is used primarily as a qualitative analysis too.

A.3. Additional Results

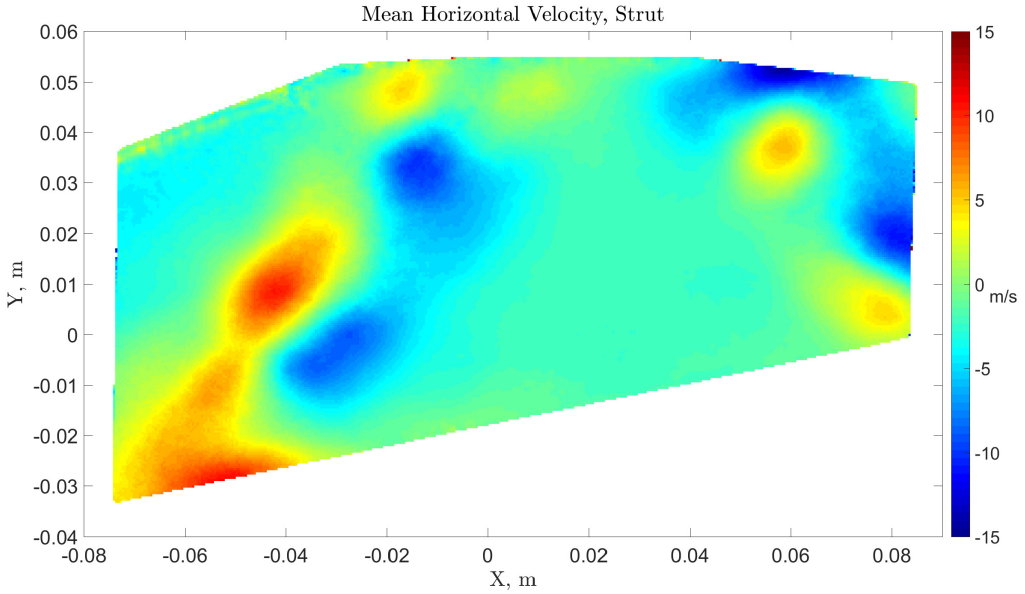

Figure 92 – PIV horizontal velocity component, simulated engine with strut

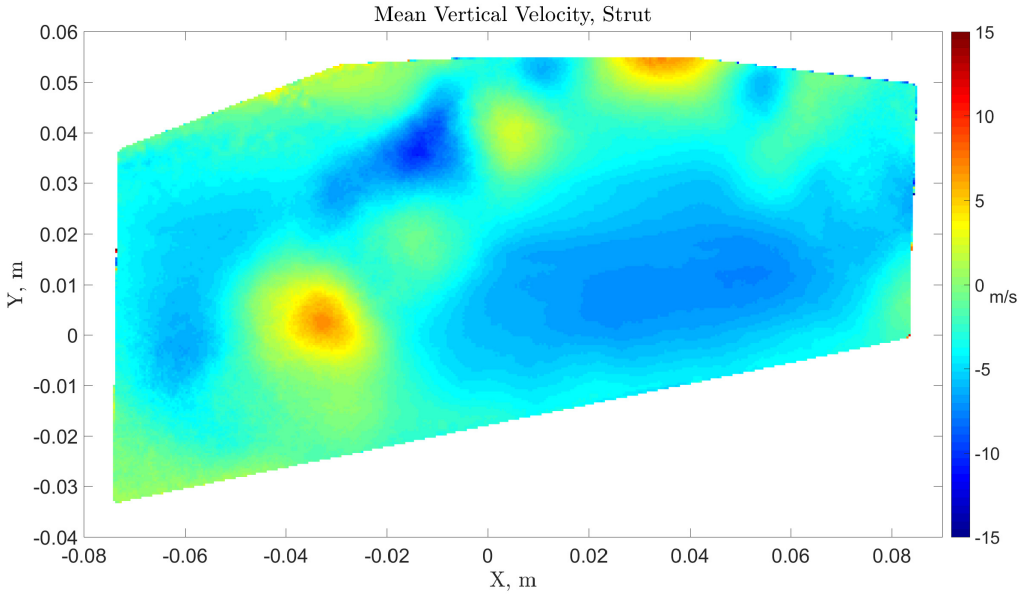

Figure 93 – PIV vertical velocity component, simulated engine with strut

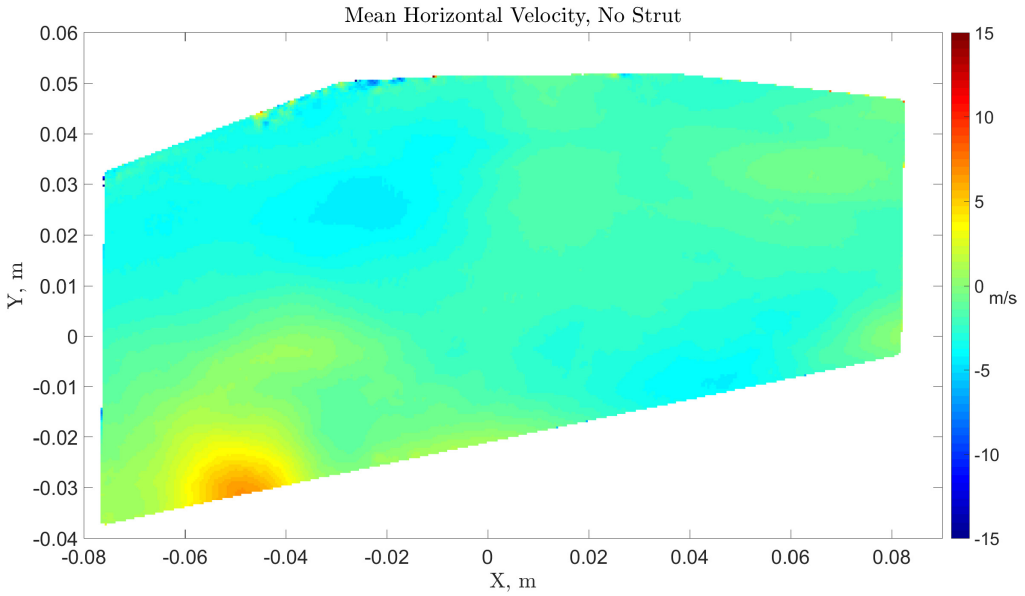

Figure 94 – PIV horizontal velocity component, simulated engine without strut

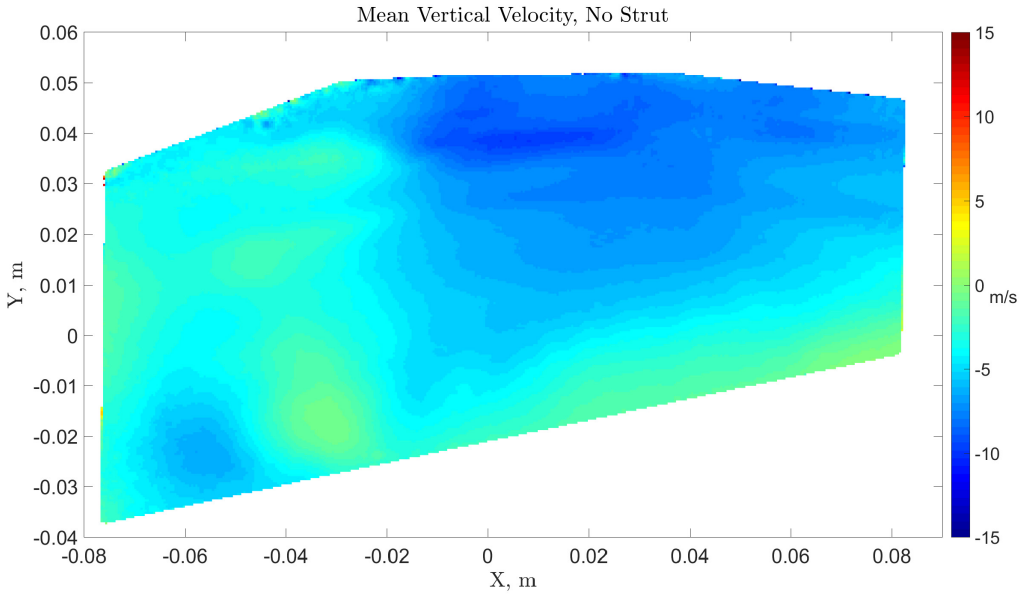

Figure 95 – PIV vertical velocity component, simulated engine without strut

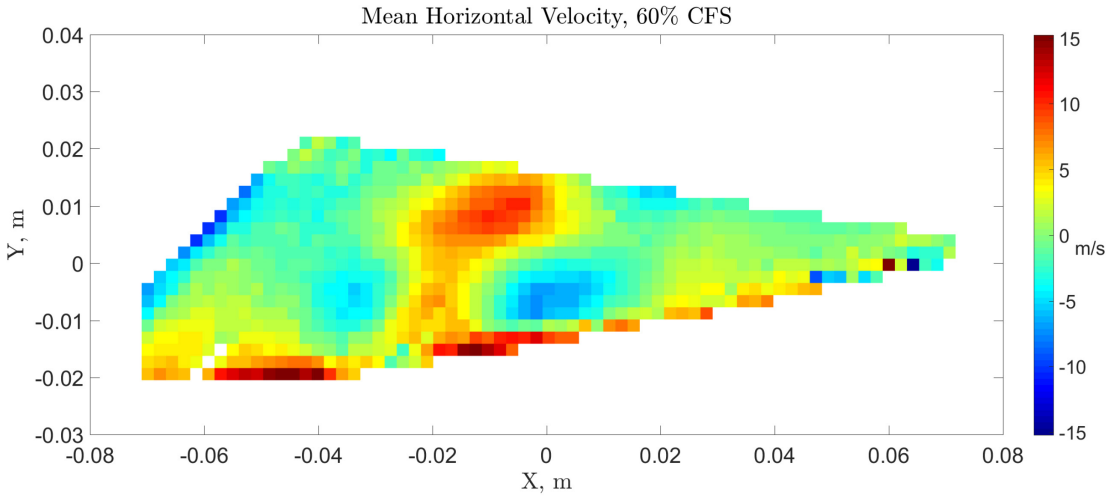

Figure 96 – PIV horizontal velocity component, 60% CFS

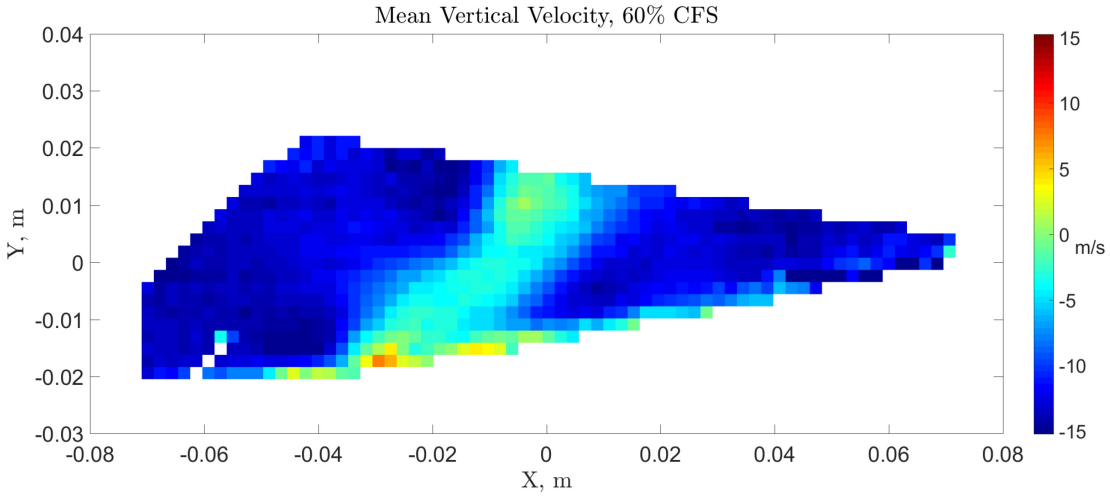

Figure 97 – PIV vertical velocity component, 60% CFS

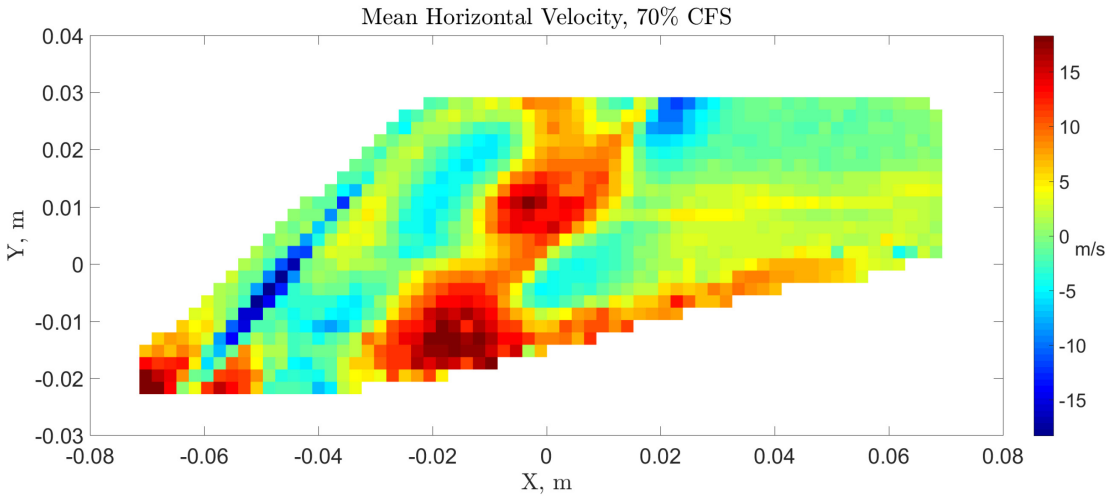

Figure 98 – PIV horizontal velocity component, 70% CFS

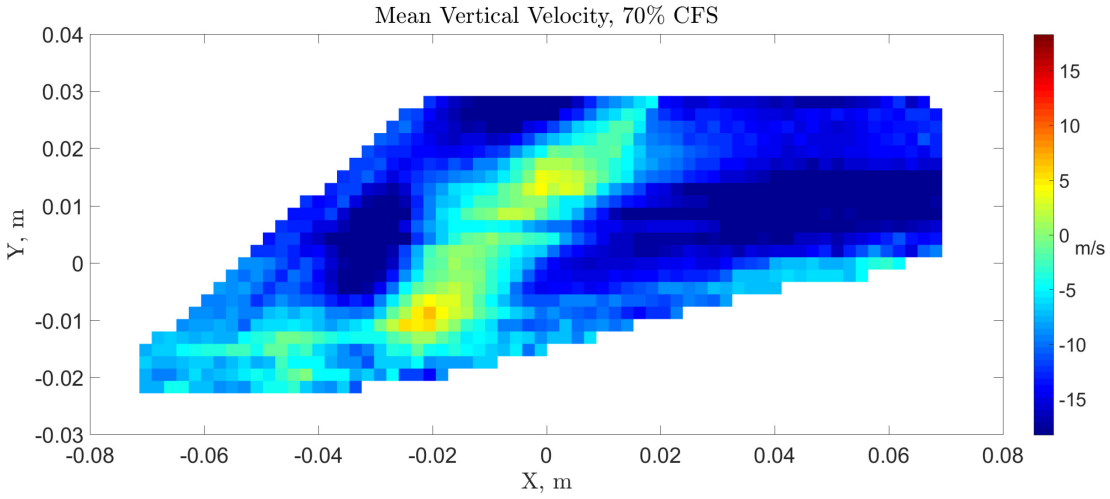

Figure 99 – PIV vertical velocity component, 70% CFS

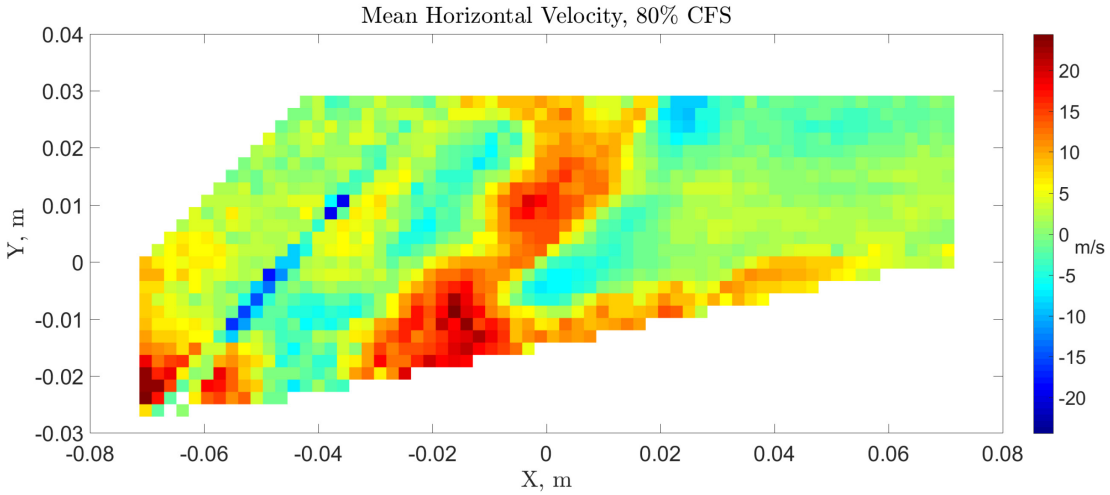

Figure 100 – PIV horizontal velocity component, 80% CFS

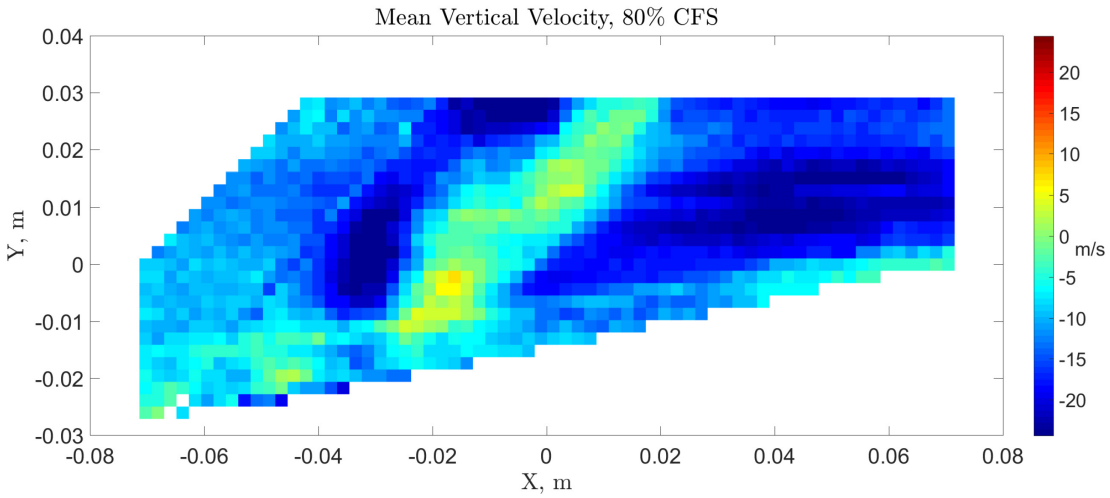

Figure 101 – PIV vertical velocity component, 80% CFS

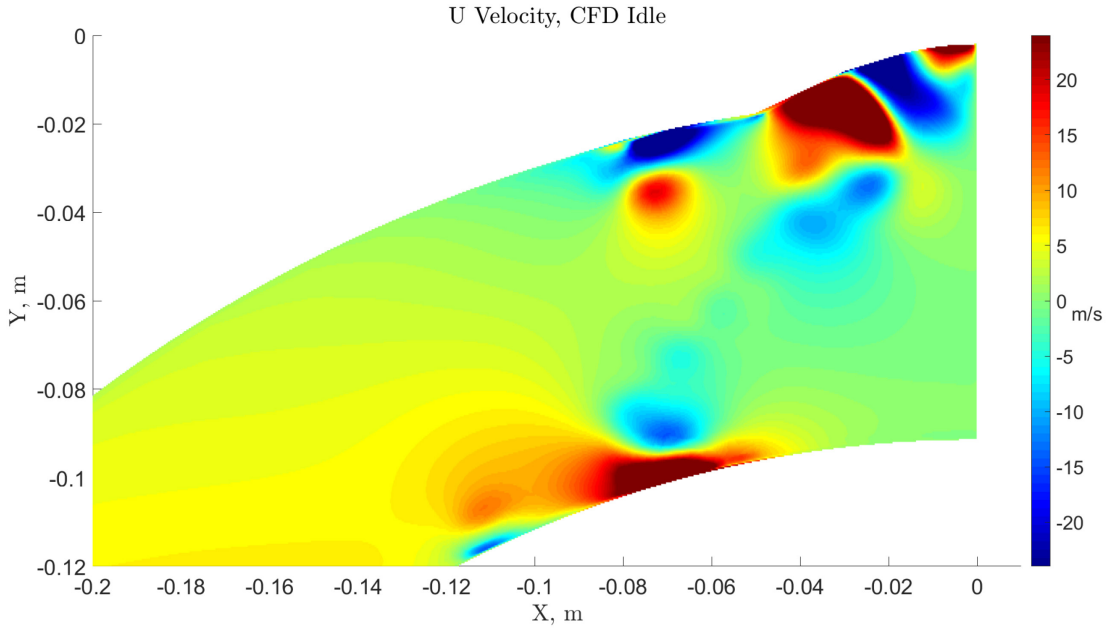

Figure 102 – PIV vertical velocity component, 80% CFS

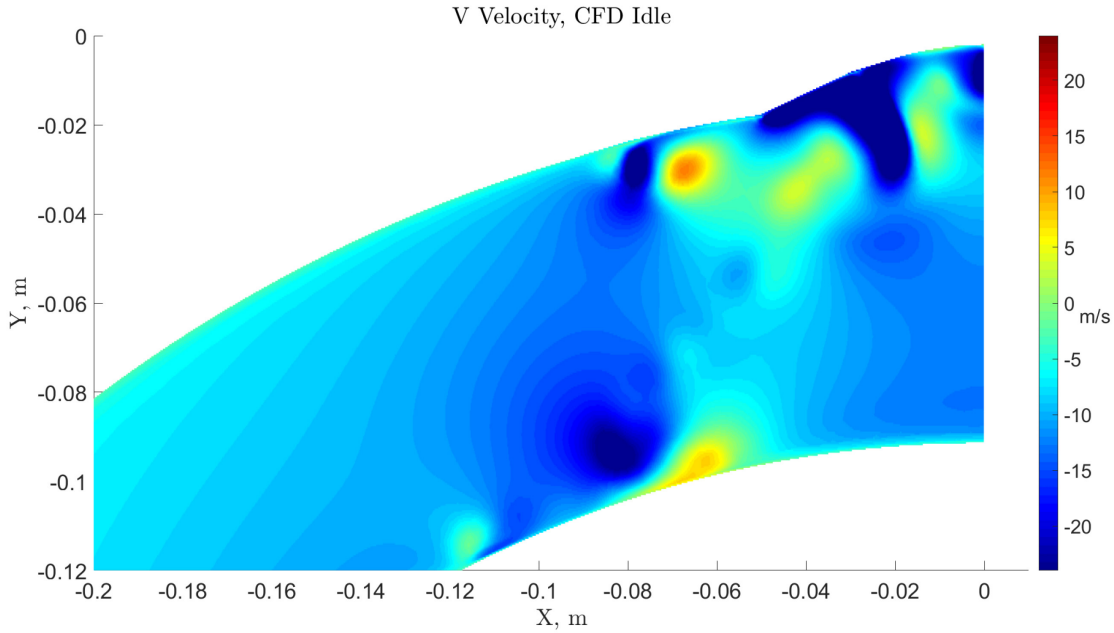

Figure 103 – PIV vertical velocity component, 80% CFS

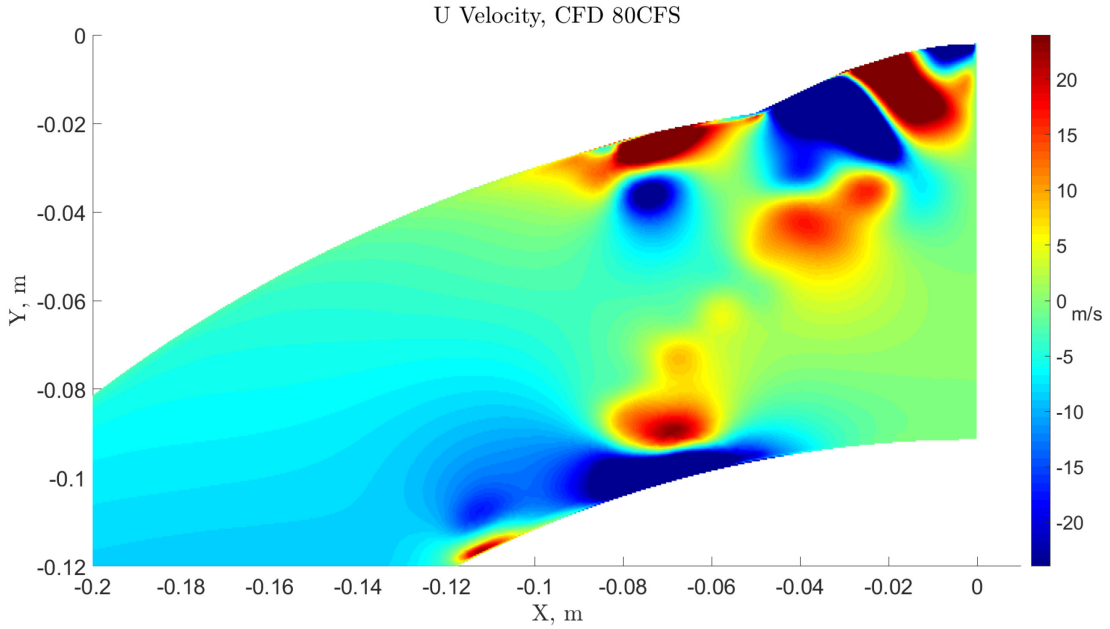

Figure 104 – PIV vertical velocity component, 80% CFS

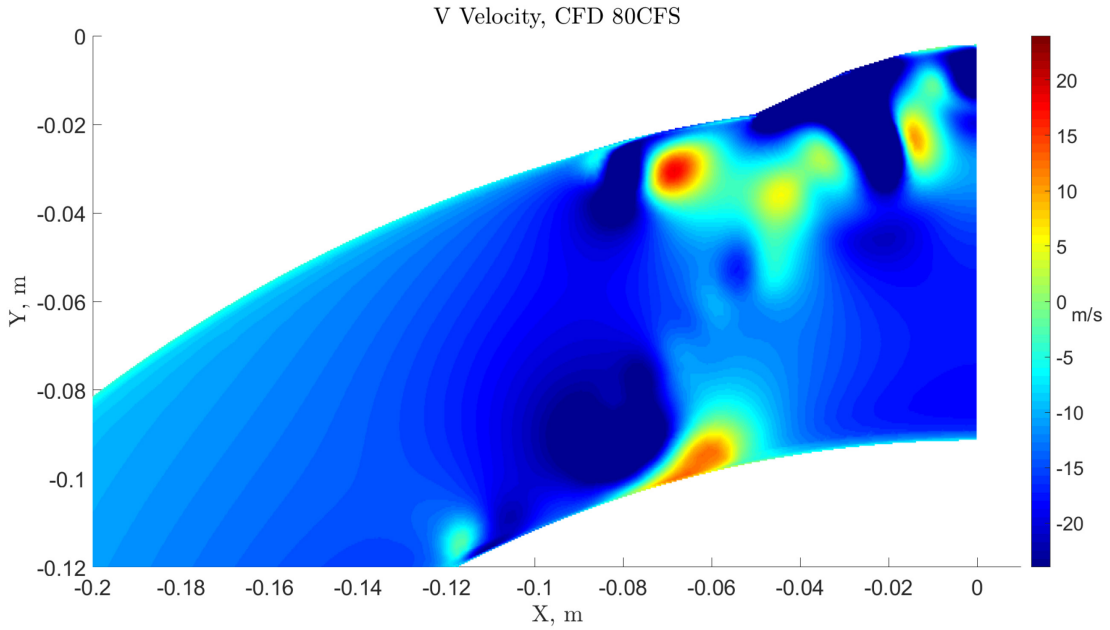

Figure 105 – PIV vertical velocity component, 80% CFS

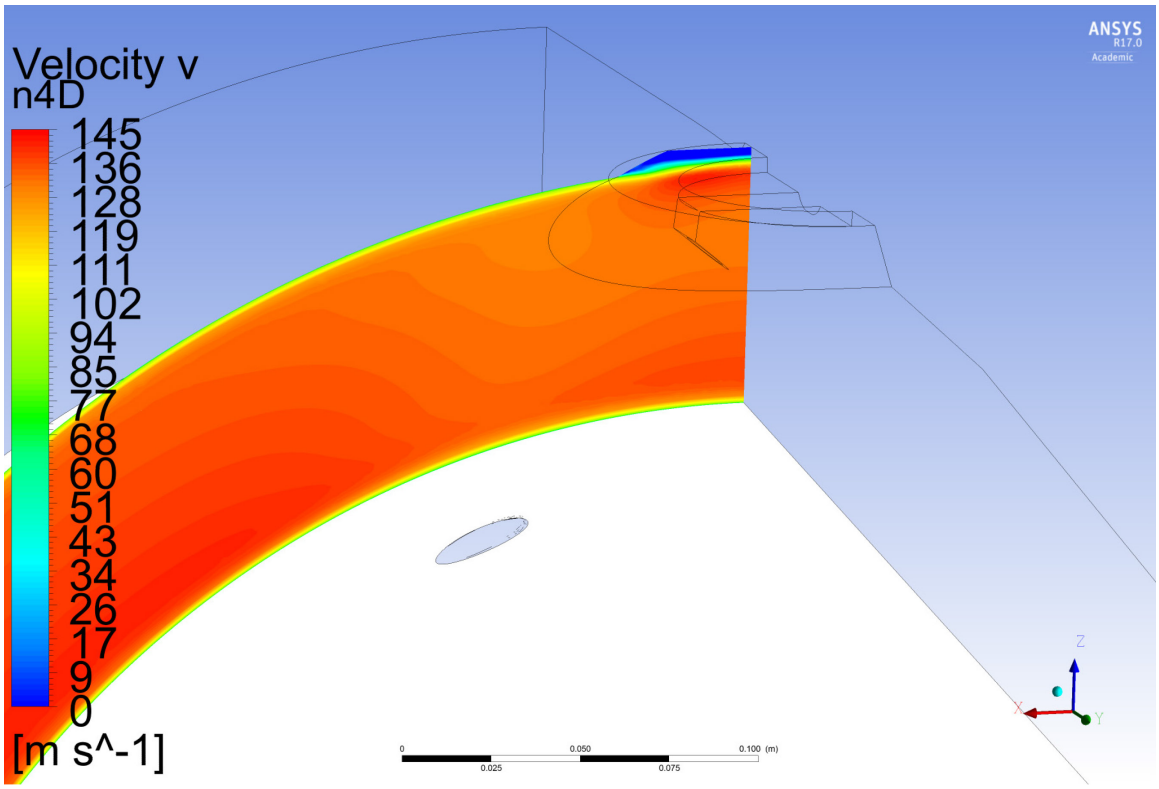

Figure 106 – Computational stream-wise velocity at -4D, 80% CFS

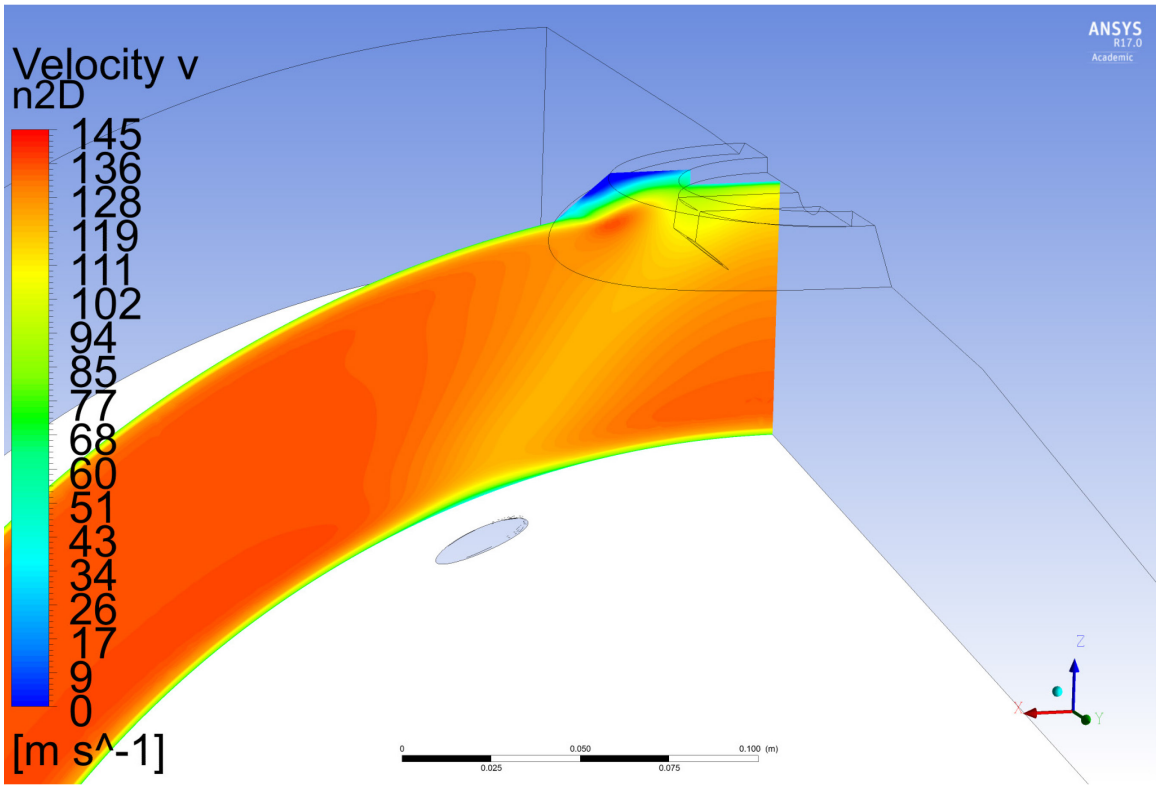

Figure 107 – Computational stream-wise velocity at -2D, 80% CFS

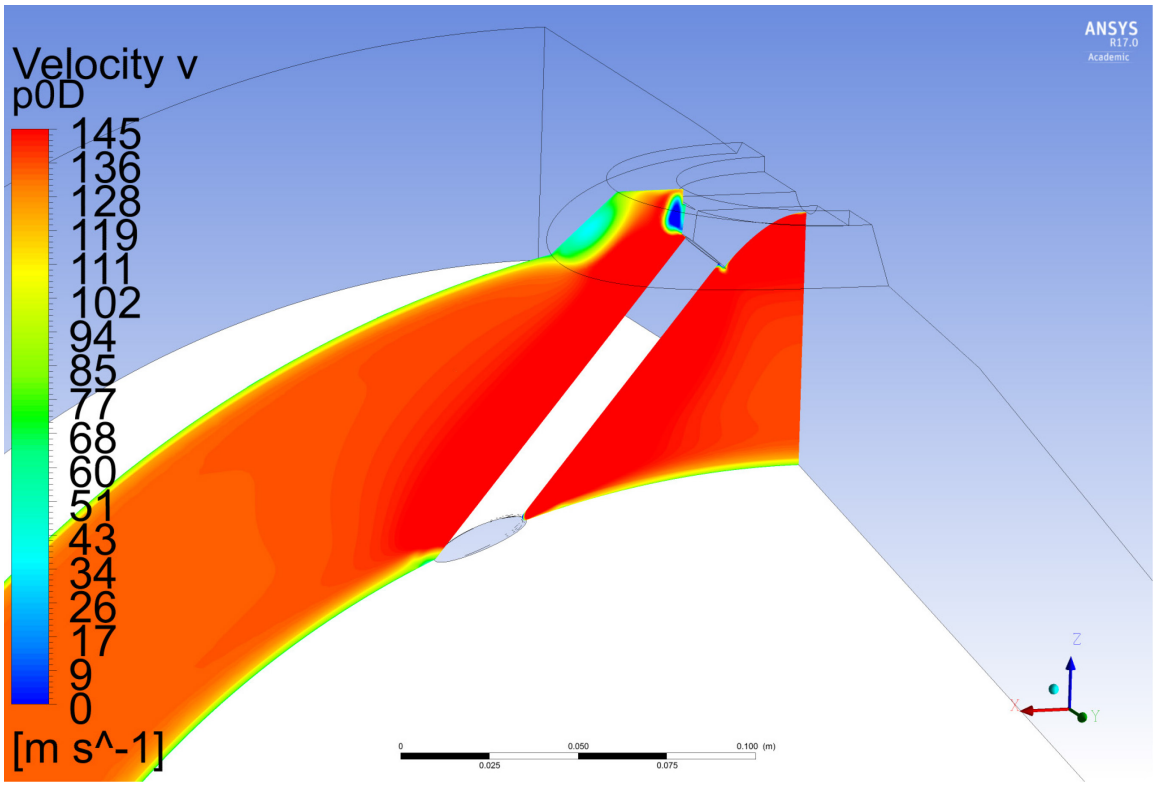

Figure 108 – Computational stream-wise velocity at 0D, 80% CFS

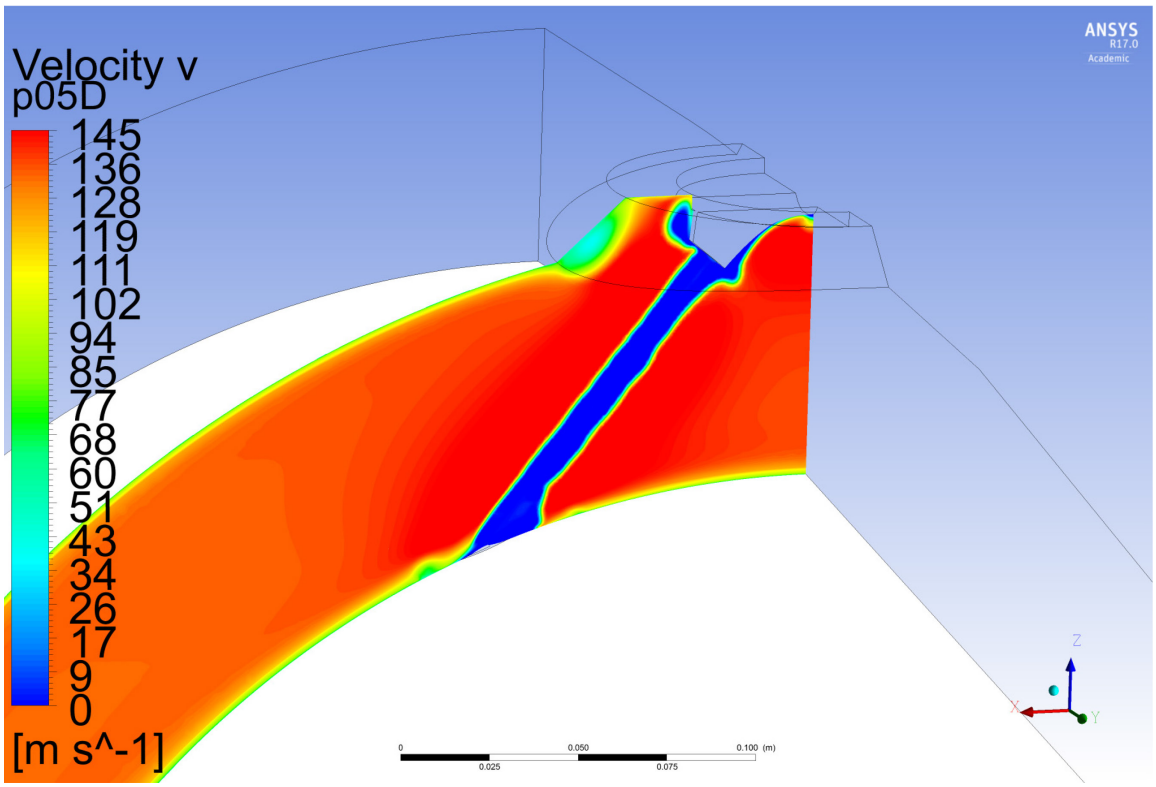

Figure 109 – Computational stream-wise velocity at 0.5D, 80% CFS

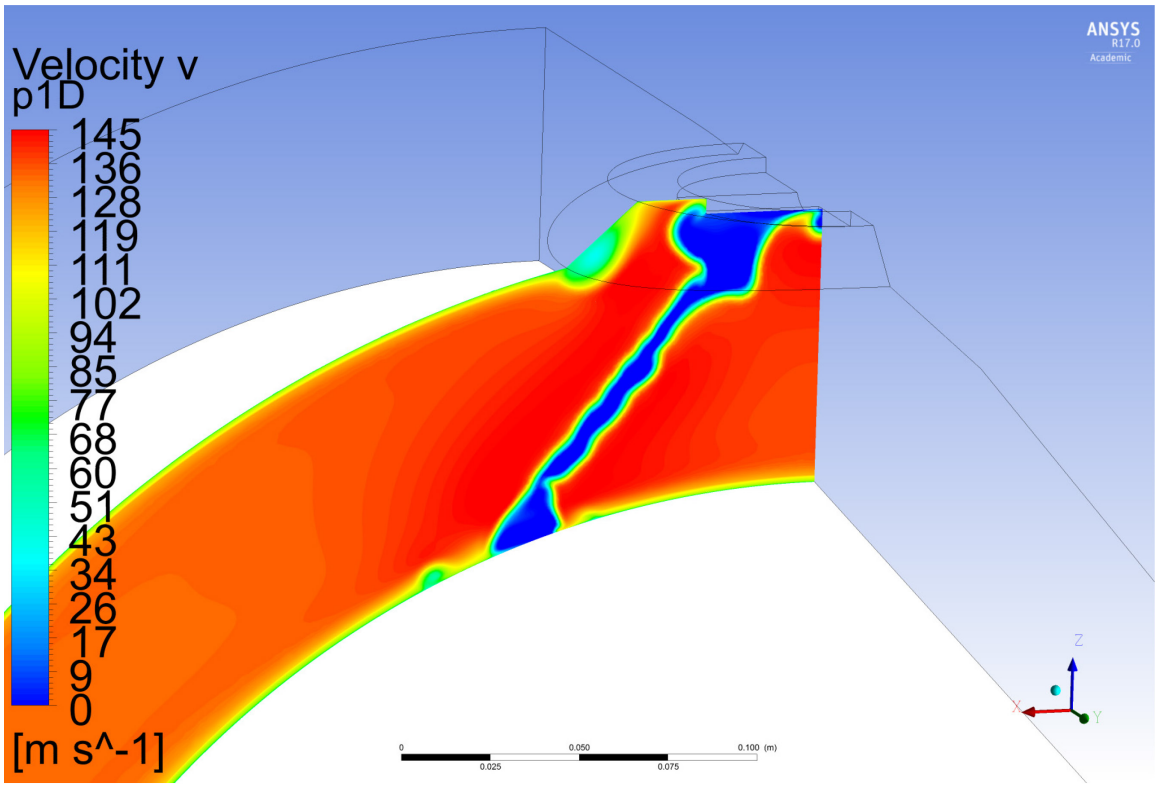

Figure 110 – Computational stream-wise velocity at 1D, 80% CFS

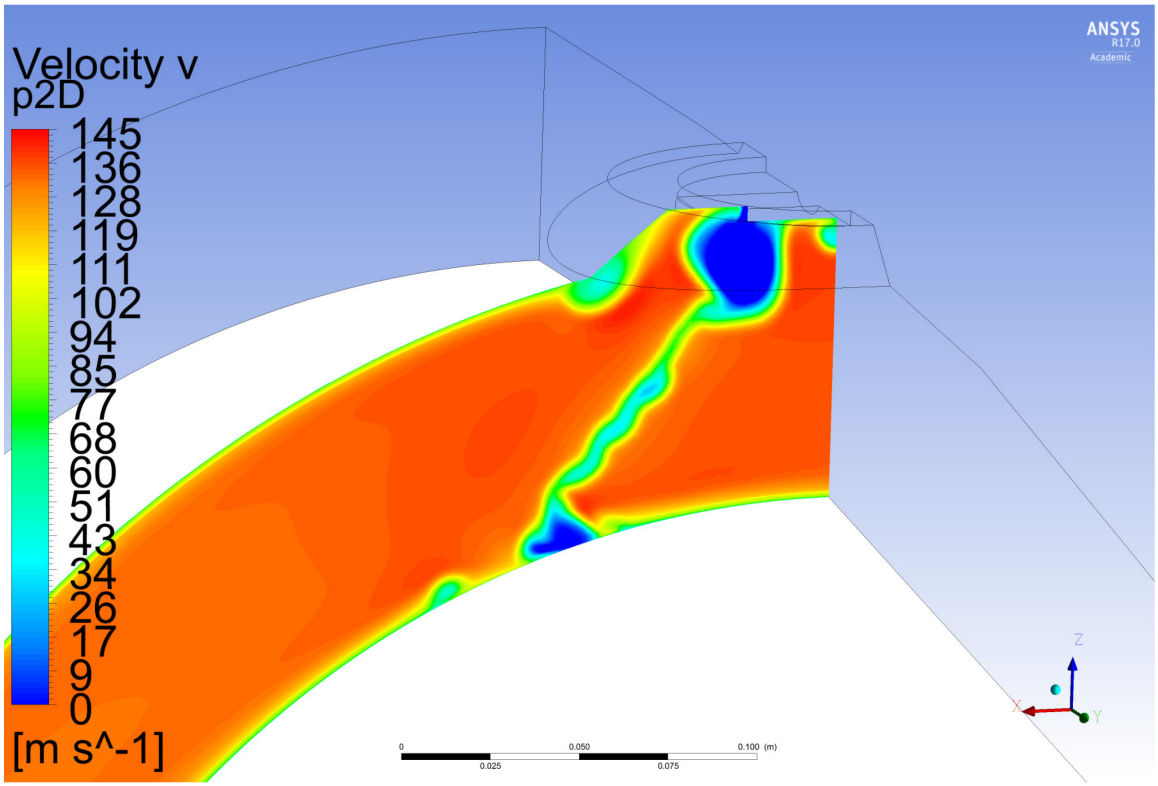

Figure 111 – Computational stream-wise velocity at 2D, 80% CFS

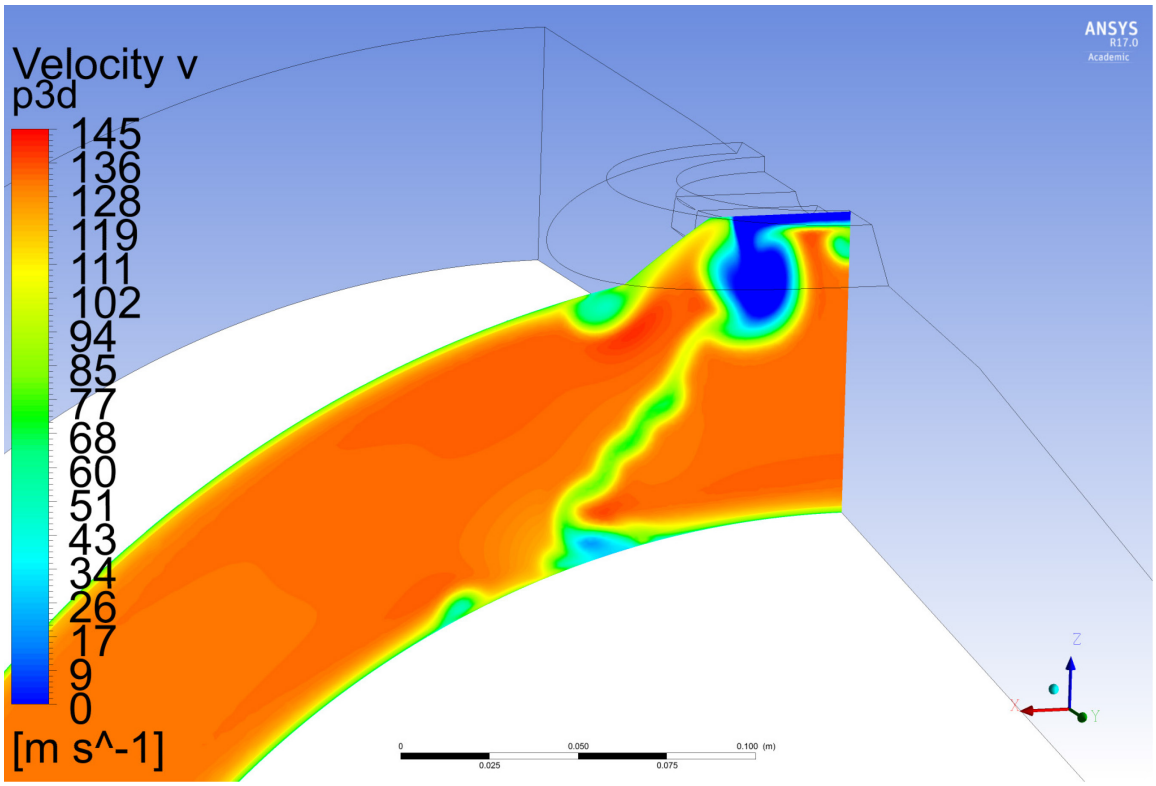

Figure 112 – Computational stream-wise velocity at 3D, 80% CFS

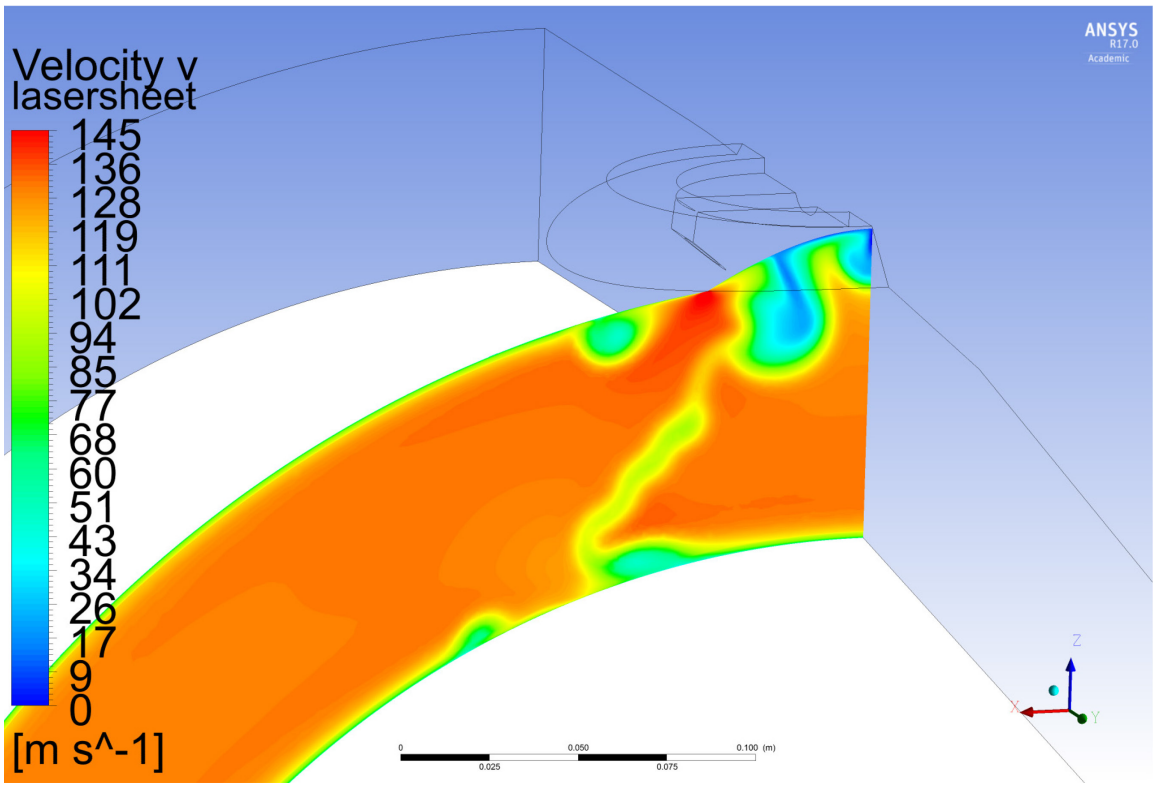

Figure 113 – Computational stream-wise velocity at 4.5D, 80% CFS

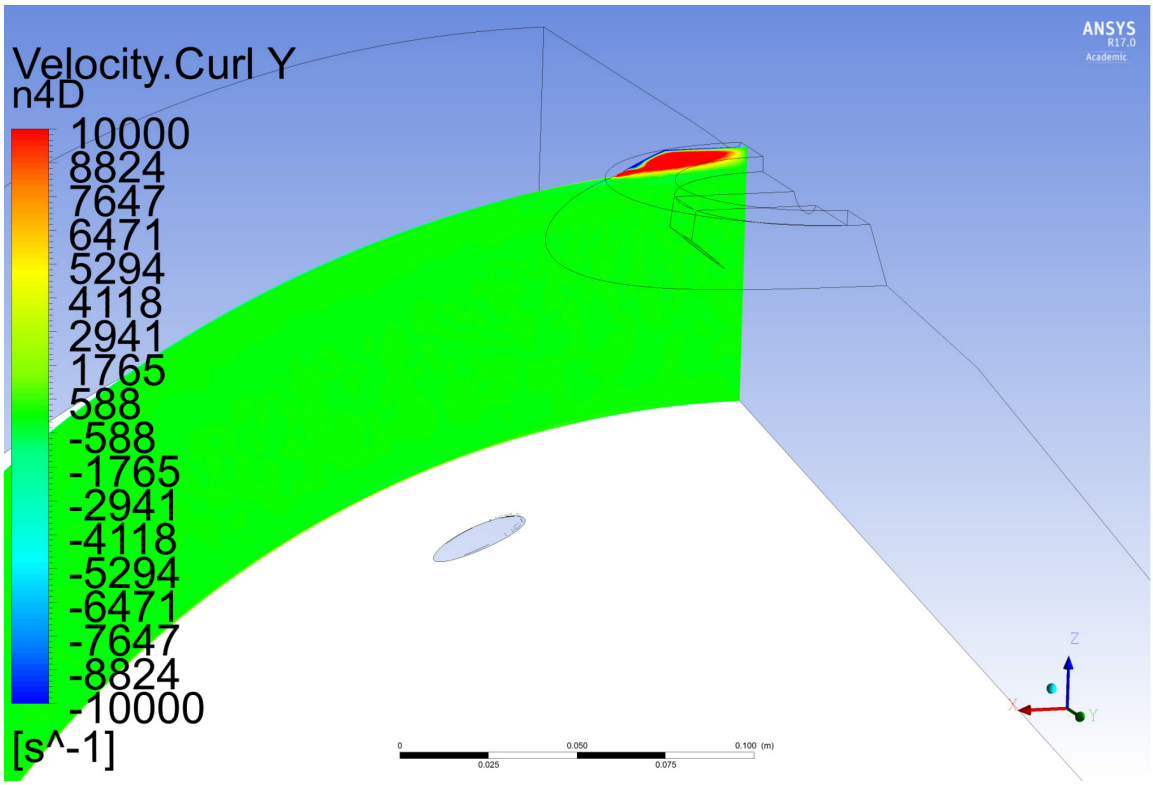

Figure 114 – Computational stream-wise vorticity at -4D, 80% CFS

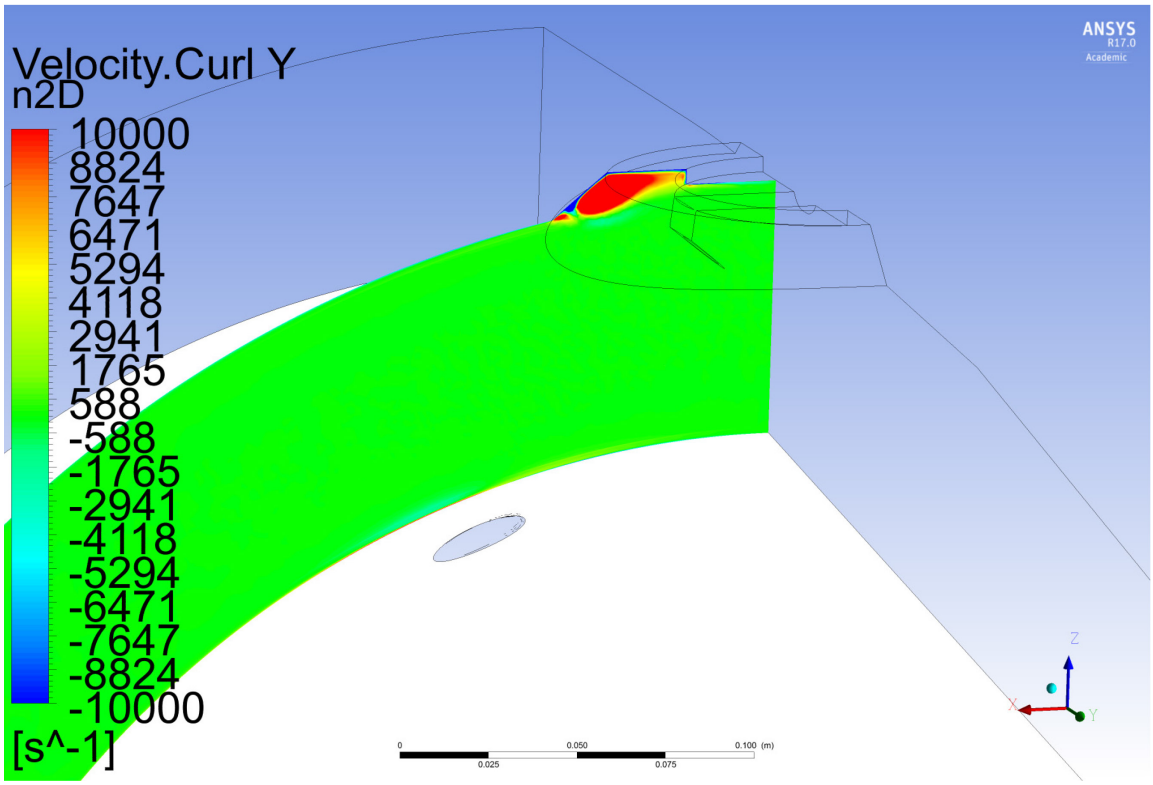

Figure 115 – Computational stream-wise vorticity at -2D, 80% CFS

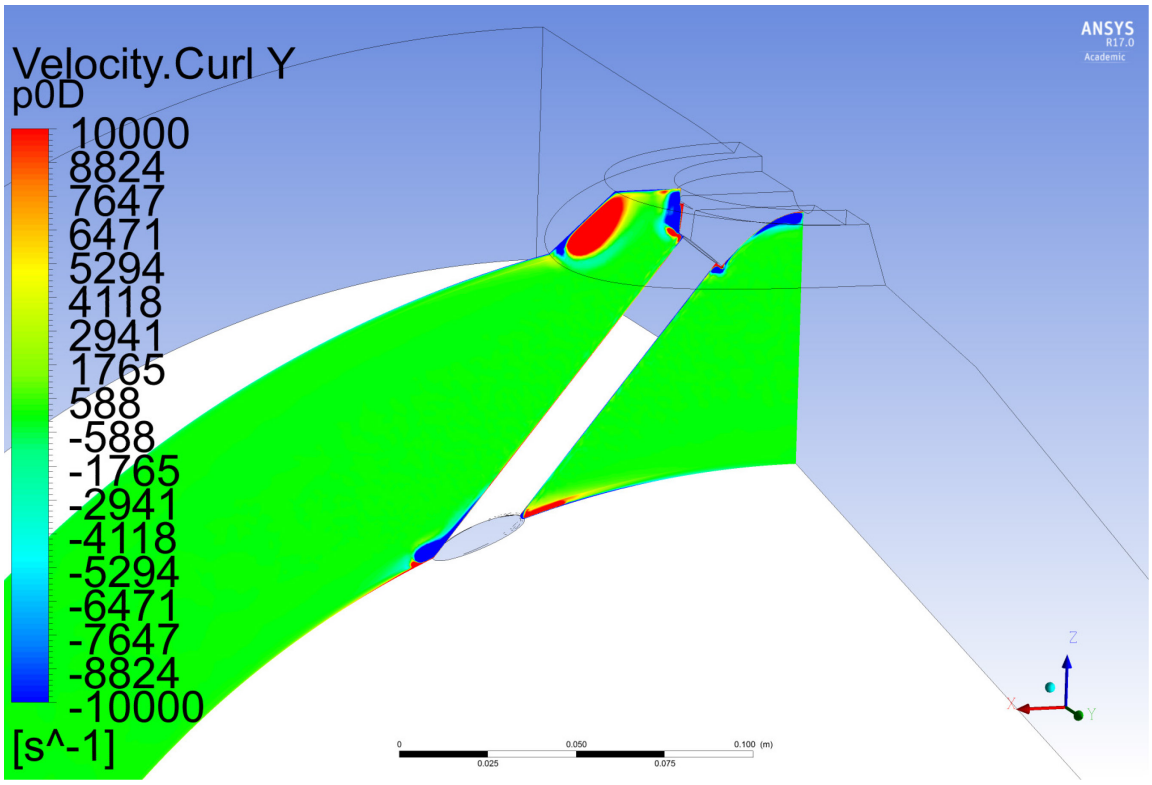

Figure 116 – Computational stream-wise vorticity at 0D, 80% CFS

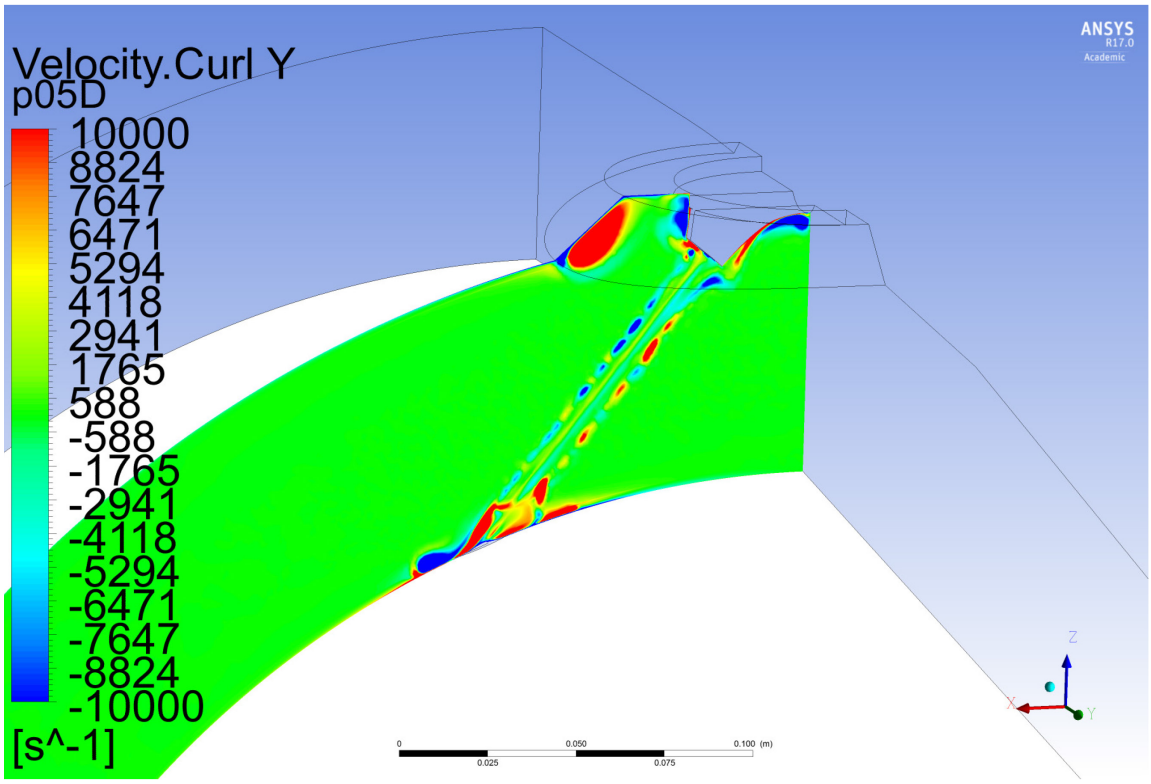

Figure 117 – Computational stream-wise vorticity at 0.5D, 80% CFS

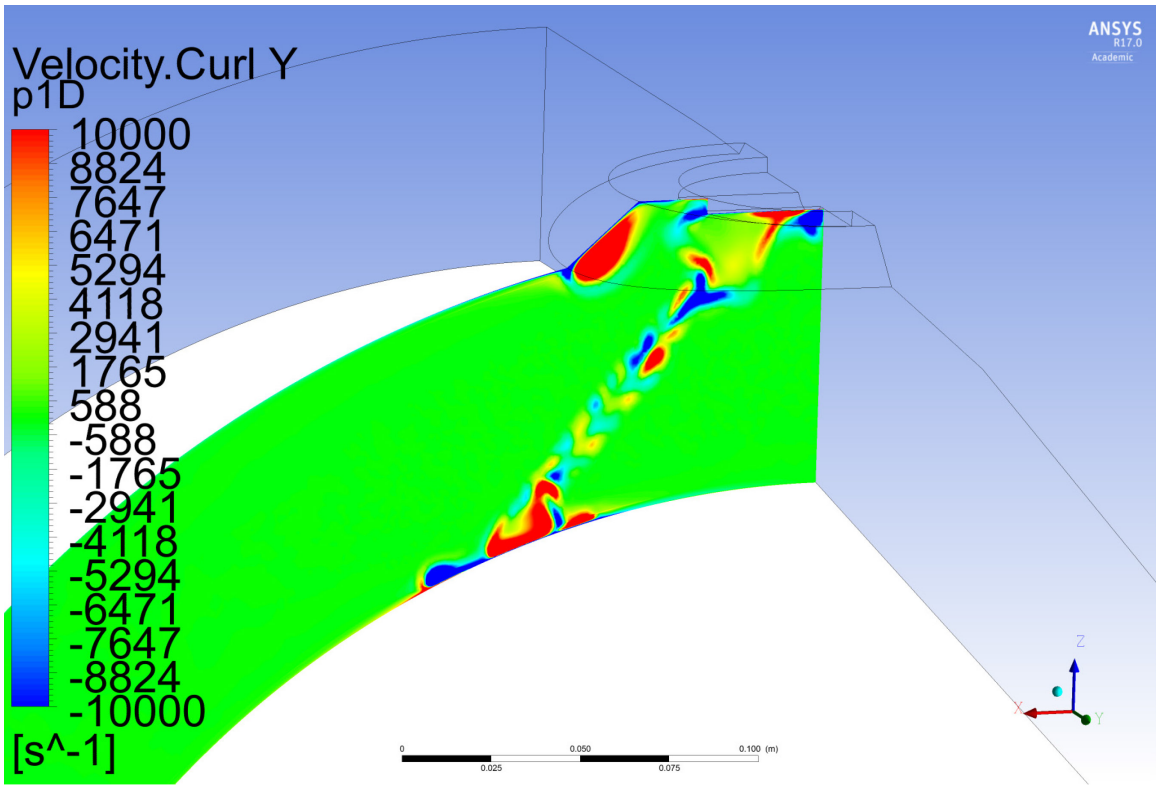

Figure 118 – Computational stream-wise vorticity at 1D, 80% CFS

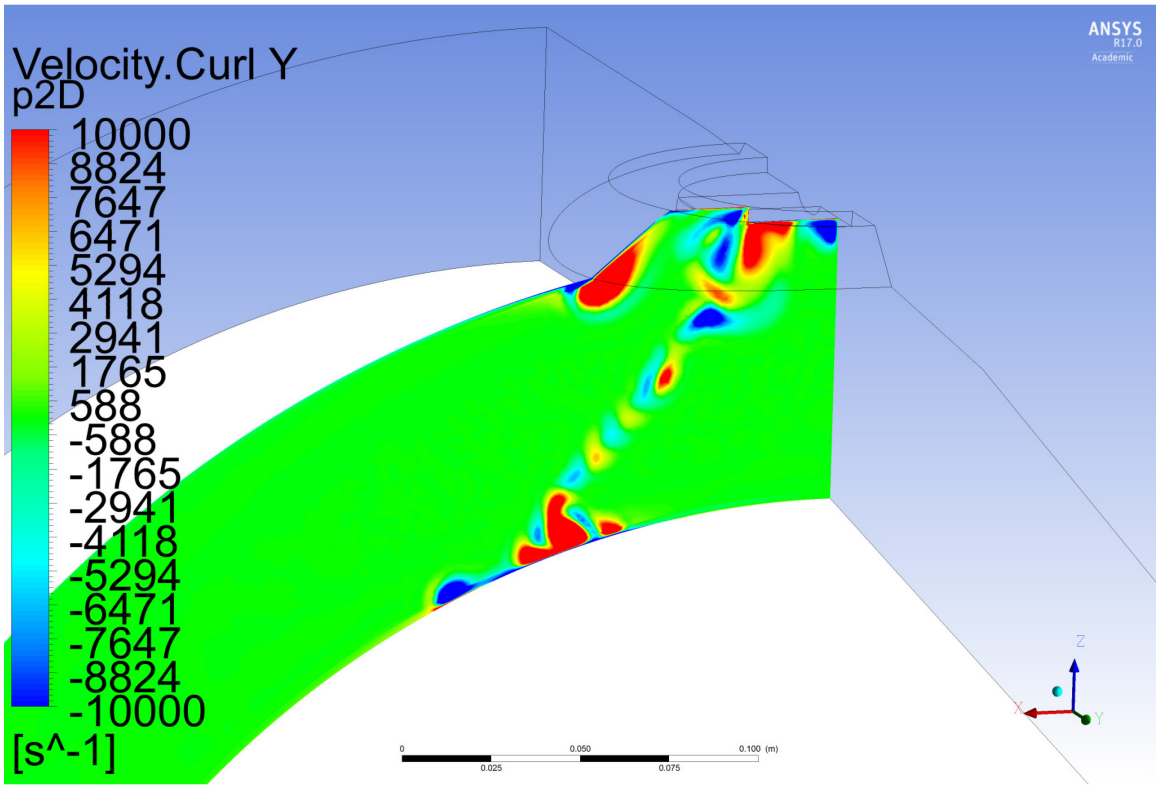

Figure 119 – Computational stream-wise vorticity at 2D, 80% CFS

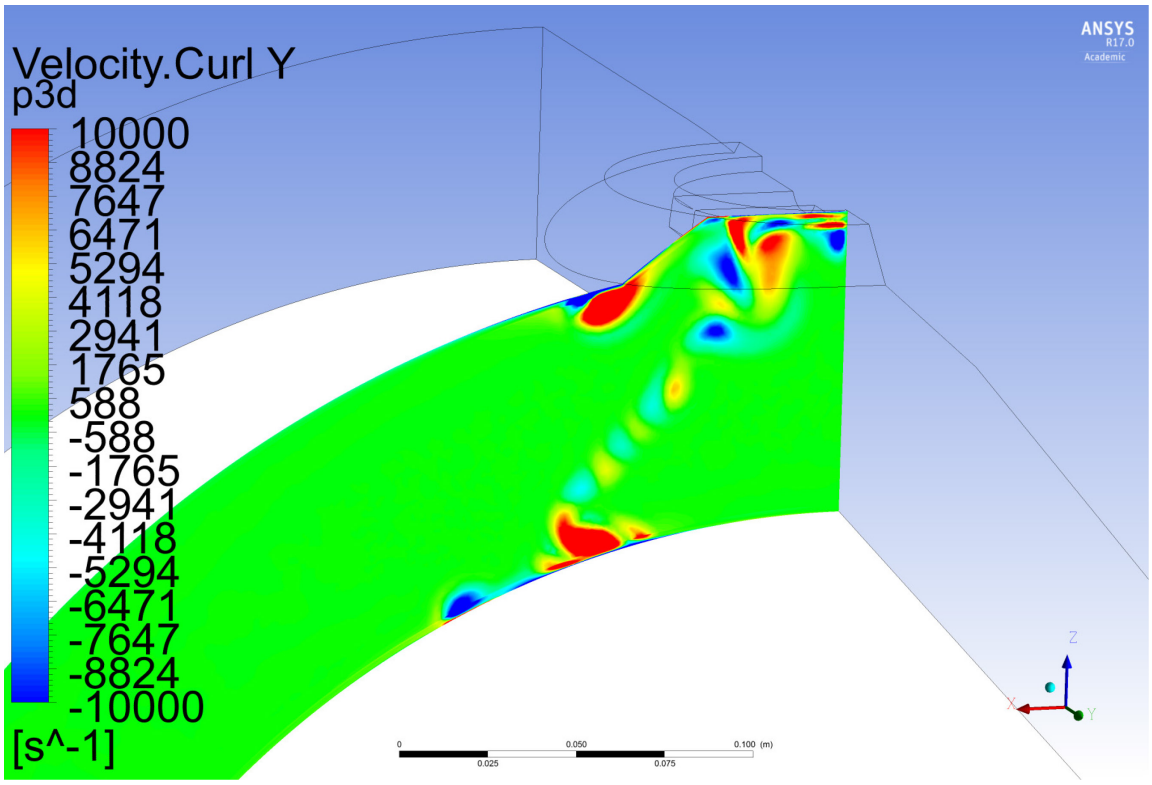

Figure 120 – Computational stream-wise vorticity at 3D, 80% CFS

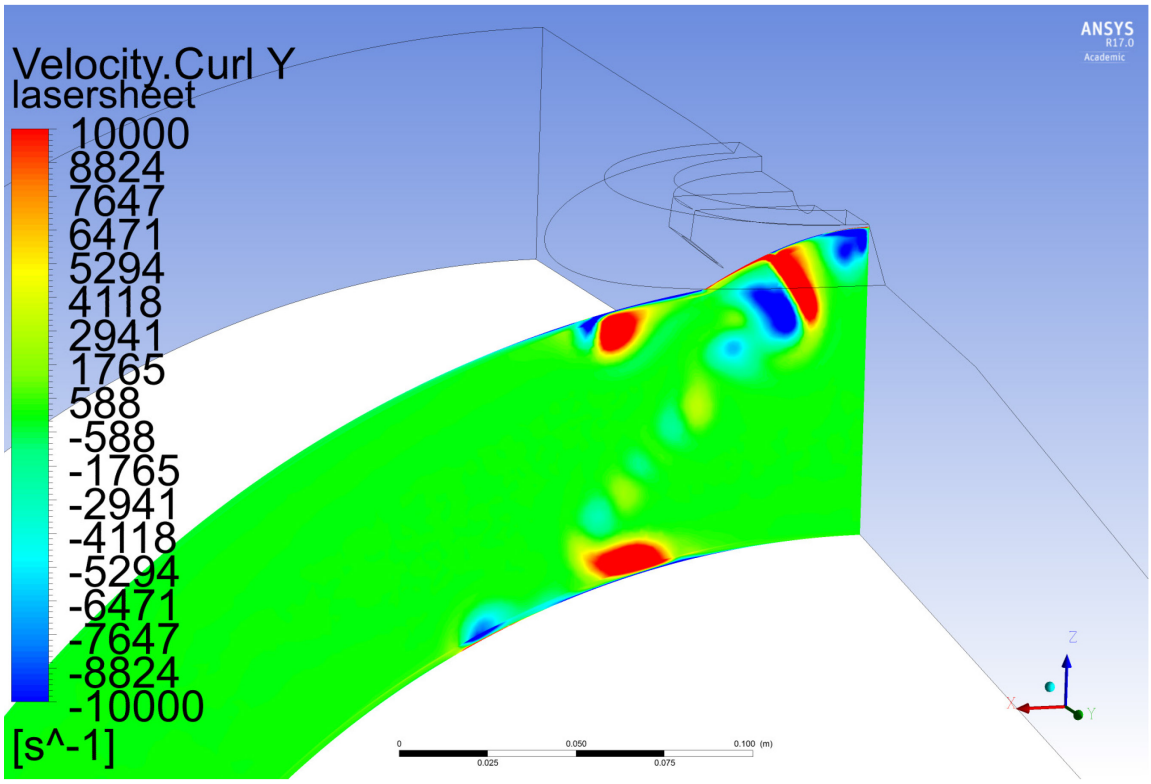

Figure 121 – Computational stream-wise vorticity at 4.5D, 80% CFS

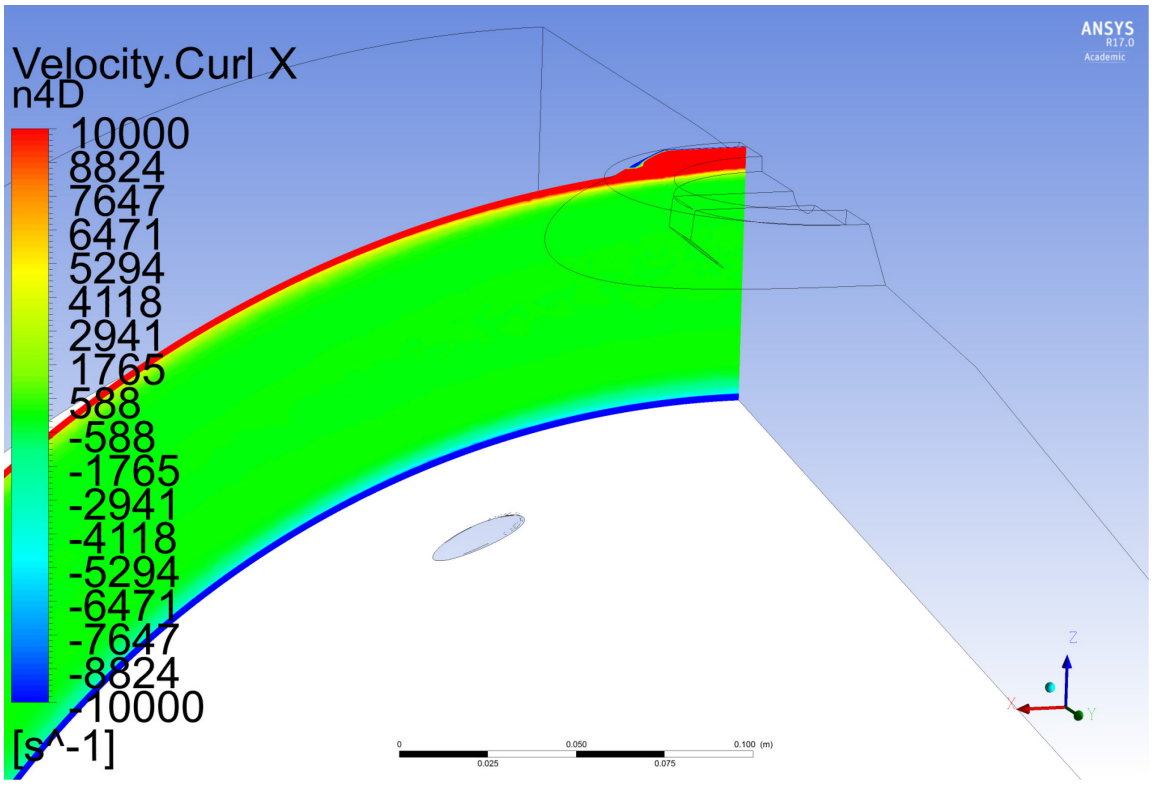

Figure 122 – Computational horizontal vorticity at -4D, 80% CFS

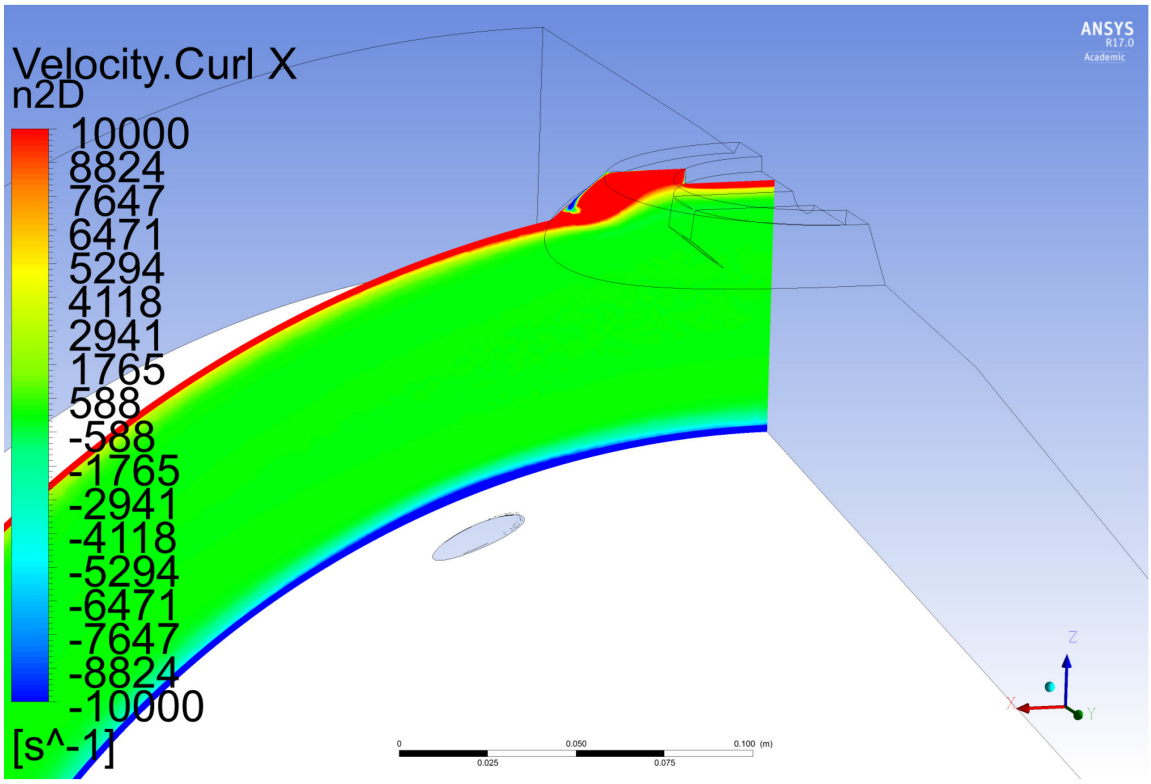

Figure 123 – Computational horizontal vorticity at -2D, 80% CFS

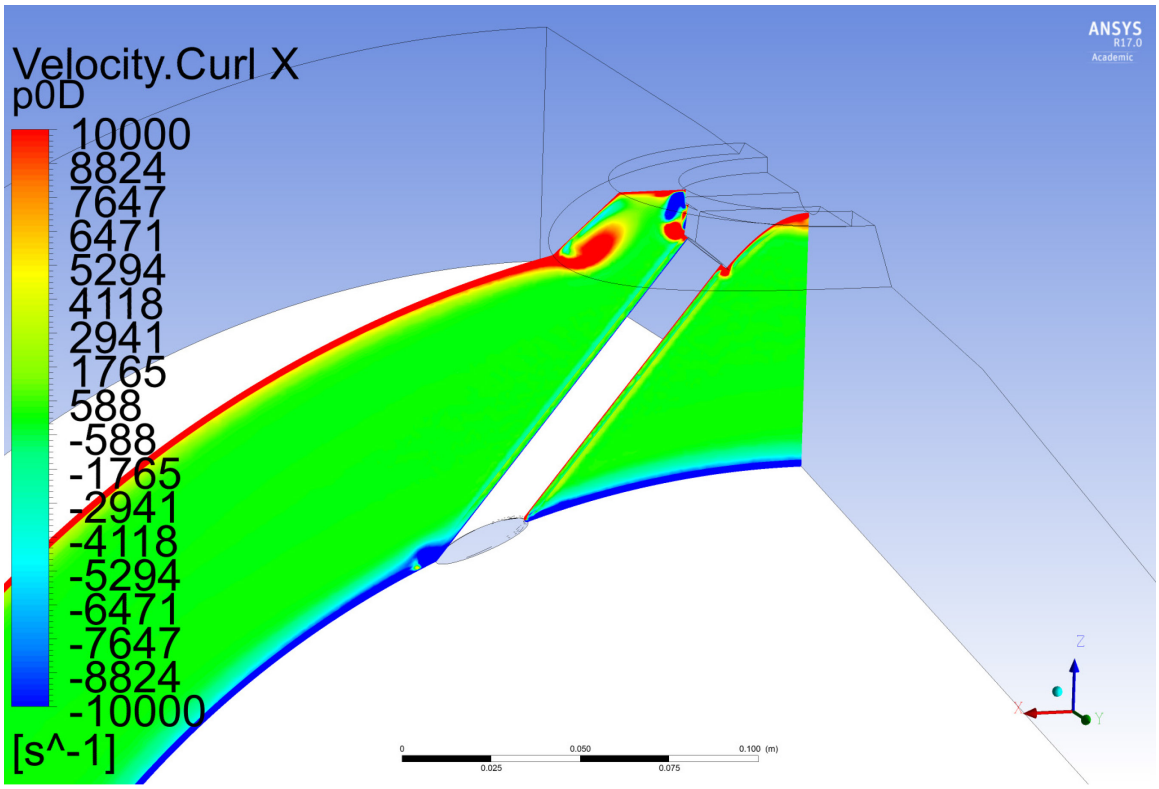

Figure 124 – Computational horizontal vorticity at 0D, 80% CFS

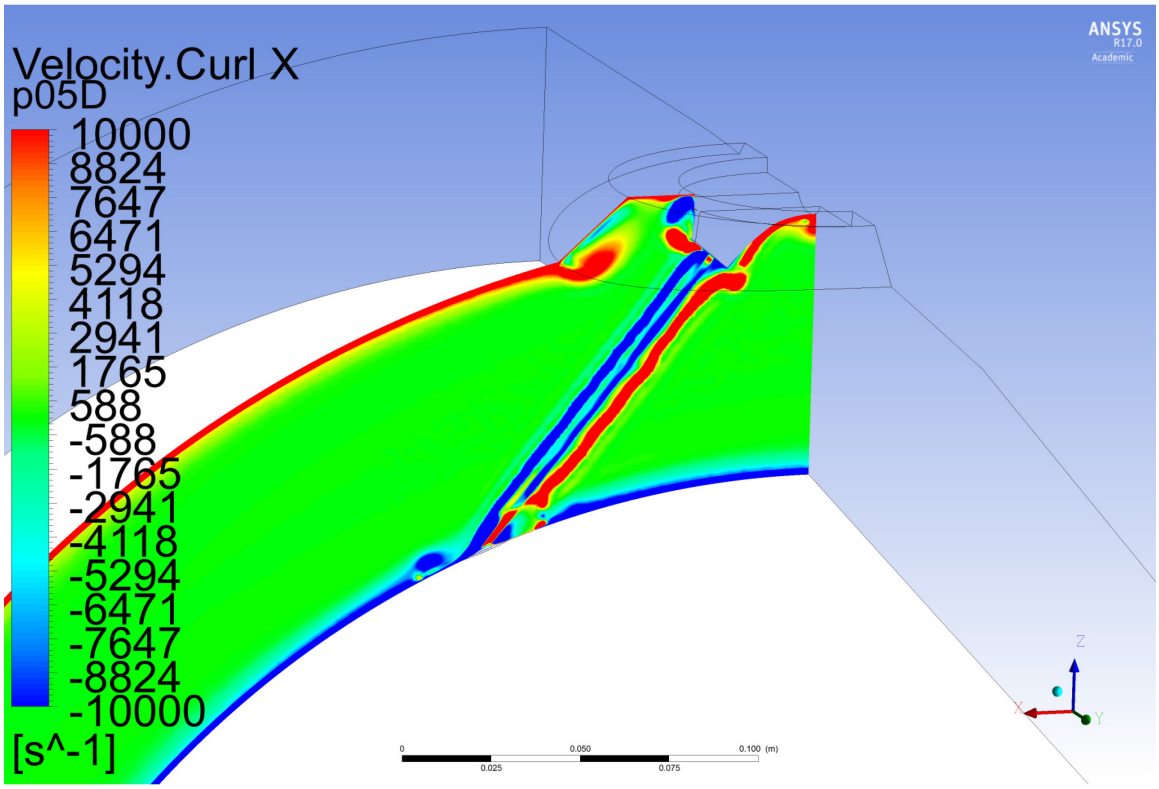

Figure 125 – Computational horizontal vorticity at 0.5D, 80% CFS

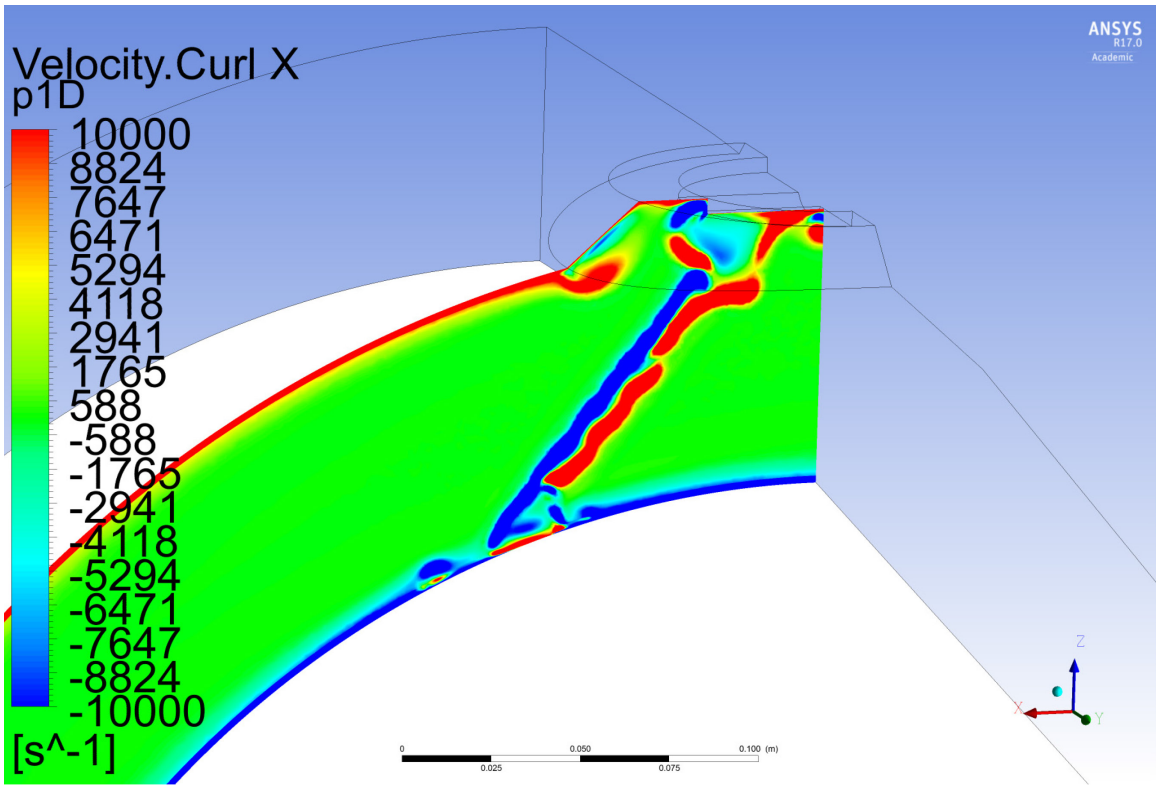

Figure 126 – Computational horizontal vorticity at 1D, 80% CFS

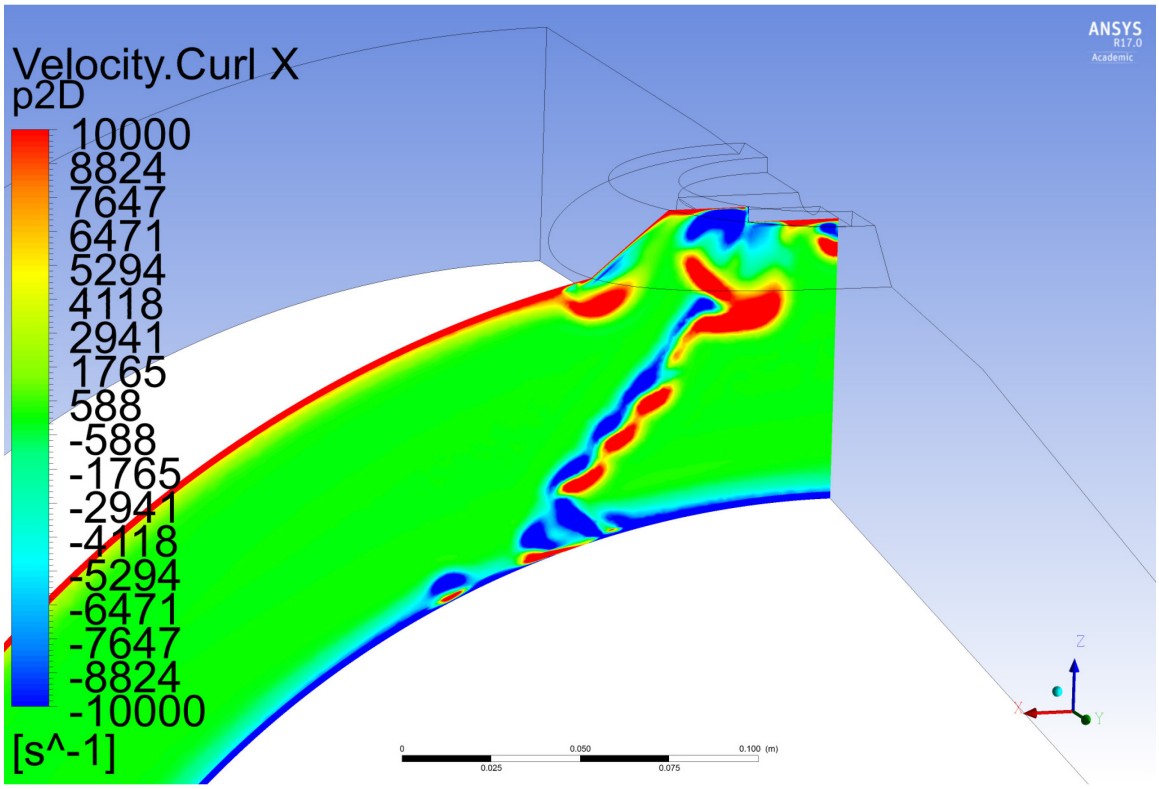

Figure 127 – Computational horizontal vorticity at 2D, 80% CFS

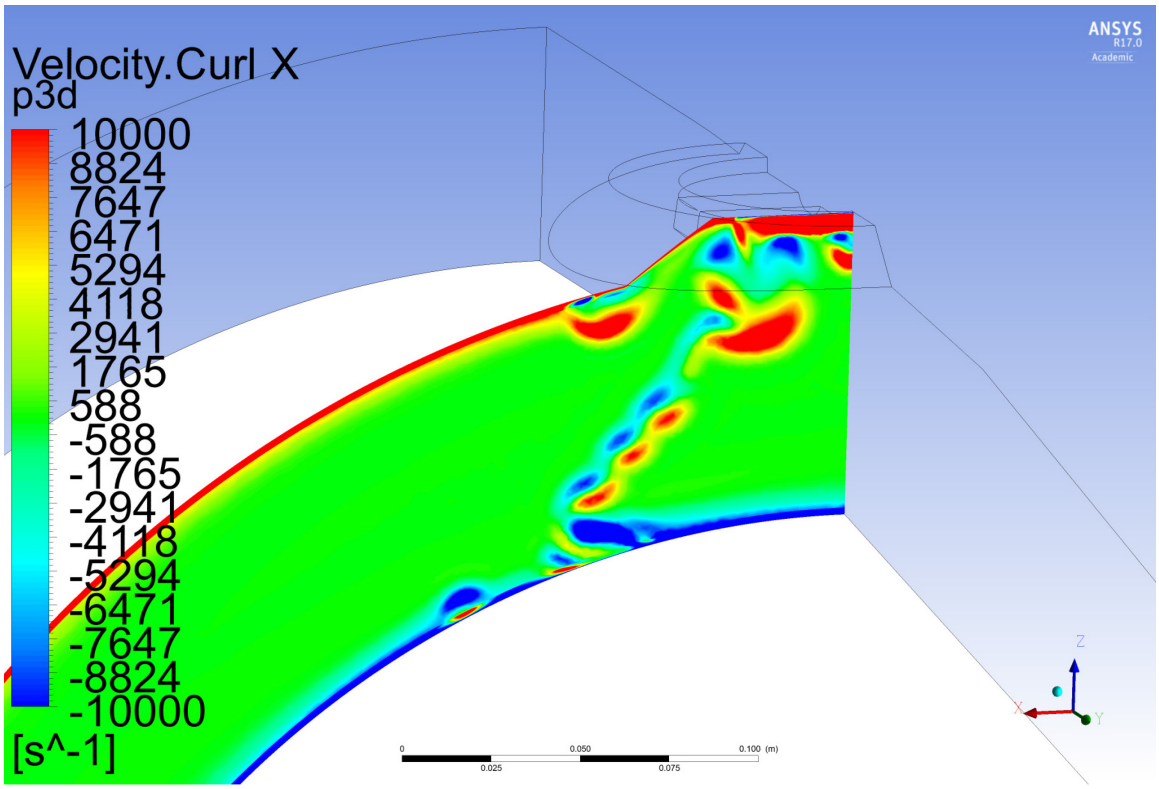

Figure 128 – Computational horizontal vorticity at 3D, 80% CFS

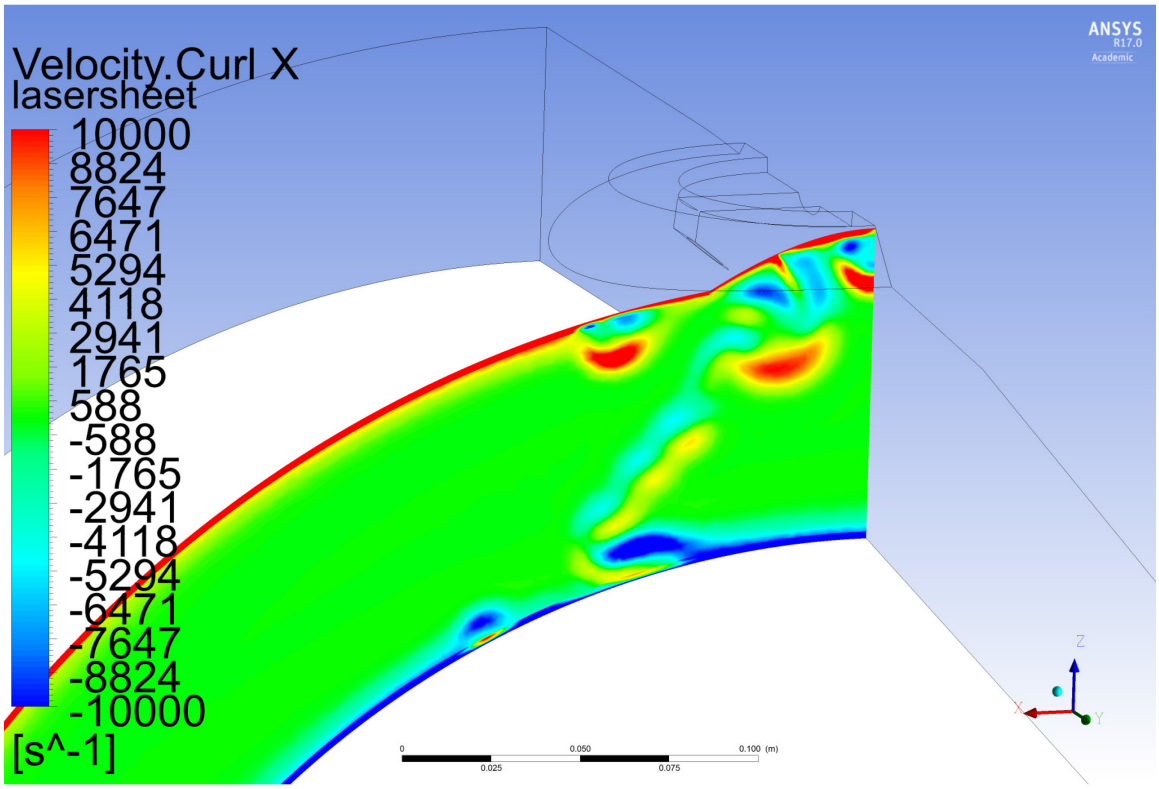

Figure 129 – Computational horizontal vorticity at 4.5D, 80% CFS

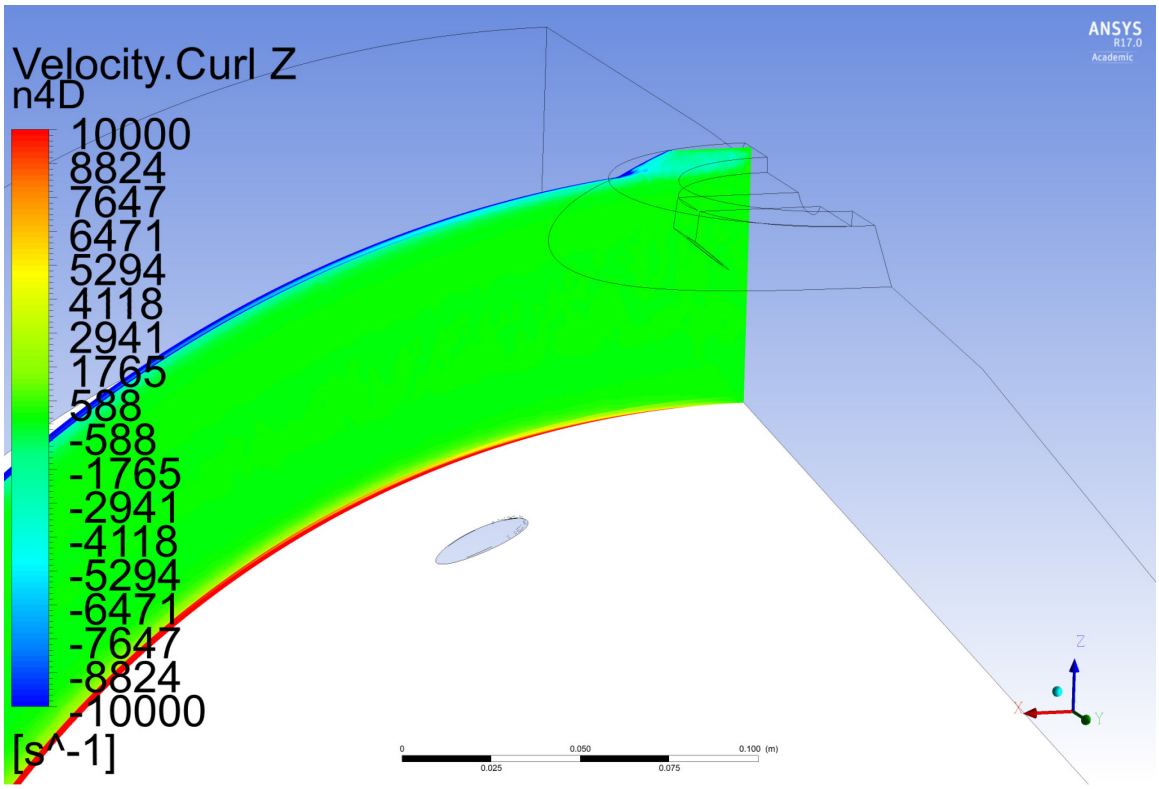

Figure 130 – Computational vertical vorticity at -4D, 80% CFS

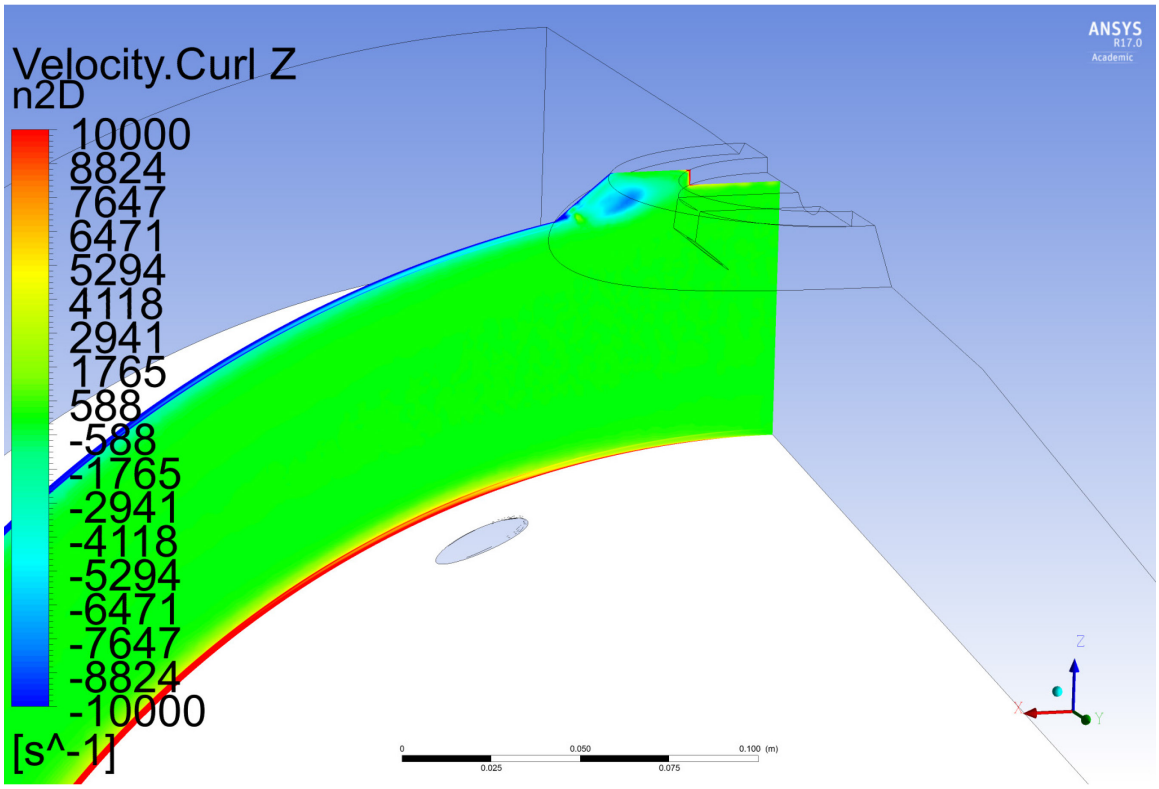

Figure 131 – Computational vertical vorticity at -2D, 80% CFS

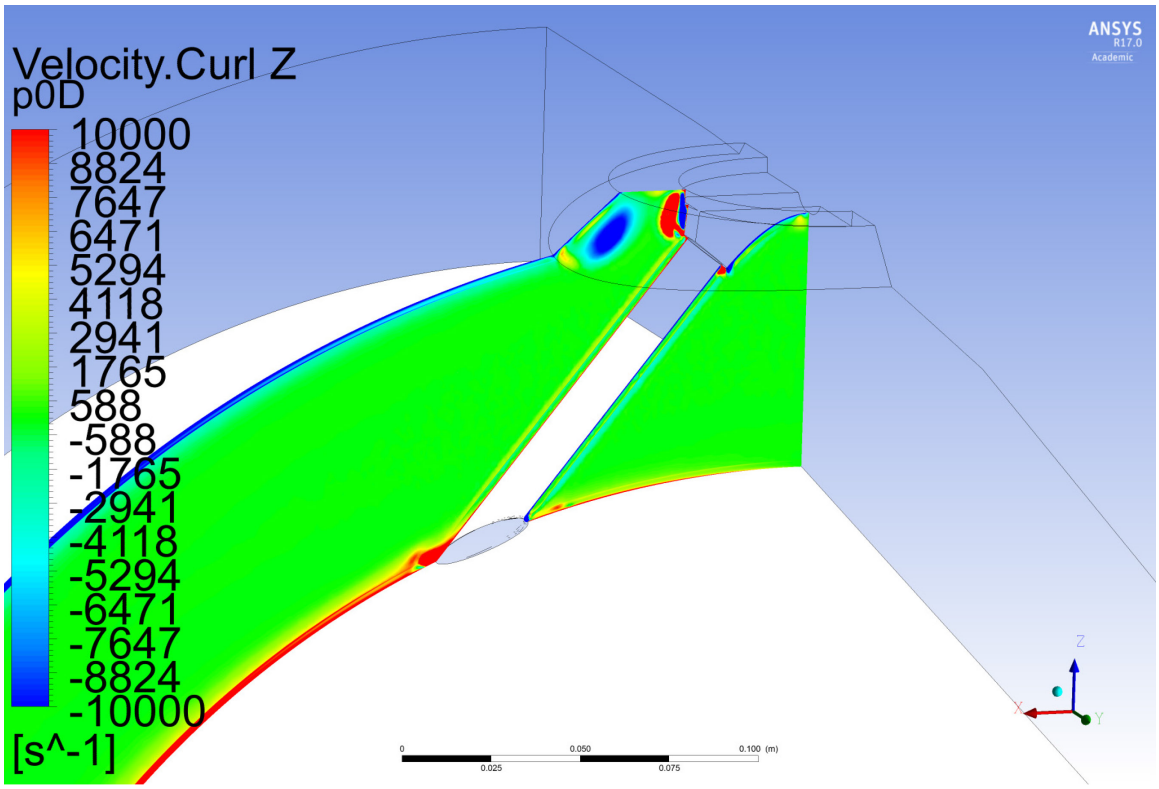

Figure 132 – Computational vertical vorticity at 0D, 80% CFS

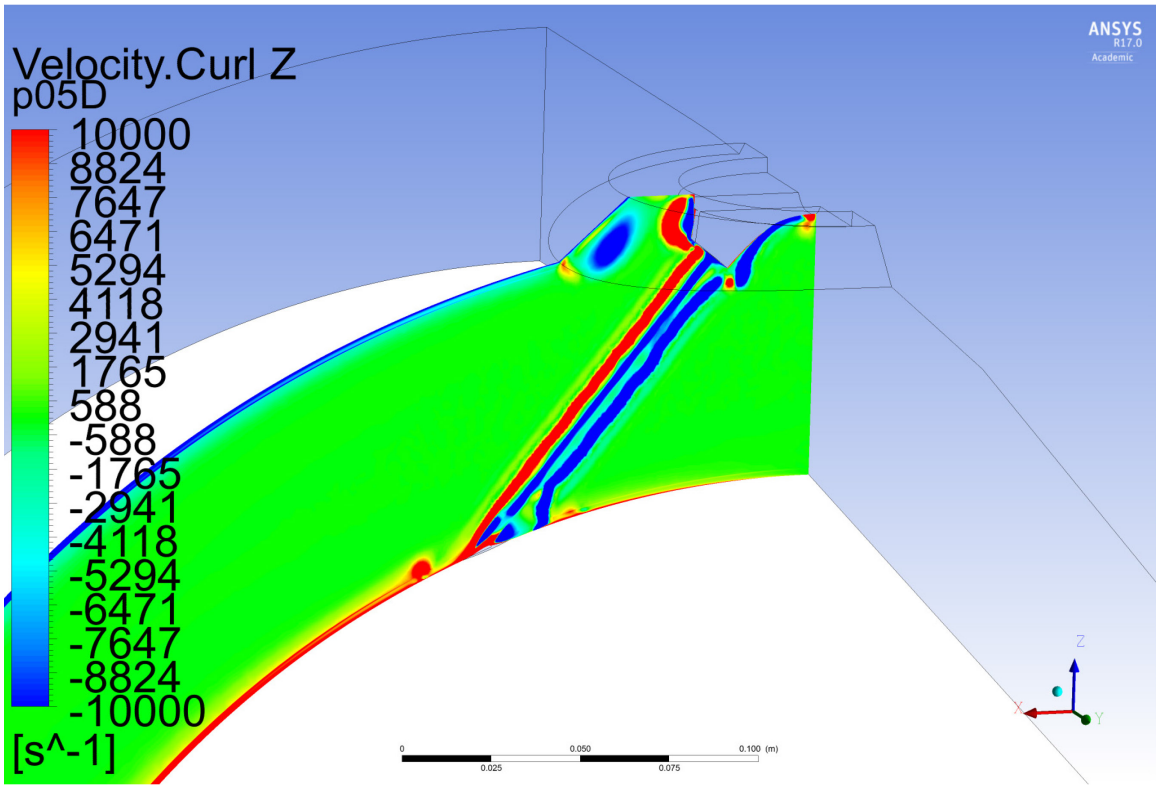

Figure 133 – Computational vertical vorticity at 0.5D, 80% CFS

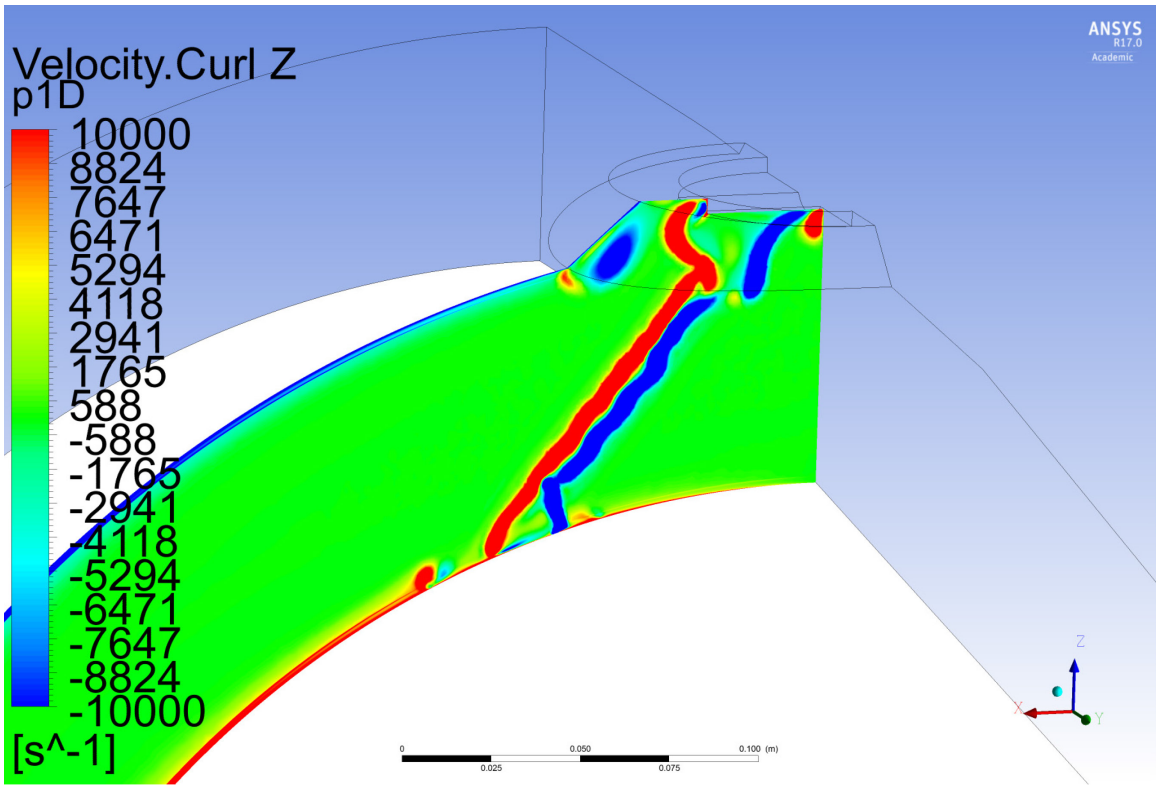

Figure 134 – Computational vertical vorticity at 1D, 80% CFS

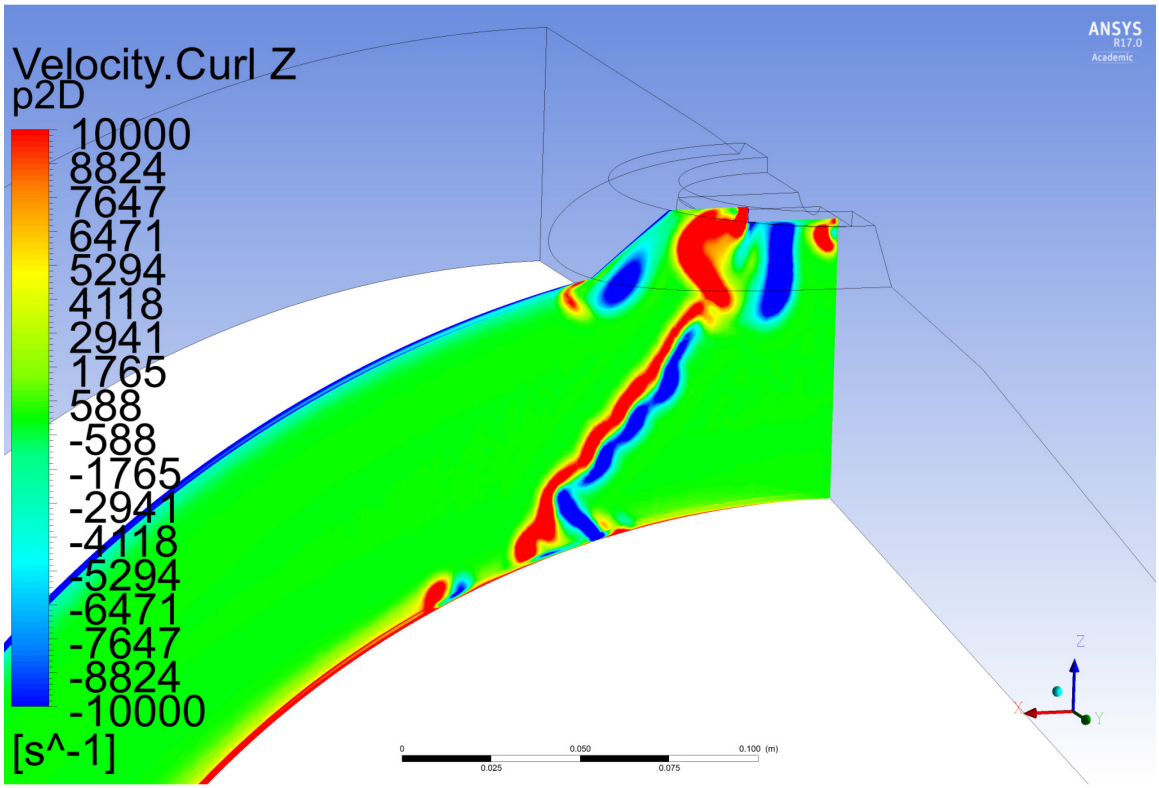

Figure 135 – Computational vertical vorticity at 2D, 80% CFS

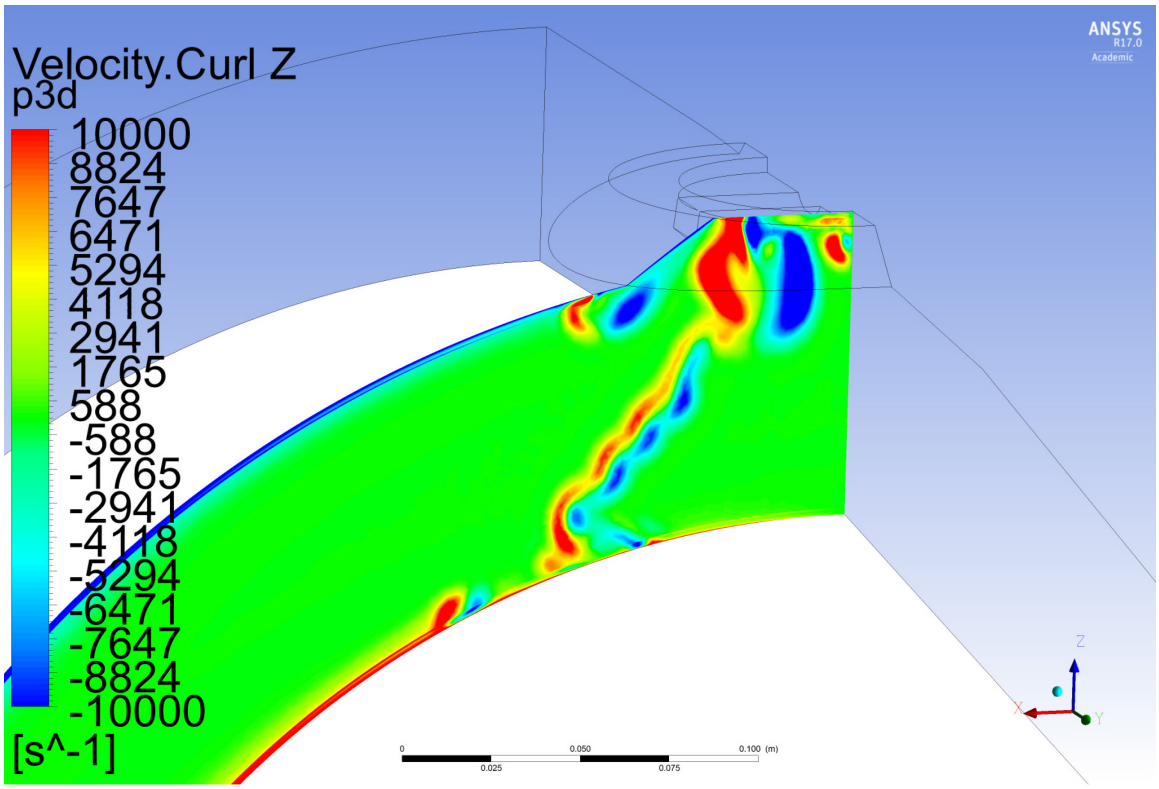

Figure 136 – Computational vertical vorticity at 3D, 80% CFS

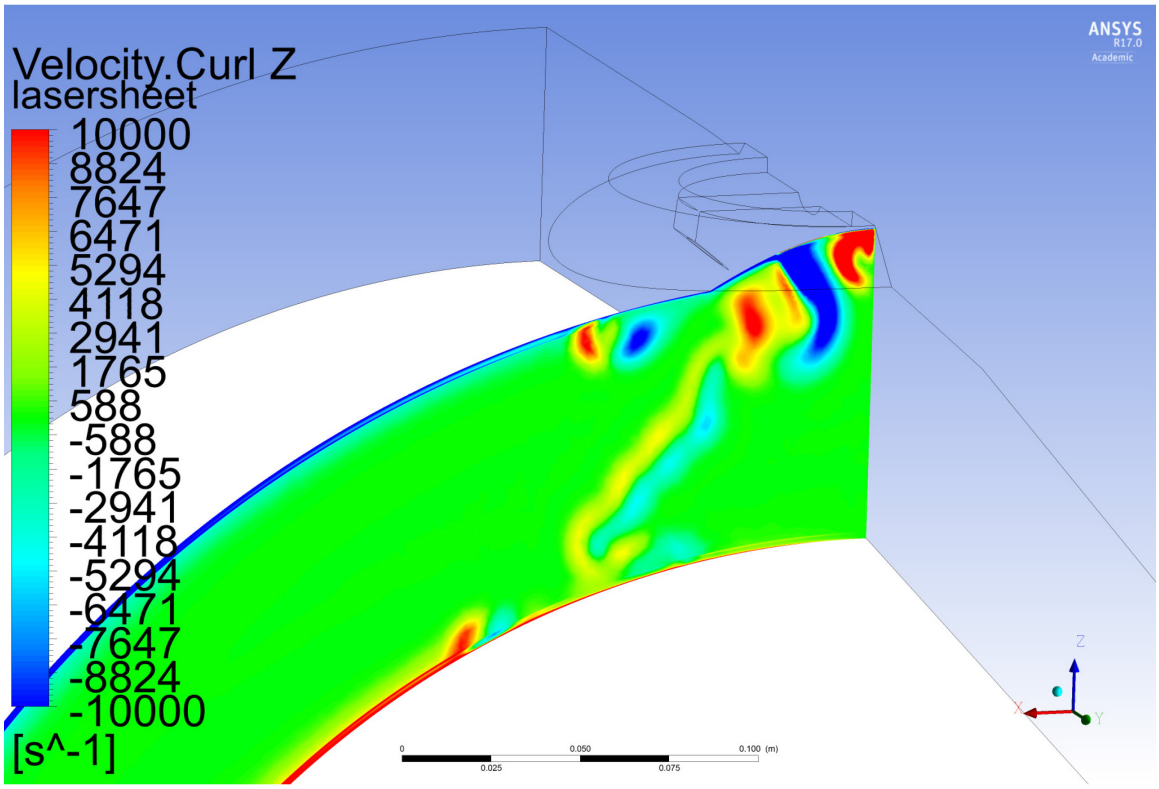

Figure 137 – Computational vertical vorticity at 4.5D, 80% CFS

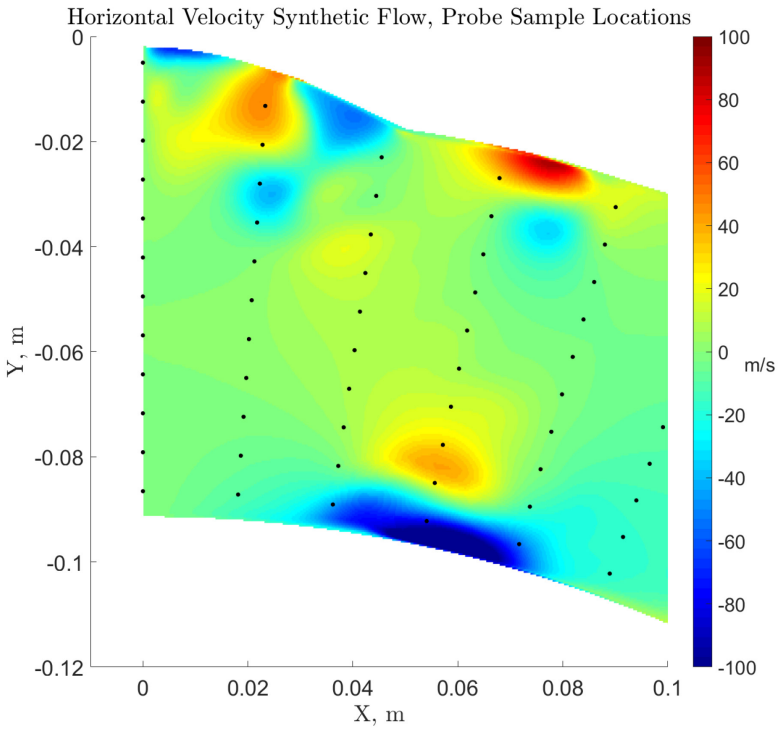

Figure 138 – Synthetic horizontal velocity with probe sampling locations

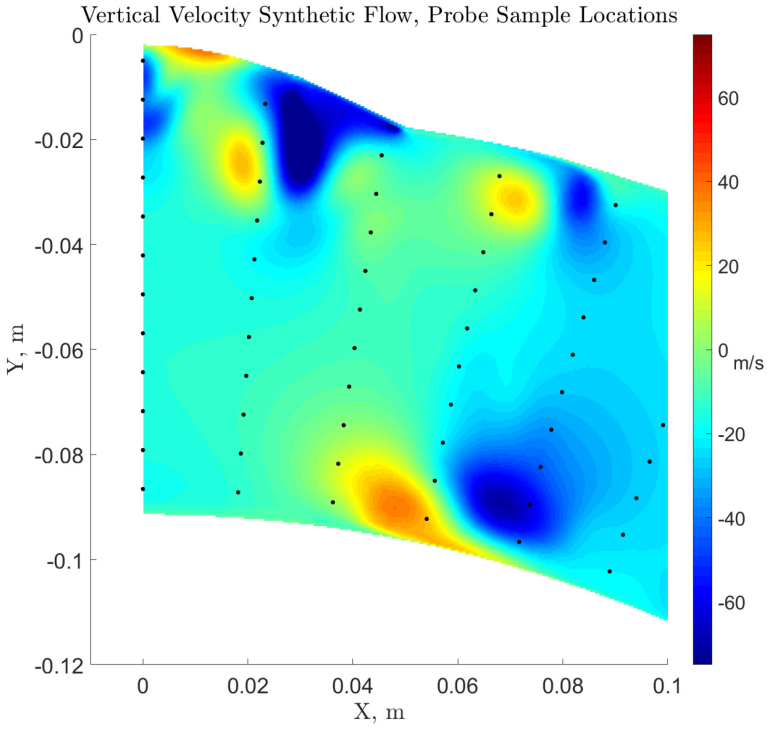

Figure 139 – Synthetic vertical velocity with probe sampling locations

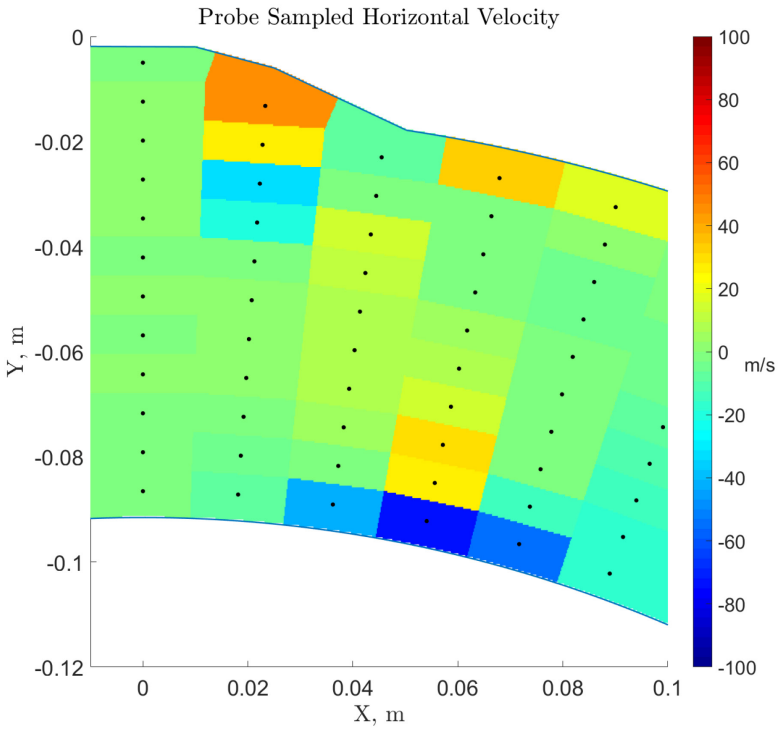

Figure 140 – Prove sampled horizontal velocity

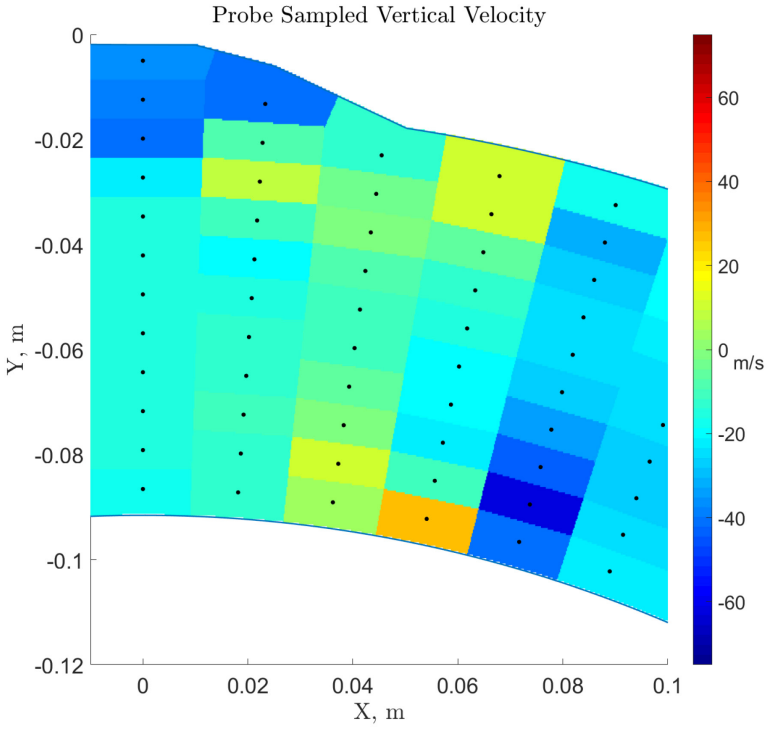

Figure 141 – Probe sampled vertical velocity

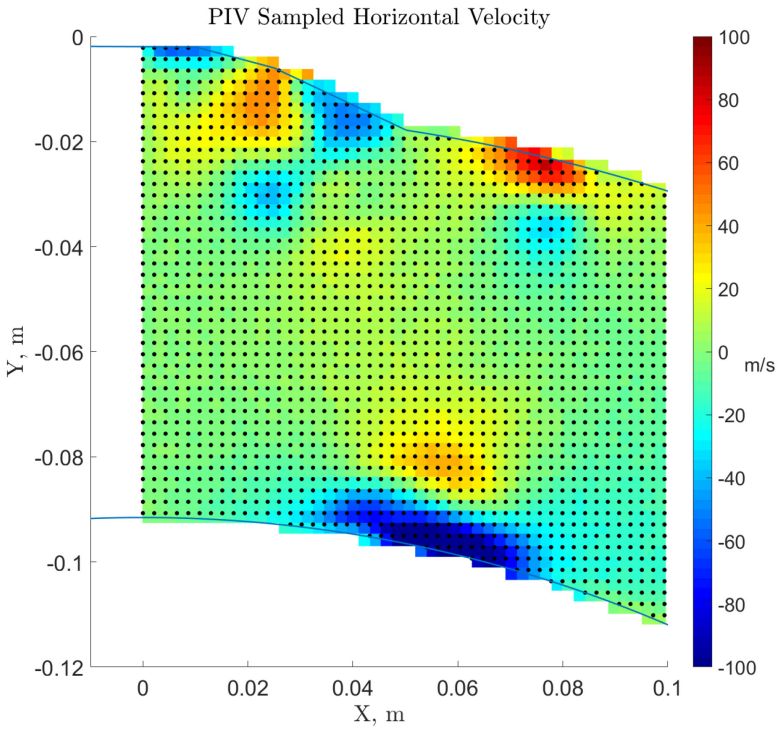

Figure 142 – PIV sampled horizontal velocity

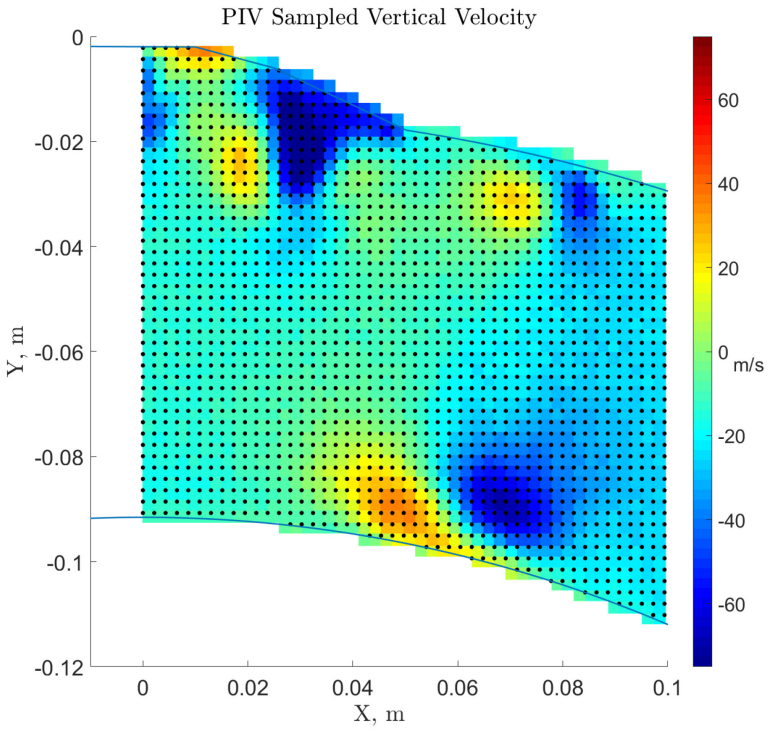

Figure 143 – PIV sampled vertical velocity

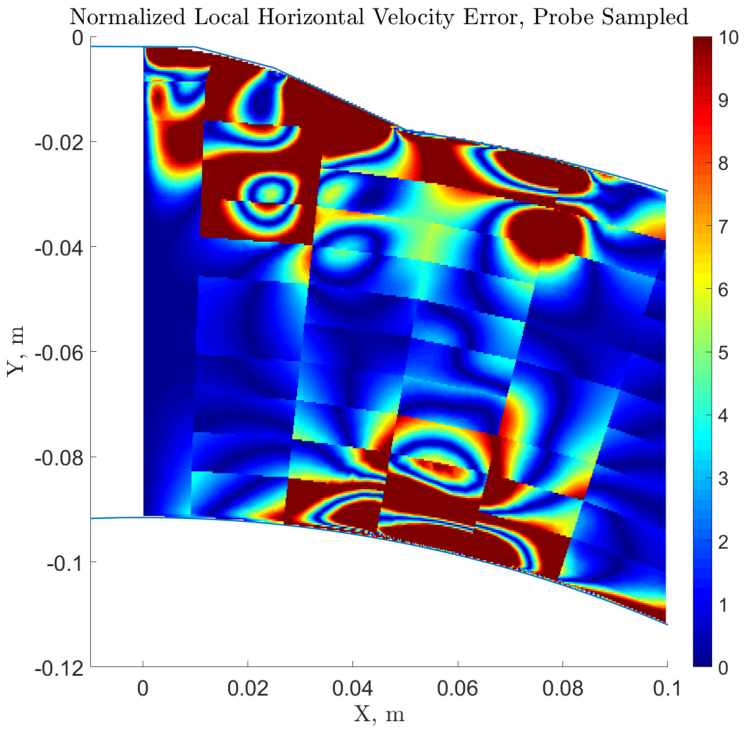

Figure 144 – Normalized local horizontal velocity error distribution, probe sampled

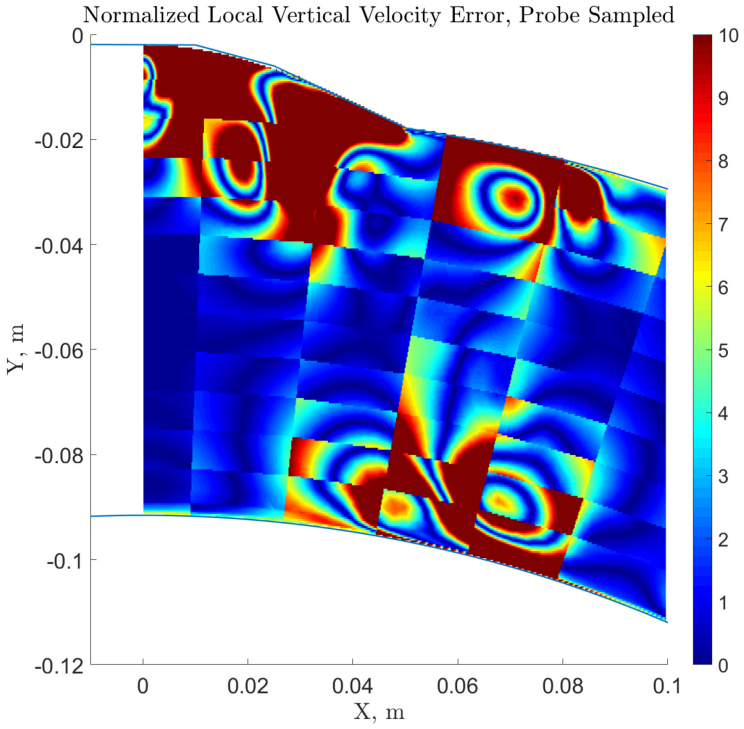

Figure 145 – Normalized local vertical velocity error distribution, probe sampled

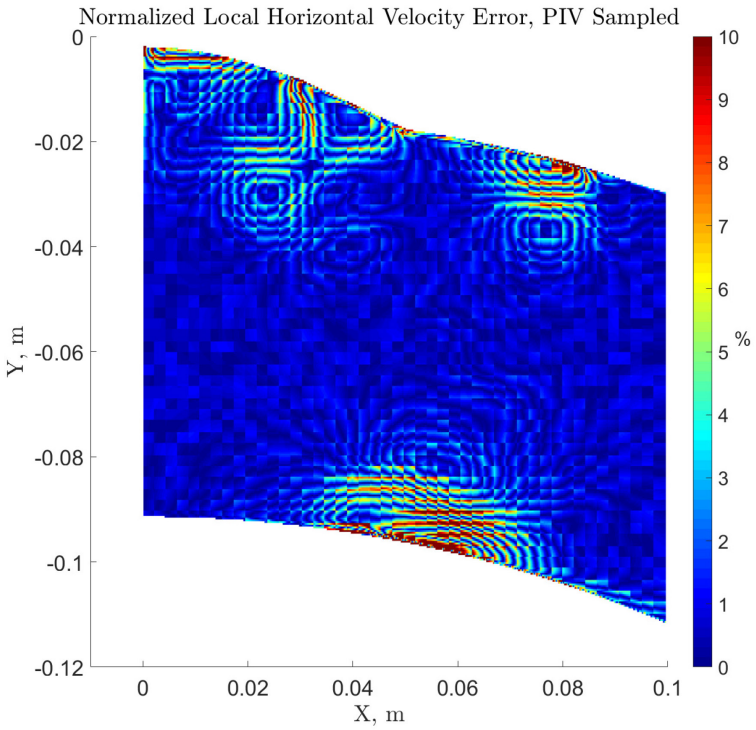

Figure 146 – Normalized local horizontal velocity error distribution, PIV sampled

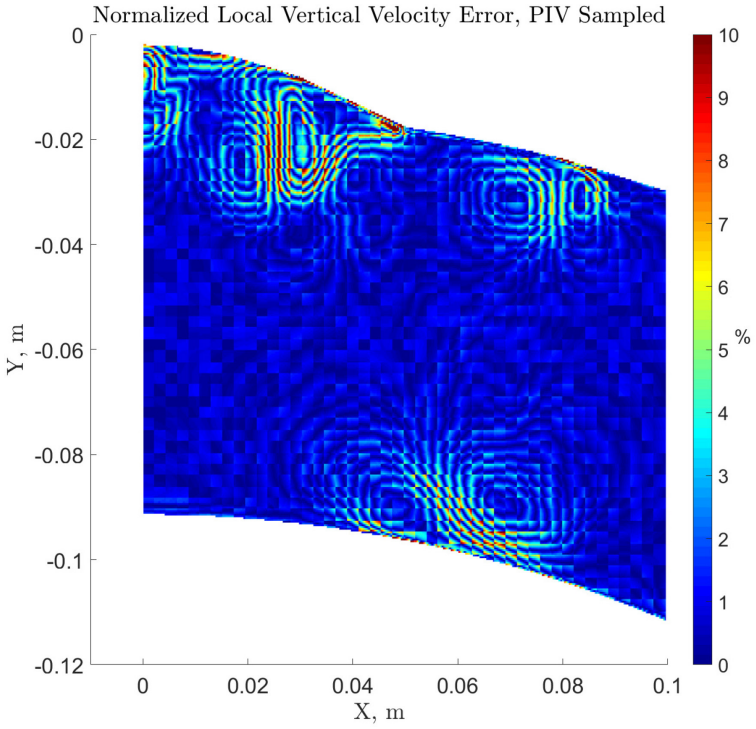

Figure 147 – Normalized local vertical velocity error distribution, PIV sampled

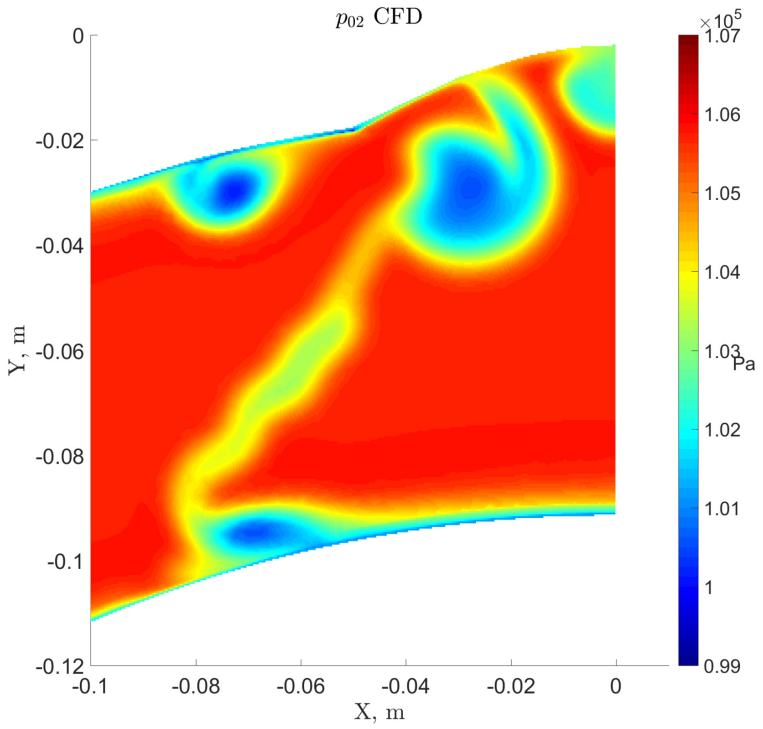

Figure 148 – Downstream total pressure, CFD Idle

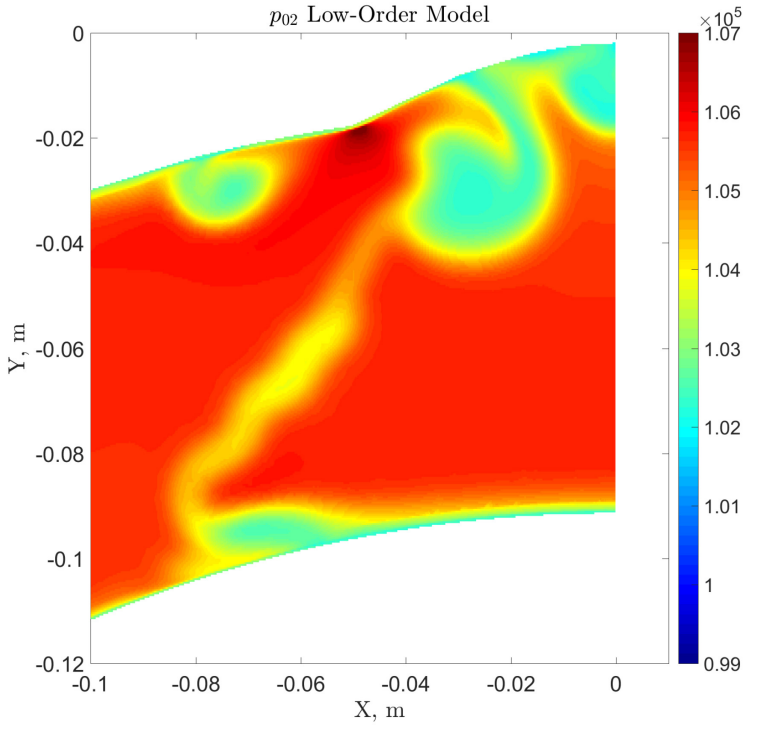

Figure 149 – Downstream total pressure, quasi-one dimensional model applied to CFD Idle

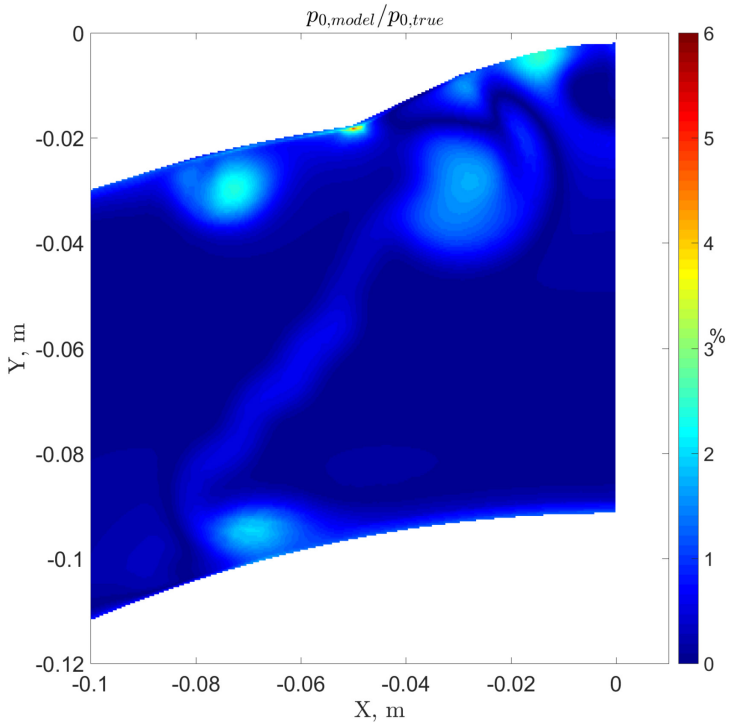

Figure 150 – Downstream total pressure error, quasi-one dimensional model and CFD Idle

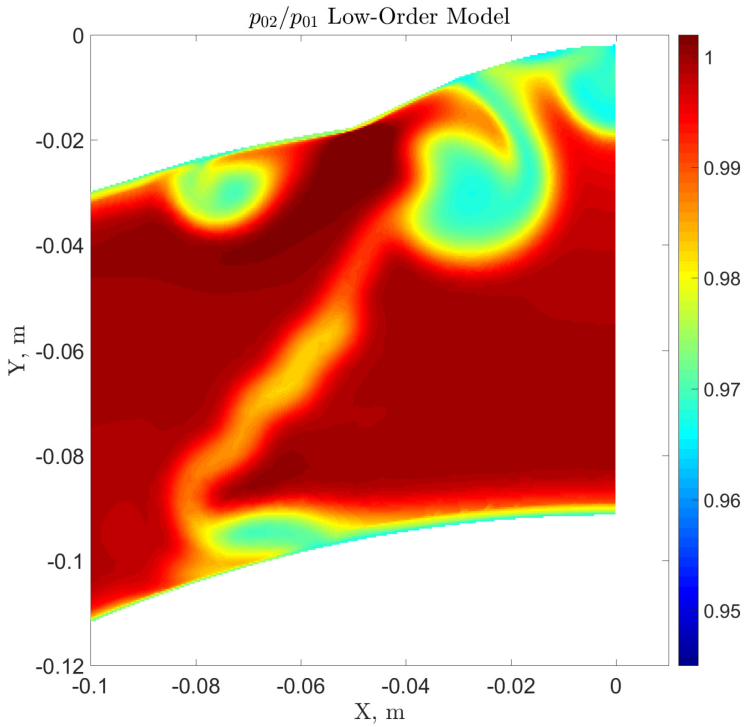

Figure 151 – Total pressure ratio, quasi-one dimensional model applied to CFD Idle

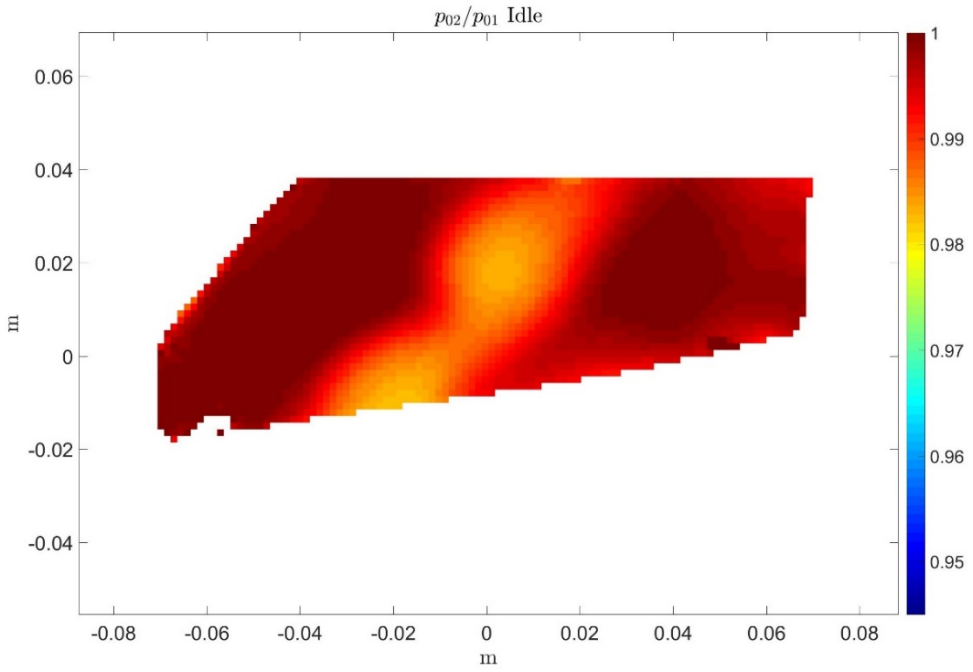

Figure 152 – Total pressure ratio, low order model applied to PIV data Idle